

INELASTIC ELECTRON-DEUTERON SCATTERING AND THE
STRUCTURE OF THE NEUTRON

by

ARIE BODEK

S.B., Massachusetts Institute of Technology

(1968)

SUBMITTED IN PARTIAL FULFILLMENT OF
THE REQUIREMENTS FOR THE DEGREE
OF DOCTOR OF PHILOSOPHY

at the

MASSACHUSETTS INSTITUTE OF TECHNOLOGY

December 1972 (i.e. Feb. 1973)

Signature of Author.....

Department of Physics, December 4, 1972

Certified by.....

Thesis Supervisor

Accepted by

Chairman, Departmental Committee on Graduate Students



-2-

INELASTIC ELECTRON-DEUTERON SCATTERING AND THE
STRUCTURE OF THE NEUTRON

by

ARIE BODEK

Submitted to the Department of Physics on December 4, 1972,
in partial fulfillment of the requirements for the degree of
Doctor of Philosophy

ABSTRACT

Deep inelastic electron-proton and electron-deuteron cross sections have been measured at 18° , 26° , and 34° using the SLAC 8-GeV spectrometer facility. Incident electron energies ranged from 4.5 GeV to 18.0 GeV. The square of the four momentum transfer ranged from $q^2 = 0.5 \text{ (GeV/c)}^2$ to a q^2 of 20 (GeV/c)^2 . Emphasis was put on extraction of proton and neutron structure functions, and extraction of the neutron to proton cross section ratios. Studies were made of the deuteron nuclear binding effects on the scattering, and these effects were incorporated into the analysis. In combination with earlier results the data on the neutron-proton cross section ratio extends from a value of the scaling variable ω of 25 down to 1.17. The neutron cross sections were determined to be almost the same as the proton cross sections at high ω , but were found to decrease to about 38 % of the proton cross section at an ω around 1.25.

Thesis Supervisor: Henry W. Kendall
Title: Professor of Physics

Acknowledgments

The analysis of this experiment was carried through by Edward M. Riordan and myself. E. M. Riordan concentrated on aspects relating to the separation of the longitudinal and transverse cross sections for the proton and the deuteron, while I concentrated on extraction of the neutron to proton cross section ratios. This close collaboration resulted in a more rigorous analysis than would have been possible otherwise. I thank my group co-leaders Jerome I. Friedman and Henry W. Kendall for their help and supervision throughout my graduate career. I also wish to thank the other physicists who participated in the running of the experiment including David Coward from SLAC and Martin Breidenbach, John E. Elias, Michael R. Sogard, J. Scott Poucher, and Kosta Tsipis all from M.I.T. . Valuable help with the computer programs was provided by Robin Verdier, Elaine Miller and Deena Dubin (who also participated in the running of the experiment). Help from Charlie Sinclair and other members of the SLAC SFC group is also much appreciated. The author wishes to thank Guthrie Miller and Charlie Jordan for valuable assistance and helpful discussions. Help from Les Cottrell, Elliot Bloom, and other members of SLAC Group A is appreciated.

Special gratitude goes to all members of the SLAC staff and management who have made SLAC a first rate experimental facility.

Financial support from the M.I.T. Physics Departement is much appreciated.

Special thanks goes to William Atwood of SLAC Group A for valuable help and numerous stimulating discussions concerning the smearing corrections to the deuteron data.

TABLE OF CONTENTS

	Page
Abstract	2
Acknowledgements	3
List of Figures	9
List of Tables	12
1. Introduction	13
1.1 Opening Words	13
1.2 Theory	19
1.3 The Experiment	25
2. Apparatus and its Use in the Data Analysis	32
2.1 General Setup	32
2.2 Beam and its Parameters	34
2.3 Charge Monitors	37
2.4 Target and Density Monitors	40
2.5 Spectrometer	50
2.6 General Setup of Particle Detectors	54
2.7 Cerenkov Counter	58
2.8 Hodoscopes, Codes and Classes	60
2.9 de/dx Counters	64
2.10 TA, TTA, and Anti-Counters	66
2.11 Electronics	71
2.12 Data Recording and On-Line Analysis	76

Table of Contents (cont.)

	Page
3. Data Analysis, Cross Sections and Errors	78
3.1 Summary of Correction Factors	78
3.2 General Off-Line Computer Programs	83
3.3 PASS1 - Event Analysis	86
3.4 PASS2 - Run Combination, Raw Cross Sections and Errors	90
3.5 Radiators in the Beam Line	94
3.6 Radiative Corrections Introduction	96
3.7 Elastic and Quasielastic Tails	97
3.8 Inelastic Radiative Corrections	103
3.9 Nuclear Binding Effects, Smearing, Unsmearing, and Structure Function Fitting	107
3.10 Final Cross Sections, σ_n/σ_p Ratios, and Error Analysis.	117
4. Interpretation of Results and Comparison with Theories	130
4.1 Investigations of a Few Scaling Variables	130
4.2 A Representative Parton Model, the Kuti-Weisskopf Model	139
4.3 Duality and Local Duality	145

Table of Contents (cont.)

	Page
4.4 $\delta s/\delta t$ for Hydrogen and Deuterium	173
4.5 Discussion	179
Appendix A: Nuclear Binding Effects in Inelastic Electron Deuteron Scattering	186
A1 Introduction	186
A2 Derivations - The Off-Mass-Shell Approach	190
A3 Derivations - The On-Mass-Shell Approach	200
A4 Smearing in the Scaling Limit and its implication on W_1/W_2 for the Deuteron	209
A5 Smear Cross Sections Directly - Questions of Flux	211
A6 Summary of Possible Indicators of the Magnitude of the Theoretical Error	218
A7 Theoretical Considerations in Smearing	219
A8 Experimental Tests of Smearing	221
A9 Corrections to the Impulse Approximation	227
A10 The Glauber Correction in Electroproduction	233
A11 Choice of a Smearing Procedure and Error Discussion	238
A12 Summary	245

Table of Contents (cont.)

	Page
Appendix B: The Nucleon Elastic Form Factors	246
Appendix C: Number of Pulses	248
Appendix D: Final Cross Sections, and σ_n/σ_p Ratios	250
D1 Introduction	250
D2 Hydrogen and Deuterium Cross Sections	251
D3 Neutron to Proton Cross section Ratios	258
D4 Combined Neutron to Proton Cross Section Ratios and Structure Function Differences as Functions of X and X'	265
References	273
Biographical Note	278

List of Figures

No.	Page
1. Inelastic Electron Scattering	18
2. The Kinematic Range of the Data in E_0 and E'	29
3. The Kinematic Range of the Data in q and W	30
4. The Stanford Linear Accelerator	31
5. The Dual Target Assembly	48
6. The SLAC 1.6 GeV/c Spectrometer	49
7. The Experimental Setup	52
8. The SLAC 8 GeV/c Spectrometer Setup	53
9. The SLAC 8 GeV/c Spectrometer Detector Assembly	57
10. The Fast Electronics	74
11. The Ratio of the Smeared Neutron and Proton Cross Sections as a Function of X	120
12. The Ratio of the Smeared Neutron and Proton Cross Sections as a Function of X'	121
13. The Ratio of the Unsmeared Neutron and Proton Cross Sections as a Function of X	122
14. The Ratio of the Unsmeared Neutron and Proton Cross Sections as a Function of X'	123

List of Figures (Cont.)

No.		Page
15	Comparison of σ_{ns}/σ_{ps} with the Predictions of the Model of Kuti and Weisskopf	144
16	Comparison of σ_n/σ_p with the Predictions of the Bloom-Gilman Local Duality Model	151
17	The Difference of the Smeared Neutron and Proton Structure Functions ($\nu W_{2ps} - \nu W_{2ns}$) as a Function of X	152
18	The Difference of the Smeared Neutron and Proton Structure Functions ($\nu W_{2ps} - \nu W_{2ns}$) as a Function of X'	153
19	The Difference of the Unsmeared Neutron and Proton Structure Functions ($\nu W_{2p} - \nu W_{2n}$) as a Function of X	154
20	The Difference of the Unsmeared Neutron and Proton Structure Functions ($\nu W_{2p} - \nu W_{2n}$) as a Function of X'	155
21	σ_s/σ_t for the Proton and the Deuteron as a Function of q^2	156
22	νW_{2p} vs. X' at $\theta = 5.988$, $q^2 = 0.25, 1.0$ and 3.0	157
23	νW_{2p} vs. X' at $\theta = 10.000$, $q^2 = 1.0, 2.0$ and 4.0	158
24	νW_{2d} vs. X' at $\theta = 5.988$, $q^2 = 0.25, 1.0$ and 3.0	159
25	νW_{2d} vs. X' at $\theta = 10.000$, $q^2 = 1.0, 2.0$ and 4.0	160

List of Figures (Cont.)

No.		Page
26	νW_{2p} vs. X for $W > 2$ GeV, $q^2 > 1.0$ (GeV/c) ²	161
27	νW_{2p} vs. X' for $W > 2$ GeV, $q^2 > 1.0$ (GeV/c) ²	162
28	νW_{2d} vs. X for $W > 2$ GeV, $q^2 > 1.0$ (GeV/c) ²	163
29	νW_{2d} vs. X' for $W > 2$ GeV, $q^2 > 1.0$ (GeV/c) ²	164
30	νW_{2p} vs. X in Combined Form	165
31	νW_{2p} vs. X' in Combined Form	166
32	νW_{2d} vs. X in Combined Form	167
33	νW_{2d} vs. X' in Combined Form	168
34	νW_{2p} vs. X for $W > 2.6$ GeV and $q^2 > 1.0$ (GeV/c) ²	169
35	νW_{2p} vs. X' for $W > 2.6$ GeV and $q^2 > 1.0$ (GeV/c) ²	170
36	νW_{2d} vs. X for $W > 2.6$ GeV and $q^2 > 1.0$ (GeV/c) ²	171
37	νW_{2d} vs. X' for $W > 2.6$ GeV and $q^2 > 1.0$ (GeV/c) ²	172
38	The prediction of the Drell-Lee model for W_{ln}/W_{lp}	185
A1	Inelastic Electron Deuteron Scattering	188
A2	Inelastic Electron Deuteron Scattering in the Impulse Approximation	189
A3	Inelastic e-p and e-d Scattering	201
A4	Definitions of Kinematic Variables	202
A5	Interference Diagrams in Single Pion Production	226
A6	The Error Band in $\delta n/\delta p$ due to the Uncertainty in the Smearing Correction.	244
B1	The Proton Form Factors	247

List of Tables

No.	Page
1. Summary of Beam Parameters	36
2. Hodoscope Codes	62
3. Radiation Lengths	95
4. Elastic and Quasielastic Tail Percentages	101
5. The Unsmearing Correction and its Error	119
6. T - The Correction Factor to ϕ_n/ϕ_p to get W _{2n} /W _{2p} as a Function of R _n and Epsilon	178
A1. Effects of the Various Choices on the Smearing Correction	242
A2. Representative Smearing Corrections	243

1 Introduction

1.1 Opening Words

Beams of monochromatic electromagnetically interacting particles have been widely used in the investigation of the inner structures of complex systems. Common examples are the study of the structure of crystals and large organic molecules by the use of X-rays and low energy electron scattering. The study of the atom by alpha particle scattering (the Rutherford experiment) established the existence of the atomic nucleus; and electron scattering by Hofstadter and others has established the size of nuclei and the nucleon^{charge} density in nuclei. Information about the inner structures of the neutron and the proton can be obtained from the scattering cross sections if the De-Broglie wavelength of the particle that is used as a probe is on the order of or smaller than the size of a nucleon. Electrons are particularly suitable since our knowledge of quantum electrodynamics allows us to understand the electromagnetic part of the process and separate out the electromagnetic effects from the effects caused by the studied nucleon. Beams of protons and mesons have been also used to study nucleon structure. Difficulties arise in the interpretation of the results, since the strong interactions are not

understood anywhere nearly as well as the electromagnetic interactions. With the availability of electron energies in the multi GeV range at SLAC, it has become possible to study the inner structures of the neutron and the proton.

In the asymptotic region where energies and momenta are much greater than the mass of the nucleon theoretical approximations are possible that enable one in principle at least to learn about possible nucleon constituents without a detailed knowledge of the dynamic theory of strong interactions. One hopes that the information gained will contribute to the understanding of the nucleon and thus help in the formulation of a strong interaction theory.

Studies of the structure of the proton have been done by elastic and inelastic electron proton scattering experiments. The measurements of the proton elastic form factors have provided information on the charge and magnetic moment distributions in the proton. Inelastic electron proton scattering has opened a new channel of information. Unlike the elastic case, where the final hadronic state is a free proton, the final hadronic state in the inelastic process can include any number of additional particles. In

the present experiment only the final scattered electron is detected, and no detailed information is known about the final hadronic state except its total mass (W) and the square of the momentum transfer (q^2). The information about the proton that can be obtained in this type of experiment can be summarized in the form of two proton inelastic structure functions $W_1(q^2, W)$ and $W_2(q^2, W)$.

No study of nucleon structure can be complete without a corresponding study of the structure of the neutron. Unbound protons are easily available in the form of a liquid hydrogen target. There are no neutron targets available. Experiments utilizing the scattering of neutron beams from atomic electrons have been done, but kinematic considerations limit such experiments to very low momentum and energy transfers. People have been thinking about experiments between an electron beam and reactor thermal neutrons, but flux considerations render this type of experiment unfeasible. The simplest system in which bound neutrons can be found is the deuteron. Since the deuteron is a two particle system bound by only 2.225 MeV, one might think that the binding effects can be neglected when the momentum transfers are on the order of a few (GeV/c) . Unfortunately, that is not the case, but the complications

arising from the nuclear binding effects in the deuteron can be handled theoretically (see appendix A), and the error arising from the theoretical uncertainty resulting from the internal motion in the deuteron is comparable to the statistical and systematic experimental errors. Elastic and quasielastic electron deuteron scattering, pion-deuteron, proton-deuteron, and other deuteron experiments have contributed to our increased understanding of the deuteron structure. The limit of the error in the extraction of the neutron structure functions is set by the limitations of the impulse approximation. Fortunately, the impulse approximation becomes better and better at high energies and high momentum transfers.

The interaction strength for electromagnetic processes is α where α is about $1/137$, and therefore the dominant process is one photon exchange. Figure 1 illustrates the Feynman diagram for a general inelastic electron scattering event in the one photon exchange approximation. $p(\vec{p}, E_0)$ and $p'(\vec{p}', E')$ represent the initial and final four-momentum of the electron. $P(P^2 = -M^2)$ and $P'(P'^2 = -W^2)$ represent the initial and final state of the proton. The four-momentum transfer to the hadronic system is $q(\vec{q}, \nu) = p' - p$.

Previous experiments (3,5) have established the fact that the two proton inelastic structure functions $W_1(q^2, W)$ and $W_2(q^2, W)$ can be described by two functions $F_1(\omega)$ and $F_2(\omega)$ for $W > 2.6$ GeV and $q^2 > 1$ (GeV/c)², where $\omega = 2M\nu/q^2$. This property is known as scaling. The previously measured electron proton data ranged from a value of ω of 25 down to an ω of 1.17. In a later experiment (13) inelastic electron deuteron cross sections have been measured over the range of ω from an ω of 25 down to an ω of 2.0. The measurements of this experiment extend the range of the measured deuteron data down to an ω of 1.17 for $W > 2$ GeV.

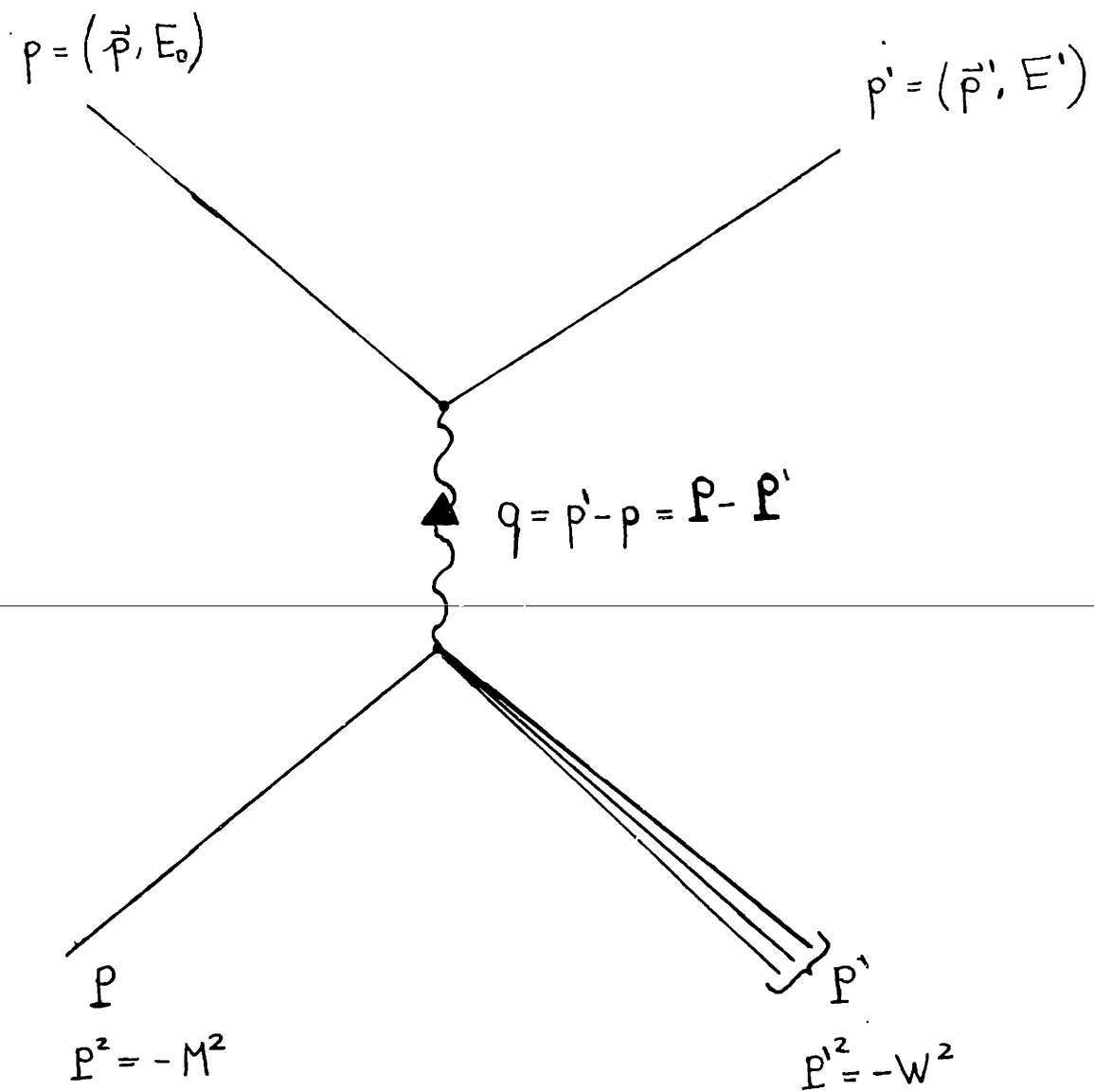


Figure 1. Inelastic Electron Scattering

1.2 Theory

We give a few kinematic definitions . For a given incident electron energy E , scattering angle θ , and scattered energy E' , we have the following:

The square of the four momentum transfer q

$$q^2 = 4 E_0 E' \sin^2 \theta/2$$

The invariant hadronic final state mass W

$$W^2 = M^2 + 2M\nu - q^2$$

where $\nu = E_0 - E'$ is the energy transfer and M is the mass of the nucleon.

The two scaling variables that have been studied in most detail are

$$\omega = 2M \nu / q^2 \quad , \quad X = 1/\omega$$

$$\omega' = 1 + W^2/q^2 = \omega + M^2/q^2 \quad , \quad X' = 1/\omega'$$

The cross section for the electromagnetic scattering is generally described by two structure functions (4).

$$d^2\sigma/d\Omega dE' = \sigma_{\text{MOTT}} (W^2 + 2 \tan^2 \theta/2 W_1)$$

where

$$\sigma_{\text{MOTT}} = \frac{\alpha^2}{4 E_0^2} \frac{\cos^2 \theta/2}{\sin^4 \theta/2}$$

W_1 and W_2 describe the γ -nucleon vertex and are generally functions of the two invariants q^2 and ν ($=q \cdot P/M$). It has been established in previous experiments that for W greater than 2.6 GeV, and ν and q^2 large ($\nu > 1.0$ GeV, $q^2 > 1(\text{GeV}/c)^2$), the proton structure functions become functions of the variable ω only (2,5,49). In this experiment we establish the fact that a similar behavior is true for the neutron within the experimental errors. Other scaling variables that have been proposed reduce to ω at very large q^2 . The variable ω' extends the scaling down to a W of 1.8 GeV (see sections 4.1,4.3).

Scaling is a necessary but not a sufficient condition for the existence of point like nucleon constituents (partons) (8,10,34,35,36). The term parton is used as a general term for any possible point like nucleon constituents. Different theories that are compatible with scaling identify the partons with quarks, antiquarks, bare nucleons and bare pions, and other particles such as gluons (the carriers of the quark-quark interaction). Other

theories attempt to explain scaling through the applications of Regge theory (44), vector meson dominance (41,52,53) and studies of the electromagnetic commutators near the light cone (45,42).

We now show how the assumption that partons exist coupled with the condition that q^2 and ν are much greater than the mass of the proton (the binding energies of the partons are assumed to be on the order of the mass of the proton) yields the scaling prediction for the behavior of the nucleon structure functions(10,55). We go to a frame where the virtual photon has zero time component. In that frame the nucleon has $\beta = \nu / \vec{q}_3$ and $\gamma = \sqrt{1 + \nu^2/q^2}$. When we fix ν/q^2 and let ν and q^2 go to infinity γ becomes very large, and relativistic time dilation slows down the transverse motion of the nucleon constituents. The incoming electron scatters incoherently from the partons which are essentially non interacting with one another during the time that the virtual photon is exchanged. We can say that in that frame the transverse momentum of the parton is much smaller than its longitudinal momentum, and a parton of longitudinal 3-momentum \vec{P}_i can be said to have

$$\vec{P}_i = x_i \vec{P}$$

where \vec{P} is the longitudinal 3-momentum of the nucleon and X_i is the fraction of the longitudinal momentum carried by the parton. Now, at small angles the cross section for the scattering from a parton of momentum P_i and charge e_i is
(10) (e_i is the charge in units of the electron charge)

$$d\sigma_i = e_i^2 \sigma_{\text{MOTT}} \delta(2 q \cdot P_i - q^2)$$

Since q has zero time component we have

$$q \cdot P_i = \vec{q} \cdot \vec{P}_i = q \cdot P X_i = M v X_i$$

Therefore

$$d\sigma_i = e_i^2 \sigma_{\text{MOTT}} \delta(X_i - X) / 2Mv$$

$$X = q^2 / 2Mv$$

Now we integrate over all parton momenta and over all possible parton configurations and get

$$d\sigma = \sum_{\text{All } N_i} P(N_i) \sum_{i=1}^{N_i} \sigma_{\text{MOTT}} e_i^2 F_i(X) / 2Mv$$

where $P(N_i)$ is the probability that there will be N_i partons and $F_i(X)$ is the probability that in that configuration the parton carries fractional longitudinal momentum X .

Hand (3) expresses the cross section in terms of total photo-absorption cross sections for transverse and scalar virtual photons. The electron kinematics determines the flux, polarization and energy of the virtual photon.

$$\frac{d^2\sigma}{d\Omega dE'} = \Gamma \left(\sigma_T + \epsilon \sigma_s \right)$$

where Γ is the virtual photon flux and K is the photon's effective momentum. That effective momentum is the momentum of a real photon which if absorbed will yield the same value of the final hadronic state mass W .

$$\Gamma = \frac{\alpha}{4\pi^2} \frac{2 K E'}{q^2 E_0 (1 - \epsilon)}$$

$$K = (W^2 - M^2)/2M = \nu - q^2/2M$$

ϵ is the virtual photon polarization

$$\epsilon = 1 / \left(1 + 2 \tan^2 \frac{\theta}{2} \left(1 + \frac{\nu^2}{q^2} \right) \right)$$

The above definitions are convenient if one wants to compare the electroproduction cross sections with photo-production results. As q^2 goes to 0, σ_s vanishes and σ_t becomes the total photoabsorption cross section for real photons.

Experimental separation of W_1 and W_2 is possible if data at several angles is available for overlapping regions

of W and q^2 . The separation of σ_s and σ_t is equivalent to the separation of W_1 and W_2 . Since ϵ is a function of angle, a convenient way to separate the structure functions is by plotting the cross sections divided by ϵ as a function of ϵ . A straight line fit to the data will yield σ_t as the intercept at $\epsilon = 0$ and σ_s as the slope of the line.

It is known that $\sigma_s = 0$ for elastic scattering from point like spin 1/2 particles in the $q^2 \rightarrow \infty$ limit. If inelastic scattering is to be viewed as the quasielastic scattering of spin 1/2 partons, we would expect σ_s to be zero. Corrections to a simple parton model such as the inclusion of spin 0 particles or parton binding effects will result in a non zero σ_s . However, if the dominant contribution to the scattering is from scattering from spin 1/2 particles, we would expect σ_s to be small even with those corrections. Therefore, a convenient way to present the separation of W_1 and W_2 is in the form of R .

$$R = \frac{\sigma_s}{\sigma_t} = \frac{W_2}{W_1} \left(1 + \frac{\nu^2}{q^2} \right) - 1$$

The reader is referred to chapter 4 for predictions employing various theoretical models of the structure functions of the neutron and the proton.

1.3 The Experiment

The experiment consisted of the scattering of a monochromatic beam of electrons from liquid hydrogen and liquid deuterium targets. Primary energies were in the range 4.5 to 18 GeV. Electrons scattering into a small solid angle (about 0.75 msr), and falling within a certain small momentum range ($\Delta P/P$ about 4%) were detected by a series of counters in the SLAC 8-GeV magnetic spectrometer. The spectrometer angle θ could be easily changed in less than three minutes by electrically driven motors. At each angular setting, data were taken for a few incident electron energies. Detection of electrons of different momenta could be done by changing the currents in the spectrometer magnets, and data were taken at several spectrometer momentum settings for each incident energy. The term incident energy line will denote all data taken at a given incident electron energy and scattering angle. The cross section that is measured is usually referred to as the raw cross section. The cross section after radiative corrections (See section 3.6) is the cross section for the scattering to lowest order in α . The kinematic range of the data overlapped the data taken in a previous e-p inelastic experiment done by the MIT-SLAC collaboration (2).

Deuterium data were taken for each kinematic point measured in the previous e-p experiment (2). In addition, the old proton measurements were repeated with better statistical accuracy. Each hydrogen run was taken immediately following a corresponding deuterium run. This way many of the beam related and other systematic effects canceled in the D/H ratio. Furthermore, additional data were taken in the region around $X = 0.33$ where the difference between the proton and neutron structure functions exhibits a peak (13). The hydrogen data agreed well with the old experiment. In order to allow the separation of the two structure functions, measurements were taken at 18, 26 and 34 degrees for overlapping ranges of W and q^2 . In addition to the data at these angles, data taken at 6 and 10 degrees were available from a previous experiment done by the MIT-SLAC collaboration (13).

For the three low energy lines at 18 degrees the data points were closely spaced for W less than 2.0 GeV where the data displayed resonance structure. Since the main purpose of the experiment was the measurement of the high q^2 deep inelastic structure functions, the only other data taken in the resonance region were widely spaced for use in the radiative corrections programs (see section 3.8).

The radiative corrections procedure required knowledge of the behavior of the cross sections as a function of E_0 and E' for a given angle. The kinematic range of the data is shown in figure 2 in the form of what is usually referred to as radiative corrections triangles (see section 3.8). Figure 3 displays the data in the W^2, q^2 plane in order to show the range over which a structure function separation could be done. As can be seen in figure 2 and 3 the span of q^2 of the data ranged from $q^2 = 0.5$ $(\text{GeV}/c)^2$ to a maximum q^2 of 20 $(\text{GeV}/c)^2$. For the angles 18, 26 and 34 degrees incident energies varied from 4.5 GeV to 18.0 GeV. The data ranged from an ω of 10 down to an ω of 1.17 for W greater than 2.0 GeV. The previous 6 and 10 degree data extended the range in ω up to an ω of 25.

For each incident electron energy line the spectrometer was initially degaussed and then triplet data runs were taken starting with the highest momentum setting (see figure 2) and going down in momentum in steps ranging from 0.05 GeV/c to 0.5 GeV/c depending on the kinematic region. Each triplet consisted of a hydrogen run, a deuterium run and an empty target run. In addition to background scattering from the target walls, there were other background electrons coming from pair creation processes such as $\pi_0 \rightarrow \gamma + e + e^-$ and $\gamma + \text{nucleus} \rightarrow e^+ + e^-$. These processes

yielded considerable backgrounds at low secondary energies and were taken into account by taking hydrogen, deuterium and empty target runs with the spectrometer polarity reversed. Since that background came from charge symmetric processes, the positron measurements were adequate to allow corrections to be made.

The experimental data were taken in two separate two week periods (known as cycles) during September and October, 1970.

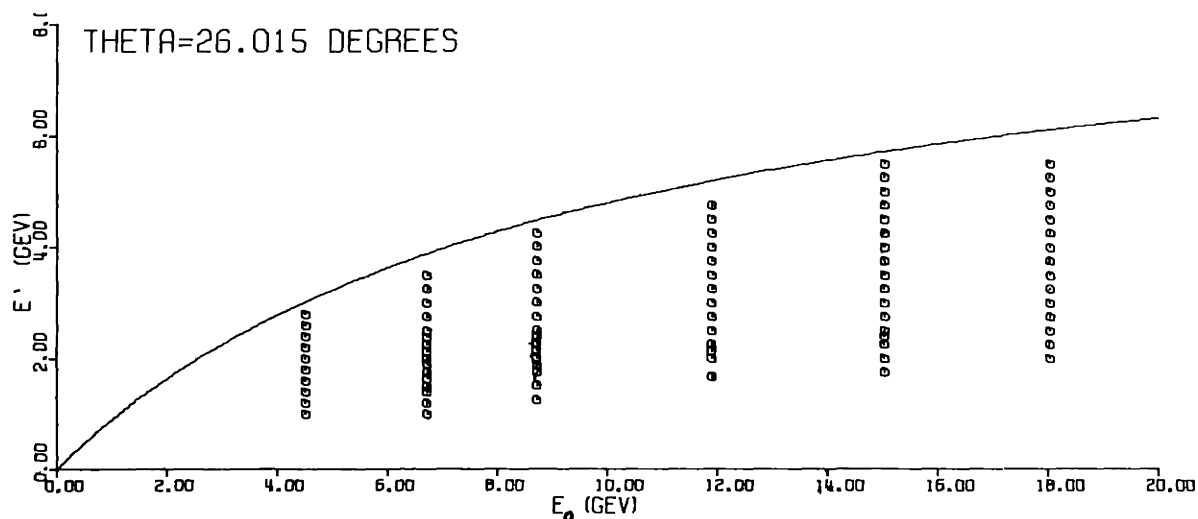
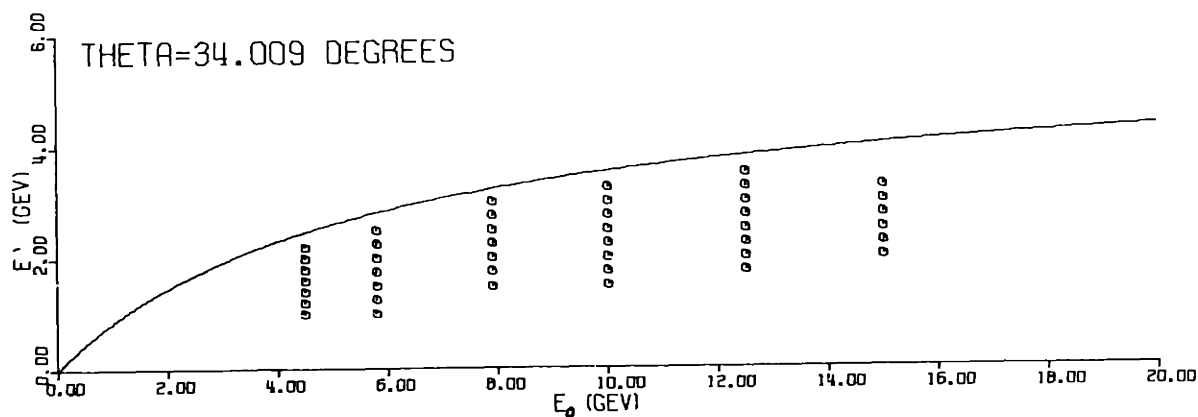
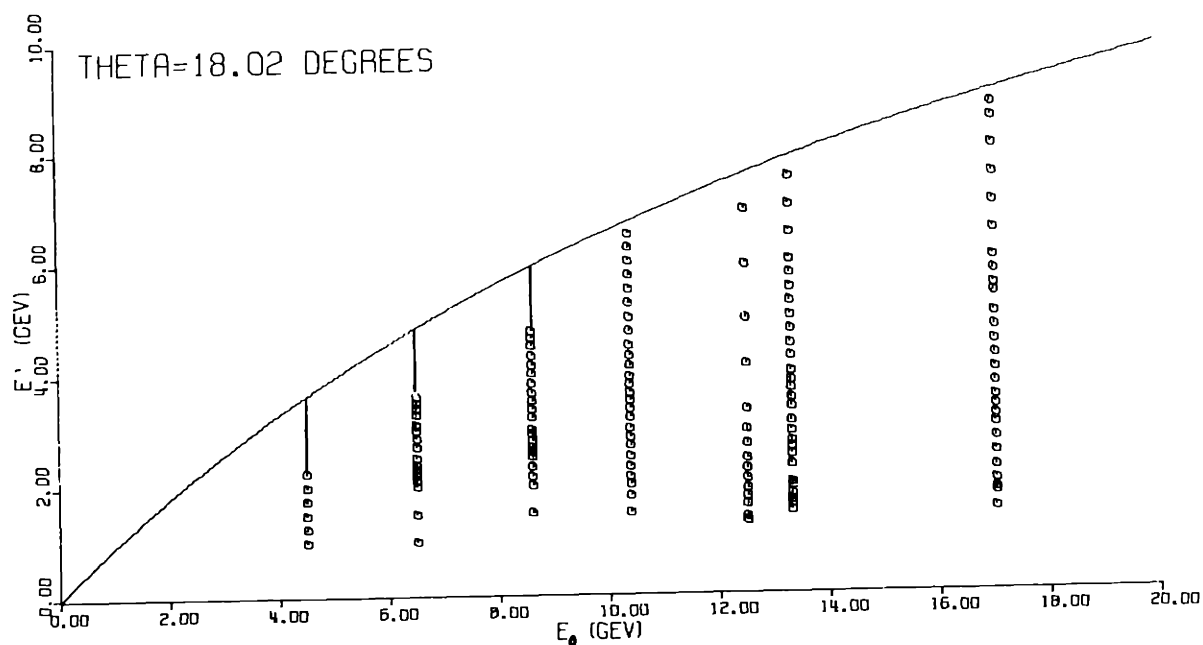


Figure 2 - The kinematic range of the data in E_0 and E' . The circles on the radiative corrections triangles represent spectrometer momentum settings where data was taken. The solid line represents the position of the elastic peak.

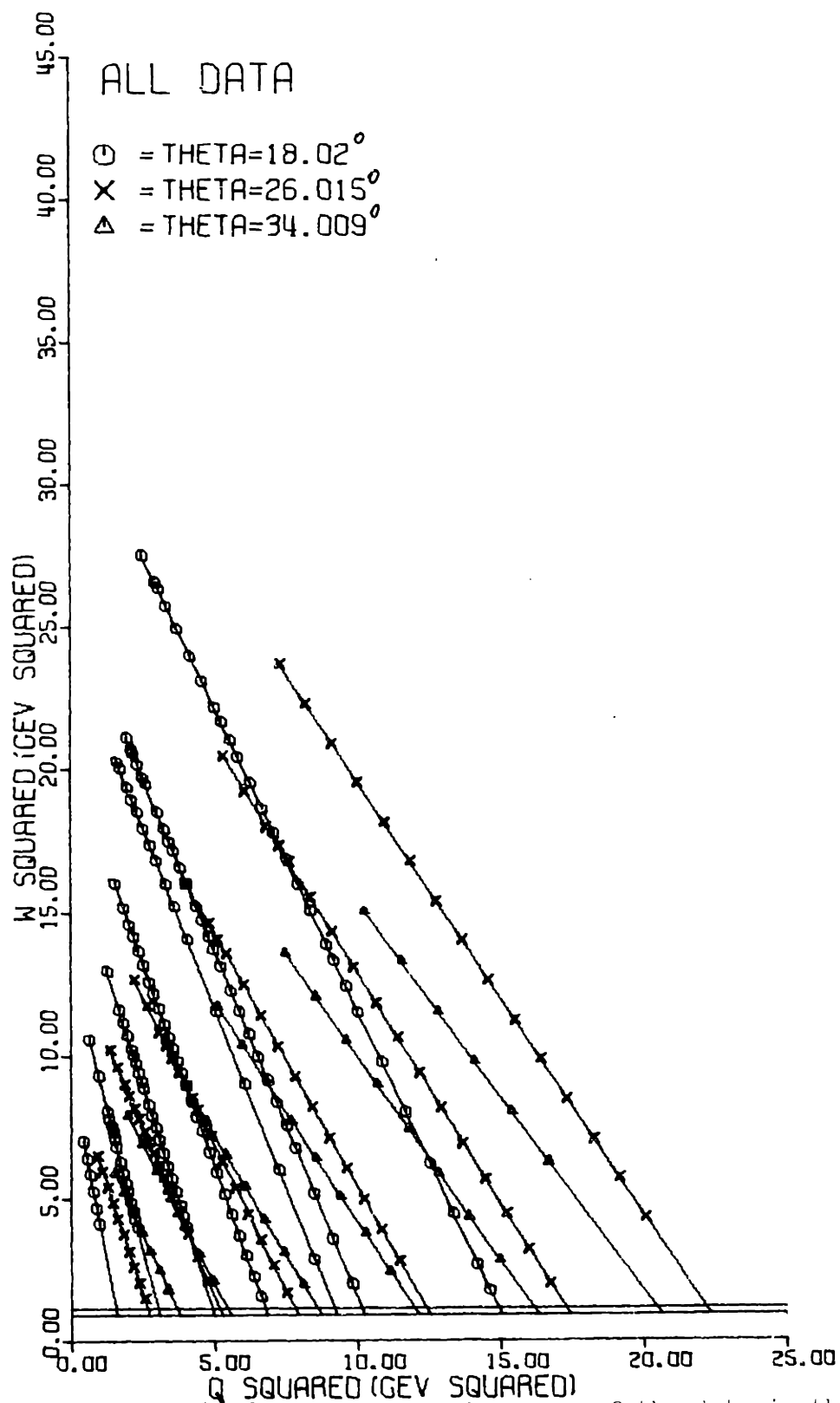


Figure 2 - The kinematic range of the data in the q^2 , W^2 plane. The lines represent constant E_0 lines and the various symbols represent spectrometer settings at 18° , 26° , and 34° .



Figure 4 - The Stadium in Los Angeles

2. Apparatus and its Use in the Data Analysis

2.1 General Setup

The experiment made use of the SLAC 8-GeV spectrometer facility located in End Station A of the Accelerator. The Stanford Linear Accelerator Center (SLAC) (1) is a two mile linear electron accelerator capable of accelerating electrons up to a maximum energy of 20 GeV (see figure 4). The accelerator runs at a beam repetition rate of 360 pulses per second with each pulse having a length of around 1.5 microseconds. Several experiments made use of the accelerator at the same time and each experimenter was allocated a fraction of the pulses. We shall discuss each important part of the apparatus separately in following sections. In addition to describing the physical dimensions and setup of each piece of relevant equipment, we present a description of the efficiencies and related properties involving its use in the data analysis. For a more detailed description of detector efficiencies the reader is referred to the Ph.D. thesis of E. M. Riordan (11).

The general setup is shown in figure 7 . The scattered particles were detected by the 8-GeV/c magnetic spectrometer (see figures 7,8), which consists of two bending and three

quadrupole magnets. The mometum and angle of a scattered particle were determined by crossed arrays of scintillation counters (hodoscopes), and particle identification (electron or pion) was achieved by the use of a gas threshold Cerenkov counter, a total absorption shower counter, and two sets of counters which sampled the early development of an electron shower (see figure 9). The target assembly (see figure 5) consisted of two liquid targets (hydrogen and deuterium), two empty cell target of different thicknesses and a variety of solid targets. The target assembly could be moved by computer control and a target change could be made in less than three minutes. The data were recorded by an XDS 9300 computer which read the event information from electronic buffers fed by the electronic logic and diagnostic circuits (see figure 10). The computer also performed numerous other checks and tasks such as on-line analysis in order of preassigned priority interrupts.

2.2 Beam

The accelerator beam pulses were channeled into different experimental stations by the use of pulsed magnets in the beam switchyard. The beam was first deflected 0.5 degrees by the use of pulsed magnets and then passed through various quadrupole and bending magnets resulting in two 12 degree bends. Between the two 12 degree bends was a set of high power momentum defining slits, which were typically set to pass a $\pm 0.15\%$ range in momentum for nucleon resonance measurements and a $\pm 0.25\%$ range in momentum for the majority of the deep inelastic data. Beam alignment in the End Station was achieved with the help of three ZnS fluorescent screens and a few steering magnets. Two of the screens were normally retracted during the regular experimental running. The first screen was 10.8' upstream of the target and the second was 42.3' upstream of the first screen. The third screen was located downstream of the target and was normally left in place for the entire running period of the experiment. Alignment of the beam was usually better than 0.1 milliradians. A ZnS screen on the movable target assembly enabled the measurement of the beam spot

size and location at the position of the target. The beam spot was usually an ellipse with a vertical diameter of 0.2 cm and a horizontal diameter of 0.4 cm. As mentioned previously beam energies ranged from 4.5 GeV to 18 GeV. The beam spill width was measured using a lucite Cerenkov counter located in the vicinity of the target. The beam spill was continuously watched and adjusted to be flat in order to minimize the dead time corrections. The beam spill width was normally 1.5 to 1.6 microseconds. At low energies however, the machine was not very stable and the spill was not very rectangular, and was typically 1.2-1.4 microseconds. Instantaneous beam currents ranged from 3 milliamperes to a maximum of 55 milliamperes. The highest currents were used for the threshold region measurements ($\omega < 1.5$) where the cross sections were small. In the regions where the cross sections or background rates were large the primary electron current was reduced in order to limit the dead time corrections and false event contributions to the data. The beam energy was determined by the current in the A-beam bending magnet (A-Bend) and by a flip-coil magnetic field measurement of the field in an identical magnet in series with A-Bend. The relative calibration of the beam energy with respect to the 8-GeV spectrometer momentum was determined by looking at the positions of several elastic peaks. The absolute normalization of the beam energy was

known to $\pm 0.1\%$. A summary of the beam parameters and the various errors in their measurements is shown in Table 1.

Table 1
Summary of Beam Parameters

Beam Parameter for a Run	Range	Random Error	Absolute Calibration	Defined by or measured
Energy	4.5-18 GeV	$\pm 0.25\%*$ $\pm 0.15\%$	$\pm 0.1\%$	Slits, Flip Coil A-Bend Current
Spill	1.2-1.6 μSec	± 0.2 μSec	$\pm 5.0\%$	Cerenkov Spill Counter
Inst. Current	2-55 mA	$\pm 10\%$ drift	$\pm 0.5\%$	Charge Monitors
Beam Spot	(2-3)X (4-6) mm	1X1 mm	1X1 mm	ZnS Screen
Charge		$\pm 0.25\%$	$\pm 0.5\%$	Charge Monitors
Alignment		$\pm 0.1\text{mr}$	$\pm 0.1\text{mr}$	ZnS Screens

* when running with $\pm 0.25\%$ slits

2.3 Charge Monitors

The primary charge monitors were a pair of toroidal pulse transformers (12). The beam formed the primary winding of the toroid. The toroid responses to each machine pulse were essentially the response to a delta function excitation. The toroids were driven in a resonant mode and the amplitude of the response was sampled to determine the total charge in each machine pulse. The toroids were internally calibrated by passing a precisely determined charge through a single turn of wire. Frequent absolute calibrations were made by putting a Faraday cup in the beam. The Faraday cup could not tolerate the normal average beam power so lower beam repetition rates (usually one beam pulse per second) were used for those calibration runs. The two toroids usually agreed to better than 0.5% and the Faraday cup calibrations always agreed to better than 1%. A study of those frequent calibrations (38) yielded a random error of $\pm 0.25\%$ and an absolute calibration error of $\pm 0.5\%$ in the value of the measured charge. A secondary emission monitor was also in the beam, but it was only used as a check on possible toroid malfunctions.

The toroids determined the charge for each pulse, the integrated charge for a run, and the integrated number of

machine pulses for each run. The knowledge of the total number of non-zero charge pulses for each run was necessary for the purpose of making the dead time corrections and other rate dependent corrections. Similarly, the average pulse length for each run was also needed for that purpose. The pulse length was recorded frequently by looking at the output of the lucite Cerenkov counter located in the vicinity of the target, while the average number of non zero-charge pulses was determined in several different ways. The integrated number of pulses accumulated by the toroids for each run served as an upper limit, since it included all machine pulses independent of their charge. In addition to that, for each event the computer recorded the charge of the pulse on which that event occurred yielding a histogram of the charge per pulse weighted by the probability of having an event in a pulse (this probability is proportional to the charge of a pulse). Using that histogram one could obtain the weighted average charge per pulse, and combining that with the charge information for the run one could obtain the average number of non-zero charge pulses. It is shown in Appendix C that this weighted average is the average that is really needed for the purpose of dead time calculations. During the second cycle of the experiment we had additional information on the charge per pulse distribution for each

run. Using a charge per pulse hardware computer interrupt, the computer could read the charge of each pulse and form a true histogram of the charge per pulse distribution in addition to the histogram weighted by the event distribution. This way we could form any weighted average we wanted and compare it with the result obtained from the event weighted histogram. The details of that comparison is shown in Appendix C. In addition to all the above information we had a scaler that was driven by a discriminator which was driven by the Cerenkov spill counter. This scaler yielded the total number of pulses with enough charge to produce a Cerenkov signal above the discriminator threshold.

2.4 Target Assembly and Density Monitors

The experiment utilized a target assembly used in a previous e-p,e-d electron scattering experiment (SLAC experiment E49A) (13). Separate systems were used for the liquid hydrogen and liquid deuterium targets. In addition there were several solid targets located underneath the two liquid targets. A computer controlled mechanism enabled one to change targets in less than three minutes (see figure 5). Each liquid target was contained in a vertical cylindrical aluminum walled pillbox about 3.0 inches in diameter and approximately 0.003 inches thick. Each target was part of a loop through which the liquid was forced to circulate by a small motor driven fan. The upper part of the loop constituted the heat exchanger where a large reservoir of liquid hydrogen absorbed the heat deposited by the beam. Unfortunately, the motor driven fan of the deuterium target did not operate for part of the experiment, and for runs taken during that time period the only heat exchange was achieved through convection currents. For that part of the experiment, the SLAC 1.6 GeV/c magnetic spectrometer provided a density correction which was adequate as a correction for the density variations (more details will be given later in this section).

Two types of empty target cells were used each having the same circular pillbox geometry, but different wall thicknesses. The thin one had a wall thickness which was very close to the wall thickness of the actual liquid targets, while the thick one had a wall thickness which was about six times greater. The thick empty target cell was the one which was mainly used for the purpose of measuring the target wall background contribution. The thick cell had six times the counting rate of the thin one. Also the radiation length of the thick cell was approximately the same as the radiation length of the liquid target and therefore simulated the radiative effects for the actual target wall contribution. Careful measurements of all target wall thicknesses were made by the use of a precision micrometer and by the weighing of equal area circles punched from the target walls after the experiment.

Two independent target density monitor systems were used. The first employed two hydrogen vapor pressure thermometers located above and below the target cells. The second employed the SLAC 1.6 GeV/c magnetic spectrometer (14) (see figure 6) to measure the cross section for the detection of protons from elastic (H) and quasielastic (D) scattering at a fixed proton momentum and angle. When the target fans were working properly, the density corrections of the two density

monitors were the same within the statistical error of the counts in the 1.6 GeV/c magnet (usually better than 0.3%).

Each of the hydrogen vapor pressure thermometers consisted of a hydrogen filled bulb in good thermal contact with the target, and a capillary tube leading to a mechanical pressure gauge and a pressure transducer. In this hydrogen two phase system the temperature of the liquid hydrogen in the bulb determined the vapor pressure at the end of the capillary tube. The electrical properties of the pressure transducer were calibrated with an accurate mechanical pressure gauge. At 21 degrees Kelvin the equilibrium concentration of para hydrogen is 99.8%, and the saturation(†) density of para hydrogen at that temperature is .069380 atomic weights/cc. The saturation density of normal deuterium at that temperature is 0.1690 gram/cc. The available cryogenic data (37) in the region around 21 degrees Kelvin was well represented by the following fits

$$T = 15.48 + 6.385 P - 1.852 P^2 + 0.2518 P^3$$

$$Dh = 0.07714 + .000443 T - .00003866 T^2$$

$$Dd = 0.1853 + .0006677 T - .00006872 T^2$$

(†) The saturation density is defined as the density of the liquid under a pressure equal to its vapor pressure.

Where T is the temperature in degrees Kelvin and P is the vapor pressure of para hydrogen in atmospheres. D_h is the saturation density of para hydrogen in atomic weights/cc and D_d is the saturation density of normal deuterium in grams/cc . The conversion rate of normal hydrogen to para hydrogen is fast and hydrogen is 70% para after approximately six days(57). The conversion of normal deuterium to the equilibrium ortho form is extremely slow (of the order of months) and it is reasonable to assume that the deuterium is in its normal state (see ref. 57 for rates of conversion).

The targets were operated under pressure in order to raise the boiling point of the target liquid. The usual running pressures were between 25 and 30 PSIA. At those pressures the boiling points are about 23 degrees Kelvin for hydrogen and 28 degrees Kelvin for deuterium. Under atmospheric pressure the boiling points are about 20.3 degrees for hydrogen and 23.5 degrees for deuterium. Deuterium and hydrogen in the liquid form are slightly compressible (57) and a correction of about 0.2% was applied to account for the density change.

The temperature information was updated once every second and the computer recorded this information for each event. The average target temperatures for each run were determined

by the averaging of the temperature information for all the events in a given run. For the runs where the target fans were working it was found that the upper target temperatures correlated well with the 1.6 GeV/c magnet information, while the lower temperature did not change enough to agree with the 1.6 magnet results. The density correction for the runs with properly working target fans was taken as the ratio between the density at 21 degrees Kelvin and the density at the average upper target temperature for the given run. For those runs the density correction deviated from unity by less than 1%. A random error of 0.25% was assigned to the density correction due to random fluctuations in the properties of the pressure transducer and its power supply. A systematic error coming from the uncertainty of the normalization density at 21 degrees Kelvin is quoted as 0.6%.

As mentioned previously the second density monitor was the SLAC 1.6 GeV/c magnetic spectrometer (14) (see figure 6), which was used to measure the cross section for the detection of protons from elastic (H) or quasielastic (D) scattering at a fixed proton momentum and angle. The 1.6 GeV/c spectrometer provided the only density correction for the deuterium runs (25% of the runs) for which the target fan stopped working. The SLAC 1.6 GeV/c magnetic spectrometer is a single 80 ton magnet which deflects charged particles of

the right momentum vertically through a 90 degree bend in a 100 inch radius. Particles from the target travel through a vacuum chamber mounted in the magnet gap, into a counter cave surrounded by 200 tons of concrete shielding. The effective target length viewed, and the range of azimuthal angle (ψ) accepted are set by movable horizontal and vertical pairs of lead jaws. Those jaws enabled us to limit the singles rate to less than 1.5 per machine pulse in order to make the dead time corrections less than 1.2%, while at the same time making sure that the entire target length was viewed by the magnet. The counter assembly that was used consisted of 8 momentum counters sandwiched between two scintillation counters C9 and C10, followed by a lucite threshold Cerenkov counter (C_{π}) designed to count pions and not count protons, followed by another scintillation counter C11. The monitored rates were singles (C9), telescope coincidence (C9XC10XC11), pion coincidence (telescopeXC $_{\pi}$), and a false coincidence (C9XC10 delayed). The 1.6 magnet current was checked periodically as well as the position of the proton elastic peak on the eight momentum counters. This way there was a frequent check on possible magnetic field drifts in the 1.6 magnet. For each incident energy and angle a normalization run was taken at very low beam current (3 mA instantaneous current), such that the beam heating effects

were negligible. Using a solid aluminum target, a few test runs were taken at different beam currents to determine the effective dead time for the 1.6 coincidence circuits and their components as a function of the false coincidence percentage (this way we eliminated the need to know the pulse width and the number of pulses for the purpose of making this particular dead time correction). The quantity TC, the telescope coincidence counts corrected for dead time and target wall contribution and divided by the total incident charge, was calculated for each run. The multiplicative density correction for each run was $TC(\text{for the normalization run})/TC(\text{for the run})$ times the density at 21 degrees Kelvin divided by the density at the target temperature of the normalization run. Since each energy and angle had a different normalization run, the random error of 0.25% in the temperature, and the statistical error in TC for the normalization run were added in quadrature to the statistical error in TC for each run yielding the total random error in the density correction. The cross section each run was calculated on the basis of the density at 21 degrees K, and then multiplied by the density correction.

It was discovered that the deuterium fan was not working during the entire data taking period for the 8.6 GeV 18 degree line. This line was taken before the 1.6 GeV/c spectrometer was connected, and therefore there was no

reliable density monitor for that line. While the target fans were not working the temperature correction did not represent the true density correction since it only accounted for the temperature changes and did not account for density changes due to boiling. When there was target boiling we found that for a constant beam spot the density correction was a function of the average beam current only. However, it varied markedly for different sizes of beam spots. We therefore took the density correction for this line to be the density correction for a typical beam spot at the average current for each run, and its error to be the deviation in the density correction due to the spread in the size of the beam spots during the experiment. This line was only used for the purpose of radiative corrections and was neither used in the extraction of structure function, nor in the extraction of the neutron to proton cross section ratios.

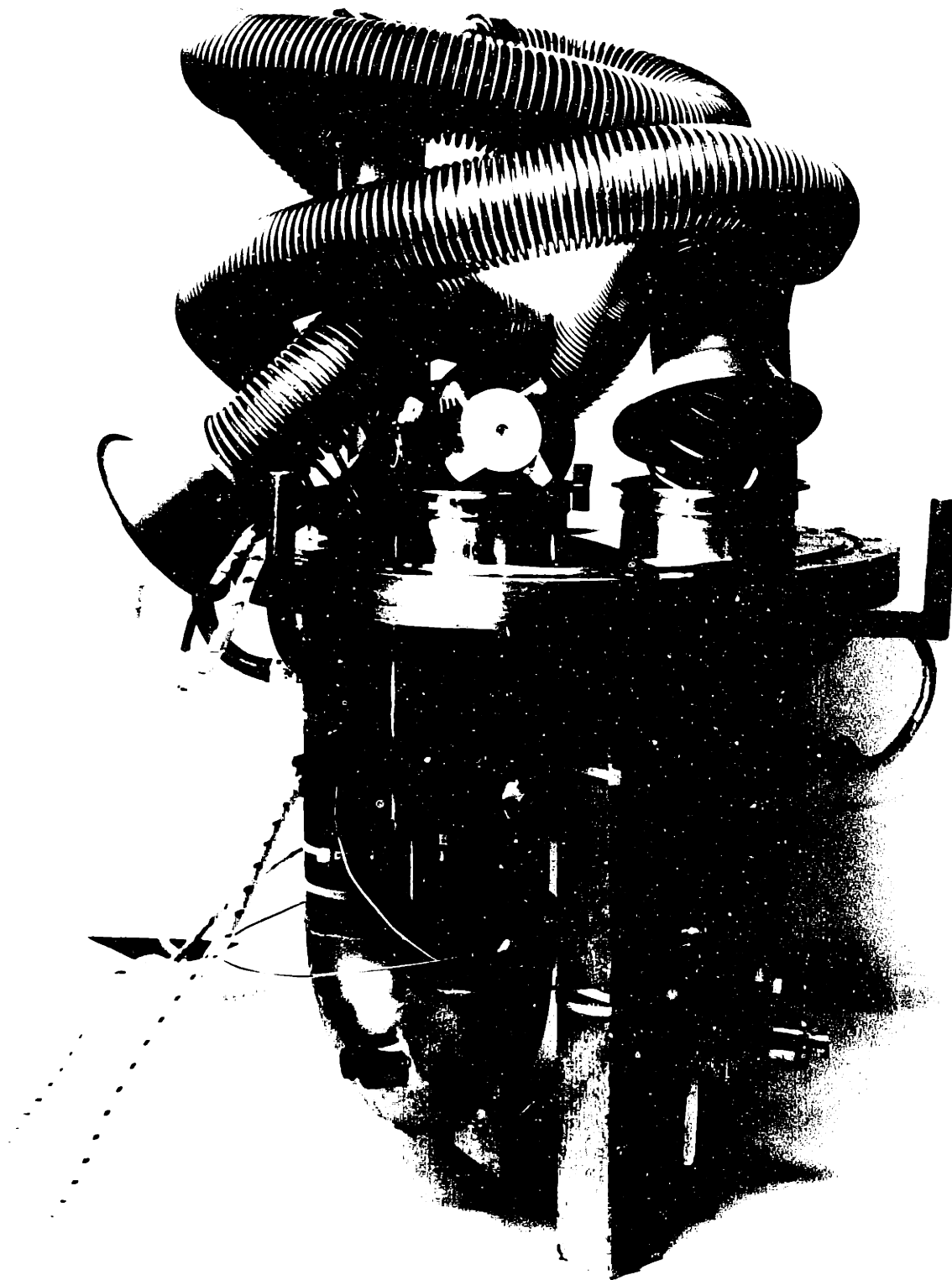


Figure 5 : In-Door Target Assembly

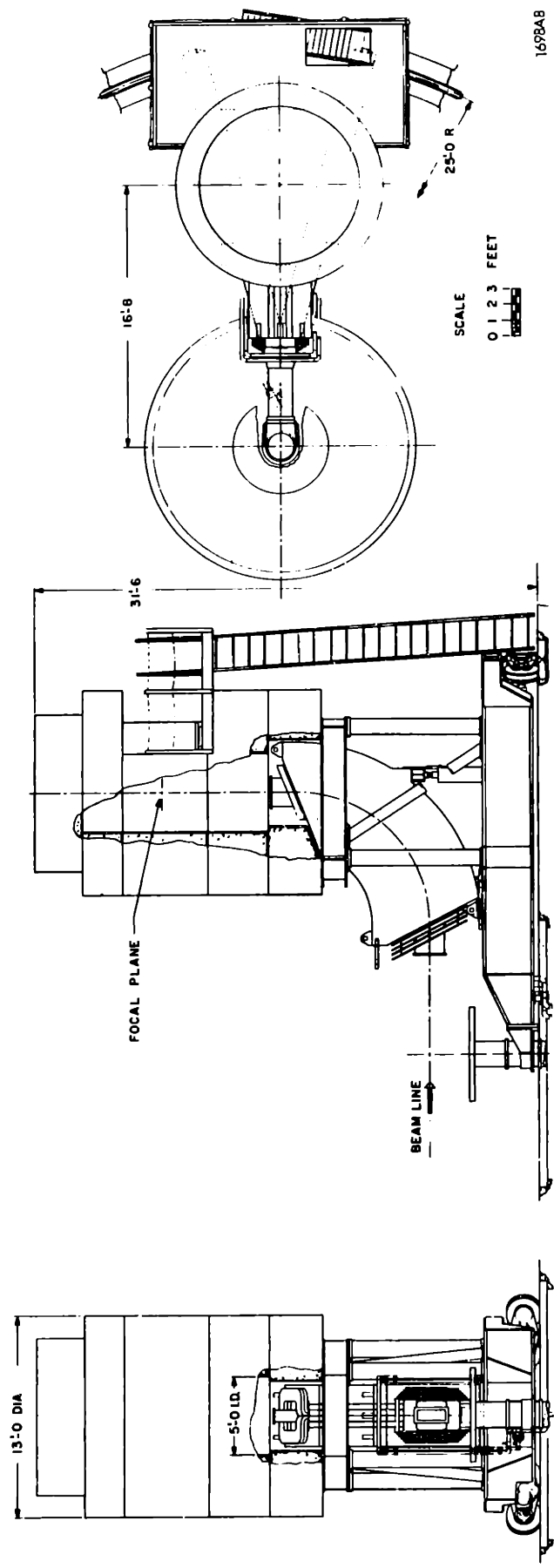


Figure 6 - The SIAC 1.6 GeV/c magnetic spectrometer

2.5 Spectrometer

The SLAC 8 GeV/c magnetic spectrometer (2,9) is a magnetic focusing spectrometer consisting of two bending magnets and three quadrupole magnets (see figures 7,8) followed by an array of detectors surrounded by 750 tons of movable concrete shielding (see figure 9). The momentum and angle of a charged particle passing through the magnetic elements was determined by the particle's vertical and horizontal position in the final focusing plane. The total momentum acceptance was around 4% . Twenty momentum bins allowed a resolution of 0.2% in the measured particle momentum. Similarly the total angular acceptance was 16.2 milliradians. Fifty four theta bins allowed an angular resolution of 0.3 milliradians. The magnetic properties of the spectrometer were measured during a series of optics tests conducted in November 1967. A great deal of work has gone into theoretically reproducing the optics tests results by employing various models of the spectrometer. The models usually represented the spectrometer as a series of ideal bending and quadrupole magnets with effective field strengths, field lengths and pole face rotations. The results of those studies are found in the PhD. thesis of E. M. Riordan(11) . The spectrometer acceptance ($\Delta\psi \Delta\theta \Delta P/P$)

was calculated using a Monte Carlo ray tracing program which made use of the transport coefficients of the various models. The error in the acceptance was determined by the variation of the acceptance with various spectrometer models. Another contribution to the error in the acceptance came from the experimental errors in the measurements of the focussing properties of the spectrometer. The focussing properties of the spectrometer were measured at the momenta of 9.0, 8.0, 6.0 and 3.0 GeV/c. The calculated acceptance varied slightly depending on which set of optics measurements one used. This variation was also included in the error estimate. The spectrometer acceptance that was used was limited to momentum bins 2-19 and theta bins 2-53. The average value of that acceptance was $0.2494 \times 10^{-4} \text{ *P}$ steradians-GeV and its error was taken to be $\pm 1.5\%$.

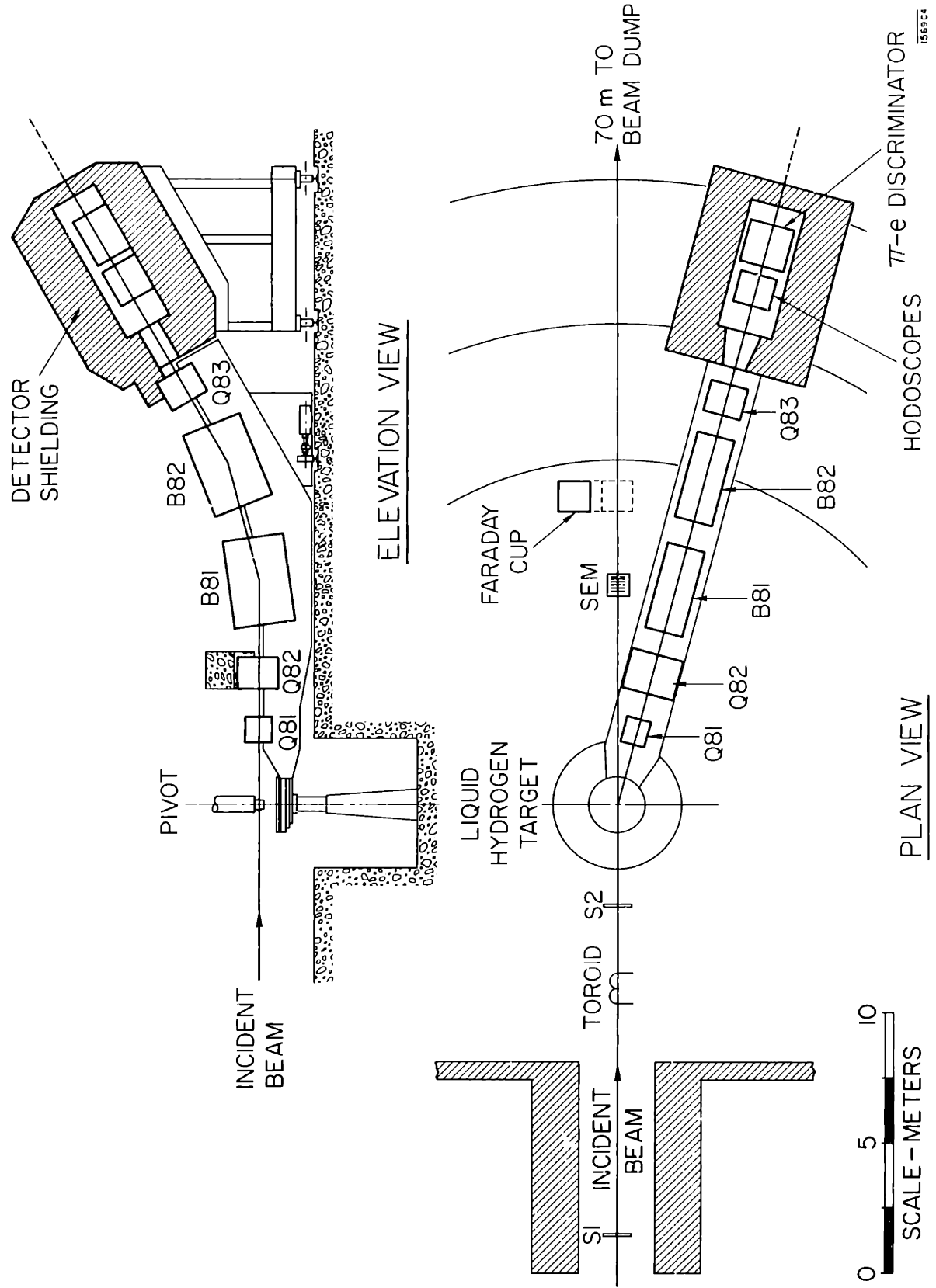


Figure 7 - The experimental setup

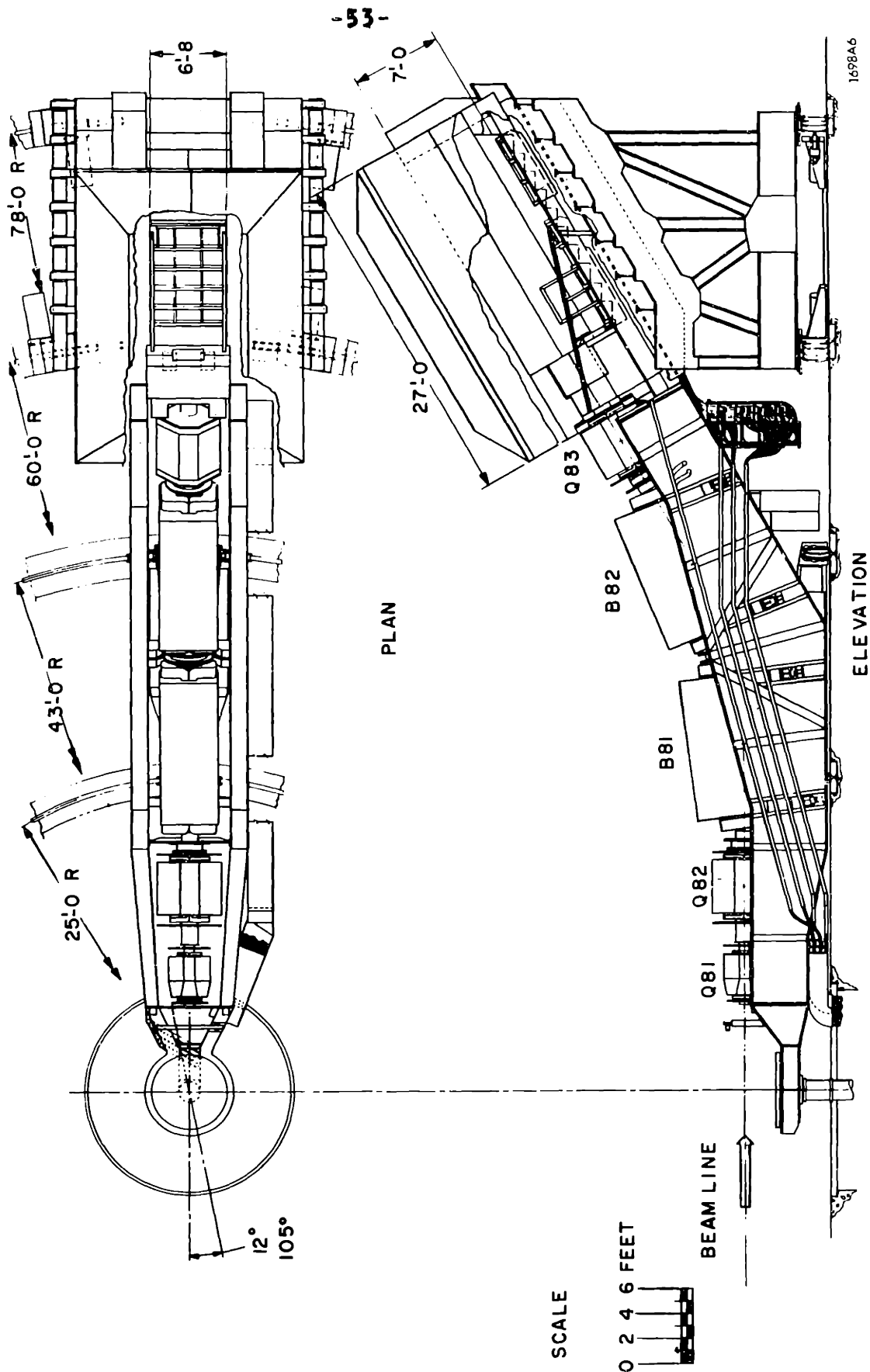


Figure 8 - The SLAC 8 GeV/c magnetic spectrometer

2.6 General Setup of Particle detectors

After traversing the last quadrupole magnet a scattered particle passed through a series of detectors whose task was the identification of the particle and the determination of its momentum and angle. The first detector was a threshold gas Cerenkov counter. Following it were the track defining elements which consisted of a five segment scintillator front trigger counter (FT) followed by a 55 segment (54 bins) theta hodoscope, a 21 segment (20 bins) momentum hodoscope, and another five segment scintillator rear trigger counter (RT). Next was a one radiation length lead slab which served as an initial radiator followed by three dE/dx scintillation counters. The initial radiator was the first of the 16 one radiation length lead slabs interspersed with lucite counters and forming the total absorption shower counter (TA) . The first three slabs of the total absorption counter served as another dE/dx counter or as a truncated total absorption counter (TTA) viewing the initial development of an electron shower. Following the TA was a 16 radiation length lead absorber followed by two scintillator Anti-counters. An ideal electron should have registered acceptable signals in the Cerenkov counter, the three dE/dx counters and the TA and TTA counters, but should not have registered in the Anti-counters. A single electron

would have been characterized by a FTxRT coincidence (C1) and would have registered signals in two or three adjacent counters in the theta and momentum hodoscopes.

A single ideal pion should not have registered a signal in the Cerenkov counter, and the amplitude of its signal in each of the three de/dx counters should have been that of a single minimum ionizing particle. It should also have registered signals corresponding to a single minimum ionizing particle in the TTA (channel 43) and in the TA (channel 56). It should have also triggered the Anti-coincidence.

In practice 90% of the electrons triggered the Cerenkov counter, and 53% to 77% registered signals greater than that of 1.5 minimum ionizing particles in each of the three de/dx counters. Also 90% of all electrons fell above the TTA electron defining cut, and 99.1% fell above the TA electron defining cut. Electrons only triggered the Anti-counter by a chance coincidence. On the other hand only 0.7% of the pions triggered the Cerenkov counter, 3% of the pions had de/dx signals greater than 1.5 minimum ionizing particles, 3% fell above the TA electron defining cut, and

less than 1% fell above the TTA electron defining cut. Only 30% of the pions triggered the Anti-counter. More than one pion within a period of 50 nanoseconds had a much higher probability of registering acceptable electron signals in the various counters.

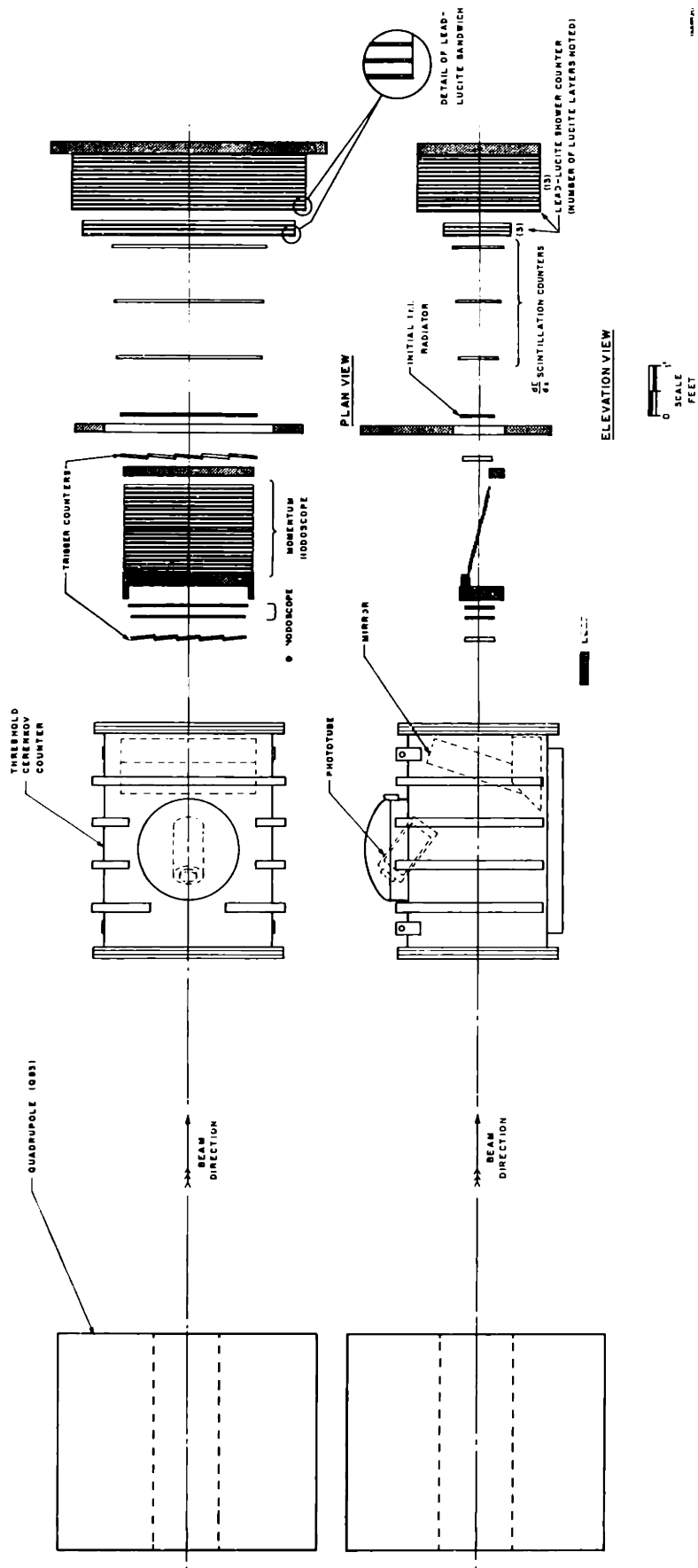


Figure 9 - The SIAC 8 GeV/c spectrometer detector assembly

2.7 The Cerenkov Counter

The threshold Cerenkov counter contained Freon gas (CCl_2F_2) at 589 mm absolute pressure. The Cerenkov light was produced in a narrow cone and was focused on to the face of a photomultiplier tube by an aluminum coated mirror. Pions did not register a signal in the Cerenkov counter for momenta below 3.5 GeV/c. The total integrated charge of the pulse output of the Cerenkov counter was read by the computer for each event. The output of the Cerenkov hardware discriminator was put in coincidence with C1 forming the C2 coincidence circuit. A C2 coincidence ensured that the Cerenkov signal was within 17 nanoseconds of the time determined by a particle's passage through the trigger counters and the hodoscopes. After corrections for dead time in the trigger counter and Cerenkov discriminators, the C2 efficiency was 0.898 for the first cycle of the experiment and 0.881 for the second cycle of the experiment with a 0.3% error. The Cerenkov discriminator dead time correction was typically less than 1% (17 ns dead time with rates less than 1 per pulse). The efficiency of the Cerenkov counter for detecting pions was about 0.7%. The primary mechanism for the pion signals was the production of a knock-on

electron in the material in front of the counter. The efficiency of the Cerenkov counter varied as a function of the track position due to a slight misalignment of the mirror assembly. The efficiency varied by 10% from the center to the edge of the counter. A momentum-angle dependent correction factor was applied to the data in the region where the data was binned into fine mesh intervals. This was only done in the resonance region. A similar correction was applied to the deep inelastic data and the momentum-angle dependent correction was applied to the data in each P-Theta bin before averaging the cross section over the spectrometer acceptance.

2.8 Hodoscope Codes and Classes

The 55 theta and 21 momentum hodoscope elements were grouped to form 54 theta and 20 momentum bins. Each hodoscope consisted of two arrays of counters. The theta hodoscope consisted of two arrays with 27 and 28 counters each, while the momentum hodoscope consisted of two arrays with 10 and 11 counters each. The momentum hodoscope was located at the momentum focal plane of the spectrometer. The second array in each hodoscope was displaced by a half a counter with respect to the first. A momentum or theta bin was the geometrical intersection of two following counters from each array. Therefore, the physical size of a bin was half the size of a counter. The event signature in the hodoscopes was read by the computer in the form of 55 and 21 bits. A set bit denoted that the corresponding counter fired. The bit patterns in the hodoscopes were classified into codes which are summarized in Table 2. The codes were categorized as good single tracks (codes 1,2-6,9,12-16,19,20), double tracks (codes 7,17), ambiguous tracks (codes 8,10,11,18,21,22) or bad (code 0). The only bad code was a blank hodoscope and events with this code were rejected as trajectories which did not pass through the solid angle defined by the hodoscope. The code categories in both hodoscopes were grouped into event classes.

Class 1 (Good-Good) - A single track in both hodoscopes

Class 2 (Good-Double) - A single track in one hodoscope
and a double track in the other

Class 3 (Double-Double) - A double track in both hodoscopes

Class 4 (Ambiguous-Any) - An ambiguous track in either
hodoscope

Events in all four classes were considered to be good electron events. The reason for the class separation was the different dE/dx and TA spectra that each class exhibited. A detailed study of hodoscope codes can be found in the Ph.D. thesis of P. N. Kirk (23).

Table Two

Hodoscope Codes

-----+-----+-----+-----+
Code 0 A blank
 Bin -1

-----+-----0-----+-----+
Code 1 One bit
 Bin 10

-----+00-----+-----+-----+
Code 2 Two adjacent
 Bin 7

-----+-----+000-----+-----+
Code 3 Three adjacent
 Bin 12

0000+-----+-----+-----+
Code 4 Four adjacent
 Bin 2

-----+00000-----+-----+
Code 5 Five adjacent
 Bin 8

--000000+-----+-----+-----+
Code 6 Six or more
 adjacent
 Bin 5

--00+-----+000-----+-----+
Code 7 Two tracks
 Bin -1

0000+--00+--00-----+
Code 8 More than two
 tracks
 Bin -1

-----+0-0-----+-----+
Code 9 Two singles
 with only one
 intervening blank
 Bin 7

-----+0-----+0-----+-----+
Code 10 Two singles
with more than one blank
or multiple singles
 Bin -1

--000000+0000000000
Code 11 Zoo event
Any event with 10 or
more set bits
 Bin -1

-----+00-----+0-----+-----+
Code 12 Two adjacent
 + one single
 Bin 6

--000-----+0-----+-----+
Code 13 Three adjacent
 + one single
 Bin 4

-----+0000+-----+0-----+
Code 14 Four adjacent
 + one single
 Bin 7

-----+00000-----+0-----+
Code 15 Five adjacent
 + one single
 Bin 8

--00000000--0+----+
Code 16 Six or more
adjacent + one
single
Bin 6

----+000--+00--+0---+
Code 17 Two tracks
+ one single
Bin -1

--00+--00+--0--+00--+
Code 18 More than two
tracks + one
single
Bin -1

--000---0+-0---+0---+
Code 19 Two, three, or
four adjacent + 2
or more singles
Bin 4

----+00000-0-0+0---+
Code 20 Five or more
adjacent + two
or more singles
Bin 8

0-00+-00+-----+0-0-0
Code 21 Two tracks
+ two or more
singles
Bin -1

--00+-00-+00-0+0-0-+
Code 22 More than two
tracks + two or
more singles
Bin -1

2.9 de/dx Counters

The de/dx counters measured particle multiplicity in the electron shower following the one radiation length initial radiator. The signal in each of the three de/dx scintillator slabs was proportional to the number of minimum ionizing particles coming out of the initial radiator. Having three counters was useful since it increased the pion rejection by a factor of three as the Landau tails of pions in the three scintillators were substantially although not completely uncorrelated. The pulse height from each of the three counters was read by the computer for each event. The off-line analysis program checked whether all three pulse heights were above a low cut (which was between one and two minimum ionizing particle signals), or a high cut (which was between two and three minimum ionizing particle signals). The high cut was useful in regions where the pion to electron ratio was high and a high pion rejection was necessary. The electron detection efficiency of the de/dx counters was a function of particle momentum. It was fitted to a sum of Lagrange polynomials in $1/P$ where P is the scattered momentum. The efficiency varied from 0.530 at a momentum of 1 GeV/c to 0.773 at a momentum of 5 GeV/c for the low cut, and from 0.286 at 1 GeV/c to 0.623 at 5 GeV/c for the

high cut. The above efficiencies were for single track electrons (class 1) . The efficiency was higher for multiple track events and the efficiencies for the classes Good-Double, Double-Double and Ambiguous-Any were fitted separately. The efficiency was corrected for rate dependent effects (1% to 2%) and for pedestal shifts (less than 1%). Finally, a correction factor was applied to correct for effects stemming from the variation of the efficiency in the P-Theta plane. The error in the de/dx efficiencies was derived from the error matrices of the various fits. The typical chi-squared per degree of freedom for the de/dx efficiency fits was close to 1.0, for 60 degrees of freedom.

2.10 TA, TTA and Anti-Counters

While the de/dx counters sampled the electron's shower after the electron had gone through one radiation length of lead, the 16 element lead-lucite total absorption counter viewed the entire shower. The Cerenkov light produced in the lucite by the cascading secondary particles of the shower was viewed by sixty four phototubes. The outputs of all sixty four phototubes were linearly added, gated into an analog to digital converter (ADC), and read by the computer. For zero input pulse the output of the ADC was the pedestal channel which was normally set at channel 40. The output of the ADC for non zero-pulses was a number of channels above pedestal proportional to the magnitude of the input pulse. The gain of the system was set such that it yielded a signal of one channel above pedestal per minimum ionizing particles per slab. For each measured momentum the electron pulse height distribution was very close to a gaussian. The mean pulse magnitude was proportional to the energy of the detected electron. The center peak position was represented by the equation $C = 35.42 + 49.7P$ where P is the momentum of the detected particle in GeV/c, and C is the TA center peak position in ADC channels. The width of the distribution was caused by the 4% momentum acceptance of the spectrometer and

by the intrinsic fluctuations in the number of particles in the shower. The full width at half maximum of the distribution was represented by the equation $FWHM = 2.36\sqrt{C + (0.04C)^2/3}$, where FWHM is in units of ADC channels. A TA electron defining cut was placed at one FWHM below the center peak position and corresponded to an electron detection efficiency of 0.991. As mentioned previously, the gain of the system was set such that it yielded a signal of one channel above pedestal per minimum ionizing particle per slab. Thus, a non-interacting pion, which traversed all 16 slabs, produced a signal of 16 channels above pedestal. At a momentum of 1.0 GeV/c the electron peak fell in channel 85 while the electron defining cut fell in channel 64. Since the single pion peak was in channel 56, only multiple pions or an interacting single pion could yield pulse heights above the electron cut. Because of their high mass pions do not shower as readily as electrons but they can interact with nuclei via the strong interaction. The typical distribution of the pion pulse heights in the TA showed a peak in channel 56 and decreased exponentially to half its maximum value at channel 65.

The truncated TA (TTA) which consisted of the first three slabs of the TA served as a special kind of de/dx counter. While the scintillator de/dx measured particle multiplicity independently of the particle's energy, the TTA signal was a measure of the total energy deposited in the first three radiation lengths of the electron's shower. Unlike the de/dx counters the TTA slabs were made of lucite, and therefore insensitive to soft hadronic secondary particles which registered signals in the de/dx scintillators. The only particles counted in the TTA were particles fast enough to produce Cerenkov light in lucite. A TTA electron defining cut was set such that its electron detection efficiency was 0.910 . With the cut set at that value the TTA was a much more useful counter than the de/dx counter. It was more efficient than the de/dx in its electron detection, while its pion rejection was the same or in some momentum regions better. Since two pions produced a TTA signal of only six channels above pedestal they were rejected by the TTA while the de/dx counter accepted them as an electron. The TTA efficiency was rate independent for two reasons. The first was that soft background did not produce light in the lucite and the second reason was that the rate dependence is proportional to $D = (1.0 - \text{Efficiency})$. Since the TTA efficiency was 0.910 that proportionality constant was 0.09

for the TTA, but varied from 0.22 to 0.47 for the low cut dE/dx , and from 0.38 to 0.71 for the high cut dE/dx . The TTA signal was correlated to the particle's signal in the dE/dx , and therefore the TTA efficiency was 0.950 for particles producing a dE/dx signal above the low dE/dx cut, and 0.967 for particles producing a dE/dx signal above the high dE/dx electron defining cut.

Emitter follower transistor pickoffs were put on the TA anode cables in order to pick the signal for use in the TTA setup. A 0.1% uncertainty in the TTA efficiency came from gain fluctuations in the electronics which required frequent recalibrations. Another contribution to the error came from the sensitivity of the TTA efficiency to pedestal drifts. This sensitivity to pedestal drifts was due to the fact that the electron pulse height distribution in the TTA was a gaussian (similar to the TA distribution). The electron cut was placed on the rising slope of the gaussian at a channel which yielded an electron efficiency of 0.910. This cut was chosen in order to get a high pion rejection. Had the cut been placed at a channel such that the efficiency would have been 0.99, the efficiency would not have been as sensitive to pedestal drifts, but the pion rejection would have been lower. The dE/dx counter was also sensitive to pedestal

drifts, but not as much as the TTA, since the electron pulse height distribution in the de/dx was much different, and the electron defining cut was placed in a valley between two peaks and not on a rising slope. A TTA pedestal drift correction was applied to the TTA efficiency for each run depending on the run's momentum and amount of pedestal drift, but the position of the pedestal was only known to one third of a channel. This drift correction was 2% at the maximum. The studies which established the choice of the three-slab setup for the TTA were carried through during the first cycle of the experiment. Therefore, there was no TTA information available for the first cycle of the experiment, and for that cycle the scintillator de/dx counters were heavily used in the analysis.

The Anti-counters were almost never used, except for two high rate positron runs in the first cycle of the experiment. Aside from random chance signals, electrons never triggered the Anti-counters. However, for high background rates that chance probability was as high as 10% due to the poor shielding of the Anti-counters. The Anti-counter usefulness was limited because the 32 radiation lengths of lead in front of them was enough to stop most pions.

2.11 Electronics

The fast electronics is shown in figure 10. Not all the diagnostic circuitry is shown, and the TTA and de/dx setups are not shown either. The primary components of the fast electronics were the Cerenkov, TA, and trigger counters. Any of three real and one chance circuit signals could generate an interrupt to the computer which would read the possible electron event. The real trigger circuits were the trigger and Cerenkov coincidence (C2), TA and trigger counter coincidence (C9) and TA only. The chance trigger circuit was a trigger and Cerenkov counter coincidence with the Cerenkov signal delayed by 50 nanoseconds (C2F). The computer was only capable of reading one event per machine pulse ; Therefore the trigger logic was designed to be a simple arrangement which on the average tended to maximize the number of electron events recorded by the computer and minimize the number of pion events recorded. The TA discriminator cut was set such that it started cutting into the electron peak at a momentum of 2 GeV/c. This TA discriminator setting limited the number of pions accepted as events, which was important at low E' since the pion to electron ratio was large there. However, 90% of the electrons that were missed by the TA in the low E' region

triggered the Cerenkov and were not lost. Since the pion threshold momentum setting for the Cerenkov counter was around 3.5 GeV/c 90% of the pions triggered the event interrupt for momenta above 3.5 GeV/c. This did not present a problem since the pion to electron ratio was small at high momenta except near the electron inelastic threshold where the total event rate was low anyway. The chance event circuitry provided a mechanism by which one could study the chance events in detail, and for the case of high rate runs it provided a correction factor which was less than 1.5%.

The anode signals of the five front trigger counters (FT1-FT5) were fed into discriminators (D1-D5) and into an OR circuit (OR1). Similarly the rear trigger counters (RT1-RT5) were fed into discriminators (D6-D10) and into an OR circuit (OR2). OR1 and OR2 formed the two inputs to the primary trigger counter coincidence circuit (C1). The C1 signal was fanned (FC1) for use in multiple coincidence and diagnostic circuits. The Cerenkov signal was fed into a discriminator (D11) and fanned (FC), and the TA signal was discriminated by D15 and likewise fanned (FTA). Some of the fanned outputs of FC, FTA and FC1 were combined to form the Cerenkov-C1 coincidence (C2) and the TA-C1 coincidence (C9). The outputs of C2, C9 and TA (D15) formed the inputs to the primary real

event trigger circuit (OR4), while the chance trigger circuit (C2F) formed the input to the false event trigger circuit (OR5). As mentioned previously, the average machine pulse was 1.5 microseconds long with about 2.8 milliseconds between pulses (360 pulses per second). The electronics was normally gated off between machine pulses. It was gated on about one microsecond before the next machine pulse was due to arrive and was gated off one microsecond after the duration of the pulse by employing the machine trigger. The machine trigger was a signal provided by the central control of the accelerator about 2.5 microseconds before a machine pulse was due to arrive. The first event in a pulse (either from OR4 or OR5) would set a rapid kill flip flop circuit which was reset by the machine trigger before the next machine pulse was due to arrive. The rapid kill only prevented the computer from receiving any other event interrupts during the entire duration of the pulse following the first interrupt, although the various scalers were still counting. In addition to setting the rapid kill the first event generated a computer interrupt and two coincidence gates. A twenty nanoseconds DCD flag gate served to probe the state of the hodoscope counters and the state of the various diagnostic circuits (electronic flags) by going into various discriminator-coincidence-discriminator (DCD) units

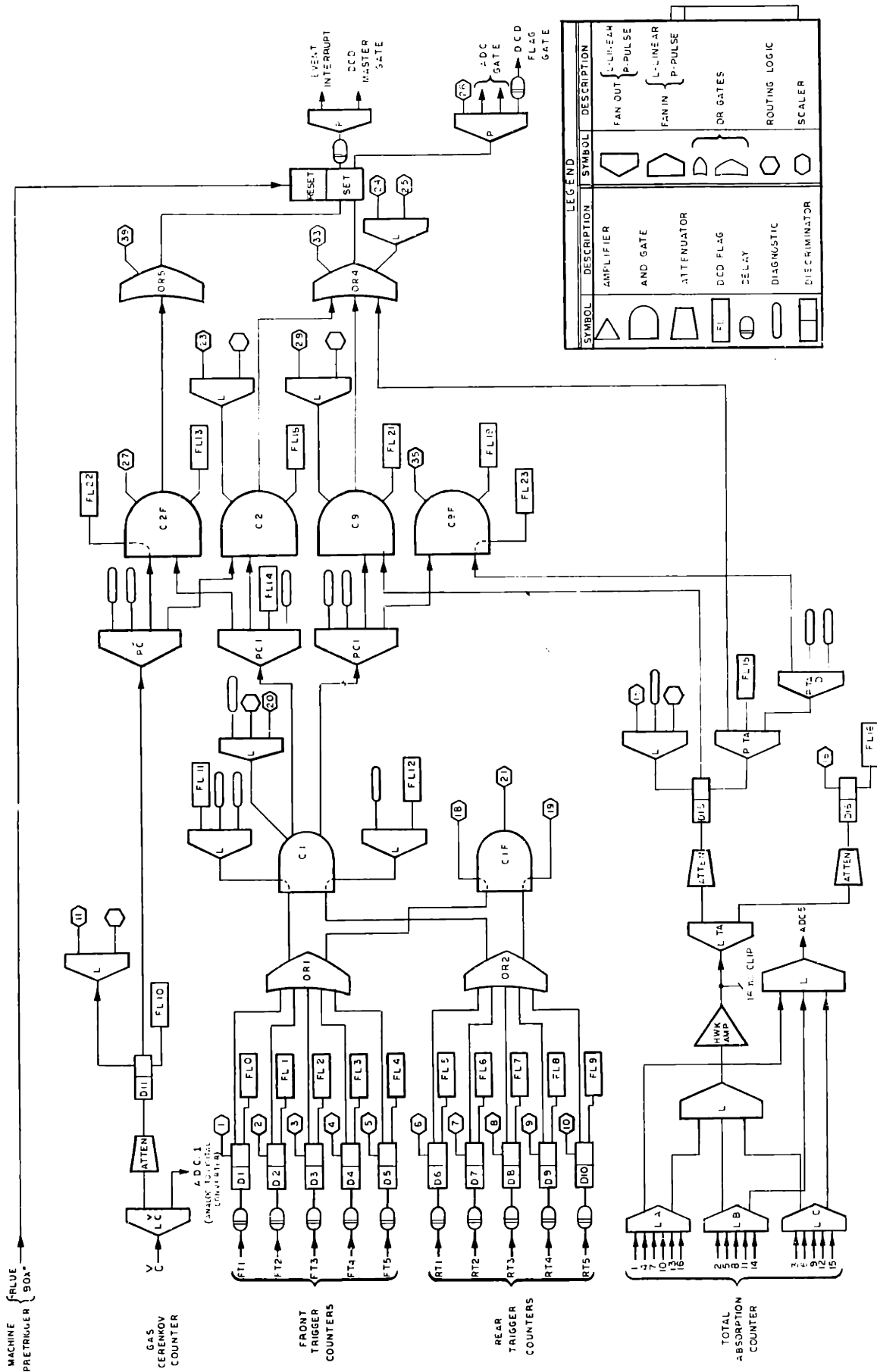


Figure 10 : The Fast Electronics

receiving inputs from the interrogated circuits. Similarly a fifty nanoseconds ADC gate served as a coincidence gate for the pulses coming out of the linear gate and stretcher units that preceded the analog to digital converter circuits (ADC) for the TA, Cerenkov, TTA, and the three de/dx counters.

The output of the various discriminators and diagnostic circuits was also counted by fast scalers. The most important were the three real event scalers (S24,S25,S33) which were used in the calculations of the computer dead time correction.

2.12 Data Recording and On-Line Analysis

Almost all the data recording functions were carried out by an XDS-9300 on-line computer. Information such as the status of individual counters, pulse heights, target temperatures and the status of various diagnostic circuits for each event was written on magnetic tape. Similarly, information such as the status of scalers and charge monitors, beam parameters, and the currents in each of the magnets was written on magnetic tape at the beginning and end of each run. The tasks to be performed by the computer were undertaken in order of preassigned priority interrupts. The highest priority interrupt was the event reading interrupt. The event logging interrupt was the next higher priority interrupt. Other tasks such as the adjustment of the magnet currents and the reading of the target temperatures were assigned lower priority interrupts and were usually performed once every second. Lower priority interrupts were assigned to other electronic checks and to the on-line data analysis and scope display tasks. On-line cross sections, efficiencies, hodoscope distributions and various corrections factors were updated continuously during the run and displayed on the scope. This on-line analysis was an essential part of the equipment checking and monitoring program. This on-line

analysis was sophisticated enough so that just a comparison of the on-line cross sections against previously measured data was a good check on the status of the experimental setup.

3 Data Analysis, Cross Sections and Errors

3.1 Summary of Correction Factors

The efficiency studies and the some of the correction factors were discussed in the previous chapter. In general we tried to include all known effects which could change the value of the cross section by more than 0.1%. It was found that if all effects of that order were included in the expressions for the efficiencies, then the chi-squared per degree of freedom for the various fits was 1.0 . Therefore, we felt confident that the error matrices of the fits yielded errors which were representative of our knowledge of the base efficiencies. The uncertainties in the various corrections such as rate and pedestal drift corrections were added in quadrature to the errors in the base efficiencies. We present a summary of the various correction factors and efficiencies and mention the effects that were included in their evaluation or were not included since they were negligible.

1. The computer dead time correction. This correction could be as high as 30%, but was well understood. It was obtained from the Event Interrupt Scaler by taking the ratio of the

OR4 possible real event interrupts to the actual number of OR4 real events read and logged by the computer.

2. The C1 dead time correction. This correction accounted for dead time in the trigger counter discriminators. Since 'TA only' was one of the possible event triggers, we were able to compute the ratio of the number of events which exhibited a good trajectory in the hodoscopes, but with no C1 coincidence to the total number of good trajectory events which had a TA signal. This measured dead time was 3% at the most and agreed well with theoretical calculations based on rates.

3. The OR4 circuit dead time correction. It was calculated using the 35 nanosecond dead time of the OR4 circuit and the OR4 event rate. It was usually less than 1%.

4. The C2 (Cerenkov*C1) efficiency. It was known to 0.3% and was fitted separately for each of the two cycles of the experiment. Included were the C1 dead time contribution ($<3\%$) and the Cerenkov discriminator dead time contribution ($<1\%$). In addition, the variation of the efficiency with the track position due to the slight misalignment of the mirror was included in the analysis.

5. The TTA efficiency (0.91) was known to 0.1% except in the low E' region (<1.5 GeV). A TTA momentum dependent cut was applied such that the TTA efficiency remained at 0.910. This cut sometimes fell in a fractional channel. Since only integer channels were possible, a small correction ($<0.2\%$) was applied to compensate for that effect. A TTA pedestal drift correction was also applied. The correlation between the TTA and the de/dx was studied and a higher efficiency was used when a de/dx requirement was also used. Finally, the fact that double tracks had a higher efficiency was also included in the correction. There was no variation of the TTA efficiency with track position across the counter. Also the rate dependence of the efficiency was negligible.

6. The TA efficiency was 0.991 . A TA momentum dependent cut was applied such that the TA efficiency remained constant. The TA efficiency for multiple track electron events was 1.0 . Rate dependent effects, pedestal drift effects and effects due to the integerized cut were totally negligible. There was no variation of the TA efficiency with the track position across the counter.

6. The de/dx efficiencies for the low and high cuts were fitted as a function of momentum. The momentum ranges 1-3

GeV/c and 3-6 GeV/c were fitted separately. Also a gain shift between the two cycles of the experiment was included in the fit. Also included were rate dependent effects, pedestal drift effects, and effects stemming from the variation of the efficiency with the track position across the counter. In addition, the efficiencies for the four code classes were fitted separately since multiple track electron events had a much higher efficiency in the de/dx counter.

7. No electron ever triggered the Anti-counters except through a chance coincidence. For the two runs where the Anti-counter was used the chance contribution was subtracted.

8. The density correction was applied to each run. It accounted for temperature variations (when the fans were working) and local density variations (when the fans were not working).

9. A correction was applied for the hydrogen contamination in the deuterium (see section 3.4).

10. Whenever the C2 condition was used for a cross section a

C2F chance event contribution was subtracted from the cross section. This correction was usually less than 1.5%.

11.A correction was applied to account for the fact that the cross sections are actually cross sections averaged over the spectrometer acceptance (see section 3.9).

3.2 Off-Line Analysis - A General Description

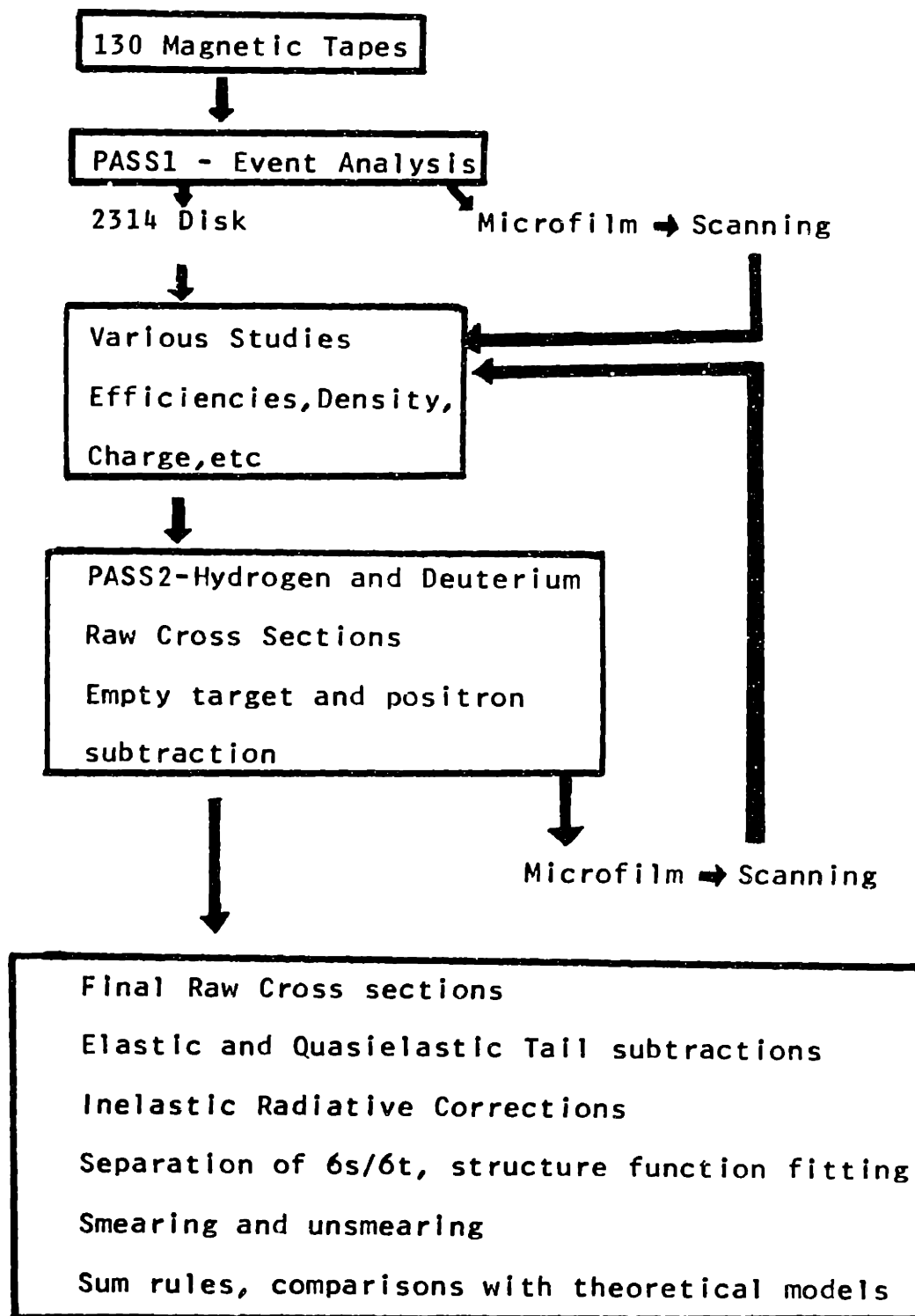
The off line analysis was done partly on the IBM 360/91 computer at SLAC, and partly on the IBM 360/65 at MIT. The off-line analysis was carried through in several stages. In the first stage (PASS1) the experiment was 'played back' to the computer by the reading of the event data tapes. The computer programs in the PASS1 package handled the event-by-event analysis for each run. Each event was categorized and various event sums and histograms were accumulated for each run. The various sums and histograms and other essential information for each run were stored on an IBM 2314 magnetic disk. All the essential information on the 130 magnetic data tapes was thus condensed on to one 2314 direct access device. Similarly, the condensed information for each run was also recorded on microfilm for the purpose of visual scanning. The condensed disk data was used for various essential studies such as the counter efficiency studies and the density correction studies. While those studies were being pursued, the microfilm output of the PASS1 analysis was visually scanned for irregular results.

The second stage (PASS2) consisted of the reduction of

the run by run condensed information to final cross sections. The extraction of the final cross section included the application of final efficiency and density corrections and the subtraction of the empty target and positron backgrounds. The PASS2 program package was designed to be run through several times while its microfilm output was being visually scanned for any anomalies that were possibly missed in the visual scanning of the PASS1 microfilm (see flow chart on next page).

The next stage consisted of the elastic and quasielastic radiative tail subtraction and the application of radiative corrections to the inelastic spectrum. This resulted in the final radiatively corrected hydrogen and deuterium cross sections. The final analysis included the application of corrections due to the nuclear binding effects in the deuteron (smearing and unsmearing), extraction of the neutron, proton and the deuteron structure functions, extraction of the σ_s/σ_t ratios for the deuteron and the proton and the evaluation of sum rules. Detailed information about the structure functions, σ_s/σ_t for the proton and the deuteron, and the evaluation of sum rules can be found in the thesis of E. M. Riordan (11). We will here lay stress on the neutron to proton structure functions ratios and differences.

The following is a schematic flow chart of the off-line analysis programs.



3.3 PASS1 - Event Analysis

Each event was categorized by its hodoscope codes, code classes, and its signature in the various electron-pion discriminating devices. We first present a few definitions of various event parameters.

- C1 - The event had a front rear trigger counter coincidence
- C2 - The event had a C1-Cerenkov counter coincidence
- TA - The event signal in the total absorption counter was above the TA electron defining cut.
- TTA - The event signal in the TTA counter was above the TTA electron defining cut.
- DEDXL - The event signal in each of the three de/dx counters was above the low cut between one and two minimum ionizing particle peaks.
- DEDXH - The event signal in each of the three de/dx counters was above the high cut between two and three minimum ionizing particle peaks.
- NOANTI - The event did not register an Anti-counter coincidence

The event signature in the various electron-pion discriminating devices was categorized by 11 tribes. The event tribe categories are shown below.

Tribe	Event requirements
1	C1*TA
2	C1*TA*C2
3	C1*TA*DEDXL
4	C1*TA*DEDXH
5	C1*TA*TTA
6	C1*TA*DEDXL*C2
7	C1*TA*DEDXH*C2
8	C1*TA*TTA*C2
9	C1*TA*TTA*C2*DEDXL
10	C1*TA*TTA*C2*DEDXH
11	C1*TA*TTA*C2*DEDXH*NOANTI

For the running period in the first cycle during which the TTA was not connected the NOANTI condition was substituted for the TTA requirement in the above definitions. As mentioned previously the de/dx requirement was heavily used for the runs taken during that period.

Forty TA spectra corresponding to spectra for the four code classes for each of the first ten tribe conditions were saved on the disk for each run. Those TA spectra were also recorded on microfilm. The TA spectra were visually scanned

and the error in the cross section for each run was minimized by the choice of the tribe with the smallest number of counter requirements consistent with a pion contamination of less than 1.5%. The tribe grouping in order of increasing pion rejection and decreasing electron efficiency is shown below.

C1*TA

C1*TA*C2 , C1*TA*DEDXL , C1*TA*TTA

C1*TA*DEDXH

C1*TA*C2*TTA , C1*TA*C2*DEDXL

C1*TA*C2*TTA*DEDXL

C1*TA*C2*DEDXH

C1*TA*C2*TTA*DEDXH , C1*TA*C2*TTA*DEDXH*NOANTI

The TA spectra corresponding to the four code classes for the chosen tribe were visually scanned for estimates of the pion contaminations above the electron defining cut. These contaminations, usually kept to less than 1.5%, were fed into the computer and a correction applied to the cross section. The reason for the accumulation of the separate TA spectra for the four code classes was that the pion contaminations were usually higher for the double and ambiguous code classes. The error in the estimated pion contamination was taken to be 1/3 of the contamination.

At high scattered energies and small ω tribes 1 (C1*TA) and 2 (C1*TA*C2) were used for the cross section definitions. The de/dx and TTA were used at lower scattered energies where the pion contaminations were larger. The more restrictive tribes such as tribes 9 and 10 were in general only used for high rate and low scattered energy positron runs. In general the positron runs had larger backgrounds than the electron runs and needed large pion rejection in order to obtain TA spectra with no pion contamination. Having made the choice of tribe for a given run we then investigated the 11 tribe raw cross sections for each run in order to ascertain that the cross section for the tribes which had a larger pion rejection than the chosen tribe had a cross section which was the same as the chosen cross section within the errors. Similarly, the cross sections for the less restrictive tribes (tribes with a lower pion rejection) were confirmed to be indeed higher than the cross section for the chosen tribe, thus confirming the observation that their TA spectra included pion contamination above the electron cut.

3.4 PASS2 - Run Combination, Raw Cross Sections and Errors

Extensive studies were carried through in the period following PASS1 and before PASS2. These studies resulted in the final values for the counter efficiencies, solid angle, normalization of the incident beam energies, normalization of charge monitors and density corrections. The scanning and the tribe selections that were mentioned in the previous section were also done during that period. The PASS2 program applied those final corrections to each run. Since the PASS2 programs were designed to be run several times, it was easy to incorporate the results of any of the studies into the programs as those results became available. The PASS2 programs were run four times. After each pass the microfilm output of the PASS2 programs was scanned and the cross sections for the various tribes compared to each other. In addition to applying the final corrections to each run, the PASS2 programs performed the empty target and positron subtractions. As described in section 2.4 the empty target background was measured utilizing an empty target cell with a wall thickness of 0.018 inches. The radiation length of this cell corresponded very closely to the radiation length of the liquid hydrogen target, thus simulating the radiative effects on the actual target wall contribution. Extensive

measurements of the liquid target wall thickness were made after the experiment by the use of a precision micrometer and by the weighing of known equal area circles punched out from the liquid and empty target walls. The two target wall measurements agreed to within the measurement error of 0.001''. The cross section for the 0.018'' empty target cell was divided by the ratio of 0.018'' to the actual liquid target wall thickness (about 0.003'') yielding the real target wall contribution to the measured cross sections. For each incident energy, several normalization runs were taken with an empty target cell with a wall thickness of 0.003''. It was confirmed that the ratio of the cross sections for the 0.018'' cell and the 0.003'' cell was indeed the ratio of their wall thickness within the statistical errors of the measurements. It must be stressed that the cross section for the thick cell was always better known than the cross section for the thin cell due to the higher counting rates, and the largest contribution to the error in this cross section ratio was due to the error in the thin cell cross section. The empty target background was typically 6% for hydrogen and 3% for deuterium.

At low scattered momenta the background contribution from charge symmetric processes such as

$$\pi_0 \rightarrow \gamma + e^+ + e^-, \quad \text{and} \quad \gamma + \text{nucleus} \rightarrow e^+ + e^-$$

was measured by reversing the spectrometer polarity and taking full and empty target runs. The final raw cross section was

$$\sigma(\text{raw}) = \sigma^-(\text{full}) - \sigma^-(\text{empty}) - \sigma^+(\text{full}) + \sigma^+(\text{empty})$$

where + or - denotes the spectrometer polarity (+ for positrons and - for electrons).

Mass spectroscopic measurements have shown that the deuterium used in the experiment had a hydrogen contamination of $x \approx 0.835\%$. That contamination was in the form of hydrogen deuteride (HD). Also, the value that was used for the deuterium target density was obtained from cryogenic measurements done on standard deuterium with $y = 0.4\%$ hydrogen contamination(37). Therefore the true deuterium cross section is

$$\sigma_d = \frac{(1 - \frac{y}{2}) \sigma_{dm} - x \sigma_{hm}}{1 - x}$$

where σ_{dm} is the measured deuterium cross section and σ_{hm} is the measured hydrogen cross section.

The random errors in the efficiencies, C1 dead time, density correction and the error in the pion contamination subtraction were added in quadrature to the statistical error

in the cross section for each run. The random errors in the full, empty, positron and positron empty target runs were added in quadrature yielding the total random error in the final raw cross sections. These errors were then propagated through the radiative corrections programs to yield the final errors in the radiatively corrected cross sections.

3.5 Radiators In the Beam Line

Calculation of the total radiation length of the material before and after the scattering event was necessary in order to correct for radiative effects coming from the straggling of the electron in the material. The equations for the total average radiation lengths before (T_b) and after (T_a) the scattering were

$$T_b = \sum M_b + L + l$$

$$T_a = \sum M_a + L (\cos\theta + \theta/\sin\theta)/2 + l\theta/\sin\theta$$

L is half the length of the liquid target in radiation lengths, and l is the thickness of the target wall in radiation lengths. $\sum M_b$ and $\sum M_a$ are the sums of the radiation lengths of all other materials before or after the scattering and θ is the scattering angle. The radiation lengths for the two liquid targets as a function of the angle are given in Table 3.

Table 3
Hydrogen and Deuterium Target Radiation Lengths

Target	Tb	Ta 18°	Ta 26°	Ta 34°
Hydrogen	0.005338	0.010310	0.010255	0.010186
Deuterium	0.006349	0.011770	0.011728	0.011681

3.6 Radiative correction - Introduction

The radiative corrections procedure for deuterium was slightly different than the one for hydrogen. The procedure that was followed for hydrogen involved the subtraction of the elastic e-p radiative tail followed by a two dimensional inelastic radiative unfolding program. The procedure that was followed for deuterium involved the subtraction of the deuterium elastic tail followed by the subtraction of the deuterium quasielastic tail which was followed subsequently by the application of the two dimensional inelastic radiative unfolding program.

The term radiative corrections is applied to all those procedures employed to correct for the effect of the radiation of photons before, after and during the scattering process. The final radiatively corrected cross section is the cross section for the scattering process to lowest order in α . Theoretical discussions of the radiative corrections can be found in Maximon(15) and in Mo and Tsai(16,21,46). We now present an outline of the radiative corrections procedure. Specific formulae can be found in the Ph.D. thesis of E. M. Riordan (11).

3.7 Elastic and quasielastic tails

The elastic hydrogen tails included contributions from several processes. The most important contribution was from single photon internal bremsstrahlung calculated exactly to lowest order in α by Tsai(46). There were additional smaller contributions coming from energy losses due to bremsstrahlung in the material before and after the scattering process (straggling), radiation from the recoiling nucleons, and multiple photon processes. These latter were treated approximately. The expressions for these additional contributions were derived by Friedman(17). The elastic tail calculation required the knowledge of the elastic e-p cross section. This cross section was obtained from a fit (2) to elastic e-p form factors which had been measured in a previous experiment at SLAC(23,48) (see Appendix B).

The elastic e-d radiative tails were calculated in an identical fashion to the way the elastic e-p tails were calculated with the deuteron mass replacing the proton mass in the formulae. The necessary elastic e-d cross sections were calculated theoretically using deuterium form factors derived from the Hamada-Johnston(18) wave function. These theoretical form factors agreed well with previous elastic e-d scattering measurements(19).

Since the multiple photon corrections and corrections due to radiation by the target nucleus are extremely difficult to calculate for the case of quasielastic scattering, and since the calculation of the exact single photon internal bremsstrahlung involves a large amount of computer time for the case of quasielastic scattering, a two stage approach was used instead. First the internal bremsstrahlung process was treated as a straggling process utilizing an equivalent radiator approach formulated by M. Sogard(20). The approximation was expected to be valid in the soft photon limit and therefore correct in the region close to the maximum of the quasielastic peak. However, it was expected to deviate from the exact calculation in the region far from the peak where the tail involves large contributions from hard photon processes and two photon processes. Therefore, a correction factor which utilized the close relationship between quasielastic e-d scattering and elastic e-p and e-n scattering was applied for missing masses greater than 1 GeV. The expression for the final deuterium tail was

$$\left(\frac{d^2\sigma}{d\Omega dE'} \right)_{e-d} = \left(\frac{d^2\sigma_{EQ}}{d\Omega dE'} \right)_{e-d} \left[\frac{\left(\frac{d^2\sigma_{EX}}{d\Omega dE'} \right)_{e-p} + \left(\frac{d^2\sigma_{EX}}{d\Omega dE'} \right)_{e-n}}{\left(\frac{d^2\sigma_{EQ}}{d\Omega dE'} \right)_{e-p} + \left(\frac{d^2\sigma_{EQ}}{d\Omega dE'} \right)_{e-n}} \right]$$

where EX denotes a calculation done in the manner of Friedman using the exact single internal bremsstrahlung term and including multiple photon effects and effects due to the radiation by the target nucleus. EQ denotes a calculation done in the manner of Sogard utilizing the equivalent radiator approximation.

The quasielastic cross section needed in the tail calculation was calculated from an expression given by Durand(22) using Hamada Johnston(18) S and D state wave functions. The neutron form factors that were used were $G_E^n = 0$, and $G_M^n = (\mu_n/\mu_p)G_M^p$ (24,25), where G_E^n and G_M^n are the electric and magnetic neutron elastic form factors, G_M^p is the magnetic form factor of the proton, and μ_p and μ_n are the static magnetic moments of the proton and the neutron. The previously reported SLAC elastic e-p form factor measurements(2,23,28) extended as far as $q^2 = 25 \text{ (GeV/c)}^2$. These measurements were sufficient for the purpose of calculating the elastic tails for this experiment since the highest q^2 for the elastic peak contributing to the tails was 22.2 (GeV/c)^2 . On the other hand, the neutron form factors are known only up to a q^2 of 5 (GeV/c)^2 (24,25). However, the contribution of the neutron to the quasielastic tail was usually less than 3% of the measured raw cross section, and most of the 3% came from the contribution of

the low q^2 region of the radiative triangle. Similarly, the elastic e-d tests for the form factors predicted by the Hamada-Johnston wave function were carried through up to a q^2 of 1.33 (GeV/c)^2 (19). However, the elastic e-d radiative tail was totally negligible and was usually less than 10^{-5} of the measured inelastic raw deuterium cross section. The only data included in the $6n/6p$ analysis were data for which the scattered momenta were greater than 2.49 GeV/c and for which q^2 was greater than 1.0 (GeV/c)^2 , and W greater than 2.0 GeV . The percentage of the elastic and quasielastic contributions to the measured raw hydrogen and deuterium cross sections are listed in Table 4 only for the data used in $6n/6p$ analysis. As can be seen in Table 4 the fractional elastic and quasielastic tail contributions were usually very small. The expressions that were used for the neutron and proton form factors are given in Appendix B.

E'	H ₂	D ₂	E'	H ₂	D ₂
E = 6.5, θ = 18.0			E = 13.3, θ = 18.0		
3.612	1.57	1.53	6.500	0.27	0.32
3.498	1.70	1.57	6.000	0.31	0.30
3.382	1.78	1.61	5.750	0.37	0.34
3.261	1.92	1.69	5.500	0.42	0.40
3.099	2.27	1.92	5.250	0.51	0.45
2.997	2.53	2.07	5.000	0.58	0.53
2.855	2.83	2.11	4.750	0.76	0.63
2.697	3.39	2.69	4.500	0.87	0.79
2.498	4.55	3.49	4.275	1.14	0.96
			4.000	1.50	1.22
			3.822	1.77	1.45
			3.681	2.18	1.68
			3.502	2.58	1.95
			3.344	2.90	2.33
			3.090	4.20	3.13
			2.918	4.92	3.88
			2.737	6.84	4.62
			2.632	6.87	5.23
			2.500	8.98	6.10
			E = 17.0, θ = 18.0		
			8.000	0.22	0.28
			7.500	0.19	0.21
			7.000	0.23	0.23
			6.500	0.31	0.28
			6.000	0.42	0.38
			5.750	0.49	0.45
			5.500	0.60	0.51
			5.350	0.66	0.56
			5.000	0.89	0.74
			4.750	1.10	0.88
			4.500	1.30	1.05
			4.250	1.58	1.25
			4.000	2.00	1.57
			3.750	2.48	1.95
			3.500	3.39	2.60
			3.334	4.04	2.96
			3.152	4.80	3.66
			3.000	5.61	4.24
			2.750	8.21	5.69
			2.500	10.48	7.69
E = 10.4, θ = 18.0					
5.498	0.51	0.55			
5.250	0.49	0.51			
4.998	0.54	0.54			
4.750	0.61	0.58			
4.498	0.74	0.66			
4.311	0.84	0.77			
4.125	1.01	0.90			
3.937	1.22	1.03			
3.792	1.46	1.19			
3.640	1.71	1.38			
3.498	2.00	1.58			
3.352	2.33	1.85			
3.192	2.72	2.19			
2.998	3.53	2.70			
2.838	4.26	3.27			
2.688	5.28	3.91			
2.497	7.09	5.15			
E = 12.5, θ = 18.0					
5.914	0.33	0.34			
4.947	0.60	0.52			
4.121	1.24	1.04			
3.314	2.91	2.30			
2.944	4.65	3.48			
2.689	6.19	4.61			

Table 4 : Elastic and Quasielastic Tail Percentages for Hydrogen and Deuterium for W Greater than 2.0 GeV, q^2 Greater than 1.0 (GeV/c)² and E' Greater than 2.49 GeV.

E'	H ₂	D ₂	E'	H ₂	D ₂
E = 6.7, θ = 26.0			E = 18.0, θ = 26.0		
2.750	1.36	1.33	5.496	0.32	0.39
2.500	1.76	1.57	5.246	0.27	0.31
E = 8.7, θ = 26.0			4.996	0.30	0.32
3.502	0.74	0.78	4.746	0.39	0.38
3.252	0.86	0.83	4.495	0.47	0.47
3.001	1.07	0.98	4.244	0.55	0.56
2.751	1.46	1.26	3.994	0.74	0.71
2.502	2.02	1.70	3.745	0.97	0.87
E = 11.9, θ = 26.0			3.493	1.22	1.07
4.249	0.43	0.48	3.247	1.52	1.38
4.000	0.48	0.48	3.000	2.01	1.82
3.750	0.58	0.55	2.743	2.96	2.58
3.500	0.73	0.70	2.500	4.33	3.46
3.250	0.97	0.88	E = 7.9, θ = 34.0		
3.000	1.37	1.15	2.500	1.14	1.00
2.750	1.84	1.58	E = 10.4, θ = 34.0		
2.500	2.74	2.16	2.750	0.94	0.92
E = 15.0, θ = 26.0			2.500	1.18	1.18
5.000	0.44	0.48	E = 12.5, θ = 34.0		
4.750	0.32	0.37	3.250	0.91	0.67
4.500	0.36	0.38	3.000	0.69	0.66
4.250	0.45	0.45	2.750	0.91	0.87
4.000	0.60	0.53	2.500	1.27	1.22
3.750	0.72	0.66	E = 15.0, θ = 34.0		
3.500	0.99	0.90	3.250	0.52	0.55
3.250	1.32	1.11	3.000	0.74	0.72
3.000	1.74	1.47	2.750	1.08	0.94
2.753	2.42	1.98	2.500	1.46	1.44
2.500	3.53	2.77			

Table 4 Continued.

3.8 Inelastic radiative corrections

The computation of the elastic and quasielastic tails involved the radiative degradation of an unradiated cross section obtained from previous measurements or from a theory consistent with previous measurements. The inelastic radiative corrections required the unfolding of the already radiatively degraded measured raw cross section. Due to the immense complexity of the calculations, multiple photon processes were only included in an approximate way. The effects due to bremsstrahlung in the material before and after the scattering were included in the formalism. The single photon internal bremsstrahlung contribution has been approximated using an equivalent radiator approximation. This approximation enabled the radiative unfolding procedure to be done using data taken at one angle only. Figure 2 shows the kinematic range of the data in E_0 and E' in the form of radiative corrections triangles. Knowledge of the two inelastic proton form factors is needed for the purpose of testing the validity of a particular equivalent radiator factorization approximation. The exact tail from the one photon internal bremsstrahlung was calculated using the scaling of $\sqrt{W^2}$ in X' , and using $R = 0.18$. Similarly the

same inelastic tails were calculated using the equivalent radiator factorization approximation. The deviation of the approximate calculation was never more than a few percent(47).

The processes by which radiation could affect the measured cross section at a given E_0, E' point can be simply described by referring to the radiative corrections triangle. Also, using the equivalent radiator approximation we can treat the effects of the internal bremsstrahlung as equivalent to a straggling in some amount of 'equivalent radiator' before and after the scattering. An electron which would have had a higher scattered energy emits a photon or straggles to the final momentum E' . The contribution of all such electrons involves an integral I_1 over the unradiated cross section at fixed E_0 , and E' varying from pion threshold to the measured E' point. A different contribution comes from processes in which the electron emitted a photon or straggled before the scattering process and then scattered with a different effective incident energy. This involved an integral I_2 over the unradiated cross section at fixed E' and varying E_0 . A third correction arises from those electrons which would have been detected within the measured E_0, E' bin, but a

fraction $1/C$ of them were lost due to the emission of photons or straggling after the scattering process. The radiatively corrected cross section $(d^2\sigma/d\Omega dE')_c$ could than be expressed in terms of the measured cross section $(d^2\sigma/d\Omega dE')_m$.

$$(d^2\sigma/d\Omega dE')_c = C ((d^2\sigma/d\Omega dE')_m - I_1 - I_2)$$

Since the integrals I_1 and I_2 involve radiatively corrected cross sections one must start the unfolding procedure at the highest E_0, E' corner of the radiative corrections triangle. Starting at that highest E_0, E' point one then proceeds to correct data at lower E_0 and E' by using the higher E_0, E' corrected data. As can be seen in figure 2 the range of the measured data was not large enough and the data point spacing not small enough to allow for a successful radiative corrections procedure without extensive interpolation and extrapolation. The interpolation-extrapolation program that was used involved a two dimensional quadratic interpolation or extrapolation using four data points at a time. In order to increase the reliability of the interpolation procedure, the data was first divided by a smoothing function which utilized the scaling of the structure functions in the variable X' . The

sensitivity of the final cross sections to the type of smoothing function used was typically less than 1% (for the restricted region $q^2 > 1 \text{ (GeV/c)}^2$, $W > 2 \text{ GeV}$, and $E' > 2.49 \text{ GeV/c}$). More details about the interpolations and radiative corrections programs can be found in the Ph.D. thesis of E.M. Riordan(11), the Ph.D. thesis of J.S. Poucher (13) and in the Ph.D. thesis of M. Breidenbach(49). Detailed expressions for the equations that were used can be found in the Ph.D. thesis of E. M. Riordan (11).

3.9 Nuclear Binding Effects, Smearing, Unsmearing and, Structure Function Fits.

A complete discussion and a derivation of expressions relating to the effects of nuclear binding in the deuteron is found in Appendix A. We shall use the term smearing for all effects in the observed scattered spectra resulting from nuclear binding in the deuteron. In the impulse approximation the two basic equations relating the deuteron structure functions to the structure functions of the neutron and the proton are

$$2M\omega_1 d = M r \int |\phi(P_s)|^2 P_s dP_s / \omega \int d\omega'' 2M(\omega_1 p + \omega_1 n) + G_1 \gamma''(\omega_2 p + \omega_2 n)$$

$$\omega_1 \omega_2 d = M r \int |\phi(P_s)|^2 P_s dP_s / \omega \int d\omega'' \omega'' \gamma''(\omega_2 p + \omega_2 n) G_2$$

Detailed expressions for the integration limits, G_1 , G_2 , r , and other terms in the above expressions are given in Appendix A. The important terms are $\phi(P_s)$ which is the non relativistic deuteron wave function in momentum space and G_1 and G_2 which are relativistic tensorial corrections arising from the requirements of gauge invariance. As q^2 goes to ∞ , r goes to 1, G_1 goes to 0, and G_2 goes to 1. Uncertainties in the smearing formalism come from ambiguities in the off-mass-shell definitions of the proton

and neutron structure functions, and from unknown off-mass-shell and relativistic corrections to the deuteron wave function. Those and other uncertainties are discussed in Appendix A.

The first step in accounting for the nuclear binding effects is to introduce those effects into the hydrogen inelastic cross sections. We denote the resulting smeared proton cross sections as σ_p . Subtraction of the smeared proton cross section from the measured deuterium cross section is assumed to yield the smeared neutron cross section σ_n . The easiest and most direct way to compare the predictions of a theory to the data is by smearing the theoretical neutron and proton cross sections, evaluating the smeared ratio σ_n/σ_p and comparing it to the smeared ratio obtained from the experiment. However, there are very few theories which give a prediction for the neutron and proton structure functions over the entire range of ω . Most theories have adjustable unknown parameters, while others predict the behavior of the structure functions as ω goes to 1, or as ω goes to ∞ .

Since the smearing integrals always involve an integration over a large range of ω , a true unfolding procedure similar to the radiative corrections unfolding is almost impossible. The unfolding procedure that we employed

involved a best fit method. The proton and neutron structure functions were parametrized in terms of polynomials in $(1-X')^n$ where n varies from 3 to 7. $R_p=R_n$ was assumed since the measured values of R_p were the same as the measured values of R_d within the errors of our measurements(11) (Also see section 4.4). We now present an outline of the smearing, unsmearing and structure function fitting procedures.

After corrections for the averaging over the spectrometer acceptance, $\sqrt{W^2}$ for the proton was fitted to a sum of polynomials whose constant coefficients were determined by the fit. Only data for which W was greater than 2.0 GeV, q^2 was greater than 1 (GeV/c)² and E' greater than 2.49 GeV were included in the fit. Since very little resonance data were taken, and the threshold region can't be described solely by X' the inelastic threshold condition was introduced in a simple phenomenological way (56) by the inclusion of a threshold multiplicative factor A_w .

$$A_w = (W^2 - (M + \pi)^2) / (W^2 - (M + \pi)^2 + \pi^2)$$

where π is the pion mass and M is the mass of the nucleon. For W greater than 2.0 GeV this threshold factor was 1.0 to within 1%. The threshold factor goes to zero at pion

threshold and reaches the value of about 0.95 by the time W has reached the value of the mass of the first resonance (1.238 GeV). The form of A_W would have been more complicated if detailed resonance data had been taken. Had the latter occurred, more terms would have been added to describe the resonances and their q^2 dependence.

One fit that was tried was a fit in the variable X' using a form suggested by Breidenbach and Kuti(29).

$$\begin{aligned}
 W_2 &= A_W \sum_{i=3}^7 a_i g_i(X', q^2) \\
 g_3 &= (1-X')^3 \sqrt{X'} \sqrt{(q^2/(q^2 + q_0^2))} \quad q_0 = 0.205 \\
 g_4 &= (1-X')^4 q^2/(q^2 + q_0^2) \\
 g_5 &= (1-X')^5 q^2/(q^2 + q_0^2) \\
 g_6 &= (1-X')^6 \\
 g_7 &= (1-X')^7
 \end{aligned}$$

The first $(1-X')^3$ term was there in order to satisfy the experimental connection between the q^2 dependence of the elastic e-p form factor and the threshold behavior of the inelastic structure functions(35,6,7). Fits including a $(1-X')^2$ as the leading term were also attempted, but the coefficient of the $(1-X')^2$ term was consistent with zero. The multiplicative term $q^2/(q^2 + q_0^2)$ was included in order to obtain the correct behavior at the photoproduction limit

($\sqrt{s} \rightarrow 0$ as $q^2 \rightarrow 0$). The \sqrt{x} term was included in order to simulate the Regge model properties arising from the ρ and A_2 mesons. The chi-squared per degree of freedom for this fit was 1.0 for 192 degrees of freedom. The resulting fit coefficients were $a_3=0.3917$, $a_4=2.951$, $a_5 = -1.587$, $a_6 = -3.947$, $a_7 = 2.857$.

Another fit which yielded a chi-squared of 1.06 per degree of freedom was a fit to the following set of functions.

$$g_i = (1 - x)^i$$

The resulting fit coefficients were $a_3=0.5435$, $a_4 = 1.714$, $a_5 = 0.6723$, $a_6 = -5.971$, $a_7 = 3.313$.

The above fits included a correction due to the fact that the measured cross section was actually an average cross section integrated over the spectrometer acceptance. Each cross section was corrected by the following ratio obtained from the \sqrt{s} fit.

$$C = \sigma_{fc} / \sigma_{fi}$$

where σ_{fc} was the fit cross section evaluated at the central momentum and angle, and σ_{fi} was the fit cross section integrated over the spectrometer acceptance.

The fit to the structure functions of the proton was used to obtain the smearing correction for the proton S_p . The smearing correction was defined as the ratio between the proton cross section and the proton cross section with nuclear binding effects included, each of which was integrated over the spectrometer acceptance. Using this smearing correction we obtained the ratio of the smeared neutron and proton cross sections σ_{ns}/σ_{ps} . We then applied the unsmeared correction to that ratio in order to take out the deuteron binding effects completely.

Since the smearing integrals are integrals over a wide range of ω , and since sufficient resonance data was not taken for the majority of the lines, the way one extrapolated in order to obtain the values of the cross section in the resonance region affected both the values of the smearing and unsmeared corrections. The resulting uncertainty is not large, but it could have been eliminated if one had taken additional data in the resonance region. The assumption that was made was that the deep inelastic universal curve for the structure function averages the resonances when one uses the variable X' as the fitting variable. This averaging was found to be correct to 2% at a q^2 of $2.0 (\text{GeV}/c)^2$ (6,7). Actually the average is an average which includes the elastic peak also, but the

resulting error is small. It was found that the way one extrapolated into the resonance region did not affect the smearing correction very much (1.2% at the most).

Having obtained the smeared neutron cross section we then proceeded to do the unsmeared fit. Five structure function polynomials were smeared and the smeared neutron cross section data was fitted to those smeared polynomials. The assumption that was made was that the unsmeared neutron cross section was represented by the sum of those polynomials before they were smeared and with the coefficients obtained from the fit.

The fit to the neutron cross section was then used to evaluate the smearing correction for the neutron ($S_n = \sigma_n / \sigma_{ns}$). The unsmeared correction was $U = S_n / S_p$. Here again the way one extrapolated in order to obtain the values for the neutron cross sections in the resonance region affected the unsmeared results by a small amount. The unsmeared correction obtained from the unsmeared fit to the neutron data was slightly dependent on the number of polynomials included in the fit. The unsmeared correction remained the same for $X' < 0.6$, but differed significantly for $X' > 0.6$ depending on whether a three, four or five polynomial fit was used. The reason for the variation was that three

free parameters were not sufficient to describe both the large and small X' behavior of the neutron and proton structure functions. The unsmearing correction was also slightly different depending on whether only the data of this experiment were included in the fit, or whether the 6 and 10 degree data (13) were included also. The reason for those variations stemmed from the fact that there was little data near $X'=1$, and the different fits extrapolated differently into that region. The assumption made was that the deep inelastic neutron fit averaged the resonance region. Therefore, the way the fit extrapolated to $X'=1$ affected the smearing integrals for the neutron and therefore affected the unsmearing correction. RL will denote the extrapolated $\bar{\sigma}_n/\bar{\sigma}_p$ ratio at $X'=1$. RL is also the ratio of the coefficients of the leading $(1-X')^3$ terms for the neutron and proton structure function fits. Since the value of RL affected the unsmearing, and since it was dependent on the number of polynomials used or the amount of data included in the fit we chose to fix it at a value of 0.38. The error in the unsmearing correction was then obtained from its variation for different choices of RL. The value 0.38 was the average of the closest points to $X'=1.0$. The value of 0.25 seemed to be the value one gets if one does a linear extrapolation of the $\bar{\sigma}_n/\bar{\sigma}_p$ data. To

get some estimate of the error in the unsmearing correction we varied the fits using a value of RL varying from 0.25 to 0.51 (= 0.38 +(0.38-0.25)) with 0.38 as the mean. The error band in the unsmearing correction resulting from its variation over this range of RL, and from its variation with the amount of of the data included in the fit is shown in Table 5 of the next section (that error is 3% at the most). We included a few data points for which W was between 1.8 and 2.0 GeV ($q^2 > 10 \text{ (GeV/c)}^2$) in order to have a few additional data points in the small ω region for the purpose of helping fix the unsmearing fit near $X'=1$, and thus reduce the error in the unsmearing correction.

A step by step summary of the fitting, smearing and unsmearing procedures now follows.

1. Fit the proton structure functions to

$$\nu W_{2p}(X',W) = \sum_{i=3}^7 a_i f_i(X',W) \quad , \quad \begin{aligned} f_i &= A w \quad g_i \\ g_i &= (1-X')^i \end{aligned}$$

2. Smear the proton fit to obtain a smearing correction S_p using $R_p = 0.18$.

$$S_p = \delta p / \delta p_s$$

3. Obtain the smeared neutron cross section from the deuterium and hydrogen cross sections.

$$\delta n_s = \delta d - \delta H / S_p$$

At this point we can compare the smeared ratio δ_{ns}/δ_{ps} with the smeared ratio predictions of theoretical models.

$$\delta_{ns}/\delta_{ps} = \delta_{d Sp} / \delta H - 1$$

4. Smear the five structure function polynomials that were chosen. Smearing the functions $f_i(X', W)$ yields $f_i(X', W)_s$.
5. Using $R_n = R_p = 0.18$ fit the smeared neutron data to the sum of the smeared polynomials.

$$\sqrt{W} 2n_s = \sum_{i=4}^7 b_i f_i(X', W)_s + RL a_3 f_3(X', W)_s$$

$$\chi^2 = \sum_{\text{All data}} (\sqrt{W} 2n_s(\text{experimental}) - \sqrt{W} 2n_s)^2$$

Find the coefficients b_i that minimize χ^2 , and deduce that the least chi-squared fit to the unsmeared neutron is

$$\sqrt{W} 2n = \sum_{i=4}^7 b_i f_i(X', W) + RL a_3 f_3(X', W)$$

$RL=0.38$ and a_3 is the coefficient obtained from the proton fit.

6. Use the best fit for the neutron to form the unsmearing correction.

$$U = S_n / S_p, \quad S_n = \delta_n / \delta_{ns}$$

7. Obtain the unsmeared neutron to proton cross section ratios for each data point using

$$\delta_n / \delta_p = U \delta_{ns} / \delta_{ps}$$

3.10 Final Cross Sections, σ_n/σ_p Ratios and Error Discussion.

The final radiatively corrected cross sections averaged over the spectrometer acceptance are given in Appendix D. The information given in Appendix D includes W , the missing mass for each point, σ_H the hydrogen cross section and its associated error, σ_d the deuterium cross section and its associated error, C the correction to the hydrogen cross section resulting from the averaging over the spectrometer acceptance, S_p the average smearing correction for the proton, U the unsmearing correction which also includes a correction for spectrometer acceptance averaging, the smeared proton to neutron cross section ratio σ_{ns}/σ_{ps} , the unsmeared ratio σ_n/σ_p , and their respective errors.

Useful relations are

$$\sigma_p = \sigma_H C$$

$$\sigma_n = \sigma_p (\sigma_n/\sigma_p)$$

$$\sigma_{ns}/\sigma_{ps} = \sigma_d S_p/\sigma_H - 1$$

$$\sigma_n/\sigma_p = (\sigma_{ns}/\sigma_{ps}) U$$

The smeared neutron to proton cross section ratios σ_{ns}/σ_{ps} are shown as functions of X and X' in figures 11 and 12 respectively. Similarly the unsmeared σ_n/σ_p ratios are

shown as functions of X and X' in figures 13 and 14. Each one of the points in figures 11-20 is an average of several data points from Appendix D, binned in small bins (0.02 each) in X or X' . The unsmearing correction was obtained using the constraint that $6n/6p$ goes to 0.38 at $X'=1.0$. As mentioned previously the error band in the unsmearing correction was obtained by studying the variation in the value of the correction with different constraints for the extrapolated value for $6n/6p$ at $X'=1.0$. Additional information on the error was obtained by restricting the number of points included in the fit (only $18^\circ, 26^\circ, 34^\circ$ data or including 6° and 10° data). The unsmearing correction and its mean error is shown in Table 5. As can be seen the unsmearing correction is close to 1.0 for the majority of the points. This indicates that the smeared and unsmeared neutron to proton ratios are the same for a large fraction of the data. The error in the unsmearing correction is largest for the highest X' point at $X'=0.8316$. As mentioned previously this error is not inherent in the procedure, but is due to the fact that insufficient data was taken in the resonance region where X' is close to 1.0. The theoretical error band in the neutron to proton cross section ratio due to the theoretical uncertainty in the smearing correction is shown in figure A6 of Appendix A.

Table 5
The Unsmearing Correction and Its Error

X'	Unsmearing Correction	Error †
0.8316	0.919	0.030
0.7731	0.945	0.020
0.7174	0.964	0.007
0.6642	0.976	0.002
0.6133	0.985	0.001
0.5641	0.990	0.001
0.5181	0.993	0.001
0.4735	0.996	0.001
0.4307	0.998	0.001
0.3896	0.999	0.001
0.3501	1.000	0.001
0.2000	1.002	0.001
0.0480	1.001	0.001

† The error quoted is also $\Delta(\delta n/\delta p) / (\delta n/\delta p)$ since unsmearing correction is a multiplicative correction.

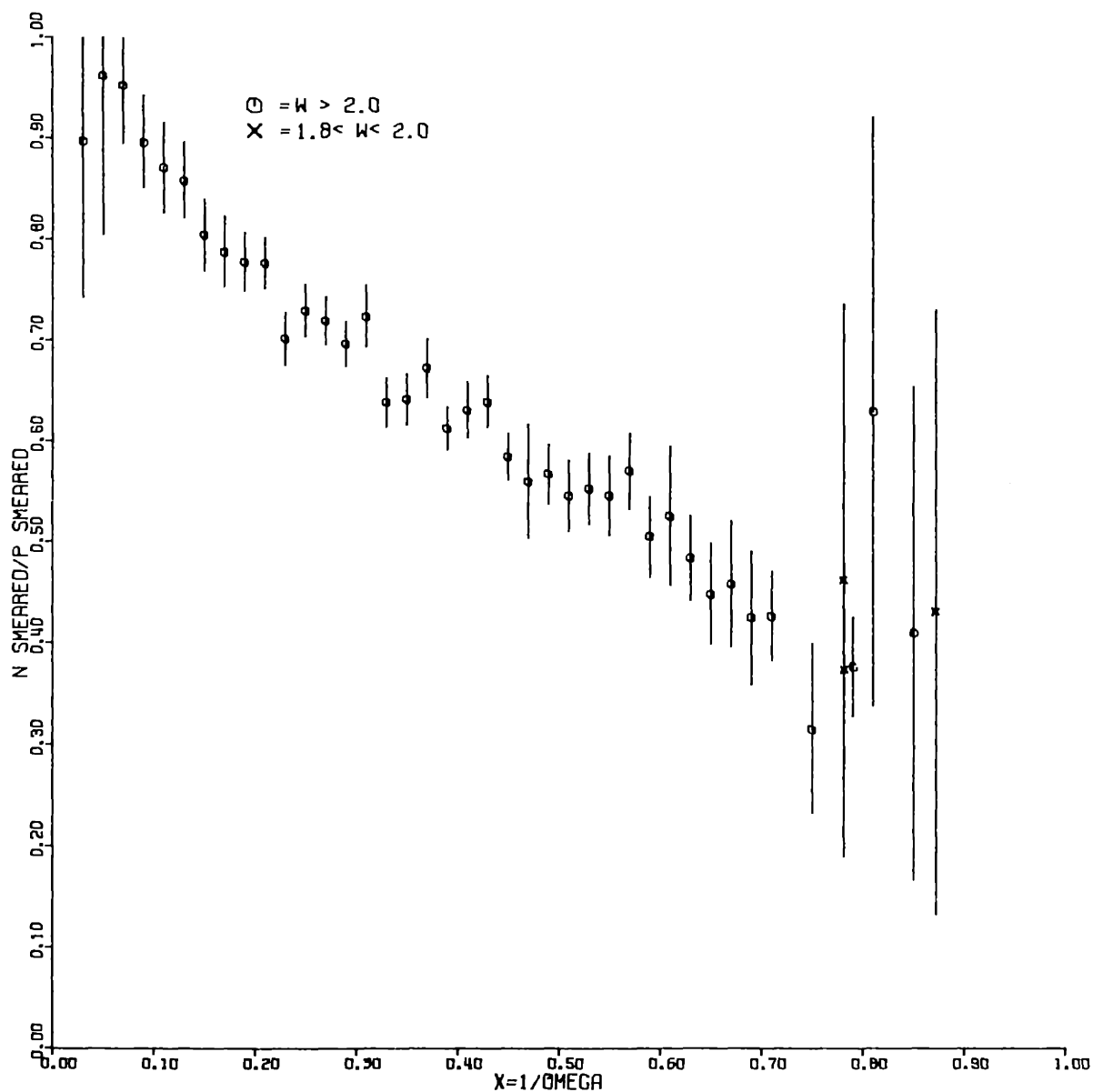


Figure 11 - The ratio of the smeared neutron and proton cross sections as a function of X . The data points presented are the result of the combining of all the data for which W was greater than 2.0 GeV, q^2 was greater than 1.0 (GeV/c)^2 and E' was greater than 2.49 GeV. Data for which W was between 1.8 and 2.0 GeV, and q^2 greater than 10.0 (GeV/c)^2 is shown in a different symbol.

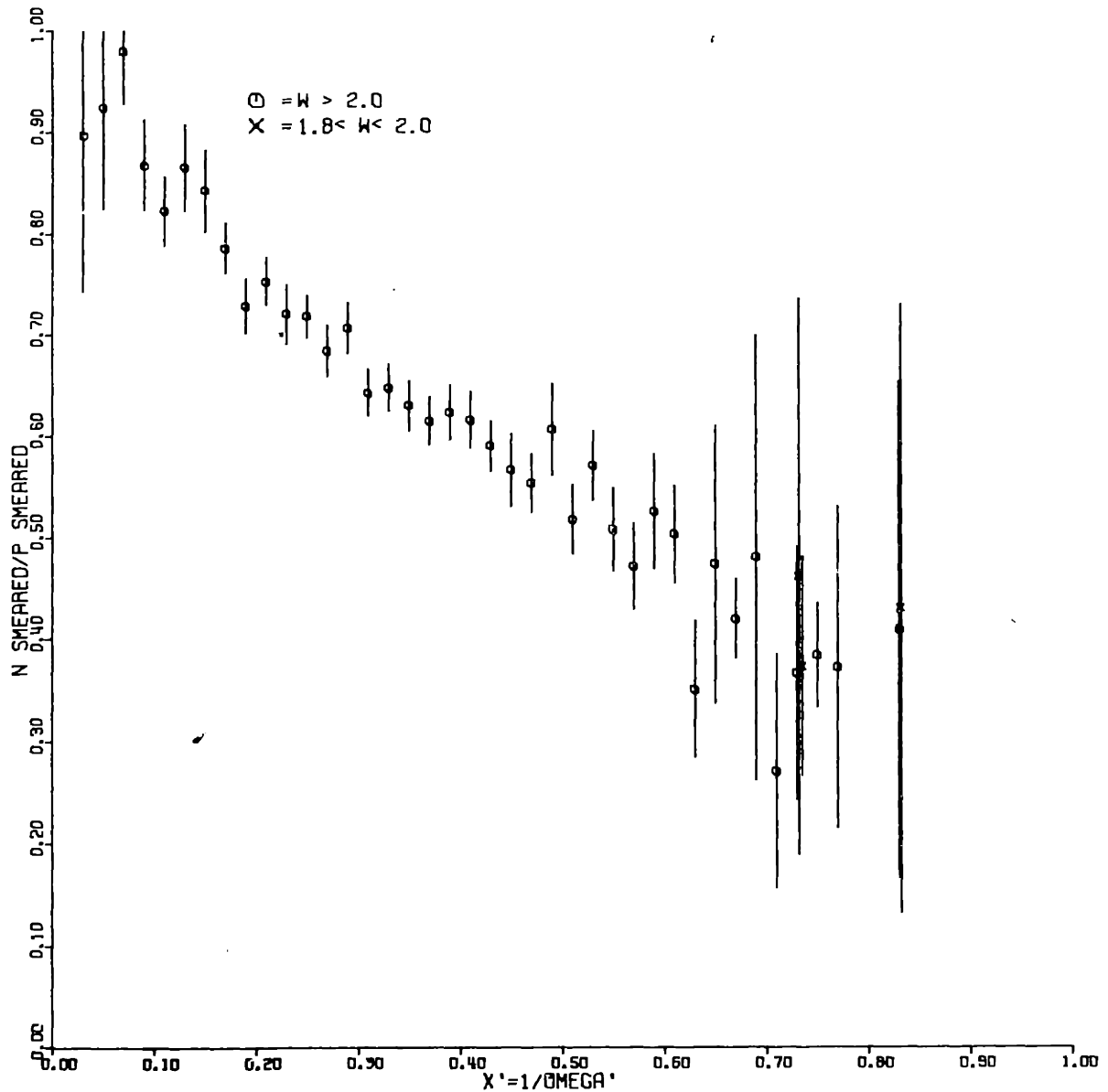


Figure 12 - The ratio of the smeared neutron and proton cross sections as a function of X' . The data points presented are the result of the combining of all the data for which W was greater than 2.0 GeV, q^2 was greater than 1.0 (GeV/c)^2 and E' was greater than 2.49 GeV. Data for which W was between 1.8 and 2.0 GeV, and q^2 greater than 10.0 (GeV/c)^2 is shown in a different symbol.

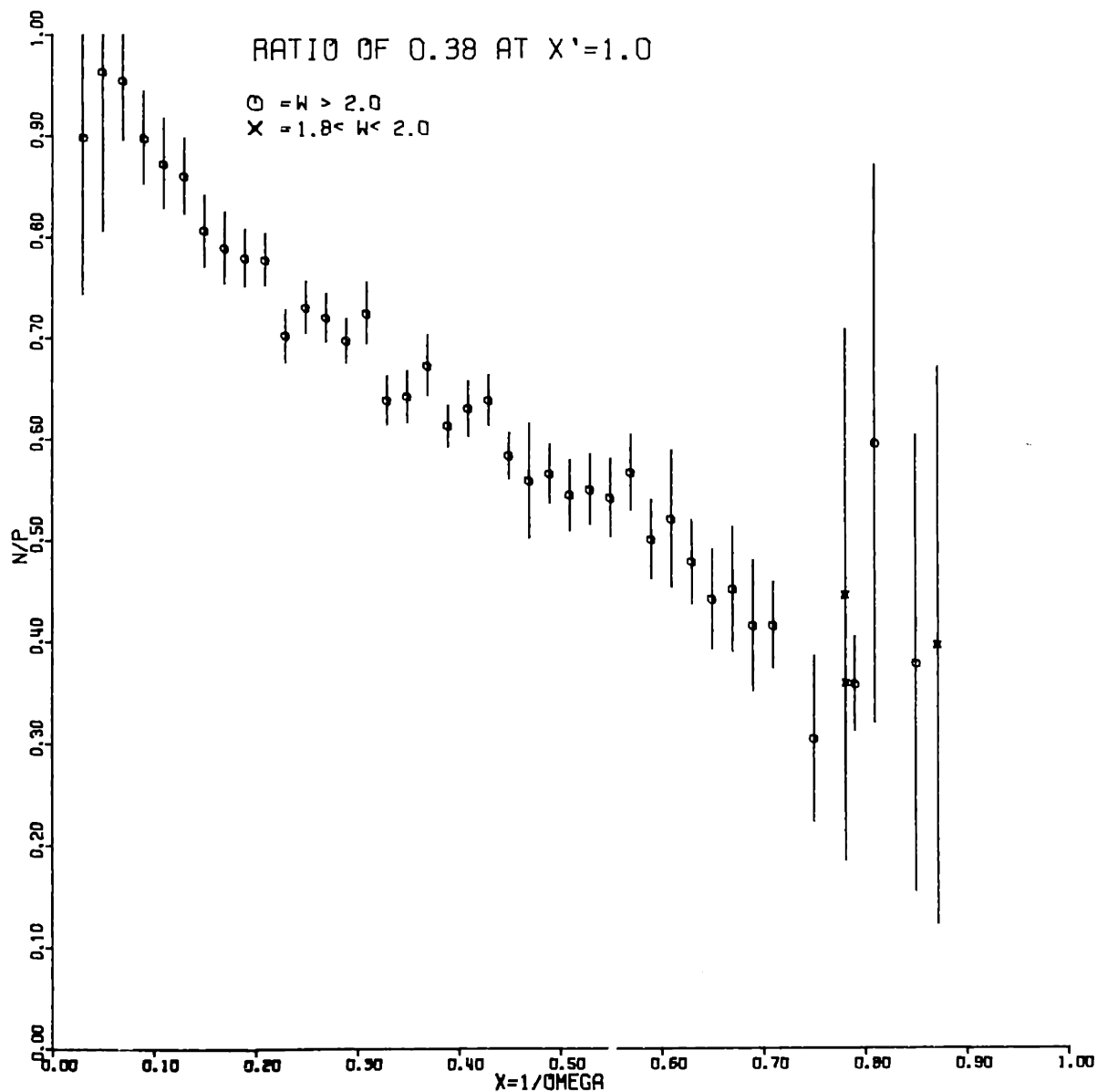


Figure 13 - The ratio of the unsmeared neutron to proton cross sections as a function of X . The unsmearing was done by fixing the unsmearing fit for the neutron to proton ratio at 0.38 for $X'=1$. The data points presented are the result of the combining of all the data for which W was greater than 2.0 GeV, q^2 was greater than 1.0 (GeV/c)^2 and E' was greater than 2.49 GeV. Data for which W was between 1.8 and 2.0 GeV is shown in a different symbol.

q^2 for the data points for W between 1.8 and 2.0 GeV was required to be greater than 10.0 (GeV/c)^2 .

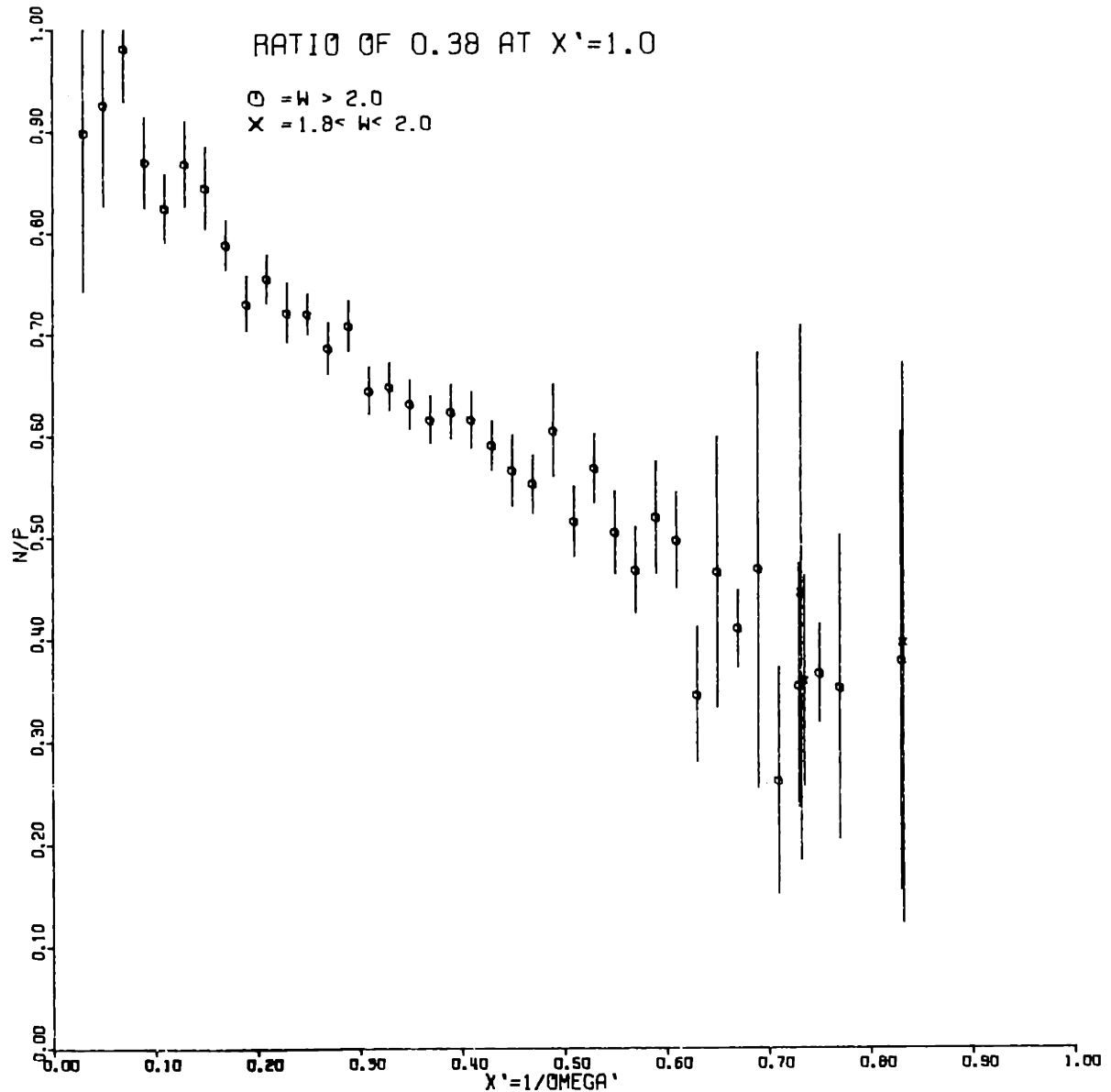


Figure 14 - The ratio of the unsmeared neutron and proton cross sections As a function of X' . The unsmeareding was done by fixing the unsmeareding fit for the neutron to proton ratio at 0.38 for $X'=1$. The data points presented are the result of the combining of all the data for which W was greater than 2.0 GeV, q^2 was greater than 1.0 (GeV/c)^2 and E' was greater than 2.49 GeV. Data for which W was between 1.8 and 2.0 GeV, and q^2 greater than 10.0 (GeV/c)^2 is shown in a different symbol.

The errors shown in figures 11-20 include only errors which had been propagated through the radiative corrections. These errors were mostly statistical and included the following,

1. Statistical errors due to event statistics in the hydrogen deuterium and empty target runs (including positron runs when applicable). The error in the pion contamination was also included (0.5% at the most).
2. The random error in the target densities obtained from the 0.25 % fluctuations in the properties of the pressure temperature transducers, or from the statistical error in the number of protons detected in the 1.6 GeV/c magnet.
3. The random error in the front and rear trigger counter dead time correction.
4. The errors in the efficiencies of the various counter detectors. These errors were partly random and partly systematic.

Most of the above mentioned errors do not cancel in the calculations of the neutron to proton cross section ratios. Part of the errors in the counter efficiencies cancel in that ratio. However, for most of the data the contribution of the uncertainty in the counter efficiencies to the total error was small. Also, a large fraction of the error in the

efficiencies was due to actual fluctuations in the properties of the counter detectors and also due to errors stemming from rate-related effects. For example, a large fraction of the error in the de/dx counter efficiency was due to uncertainties in the rate dependent coefficients. The rates for the hydrogen and deuterium were different and therefore part of the rate related errors do not cancel in the $6n/6p$ ratio. The fractional cancelation in the error in the neutron to proton cross section ratio due to counter efficiency errors was estimated to be about 0.6% on the average. Since it was not well known, and since it obviously depended on the particular target selections for the hydrogen and deuterium cross sections it was not subtracted from the error in the ratio.

We now list all the random and systematic errors which were not included in the calculation of the error of the neutron to proton cross section ratios.

1. The systematic error in the density of hydrogen at 21 degrees Kelvin was taken to be 0.6%, and similarly a 0.6% error due to the uncertainty in the density of deuterium at that temperature. These errors do not cancel in the $6n/6p$ and should be added to the error in the ratio. There is another 0.4% uncertainty in the effective density of each target due to uncertainty in the position where the beam went, calibration of temperature monitors, and amount of impurities.

2. The random errors of $\pm 0.25\%$ due to fluctuations in the properties of the charge monitors were not included. Part of those error are believed to have cancelled in the ratio since the deuterium and hydrogen runs were taken one after the other. The assumption that was made was that the fluctuations in the properties of the charge monitors varied over a larger time range. Since this error is small, the exact knowledge of the actual percent cancelation was not crucial.
3. The systematic errors of $\pm 0.5\%$ in the absolute calibration of the charge monitors cancel in the ratio.
4. The $\pm 0.25\%$ error due to the fluctuations in the beam energy (0.5% slits) probably does not introduce an error into the cross sections since the average cross section is the cross section at the central energy.
5. The 0.1% systematic errors in the calibration of the incident energy cancel in the neutron-proton cross section ratio.
6. The systematic error in the elastic e-p radiative tail is quoted as $\pm 5\%$ of the tail cross section, while the systematic error of the quasielastic radiative tail is quoted as $\pm 6\%$ of the quasielastic tail cross section. As can be seen from the tail percentages in Table 4, those errors amount to very small errors in the final cross

sections. Also, they largely cancel in the ratio since the expressions that were used for the two tails were similar in the sense that the quasielastic tail calculation included a correction obtained by using elastic e-p and e-n tail cross sections.

7. Systematic error due to the uncertainty in the deuterium elastic tail is negligible since that tail is typically 10^{-5} of the measured deuterium cross section.
8. The systematic error due to the uncertainty in the quasielastic tails arising from the lack of neutron elastic form factor measurements at high q^2 is very small. As mentioned previously the neutron contribution of the quasielastic tail was always less than 3 % of the measured deuterium cross section and most of that contribution came from the low- q^2 region of the radiative corrections triangle.
9. Systematic errors due to theoretical uncertainties in the inelastic radiative corrections formalism vary from $\pm 3\%$ at the top of the radiative corrections triangle to $\pm 10\%$ at the lowest momenta. These errors largely cancel in the neutron to proton cross section ratio, since the same expressions are used for both. More about those errors can be found in the Ph.D. thesis of E.M. Riordan(11).
10. A systematic error of $\pm 0.4\%$ is quoted for the uncertainty in the length of the hydrogen target and the same uncertainty is quoted for the length of the deuterium target. These errors

do not cancel in the cross section ratio and should be added to the total error in that ratio.

11. The systematic error due to the theoretical uncertainty in the smearing correction was not included in the error bars. The error band due to that uncertainty is shown in figure A6 of Appendix A.
12. The error originating from the unsmearing fits was not included in the error bars. The error in that correction is shown in Table 5 and should be added to the error in the neutron to proton unsmeared cross section ratios.
13. The $\pm 1.5\%$ systematic errors in the value of the spectrometer acceptance cancel in the neutron to proton cross section ratio.
14. If one wants to interpret the cross section ratio as also representing the ratio W_{2n}/W_{2p} one has to increase the error bars in order to account for a possible difference between R_p and R_n . Preliminary results indicated that they are not inconsistent with being equal(11). See section 4.4 for more details on the effects of the uncertainties in R on the structure function ratios.

We have discussed all the systematic errors that do and do not contribute to the error in the neutron to proton cross section ratios. It is clear that many of the systematic errors

that cancel in the cross section ratios do not cancel in the structure function difference $\sqrt{W_2^p - W_2^n}$. The difference between the neutron and proton structure functions (smeared and unsmeared) is shown in figures 17-20 as functions of X and X' . As in the σ_n/σ_p plots each of the data points in the difference plots is an average of several measured points which were binned in X or X' . Similarly the errors are only statistical and the errors of the several combined points were combined accordingly. The numbers and their errors for the combined ratio and difference plots are shown in section D3 of Appendix D.

4. Interpretation of Results and Comparison with Theories

4.1 Investigations of a Few Scaling Variables

Several scaling variables have been proposed in the literature. The variable $\omega = 2M\nu/q^2$ was already discussed (see section 1.2) as the variable that arises naturally in parton models (8,10,34,35,36). The variable $\omega' = (2M\nu + a^2)/q^2$ was first introduced by G. Miller (2), who found that the scaling region was extended down to $W = 1.8$ GeV when using ω' as a scaling variable. Miller had found that a best fit for a^2 was a value which was not statistically different from M^2 . Setting $a^2 = M^2$ is equivalent to setting $\omega' = 1 + W^2/q^2$. This latter form was used by Bloom and Gilman (6,7) in finite energy sum rules connecting the deep inelastic structure functions to the elastic and resonance form factors (see section 4.3). This latter expression for ω' is also equal to $\omega_s + 1$ where $\omega_s = W^2/q^2$ is a variable proposed by Jakiw (51). The variable W^2/q^2 can also be derived from dimensional arguments (see Jakiw (50)). The argument goes as follows. When W^2 and q^2 go to infinity the structure functions cannot depend on any masses of the nucleon or its possible constituents since those masses are effectively zero (in comparison to W^2 and

q^2). Therefore, the only non-zero dimensionless quantity is the quantity W^2/q^2 (or equivalently Mv/q^2). Rittenberg and Rubinstein (69) have proposed the variable $\omega_R = (2Mv + a^2)/(q^2 + b^2)$, which is useful in that it was found phenomenologically that it extends the scaling region down to $q^2 = 0$ (including photoproduction results). The values for a^2 and b^2 were obtained from a fit to the data (they obtained $a^2 = 1.43$ and $b^2 = 0.42$). Another scaling variable based on the physics of the electromagnetic current commutators in the region of the light cone is the variable $\omega_L = M / (\sqrt{q^2 + v^2} - v)$ (45,42). A simple explanation of the origin of ω_L is given in the next paragraph.

The nucleon electromagnetic tensor $W_{\mu\nu}(P,q)$ is the commutator function of the nucleon electromagnetic current for spacelike q (10).

$$E4.1 \quad W_{\mu\nu}(P,q) = \frac{1}{8\pi} \int d^4x \, e^{iq \cdot x} \langle P \xi | J_\mu(x), J_\nu(0) | \xi P \rangle$$

where ξ_μ denotes the covariant spin of the proton. As is discussed in section A2 of Appendix A, $W_{\mu\nu}$ is related to the structure functions W_1 and W_2 by the following expression (4):

$$\begin{aligned} \text{E4.2} \quad W_{\mu\nu}(P, q) &= W_1(W^2, q^2) (\delta_{\mu\nu} - q_\mu q_\nu / q^2) \\ &+ W_2(W^2, q^2) (P_\mu - (P \cdot q / q^2) q_\mu) (P_\nu - (P \cdot q / q^2) q_\nu) \end{aligned}$$

We now study the properties of the integral in equation E4.1 as q^2 and ν go to infinity while ν/q^2 is kept constant. In that limit (called the scaling limit) the exponent of the exponential becomes

$$\begin{aligned} i q \cdot x &= i (\vec{q}_3 x_3 + \nu x_0) = i (\sqrt{q^2 + \nu^2} x_3 + \nu x_0) \\ &= i \nu x_0 \left(\sqrt{1 + 2M/(\nu\omega)} \frac{x_3}{x_0} + 1 \right) \\ &\xrightarrow{q^2, \nu \rightarrow \infty} i x_0 \left(\nu \left(1 + \frac{x_3}{x_0} \right) + M/\omega \frac{x_3}{x_0} + \dots \left(\frac{1}{\nu} \right) \dots \right) \end{aligned}$$

As can be seen, the exponent becomes $i\infty$ except when $x_3 = -x_0$, which is at the light cone. Therefore, in the scaling limit all the contribution to the integral comes from the light cone region (since everywhere else the exponential oscillates very rapidly). So putting $x_3 = -x_0$ we get

$$\text{At the light cone } q \cdot x = x_0 (\sqrt{q^2 + \nu^2} - \nu) \xrightarrow{q^2, \nu \rightarrow \infty} x_0 M/\omega$$

Since M/ω is the only variable that is not integrated over in equation E4.1, the integral must be a function of that variable only. Therefore, the structure functions must scale in ω . Now, if we assume that the important contribution

to the integral comes from the light cone region as we approach the scaling region, we get

$$\omega_L = M / (\sqrt{q^2 + \nu^2} - \nu)$$

Detailed tests of those scaling variables must await the final extraction of R_p and R_d . Preliminary fits were made using the assumption that $R_p=R_d=0.18$, which is consistent with the preliminary results of E.M. Riordan (11) (also see section 4.4). The fits that were tried were of the following form:

$$\nu W^2 = \sum_{n=3}^7 a_n (1 - X_g)^n$$

where X_g could be one of the following

ω' fit	$X_g = 1/\omega'$,	$\omega' = 1 + W^2/q^2$
ω_R fit	$X_g = 1/\omega_R$,	$\omega_R = (2M\nu + 1.43)/(q^2 + 0.42)$
ω_L fit	$X_g = 1/\omega_L$,	$\omega_L = M/(\sqrt{q^2 + \nu^2} - \nu)$
ω fit	$X_g = 1/\omega$,	$\omega = 2M\nu/q^2$

The same fitting functions were used for fits over different ranges in W^2 and q^2 in order to find out ^h where the data scaled best.

In addition to the above fits, a special fit was tested for the deuteron only. This fit was the following

$$\chi^2 W_{2d} = \sum_{n=3}^7 a_n (1 - X')^n$$

where $(1-X')^n$ is the smeared function $(1-X')^n$.

The tables below show the various chi-squared per degree of freedom, and the number of degrees of freedom for each fit. The only data included in the fits were from this experiment.

Proton fits

	$q^2 > 1.0$ $W > 2.0$	$q^2 > 1.0$ $W > 2.6$	$q^2 > 3.0$ $W > 2.6$	$q^2 > 6.0$ $W > 2.6$
No. of degrees of freedom	119	83	79	45
ω_1 fit	1.22	1.19	1.12	0.66
ω_R fit	1.22	1.20	1.18	0.69
ω_L fit	1.64	1.37	1.31	0.81
ω fit	2.91	1.64	1.60	1.10

Deuteron fits				
	$q^2 > 1.0$ $W > 2.0$	$q^2 > 1.0$ $W > 2.6$	$q^2 > 3.0$ $W > 2.6$	$q^2 > 6.0$ $W > 2.6$
No. of degrees of freedom	119	83	79	45
ω' fit	1.63	1.49	1.38	1.54
$(1-X')_s$ fit	1.64	1.50	1.38	1.54
ω_R fit	1.79	1.58	1.57	1.72
ω_L fit	2.68	2.03	1.98	2.31
ω fit	5.93	2.86	2.85	3.46

We have not included systematic errors in the errors of the data points that were included in the fits. As we mentioned previously, the fits only included the data taken in this experiment. The 6 and 10 degree data that were included in the unsmearing fits were not included in the above scaling tests because of a possible systematic difference between the two experiments. Repetition of the above tests with data which included the 6 and 10 degree points resulted in the same behavior of the chi-squared per degree of freedom as

a function of the various scaling variables. Only the magnitudes of the chi-squared quantities changed.

Looking only at the deep inelastic data ($W > 2.6$ GeV, $q^2 > 1.0$ (GeV/c)², see figures 34-37), the above results indicate that if we neglect systematic errors and specifically neglect errors which can be q^2 dependent such^{as} errors due to the radiative corrections, the hydrogen data seems to be scaling slightly better in ω' than in ω . Also, neglecting those systematic errors for deuterium and further neglecting the error introduced by the smearing of the resonances into regions of higher W , the deuteron data seems to scale better in ω' than in ω . Further investigations of the effects of the smearing on scaling and the q^2 dependence of the systematic errors in the radiative corrections are necessary before we can conclude which scaling variables are better for the high W region. Currently, if we include those systematic errors we can only say that the data is consistent with scaling in all the above mentioned scaling variables in the region $W > 2.6$ GeV, and $q^2 > 1.0$ (GeV/c)². It is clear that if we include data for which W is less than 2.6 GeV (see figures 26-29) the data scales far better in ω' than in ω . More detailed tests of various scaling variables using the final values of R will be found in the thesis of E.M. Riordan(11).

Both the errors in the proton cross sections, and the errors in the deuteron cross sections contribute to the final errors in the extracted neutron cross sections. Since the final errors in the neutron cross sections are relatively large, the neutron to proton ratio appears to scale in X or X' . Therefore, the plots of the combined data points for the ratio and the structure function difference are shown as functions of both X and X' . Plots of the individual data points for $\sqrt{W}2d$ and $\sqrt{W}2p$ are shown in figures 26-29 as functions of X and X' . The same data is plotted in figures 30-33 in combined form. The proton fit shown on the X' plots is the $(1 - X')^n$ fit quoted in section 3.9. The deuteron fit shown on the X' plots is the $(1 - X')^n$ fit quoted in section 4.3. The data shown includes data for $6^\circ, 10^\circ, 18^\circ, 26^\circ$, and 34° for $W > 2.0$ GeV and $q^2 > 1.0$ (GeV/c)². Figures 34-37 also show $\sqrt{W}2p$ and $\sqrt{W}2d$ as a function of X and X' . However, the data in those figures is restricted and only the large angle data ($18^\circ, 26^\circ, 34^\circ$) is shown subject to the conditions $W > 2.6$ GeV and $q^2 > 1.0$ (GeV/c)².

All the theoretical arguments that we have discussed strictly only apply in the true scaling limit. The surprising thing is that the scaling in ω is valid for such small W

and q^2 , while this asymptotic variable should only work when W and q^2 approach ∞ .

In following sections we compare the predictions of theoretical models to the data. As mentioned before, many of the systematic errors cancel in the $\delta n/\delta p$ ratio, and therefore the ratio is a better known quantity than the structure function difference. Therefore, we limited our comparisons to the predictions of theoretical models for the ratio.

4.2 A Representative Parton Model - The Kuti-Weisskopf Model

Parton Models (originally suggested by Bjorken(34), Drell(35), and Feynman(36)) are rather attractive in that in those models the scaling prediction comes in a natural way. In order to predict the neutron to proton ratio one must identify the partons in the nucleon and make some guesses as to their momentum distributions. The model of Kuti and Weisskopf (10) is appealing in its simplicity, and in the fact that the partons are identified with quarks. We shall discuss the Kuti-Weisskopf model as a representative parton model and underline its basic assumptions and results.

The basic assumptions are:

1. The baryons are composed of three valence quarks and a core of an infinite number of quark-antiquark pairs.
2. Uncharged 'Gluons' are included among the constituents of the nucleon, and they are identified as the quanta of the quark-quark interaction. Neutral particles had to be included in order to bring the quark parton model into agreement with experimental $\nu W_2 p$ sum rules.
3. The scattering from the valence quarks is to be interpreted as the non-diffractive components, while the scattering from the core is interpreted as the diffractive component of

the cross section. By diffractive we mean that the cross section can be described by pomeron exchange.

Added to the above three basic assumptions is the assumption that the binding energies and masses are negligible in the limit of large center of mass momenta. As shown in section 1.2 this assumption yields the scaling result independently of the particular identification of the partons. Kuti and Weisskopf approximate the unknown momentum distributions by making references to Regge and phase space considerations. Next they require the following connection between the inelastic structure function νW_2 at $X=1$ and the elastic form factor $G(q^2)$ at high q^2 (35) (the expression for $G(q^2)$ is given in section 4.3 equation E4.3)

$$\begin{aligned} \text{let } \nu W_2 &\sim (1-X)^p & \text{as } X \rightarrow 1 \\ \text{and } G(q^2) &\sim (1/q^2)^n & \text{with } n=4 \text{ experimentally} \\ \text{then } p &= n-1 = 3 \end{aligned}$$

Now they are left with only one adjustable parameter in the expressions for the structure functions of the proton and the neutron. This parameter g which is the ratio of the number of gluons to the number of quark antiquark pairs is

found by making a best fit to the proton data. $g=1$ seems to be their best choice. Their final expressions for the structure functions are

$$\nu W_{2p} = F_p^V + F^C$$

$$\nu W_{2n} = F_n^V + F^C$$

$$F_p^V(X) = (3/2)F_n^V(X) = \frac{\Gamma(\gamma + 3/2)(1-\alpha)}{\Gamma(1-\alpha)\Gamma(\gamma + 2(1-\alpha))} X^{1-\alpha} (1-X)^{-1+\gamma+2(1-\alpha)}$$

$$F^C(X) = (2/9) g (1-X)^{-1+\gamma+3(1-\alpha)}$$

$$g = 1, \quad \alpha = 1/2, \quad \gamma = 3$$

and

$$R_p = R_n = 6s/6t = q^2 / \gamma^2$$

The smeared prediction of the Kuti-Weisskopf model for the neutron to proton ratio is shown in figure 15. The comparisons are done by smearing the theory since the unsmearing ratios are less certain due to the unsmearing error (see Table 5). Their predictions deviate considerably from the measured data especially at large X . One need not take this deviation to mean that the quark model is

incorrect. It must be stressed that quark binding effects, quark-quark correlations and final state interaction have been completely neglected in that model. It is known that some form of final state interaction must be there as free quarks have never been detected.

The behavior of the neutron to proton cross section ratio near $X=1$ can depend on quark-quark correlations. Totally incoherent scattering (as Kuti-Weisskopf assumed) leads to the prediction that the neutron to proton ratio at $X=1$ is just the ratio of the sum of the squares of the charges of the valence quarks.

$$\text{Incoherent Limit } W_{2n}/W_{2p} = \frac{(1/9+1/9+4/9)}{(4/9+4/9+1/9)} = 2/3 \quad \text{as } X \rightarrow 1$$

A quark model lower limit on the neutron to proton ratio is $1/4$. This limit can easily be derived by assuming a complete quark-quark anti-correlation between identical quarks. In the limit of $X=1$, a single interacting quark carries all the proton momentum leaving the other two valence quarks with zero relative velocity (aside from small transverse velocities). If there is a strong anti-correlation between identical quarks, or if there is a

very strong momentum dependent interaction which does not allow two identical quarks to have small relative momentum then one would expect the cross section at $X=1$ to be dominated by the scattering of the identical quarks. This yields

$$\begin{array}{lcl} \text{quark-quark correlation} & W_{2n}/W_{2p} & = \frac{2(1/9)}{2(4/9)} = 1/4 \\ \text{lower limit} & & \end{array}$$

The Bloom-Gilman local duality model (which is discussed in detail in the next section) is equivalent to the assumption that the scattering is coherent at $X'=1$ or

$$\begin{array}{l} \text{Coherent Lim } W_{2n}/W_{2p} = (\mu_n/\mu_p)^2 = 0.47 \\ \text{as } X' \longrightarrow 1 \end{array}$$

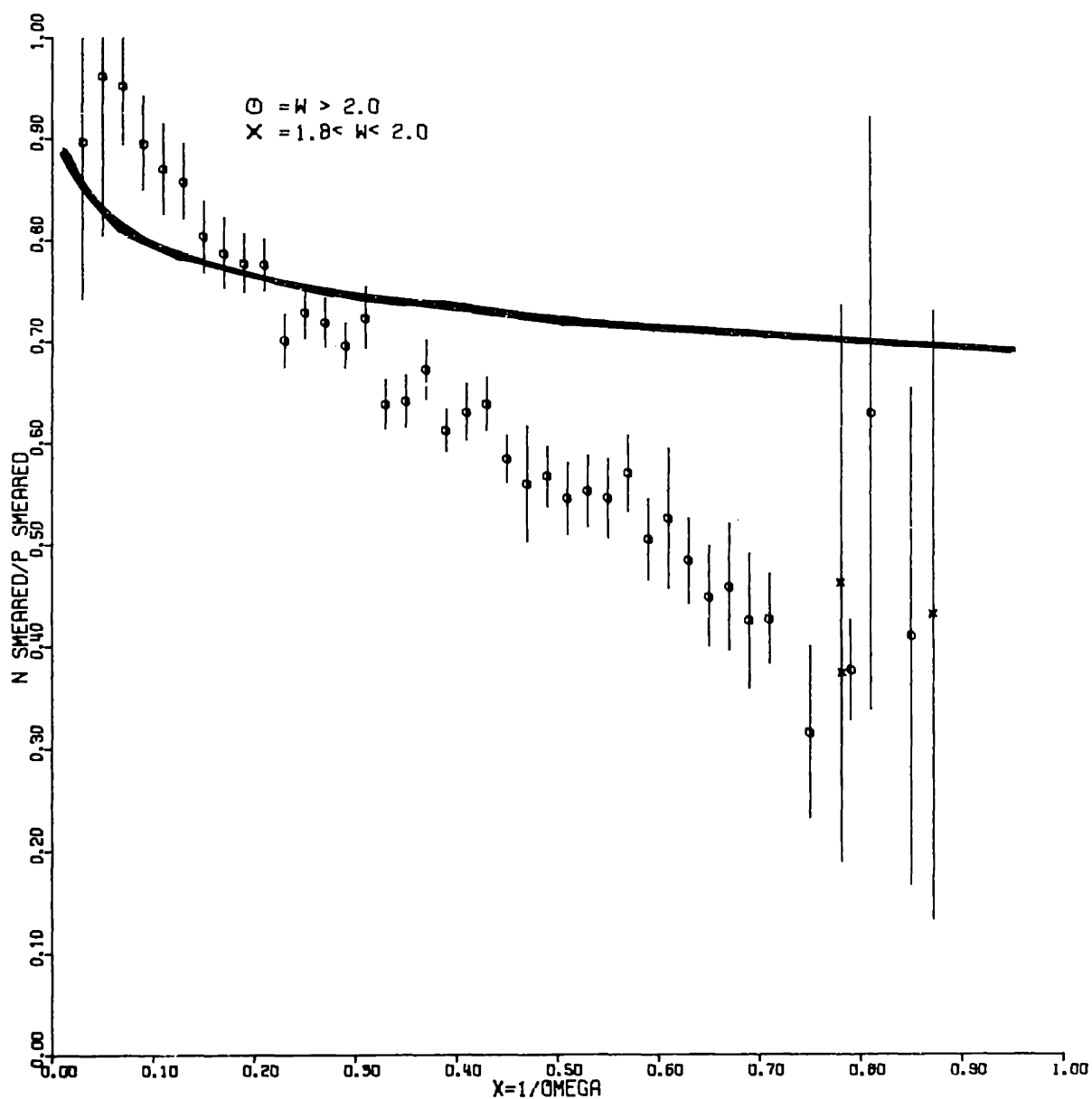


Figure 15 - Comparison of σ_{ns}/σ_{ps} with the predictions of the model of Kuti and Weisskopf. The solid line is the ratio of the smeared cross sections calculated using the model of Kuti and Weisskopf.

4.3 Duality and Local Duality

For purely hadronic processes, the presence of low energy s-channel ($s = W^2$) resonances is correlated with a decreasing cross section as E_0 increases at high energy . Particular examples are K^-P and $\bar{P}P$ scattering which exhibit substantially decreasing cross sections at high energies (above a few GeV), and many strong s-channel resonances at low energy. Other processes such as K^+P and $P-P$ scattering exhibit essentially constant cross sections at high energy (above a few GeV), and no s- channel resonances. There are indications that the deep inelastic electroproduction cross sections are related to the small W resonances. Figures 22,23,24,25 show the deep inelastic fits for γW^2p and γW^2d plotted as functions of X' on top of resonance data obtained from reference 13. As can be seen in the figures the deep inelastic curves seem to average the nucleon resonances in some sense. The fits that were used for the proton and deuteron deep inelastic data were of the following form

$$\gamma W^2 (X') = \sum_{n=3}^7 a_n (1 - X')^n$$

The coefficients for the proton fit were given in section 3.9 . The coefficients for the deuteron fit were

$$a_3 = 1.638, a_4 = -3.584, a_5 = 15.61, a_6 = -22.28, a_7 = 9.192$$

The connection of the low W resonances to the deep inelastic structure functions takes a quantitative form in terms of finite energy sum rules. Using Regge arguments and the scaling property of νW_2 in X' for $W > 2$ GeV, Bloom and Gilman (6,7) derive the following finite energy sum rule.

$$\frac{2M}{q^2} \int_0^{V_M} d\nu \nu W_2(\nu, q^2) = \int_1^{1+W_M^2/q^2} d\omega' \nu W_2(\omega')$$

where

$$W_M \approx 2 \text{ GeV} \quad \text{and} \quad V_M = \frac{W_M^2 - M^2 + q^2}{2M}$$

$\nu W_2(\nu, q^2)$ includes the elastic peak while $W_2(\omega')$ is the deep inelastic universal function. Bloom and Gilman evaluate the above integrals and find that the equality is experimentally verified to within 10% at $q^2 = 1 \text{ (GeV/c)}^2$, and that the two integrals are experimentally equal to within 2% at a q^2 of 2.0 (GeV/c)^2 . Bloom and Gilman tried to test the validity of the sum rule for more restricted integration limits. In particular they tested the following equality

$$\frac{2M}{q^2} \int_{\nu_a}^{\nu_b} d\nu \nu W_2(\nu, q^2) = \int_{1+\frac{W_a^2}{q^2}}^{1+\frac{W_b^2}{q^2}} d\omega' \nu W_2(\omega')$$

and found that for $W_a=0, W_b=1.4$ GeV the above sum rule is correct to 20%. For $W_a=1.4$ GeV, $W_b=1.6$ GeV the sum rule is correct to 13%, and for $W_a=1.8$ GeV, $W_b=2.0$ GeV the sum rule is correct to 5%. Their conclusion is that the universal curve averages not only the entire resonance region, but also averages the resonance region locally. Carrying this local duality to an extreme, Bloom and Gilman conjecture that the area under the elastic peak part of νW_2 for large q^2 is equal to the area under the scaling limit curve between an ω' of 1 and a value of ω' corresponding to a mass W_t around physical pion threshold.

$$\begin{aligned}
 \text{E4.3} \quad \int_1^{1 + \frac{W_1^2}{q^2}} d\omega' \nu W_2(\omega') &= \frac{2M}{q^2} \int d\nu \nu W_2^{\text{elastic}}(\nu, q^2) = \\
 &= [G(q^2)]^2 = \frac{[G_e(q^2)]^2 + \frac{q^2}{(2M)^2} [G_H(q^2)]^2}{1 + q^2/4M^2}
 \end{aligned}$$

Taking the derivative of the above equation with respect to q^2 they obtain

$$E4.4 \quad \gamma W_2 \left(\omega' = 1 + \frac{W_t^2}{q^2} \right) = \frac{1}{\omega' - 1} \left[-q^2 \frac{d}{dq^2} [G(q^2)]^2 \right]$$

and from that they obtain the threshold behavior of the neutron to proton ratio.

$$\frac{W_{2n}}{W_{2p}} = \frac{-q^2 \frac{d}{dq^2} [G_n(q^2)]^2}{-q^2 \frac{d}{dq^2} [G_p(q^2)]^2} = \xrightarrow[\substack{\omega' \rightarrow 1 \\ q^2 \rightarrow \infty}]{} \left(\frac{\mu_n}{\mu_p} \right)^2 = 0.47$$

Using experimental e-p data to test equation E4.4, Bloom and Gilman find that using $W_t = 1.08$ GeV yields a curve for γW_2 which is too high by a factor of 2 to 3, although it has the right shape. They find that the only way to satisfy equation 4.4 is by using $W_t = 1.23$ GeV, or in other words the proton pole is doing more than its share to satisfy the sum rule. The meaning of equation E4.4 is that if one believes local duality arguments one obtains not only a proportionality between the threshold behavior of the inelastic structure functions and the behavior of the elastic form factors at high q^2 , but a direct equality as well. Since the local duality prediction is only supposed to be valid close to $\omega' = 1$, we could not smear the theory

and compare it to the smeared ratio. Instead we compared its predictions to the unsmeared neutron to proton ratio. Since the theory predicts a ratio of 0.47 at $X'=1$, the unsmeared procedure was repeated with that constraint. The constraint of 0.47 instead of 0.38 at $X'=1$ does not change the unsmeared correction by very much. At the most extreme $X'=0.83$ data point the unsmeared correction changed by only 2.5 % (See Table 5 for the unsmeared corrections and their errors).

In order to compare the prediction of local duality to the experimental results, one must have the neutron elastic form factors. The neutron form factors have been measured only up to $q^2 = 5.0 \text{ (GeV/c)}^2$. The expressions that were used for the form factors of the proton and for the magnetic form factor of the neutron are given in Appendix B. Two expressions consistent with experimental data have been used for the electric form factor of the neutron. The first was $G_E=0$ and the second was $G_E=G_p \tau \mu_n / (1+5.6 \tau)$ (24,45) where $\tau = q^2 / (4M^2)$. We must stress the fact that the

expressions for the neutron's electric and magnetic form factors represent an extrapolation of the data from $q^2 = 5$ $(\text{GeV}/c)^2$ to a q^2 of 15 to 20 $(\text{GeV}/c)^2$. With those limitations in mind, the predictions of local duality are compared to the the data in figure 16. The predictions are not inconsistent with the data in the region where the theory is valid, however, the data does not seem to turn over towards 0.47 as the theory predicts. More data near $X'=1$ is necessary before a definite statement can be made about the trend of the data.

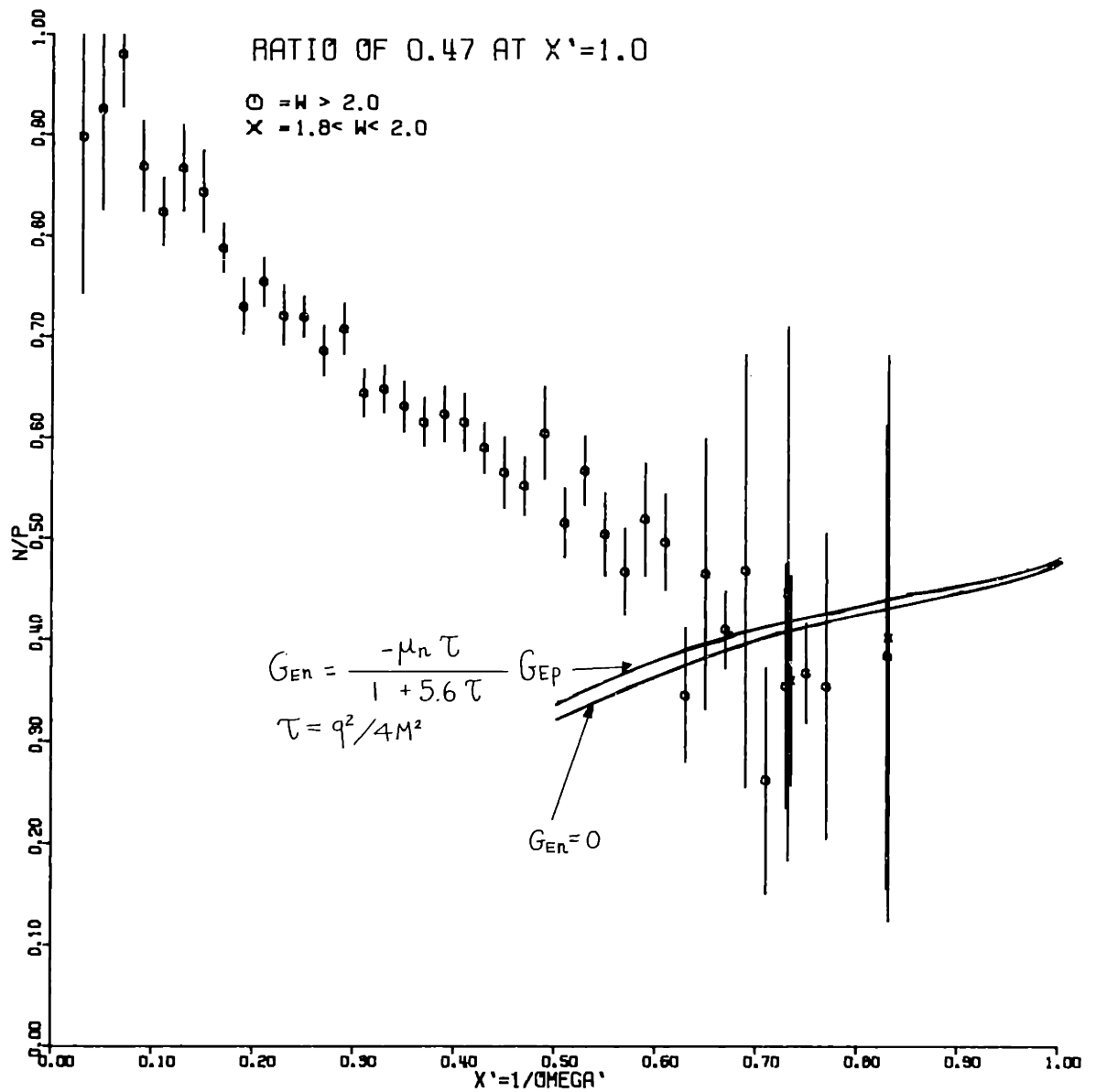


Figure 16 - Comparisons of σ_n/σ_p (unsmearred) with the predictions of the Bloom-Gilman local duality model. The model is only supposed to be valid near $X'=1$. The unsmearing was done by fixing σ_n/σ_p at 0.47 for $X'=1$.

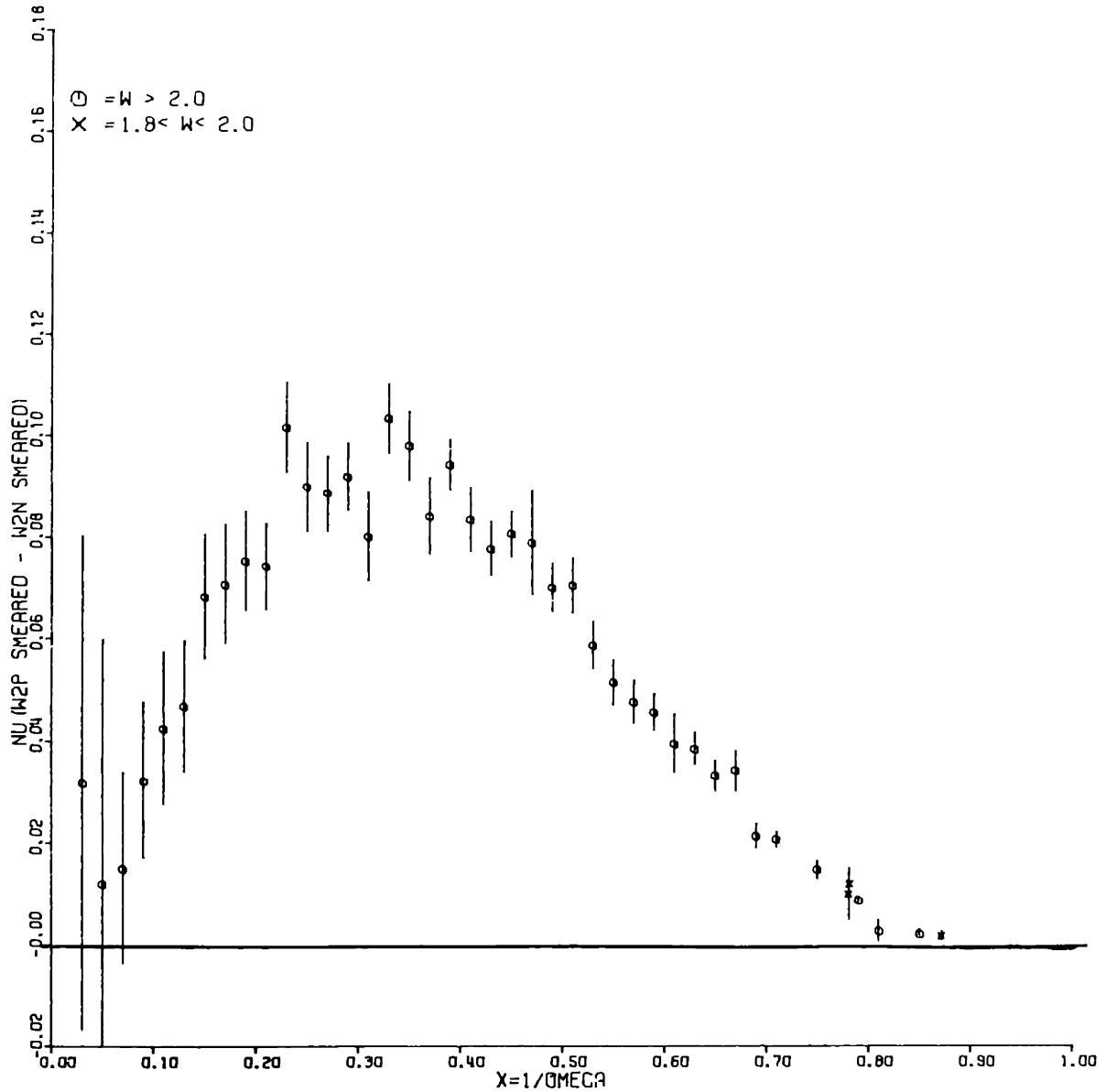


Figure 17 - The difference in the smeared neutron and proton structure functions as a function of X ($\nu W_{2p} - \nu W_{2n}$). The unsmearing was done by fixing the unsmearing fit for σ_n/σ_p at 0.38 for $X' = 1$.

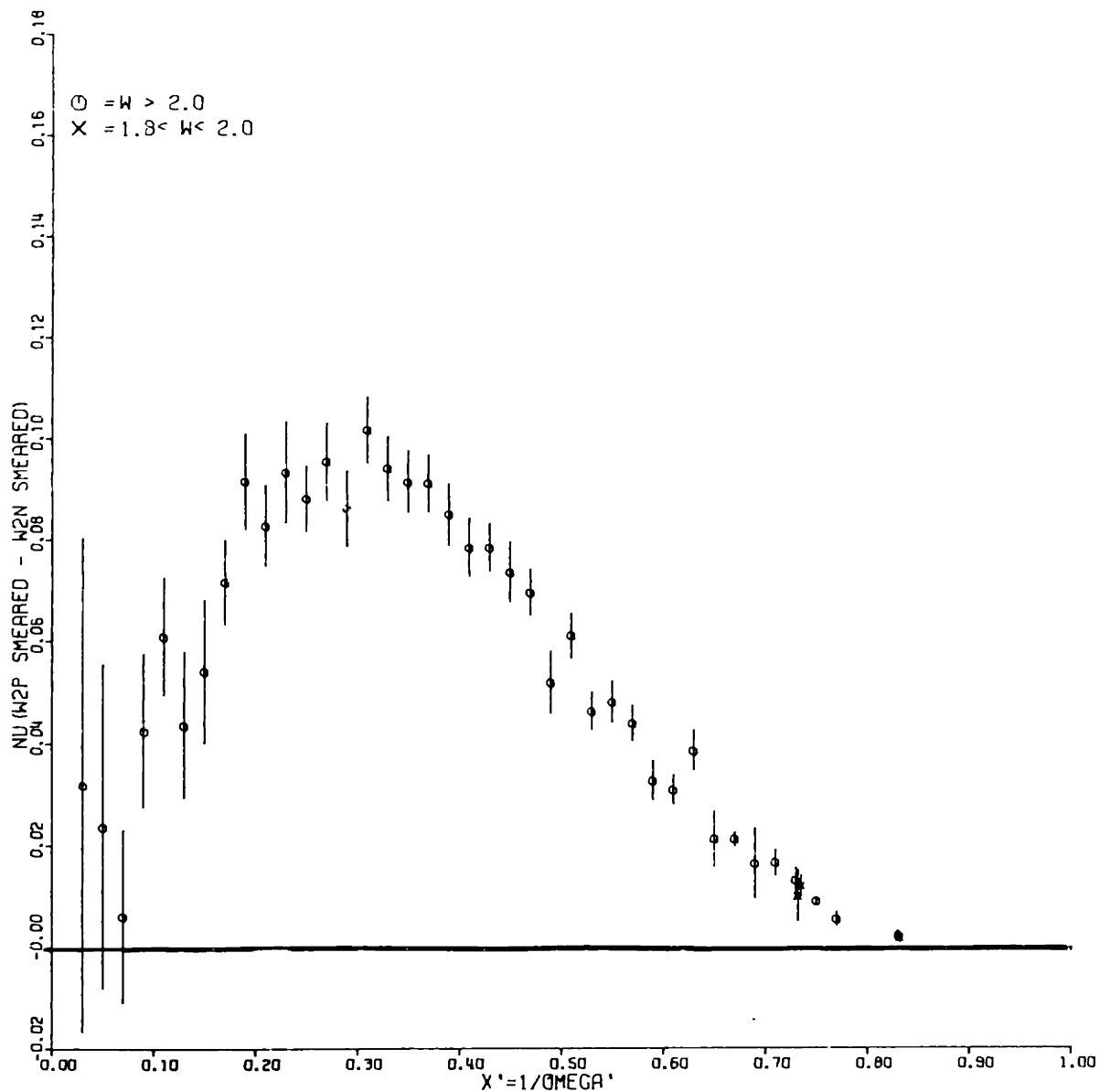


Figure 18 - The difference in the smeared neutron and proton structure functions ($\sqrt{W2p} - \sqrt{W2n}$) as a function of X' . The unsmeared was done by fixing the unsmeared fit for σ_n/σ_p at 0.38 for $X' = 1$.

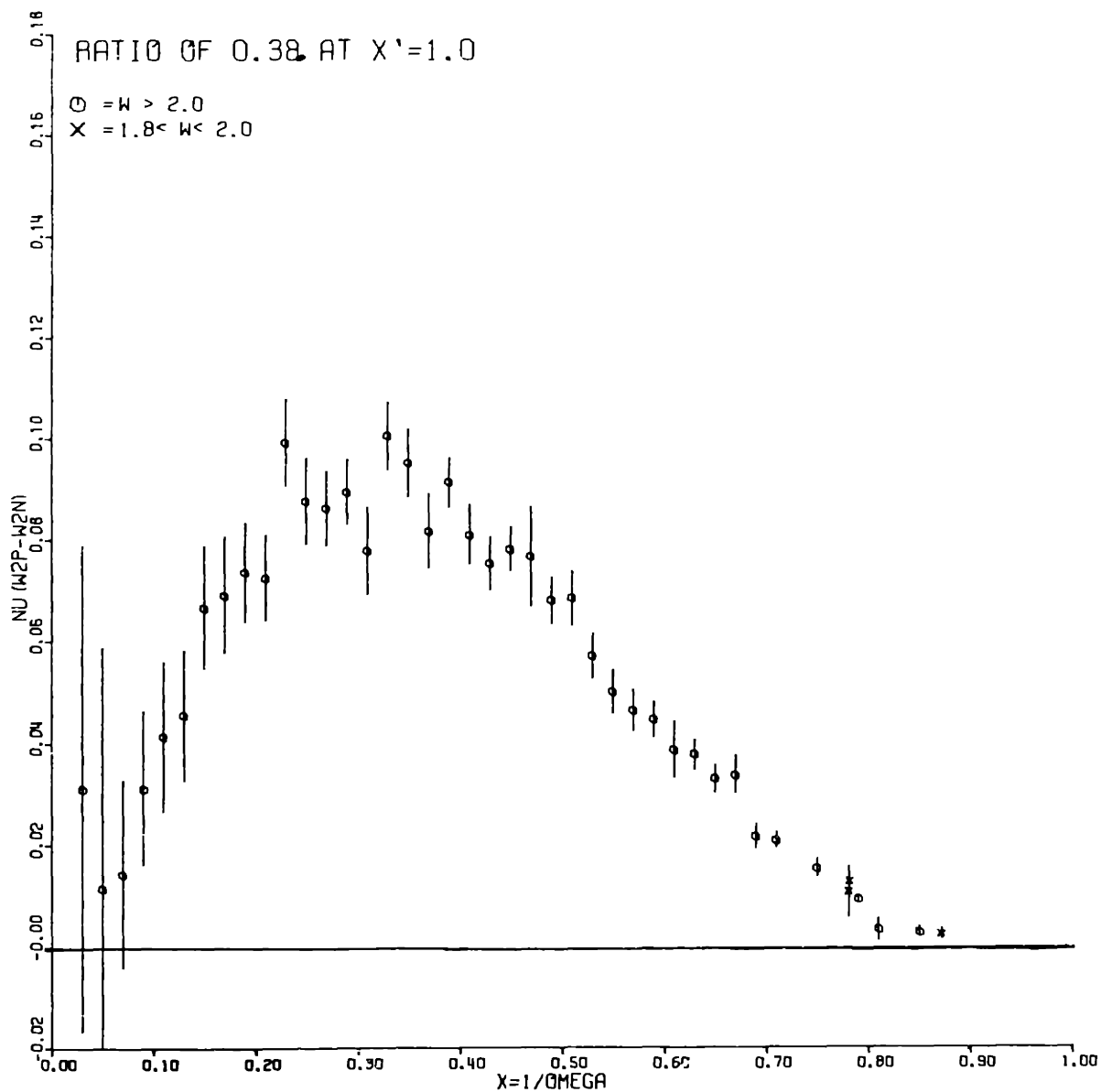


Figure 19 - The difference of the unsmeared neutron and proton structure functions ($\nu W_2p - \nu W_2n$) as a function of X . The unsmeareding was done by fixing the unsmeareding fit for $\sigma n/\sigma p$ at 0.38 for $X'=1$.

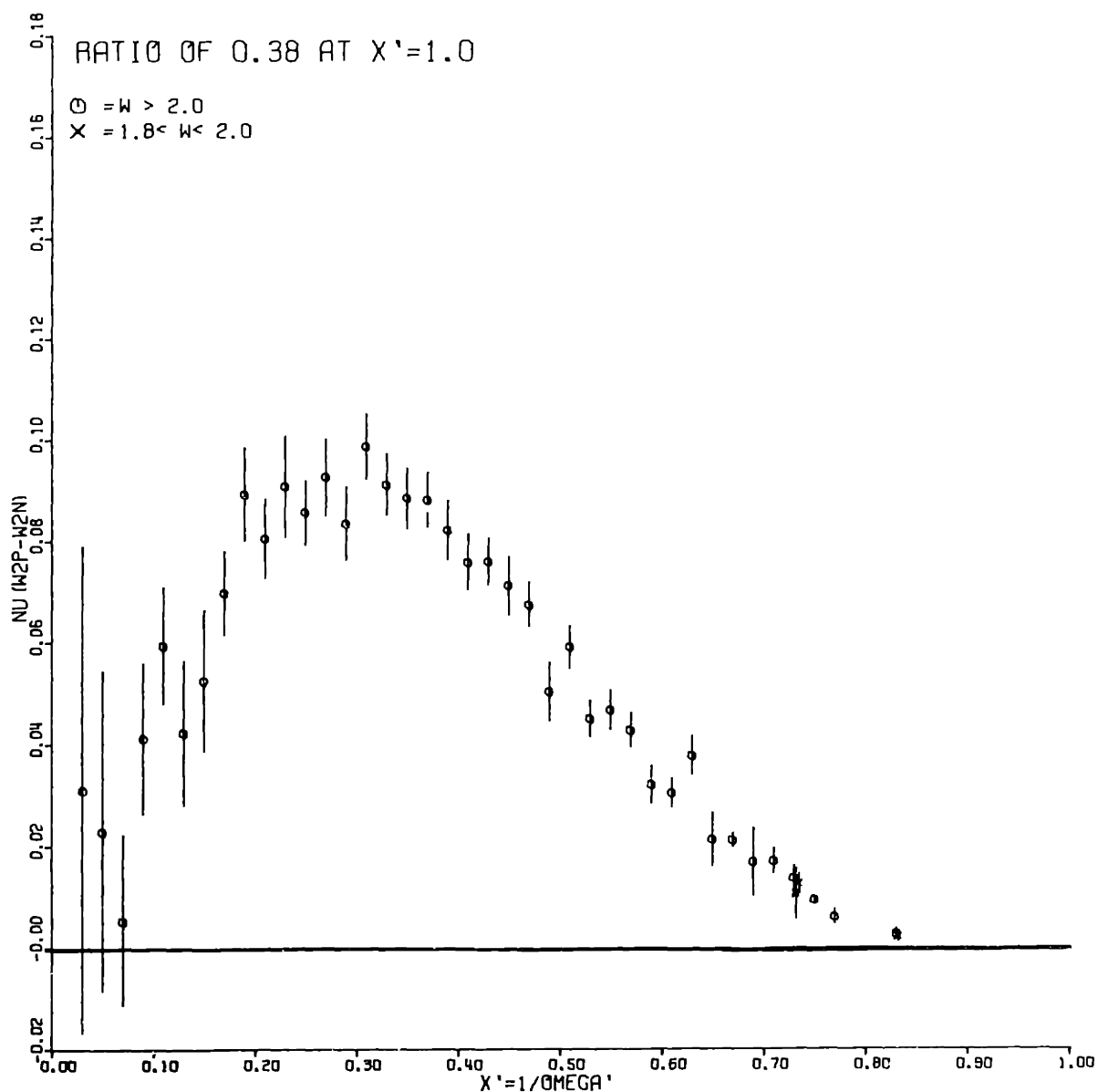


Figure 20 - The difference in the unsmeared neutron and proton structure functions ($\nu W_{2p} - \nu W_{2n}$) as a function of X' . The unsmearing was done by fixing the unsmearing fit for σ_n/σ_p at 0.38 for $X'=1$.

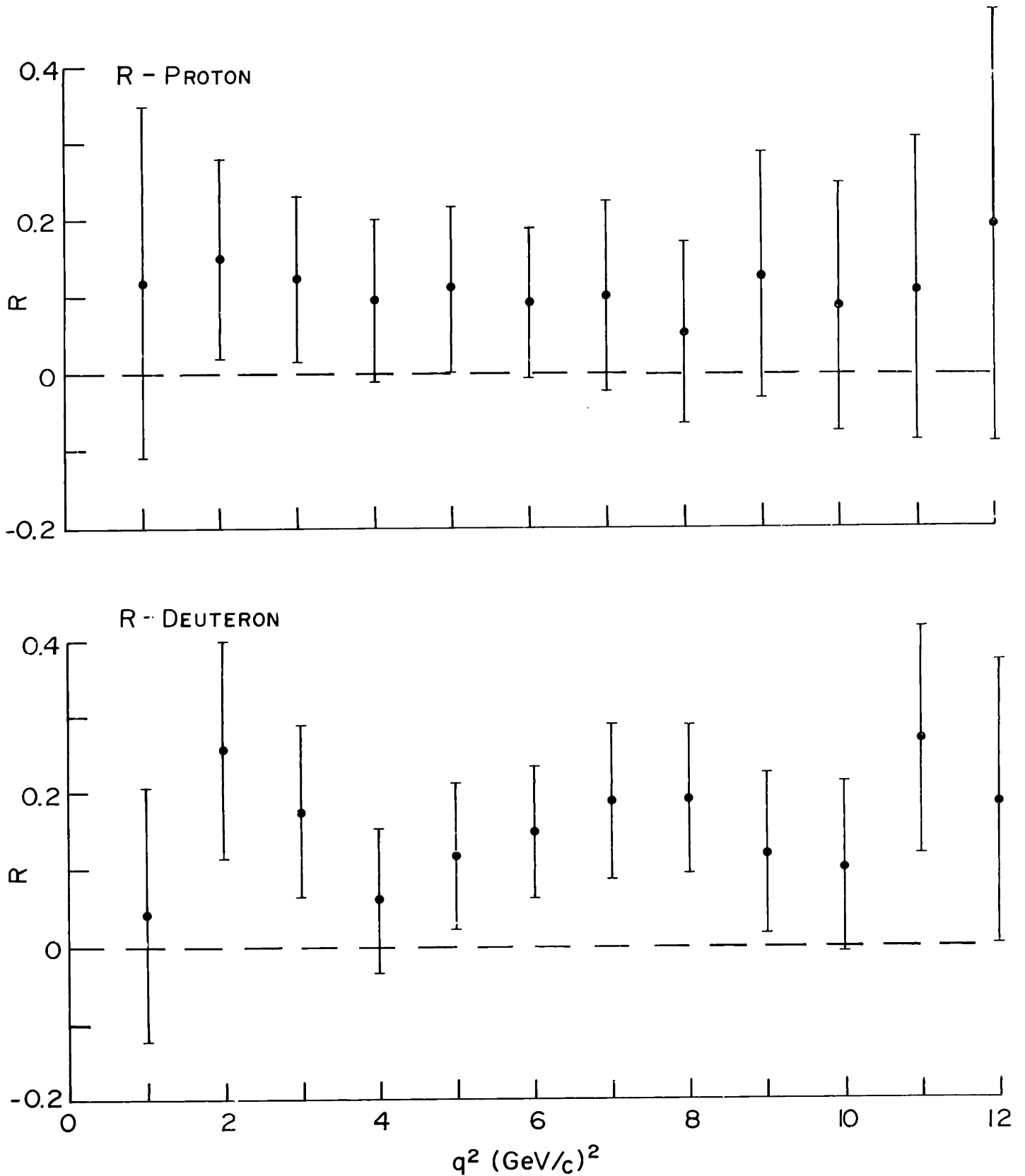


Figure 21 : σ_s/σ_t for the proton and the deuteron as a function of q^2 . Data for the same q^2 , but different W was combined.

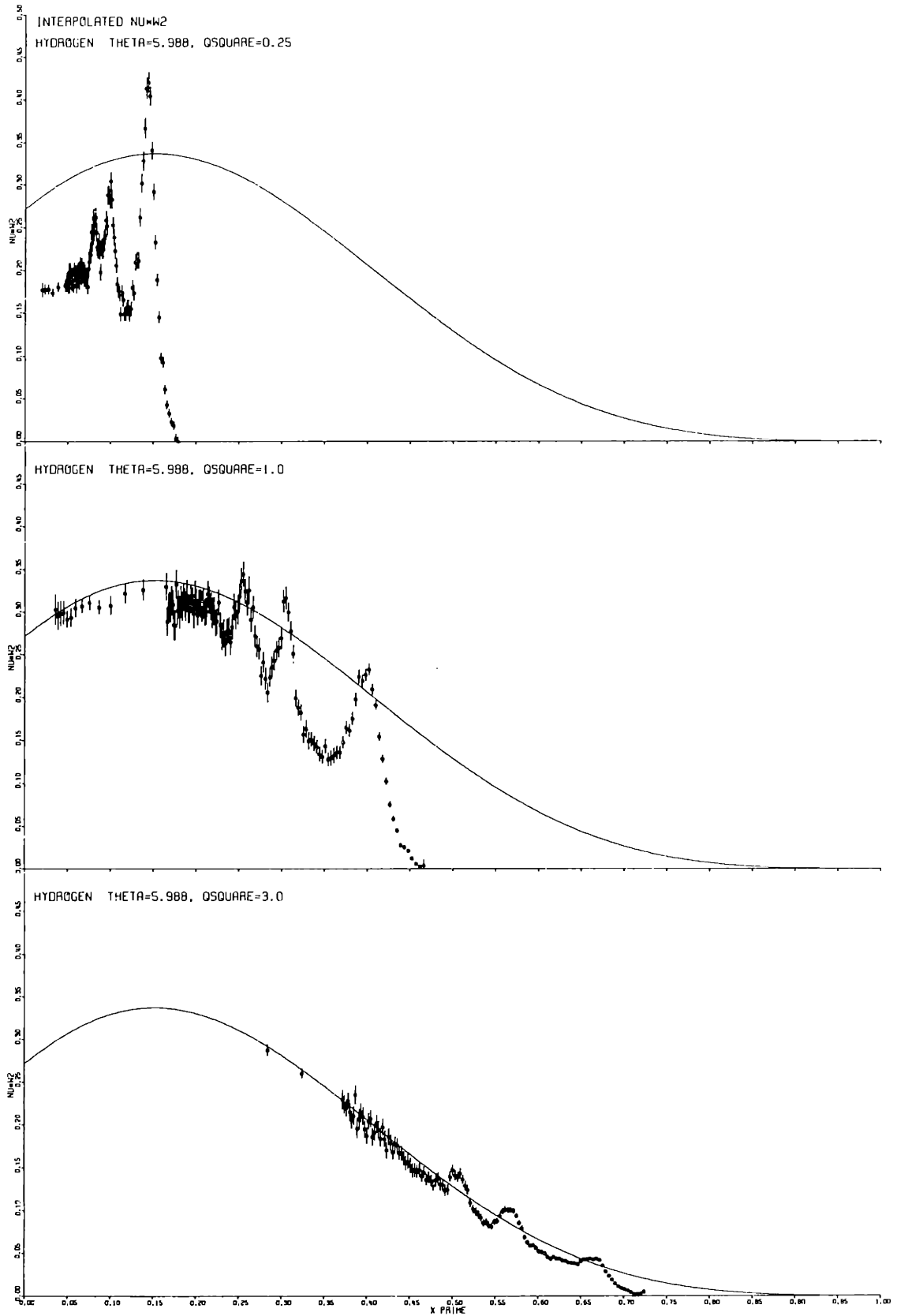


Figure 22 : $\sqrt{W_{2p}}$ vs. X' at $\theta = 5.998^\circ$, $q^2 = 0.25, 1.0$, and 3.0 (GeV/c)^2

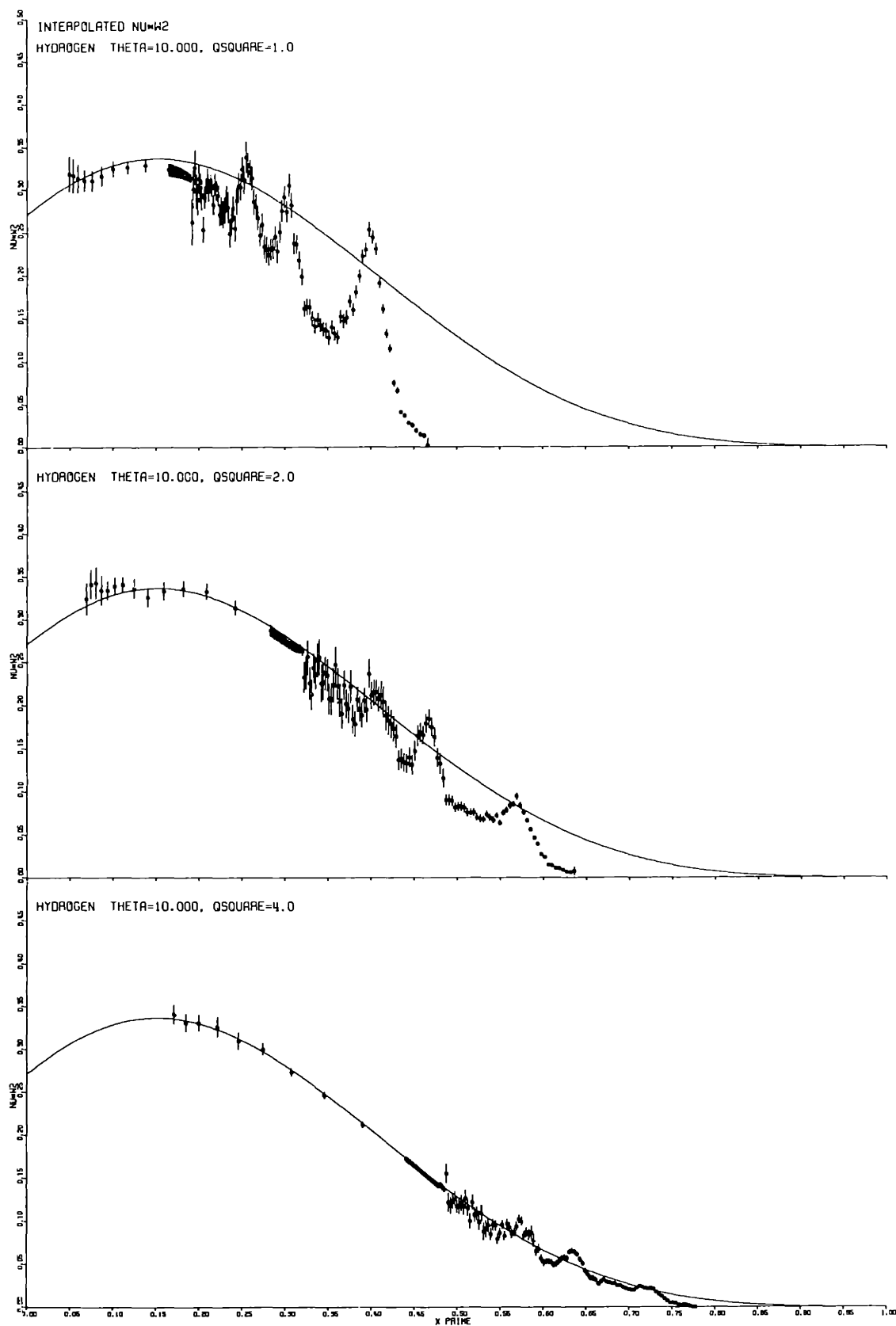


Figure 23 : νW_{2p} vs. X' at $\theta = 10.000^\circ$, $q^2 = 1.0, 2.0$, and $4.0(\text{GeV}/c)^2$

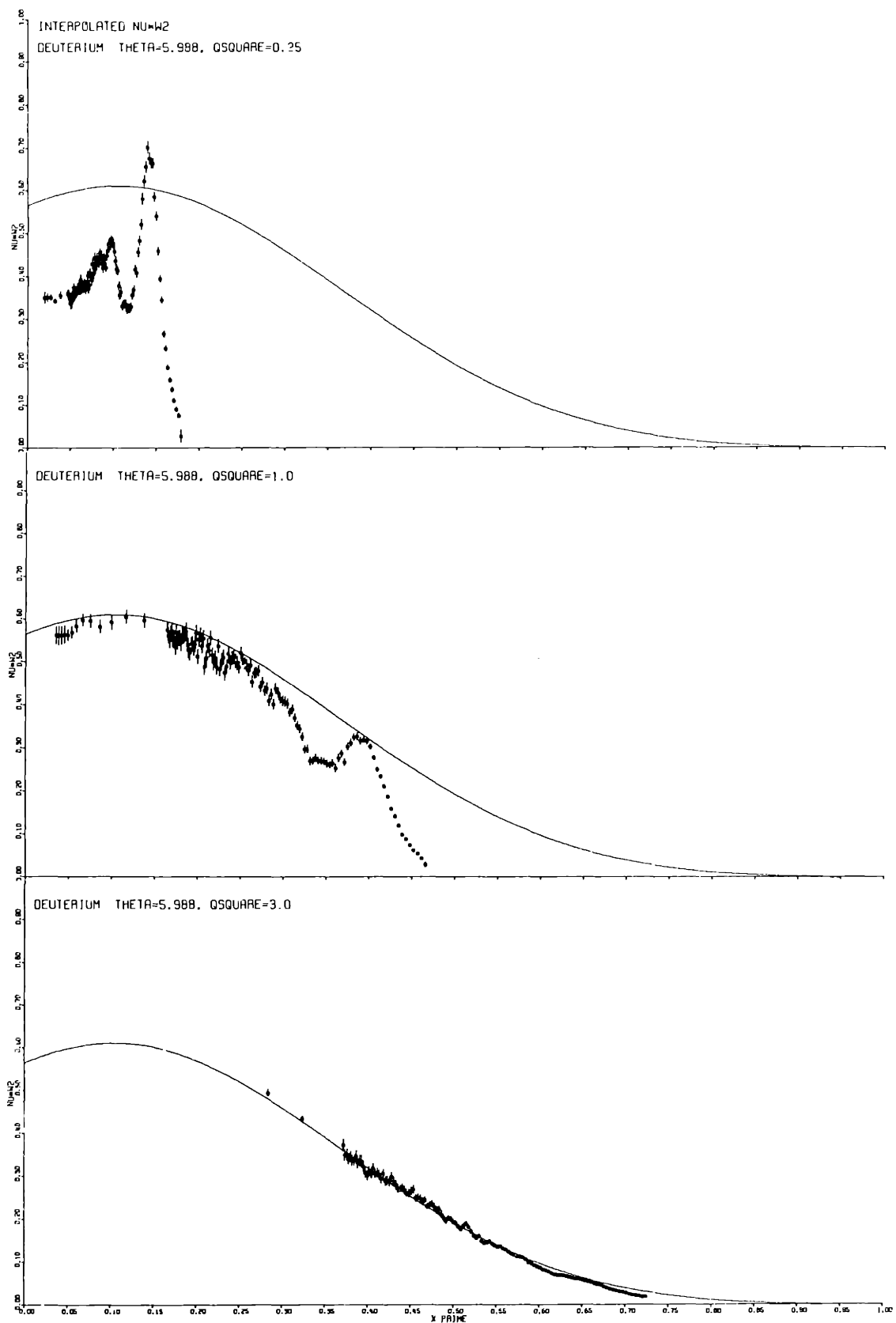


Figure 24 : W_2d vs. X' at $\theta = 5.998^\circ$, $q^2 = 0.25, 1.0$ and 3.0 (GeV/c)^2

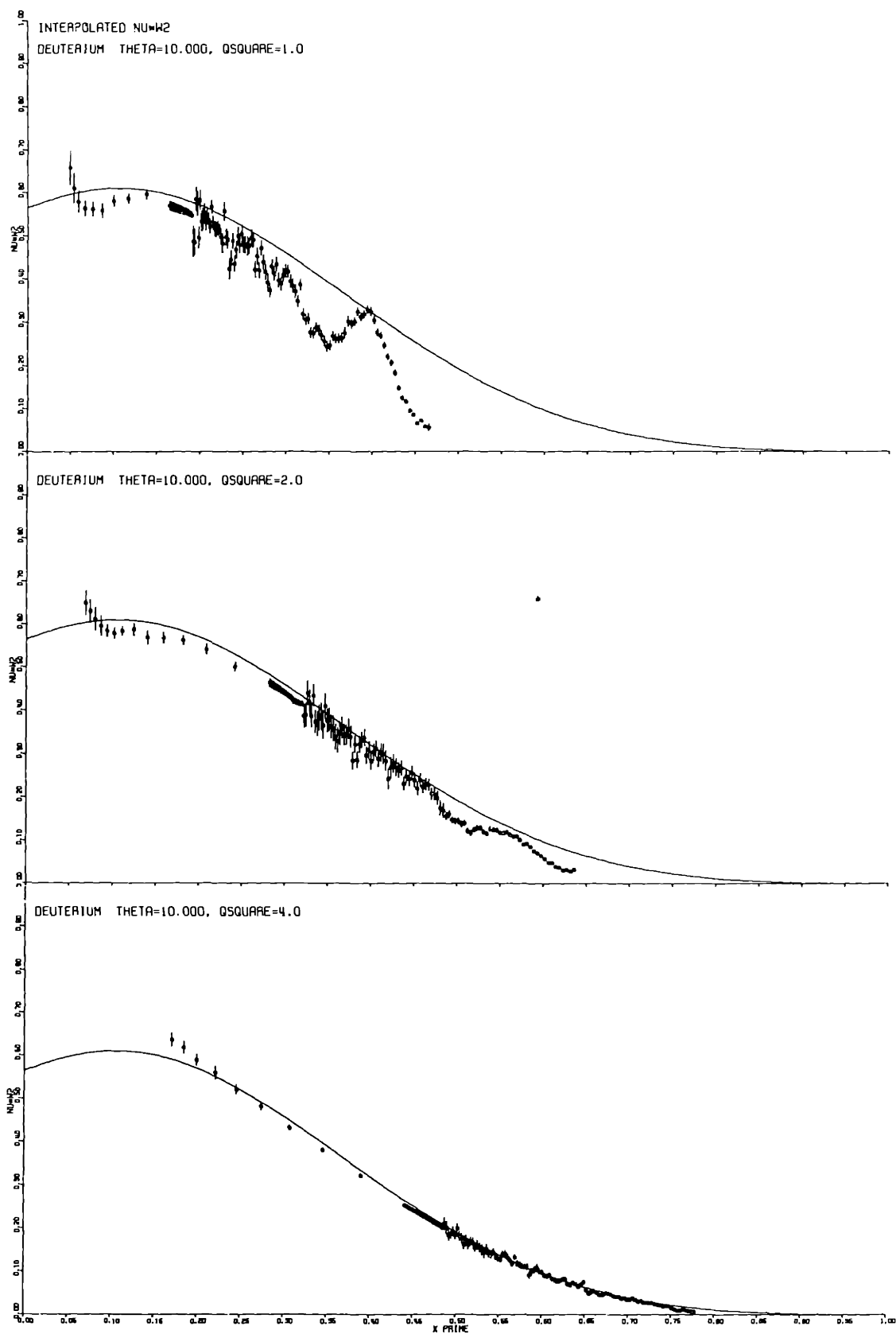


Figure 25 : $\sqrt{W2d}$ vs. X' at $\theta = 10.000^\circ$, $q^2 = 1.0$, 2.0 , and 4.0 $(\text{GeV}/c)^2$

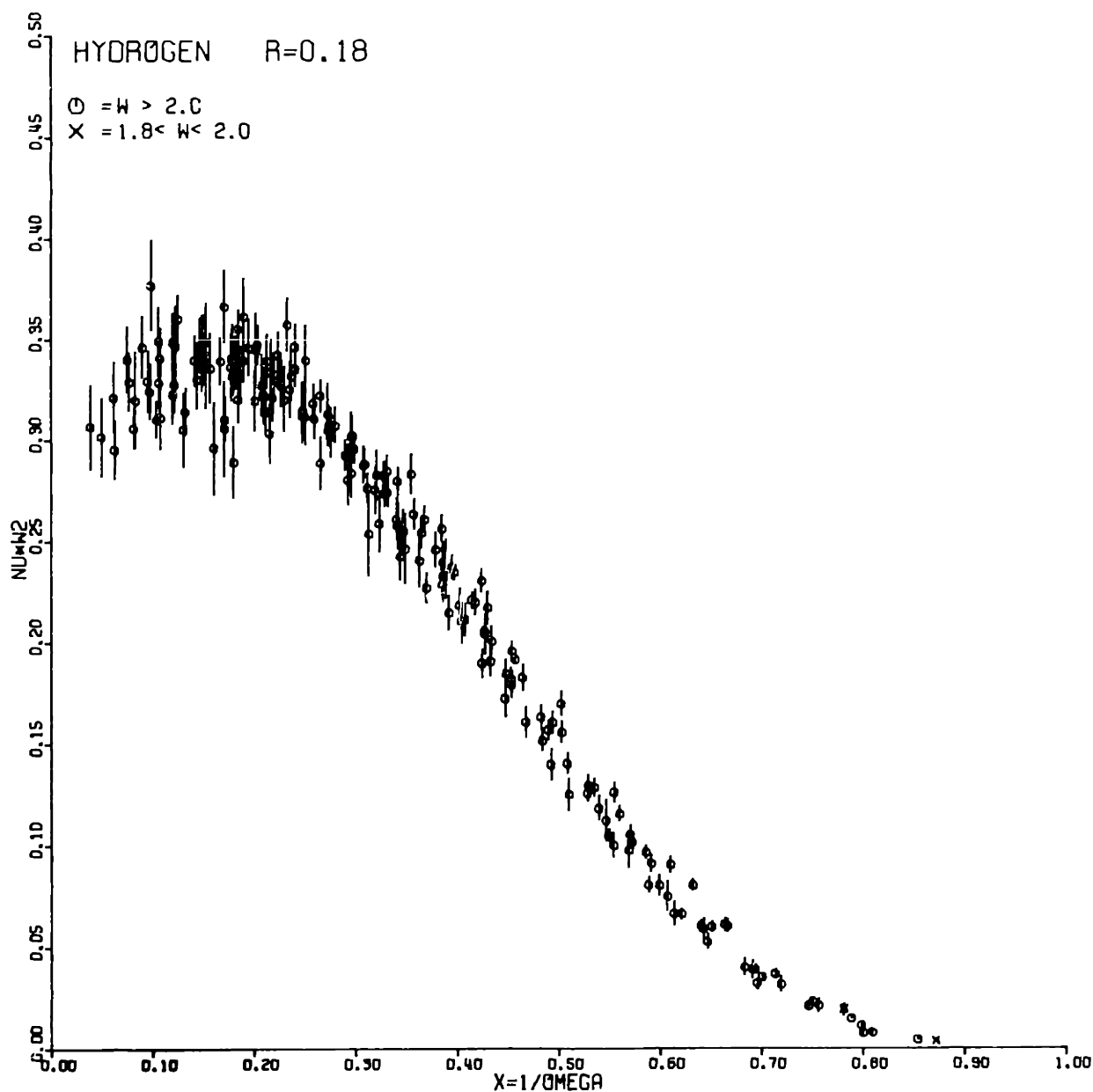


Figure 26 : $\nu W_2 p$ vs. X for W greater than 2 GeV and q^2 greater than 1.0 (GeV/c)².

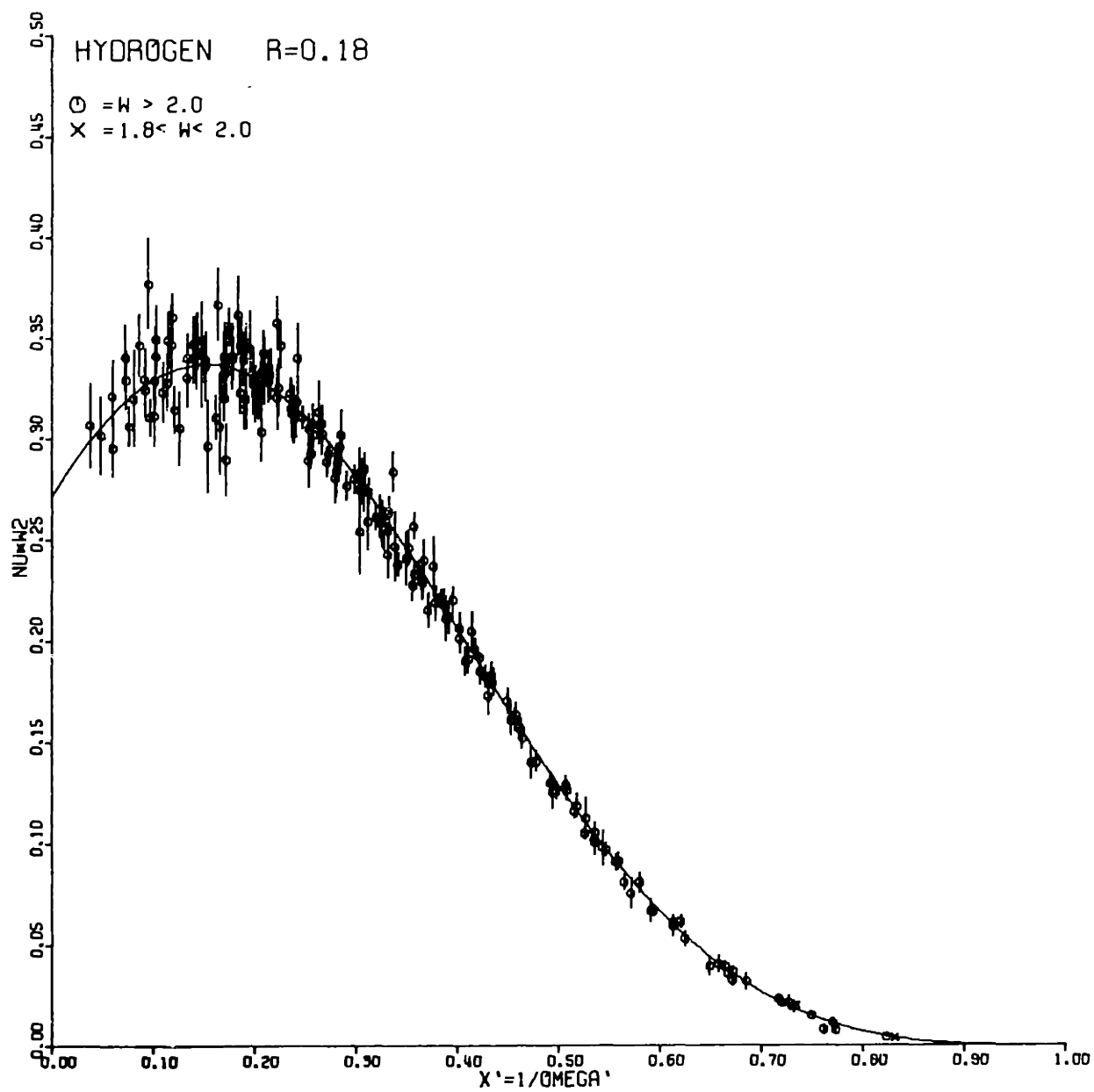


Figure 27 : $\sqrt{W}2p$ vs. X' for W greater than 2 GeV and q^2 greater than 1.0 (GeV/c) 2 .

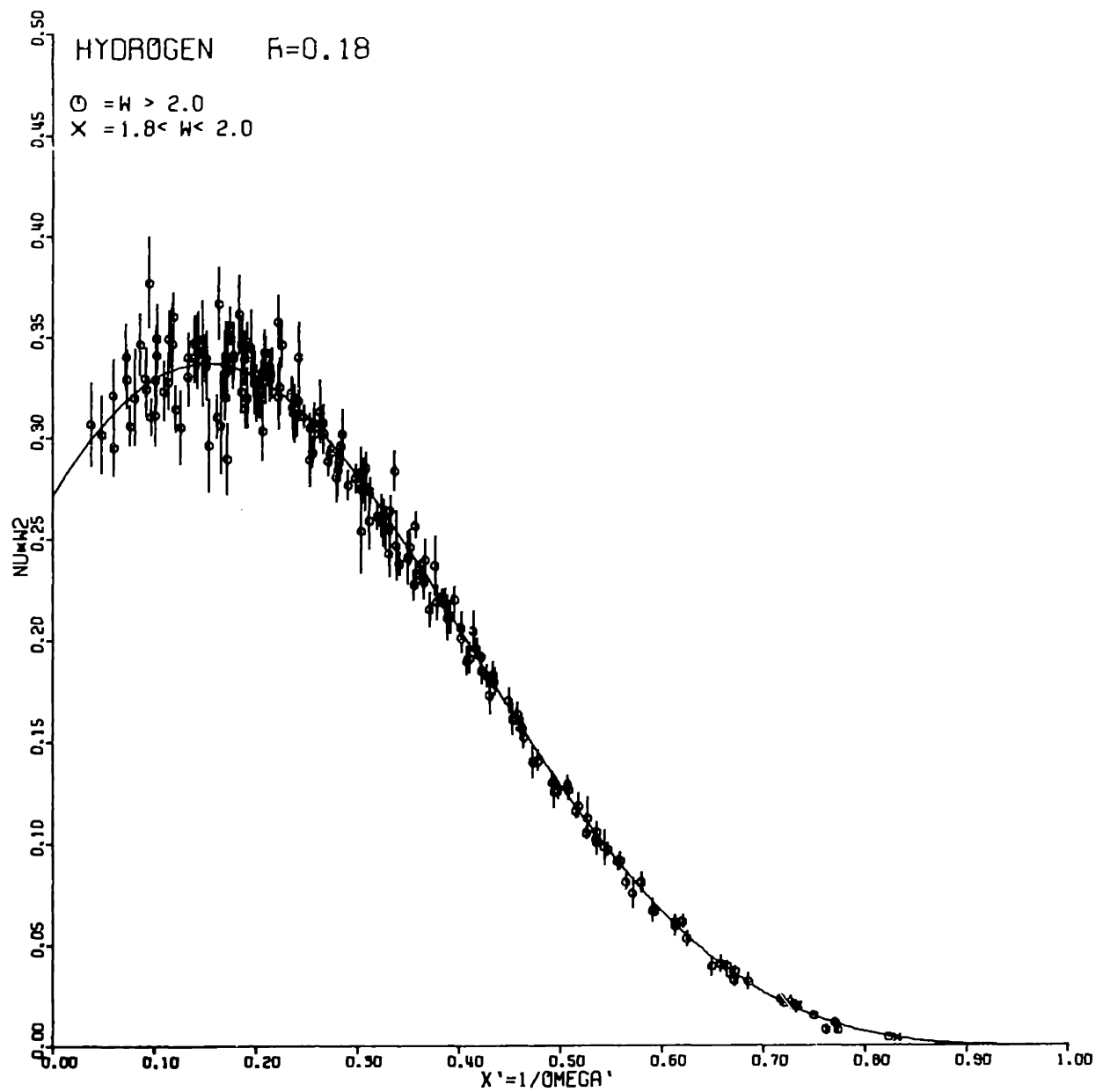


Figure 27 : $\sqrt{W}2p$ vs. X' for W greater than 2 GeV and q^2 greater than 1.0 (GeV/c)².

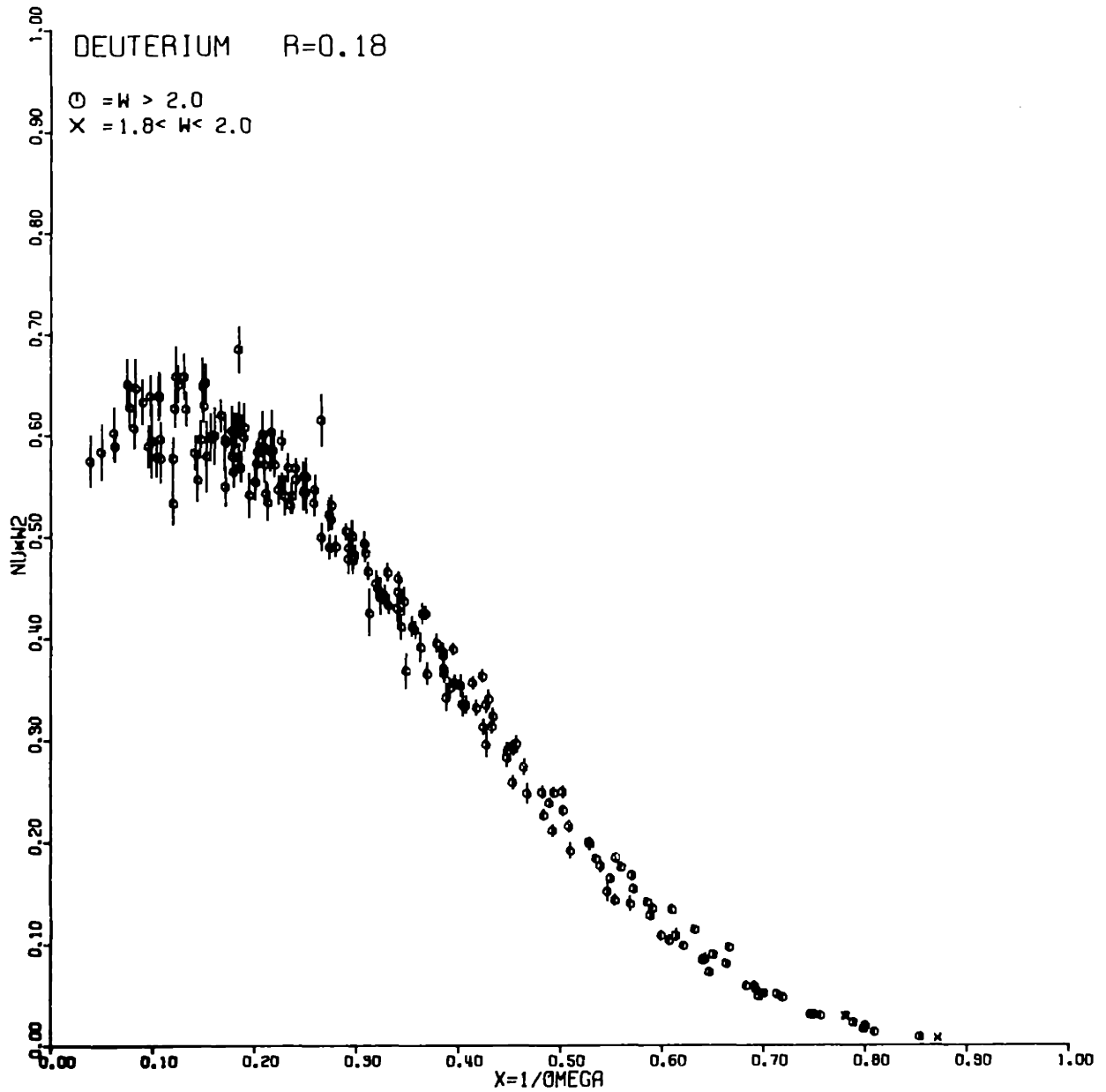


Figure 28 : N_D/N_p vs X for W greater than 2 GeV and q^2 greater than 1.0 (GeV/c)^2 .

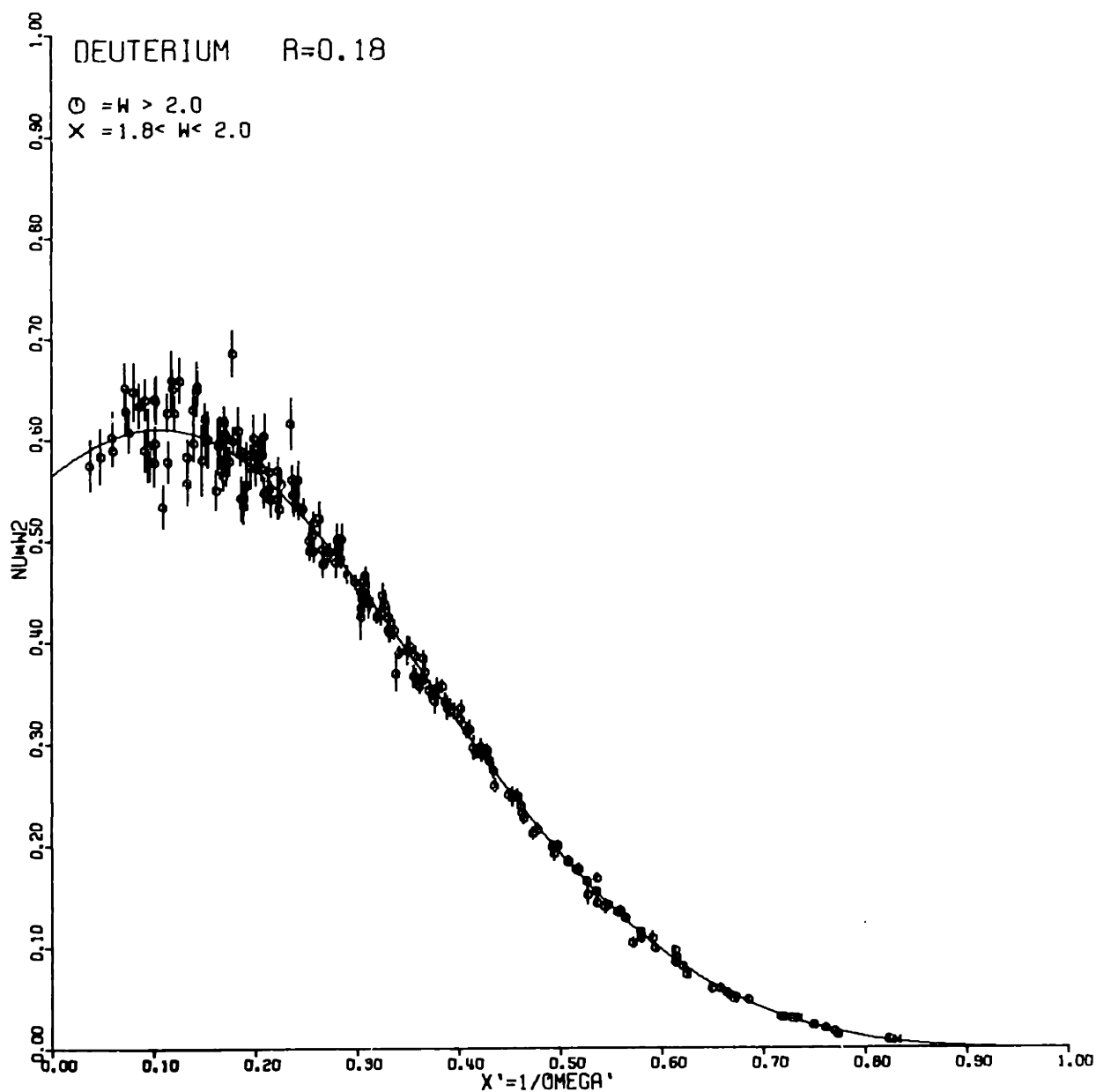


Figure 29 : $\sqrt{W}d$ vs. X' for W greater than 2 GeV and q^2 greater than 1.0 (GeV/c)^2 .

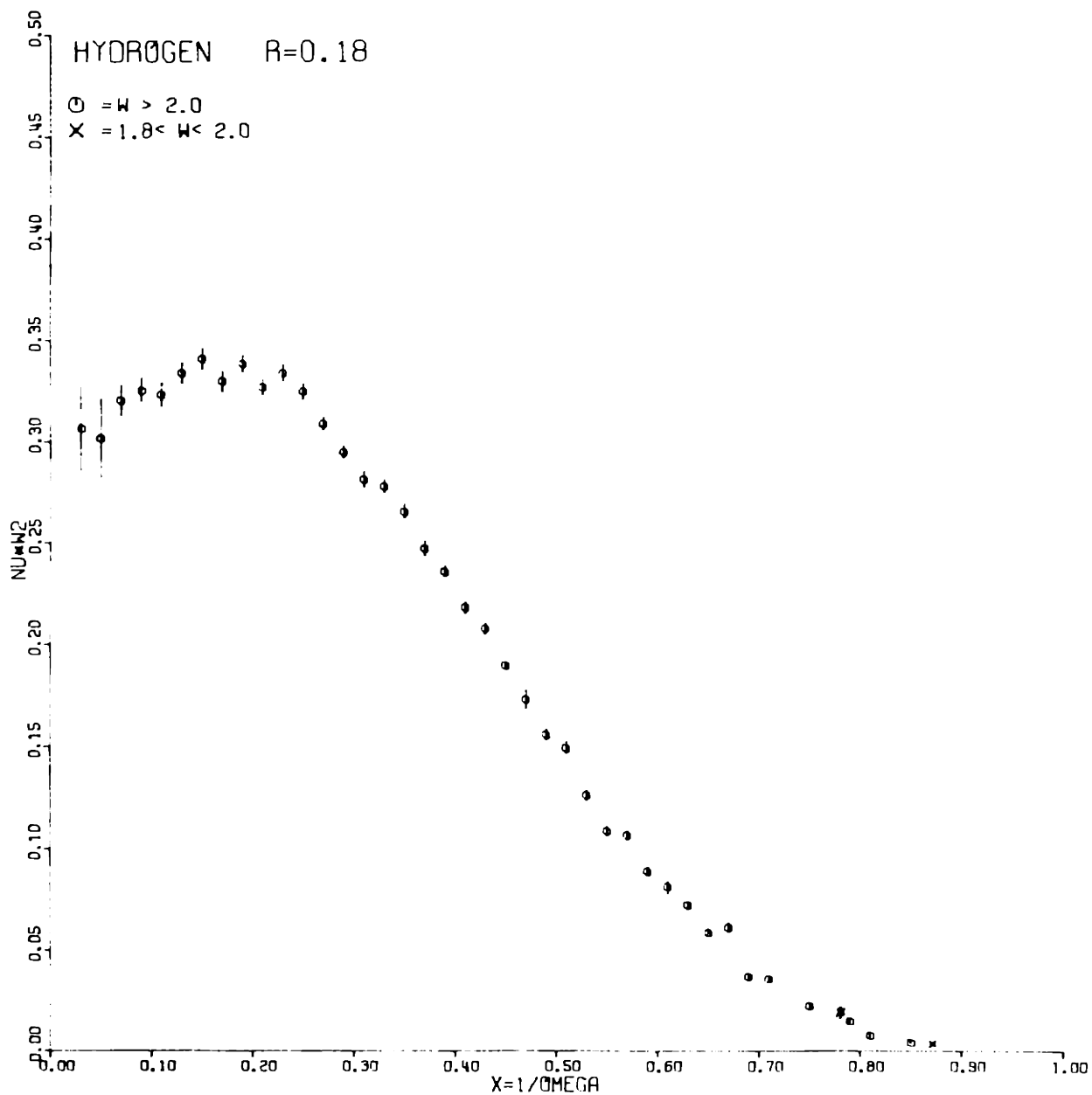


Figure 30 : $\sqrt{W^2}$ vs X for W greater than 2 GeV and q^2 greater than 1.0 (GeV/c)^2 . The data shown is the same data shown in figure 26, but here it is shown in combined form.

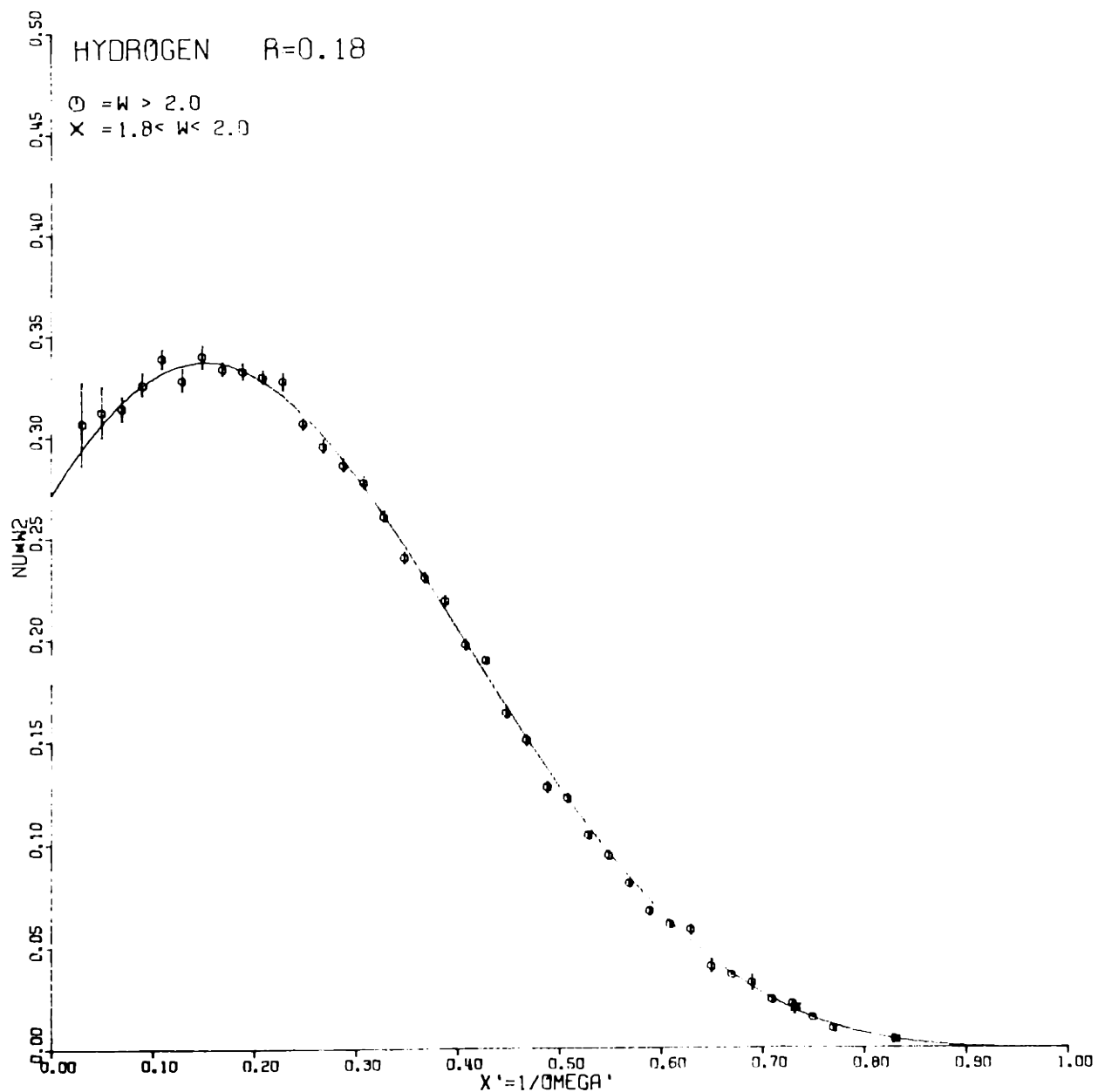


Figure 31 : $\sqrt{W^2}$ vs. X' for W greater than 2 GeV and q^2 greater than 1.0 (GeV/c)². The data shown is the same data shown in figure 27, but here it is shown in combined form.

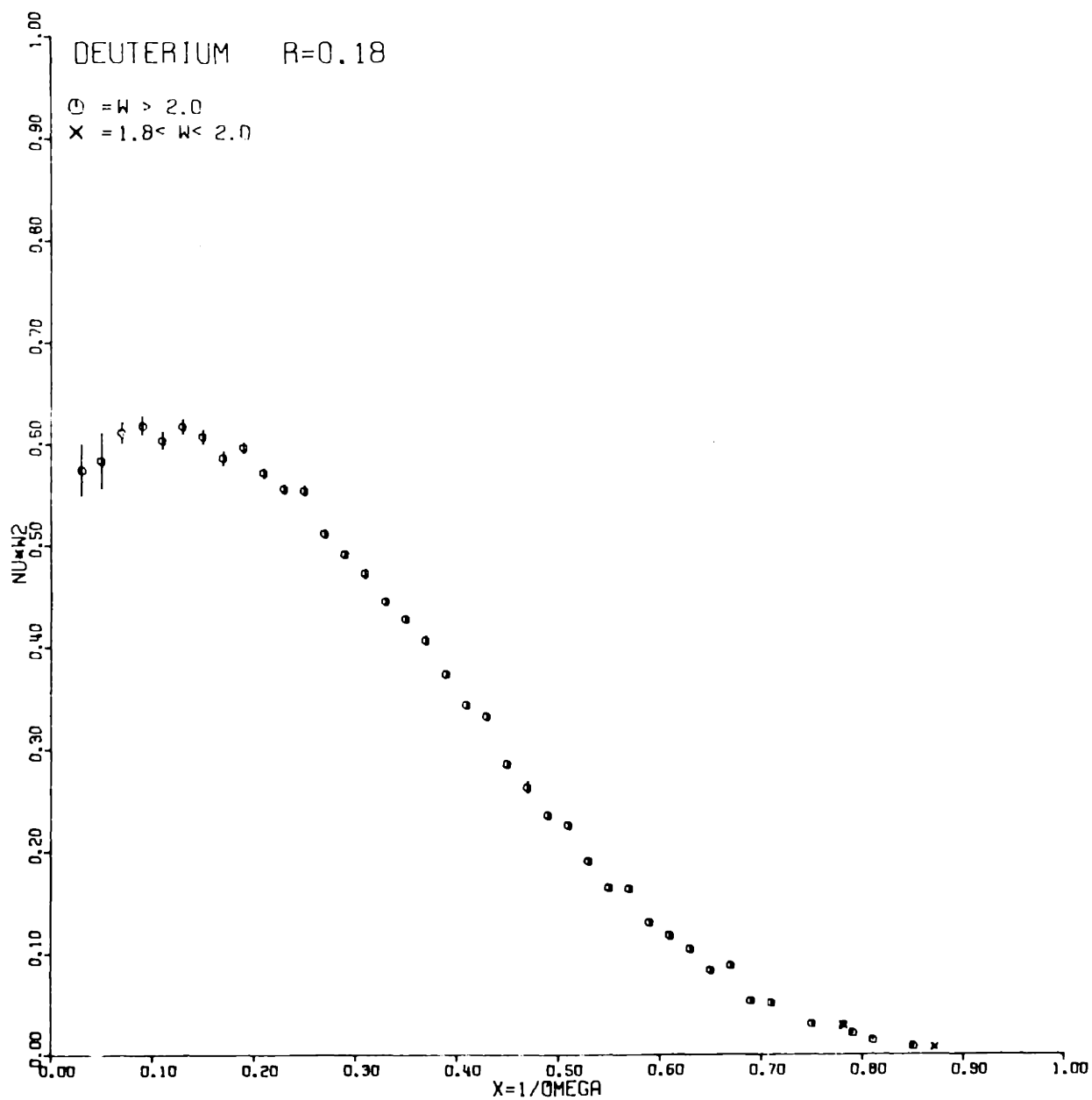


Figure 32 : νW_2^d vs X for W greater than 2 GeV and q^2 greater than 1.0 (GeV/c)^2 . The data shown is the same data shown in figure 28, but here it is shown in combined form.

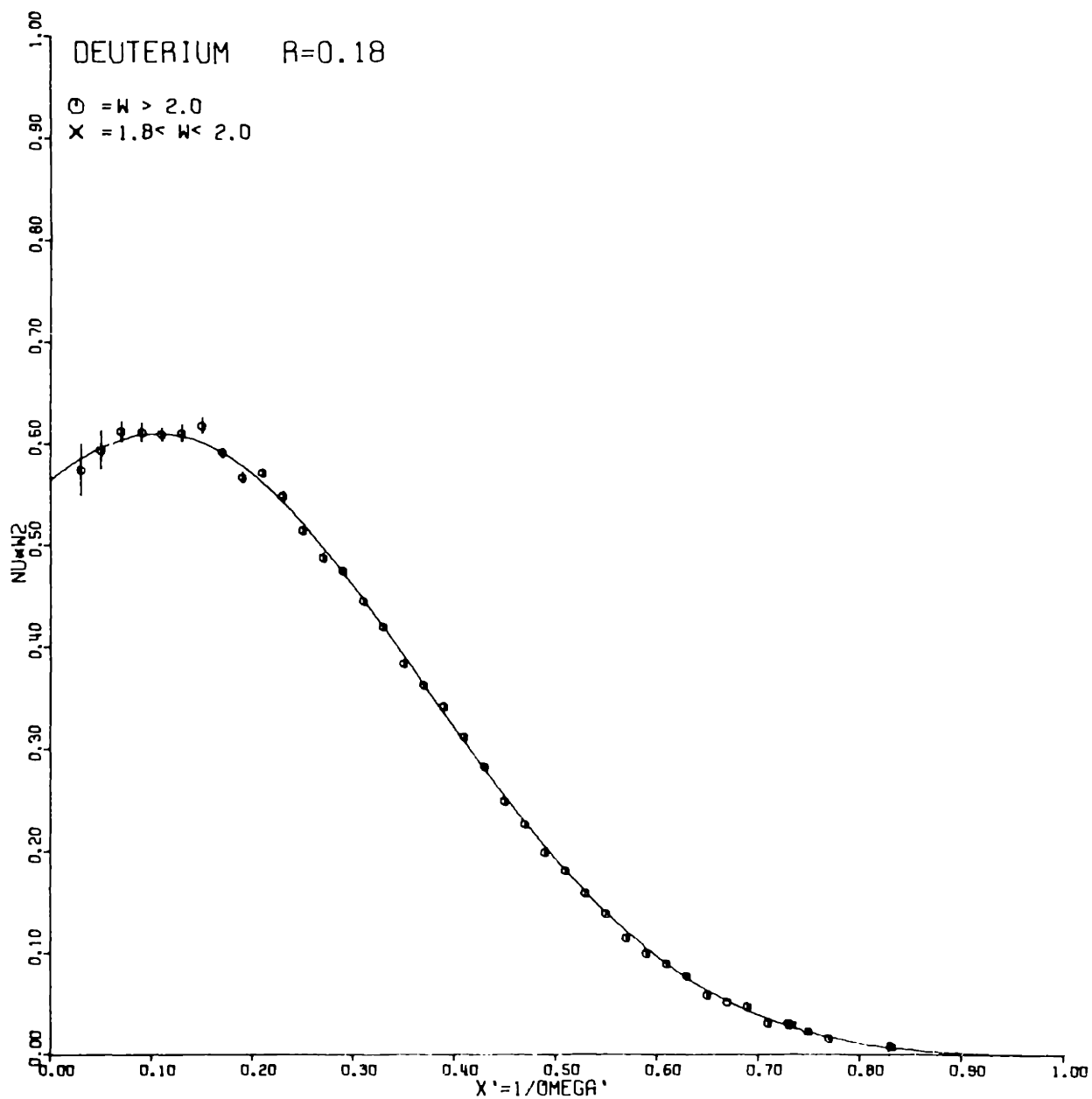


Figure 33 : $\sqrt{W^2}$ vs. X' for W greater than 2 GeV and q^2 greater than 1.0 (GeV/c)^2 . The data shown is the same data shown in figure 29, but here it is shown in combined form.

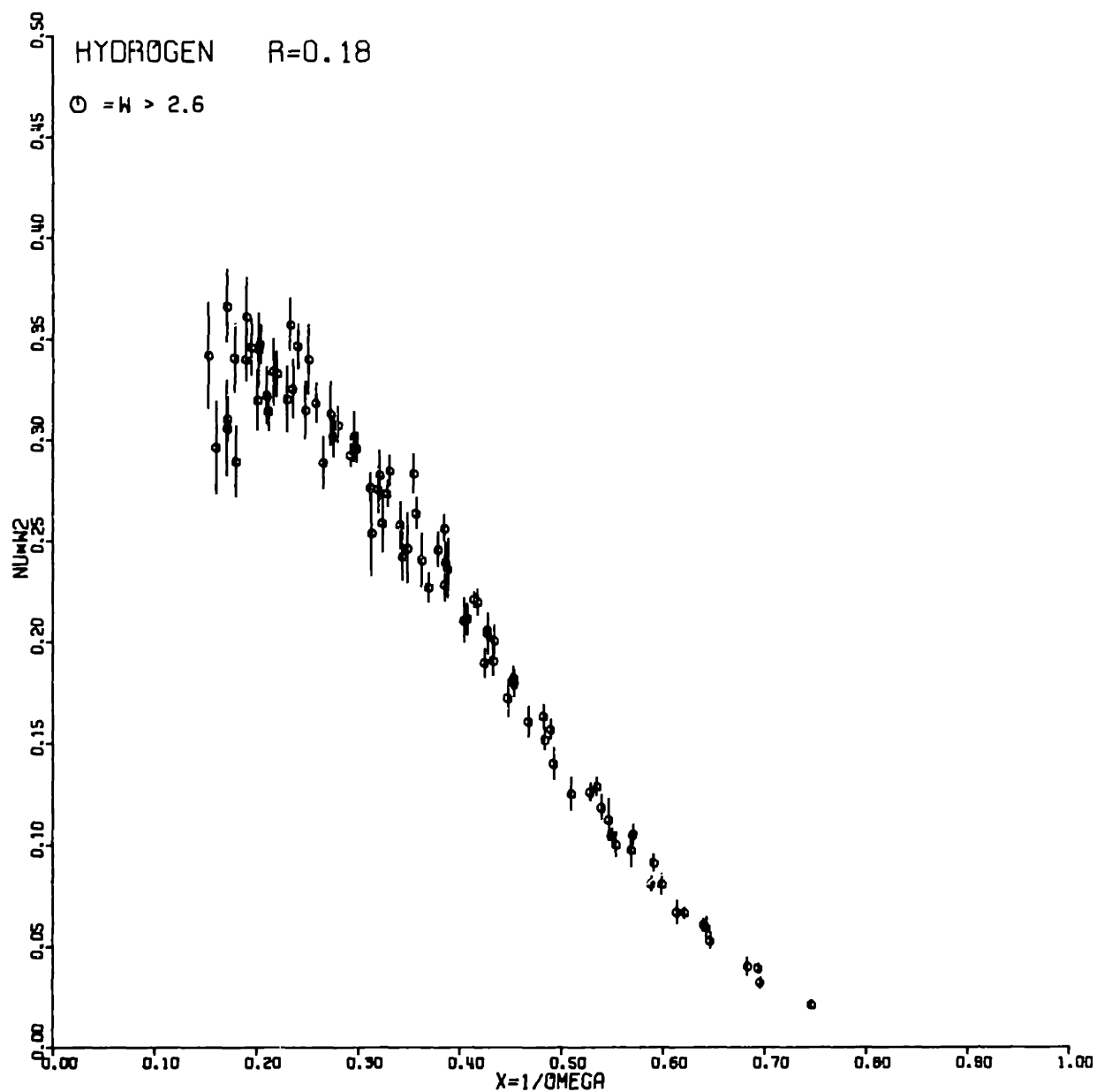


Figure 34 : ν W2p vs. X for W greater than 2.6 GeV and q^2 greater than 1.0 (GeV/c) 2 . Only 18, 26, and 34 degree data is shown.

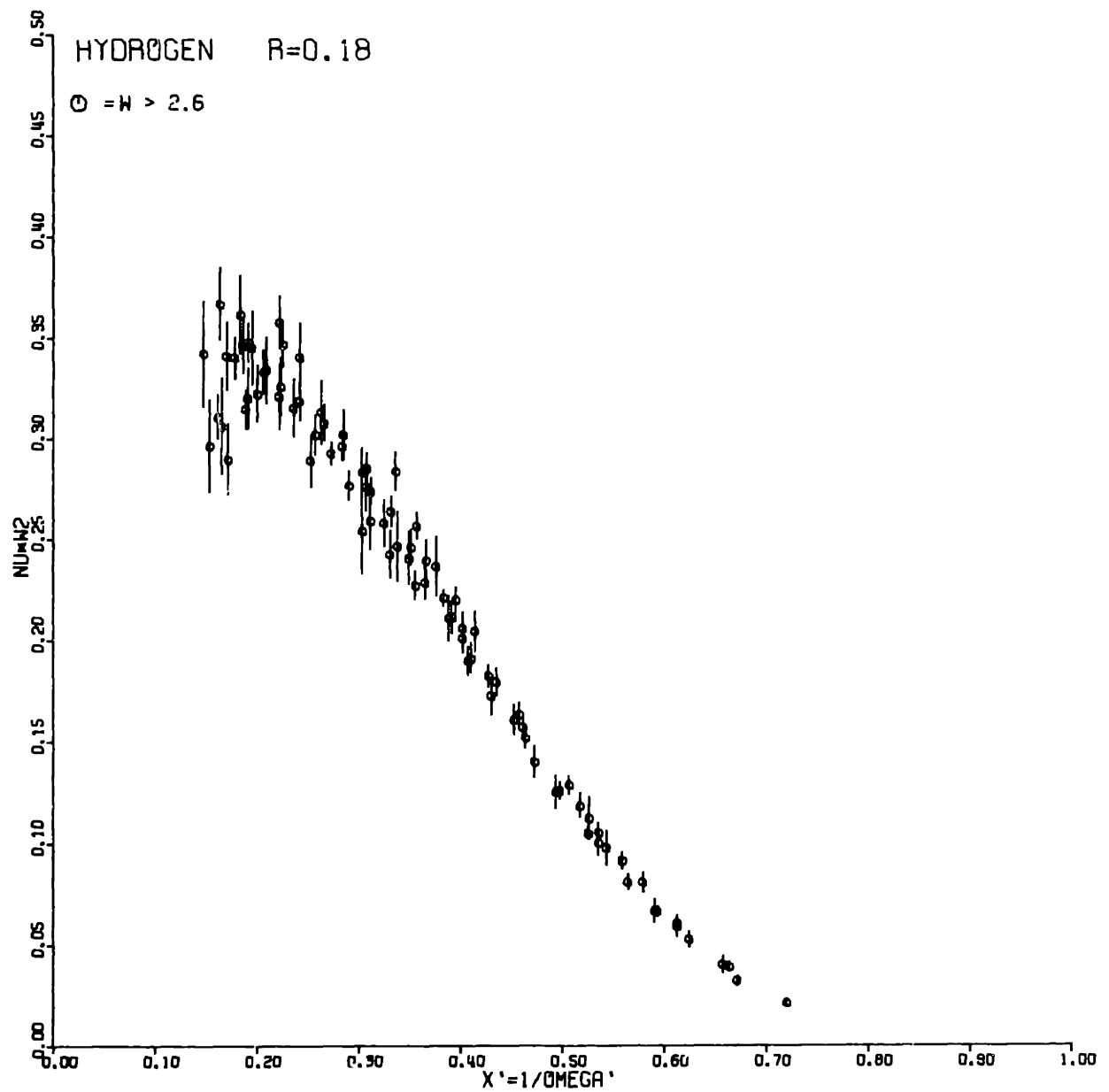


Figure 35 : $\sqrt{W^2p}$ vs. X' for W greater than 2.6 GeV and q^2 greater than $1.0(\text{GeV}/c)^2$. Only 18, 26, and 34 degree data is shown.

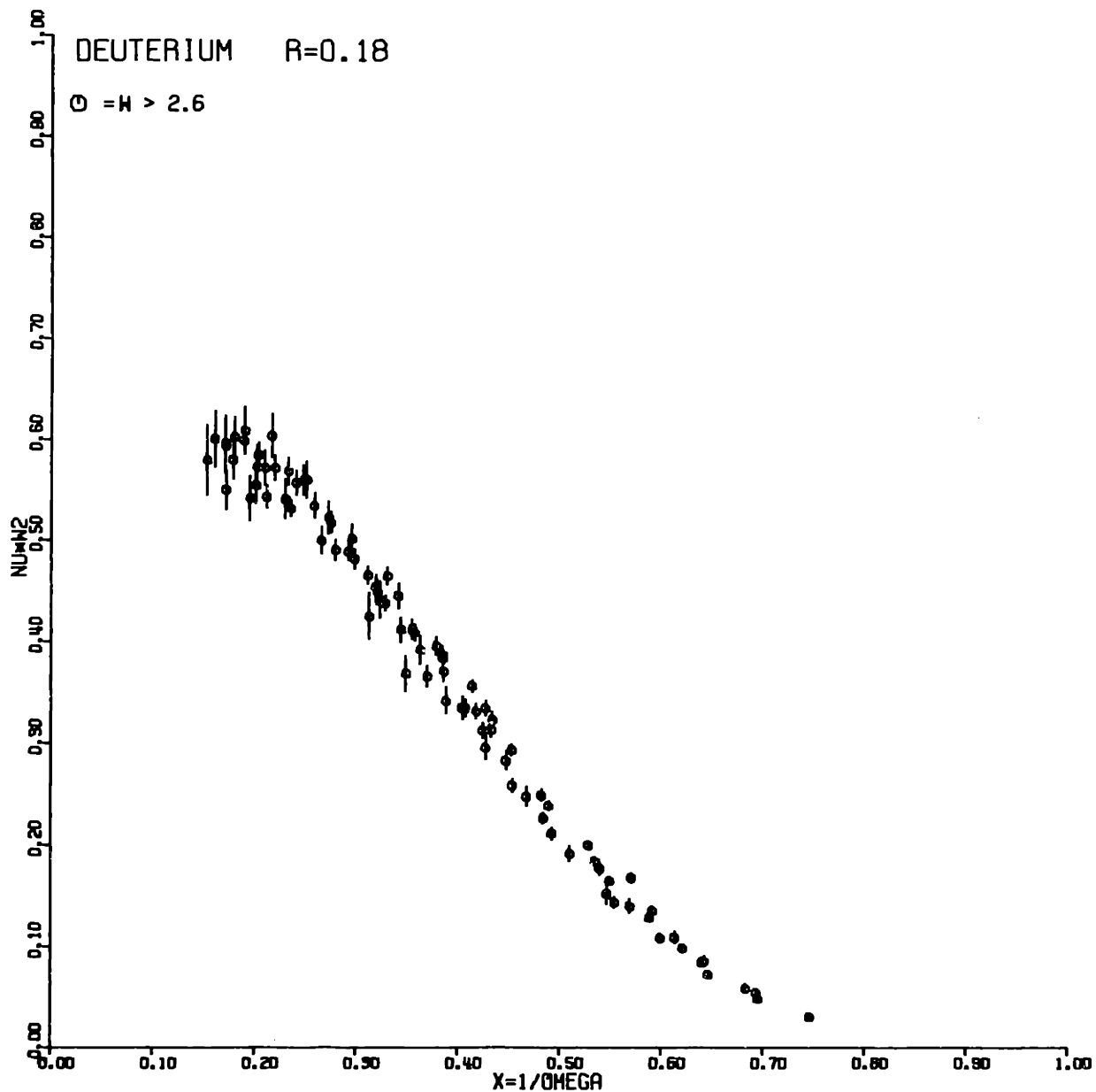


Figure 36 : σ_d/σ_p vs. X for W greater than 2.6 GeV and q^2 greater than 1.0 (GeV/c)². Only 18, 26 and 34 degree data is shown.

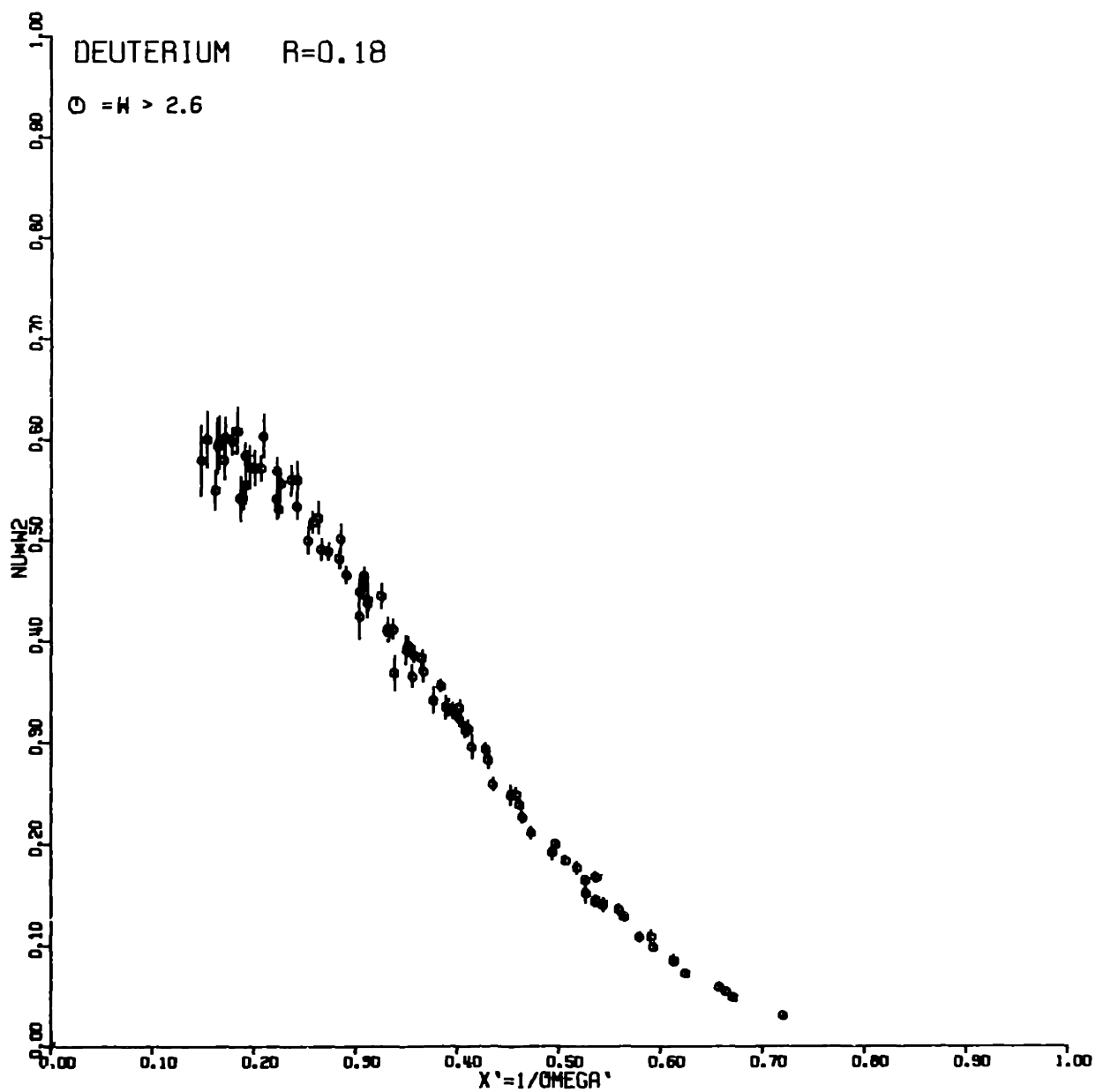


Figure 37 : \sqrt{s} vs. X' for W greater than 2.6 GeV and q^2 greater than 1.0 (GeV/c)². Only 18, 26 and 34 degree data is shown.

4.4 σ_s/σ_t for Hydrogen and Deuterium

The neutron to proton ratios that are presented in figures 11-16 are the ratios for the smeared and unsmeared cross sections. Those cross section ratios can be equated to structure function ratios only if $R_p = R_n$. The analysis of R for the proton and the deuteron is not yet completed. Preliminary results (courtesy of E. M. Riordan(11)) are shown in Figure 21. The figure shows R_d and R_p as functions of q^2 . Each q^2 point was obtained from a weighted average of points at several values of the missing mass W . The data indicates that R_d is the same as R_p with no kinematic dependence within the experimental errors. We shall show in this section that since the smearing corrections are the same for W_1 and W_2 (See Appendix A), the above statement is equivalent to the statement that R_n is the same as R_p indicating that the cross section ratios are indeed the same as the structure functions ratios for the neutron and the proton. We shall also show that the error in the extracted value of R_n is largest at small ω .

Using
$$R = \frac{W_2 (1 + \nu^2/q^2) - W_1}{W_1}$$

We obtain

$$R_d = \frac{W_{2ps}(1 + \frac{v^2}{q^2}) - W_{1ps}}{W_{1ps}} \frac{W_{1ps}}{W_{1ps} + W_{1ns}} + \frac{W_{2ns}(1 + \frac{v^2}{q^2}) - W_{1ns}}{W_{1ns}} \frac{W_{1ns}}{W_{1ps} + W_{1ns}}$$

where an s denotes a smeared quantity. Now from Appendix A (Table A1) we obtain

$$W_{2p}/W_{2ps} = W_{1p}/W_{1ps} , \text{ and } W_{2n}/W_{2ns} = W_{1n}/W_{1ns}$$

Using those expressions we get

$$R_n = R_d + (R_d - R_p)/Z$$

where $Z = W_{1ns}/W_{1ps}$

Now, since $R_d=R_p$ within the errors of the data we can say that $R_n=R_p$. Therefore, $Z = W_{1ns}/W_{1ps}$ is also equal to δ_{ns}/δ_{ps} . This quantity is shown in figures 11 and 12 as functions of X and X' . It varies from 1.0 at X' around 0.0 to 0.38 at X' around 0.8 . Since this ratio is smallest at X' close to 1.0, it is clear that the error in the extracted R_n is largest there.

Now using

$$W_2 = \frac{\sigma}{\sigma_{\text{MOTT}}} \frac{1}{1 + \left(\frac{1}{1+R}\right) \left(\frac{1}{\epsilon} - 1\right)}$$

where

$$\epsilon = \frac{1}{1 + 2 \left(\frac{q^2 + \nu^2}{q^2}\right) \tan^2 \frac{\theta}{2}}$$

we obtain

$$\frac{W_{2n}}{W_{2p}} = T \frac{\sigma_n}{\sigma_p}$$

where

$$T = \frac{1 + \left(\frac{1}{1+R_p}\right) \left(\frac{1}{\epsilon} - 1\right)}{1 + \left(\frac{1}{1+R_n}\right) \left(\frac{1}{\epsilon} - 1\right)} = \frac{1 + \left(\frac{1}{1+R_p}\right) \left(\frac{1}{\epsilon} - 1\right)}{1 + \left(\frac{1}{1+R_d + \frac{R_d - R_p}{Z}}\right) \left(\frac{1}{\epsilon} - 1\right)}$$

If $R_d = R_p$ then $R_p = R_n$ and $T = 1.0$. Any systematic error which affects R_d and R_p in a similar fashion will not contribute to the error in T . The error in T must be added in quadrature to the error in b_n/b_p if we wish to make the statement that the cross section ratio also represents the ratio of the W_2 structure functions. E. M. Rfordan's(11) preliminary results are

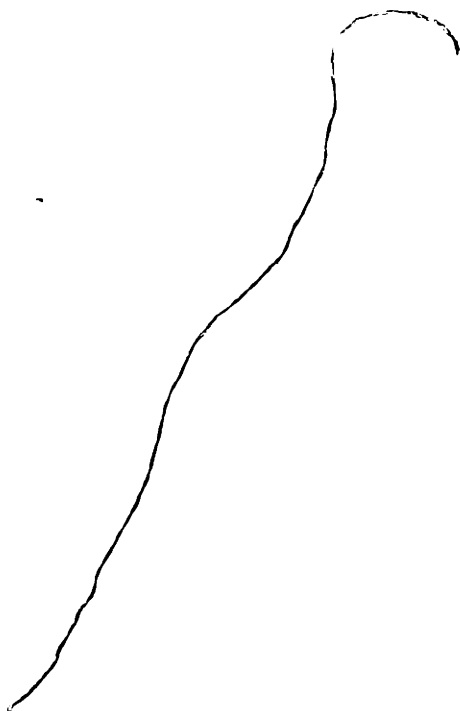
$$R_p = 0.14 \pm 0.10$$

$$R_d = 0.15 \pm 0.08$$

The above values are averages over the entire range of the data and are only meaningful to the extent that R is actually a constant. The quoted errors include a systematic error of 0.06. As mentioned previously, this systematic error should not be included in the calculation of the propagated error in W_{2n}/W_{2p} since it cancels.

A more correct way to apply the error due to the uncertainty in R is to extract $\sqrt{W_{2p}}$ and $\sqrt{W_{2n}}$ at each X, q^2 point and use the value of the measured R and its error for that X, q^2 point. Unfortunately, the separation region does not extend over the entire region in X and q^2 . We must await further analysis (or possibly additional experiments) in order to establish a possible kinematic dependence of R on X , and use this kinematic dependence, if there is one, to extrapolate the values of R to the regions where it was not measured. Currently, we can only assume that the constant value of R is valid over the entire range of X . Using this assumption we can say that $R_d - R_p = 0.01 \pm 0.045$ (statistical errors only). Using an average value of W_{lns}/W_{lps} of 0.5 we find that $R_n - R_p = 0.03 \pm 0.06$. The majority of the data was taken at 18 and 26 degrees for which the average ϵ for the data was about 0.7. Using this value of ϵ we find that the

propagated error in $W2p/W2n$ is only $\pm 1.8\%$ on the average. We must emphasize that this small error is obtained on the assumption that the small error in the global average of R is applicable to all regions of X and q^2 including the extrapolated regions. If one wishes to choose the local errors for R_p and R_d one can compute the error in $W2n/W2p$ by using Table 6. Table 6 shows the correction factor (T) to $\delta n/\delta p$ employed to get $W2n/W2p$ as a function of R_n and ϵ , using an R_p of 0.18. Helpful information for using the table is the fact that the average values of ϵ are 0.75 for 18 degrees, 0.6 for 26 degrees and 0.43 for 34 degrees.



RN	EPSILON									
	0.10	0.20	0.30	0.40	0.50	0.60	0.70	0.80	0.90	1.00
0.0	0.863	0.878	0.893	0.908	0.924	0.939	0.954	0.969	0.985	1.000
0.1	0.940	0.947	0.954	0.961	0.968	0.974	0.981	0.987	0.994	1.000
0.2	1.015	1.013	1.011	1.009	1.008	1.006	1.004	1.003	1.001	1.000
0.3	1.089	1.077	1.065	1.054	1.044	1.034	1.025	1.016	1.008	1.000
0.4	1.161	1.138	1.117	1.096	1.078	1.060	1.044	1.028	1.014	1.000
0.5	1.232	1.197	1.165	1.136	1.108	1.083	1.060	1.039	1.019	1.000
0.6	1.302	1.254	1.211	1.172	1.137	1.105	1.075	1.048	1.023	1.000
0.7	1.371	1.309	1.255	1.207	1.163	1.124	1.089	1.056	1.027	1.000
0.8	1.438	1.362	1.297	1.239	1.188	1.142	1.101	1.064	1.031	1.000
0.9	1.504	1.414	1.336	1.269	1.210	1.158	1.112	1.071	1.034	1.000
1.0	1.569	1.463	1.374	1.298	1.232	1.174	1.123	1.077	1.037	1.000
1.1	1.632	1.511	1.410	1.325	1.252	1.188	1.132	1.083	1.039	1.000
1.2	1.695	1.558	1.445	1.350	1.270	1.201	1.141	1.088	1.042	1.000
1.3	1.756	1.603	1.478	1.375	1.288	1.213	1.149	1.093	1.044	1.000
1.4	1.816	1.646	1.510	1.398	1.304	1.225	1.157	1.098	1.046	1.000
1.5	1.875	1.688	1.540	1.419	1.320	1.236	1.164	1.102	1.048	1.000
1.6	1.934	1.729	1.569	1.440	1.334	1.246	1.170	1.106	1.049	1.000
1.7	1.991	1.769	1.597	1.460	1.348	1.255	1.176	1.109	1.051	1.000
1.8	2.047	1.808	1.624	1.479	1.361	1.264	1.182	1.113	1.052	1.000
1.9	2.102	1.845	1.650	1.497	1.374	1.272	1.188	1.116	1.054	1.000
2.0	2.157	1.881	1.675	1.514	1.386	1.280	1.193	1.119	1.055	1.000

TABLE 6 - T, THE CORRECTION TO σ_n/σ_p TO GET w_{2n}/w_{2p}
AS A FUNCTION OF RN AND EPSILON ASSUMING $RP=0.18$

4.5 Discussion

We have shown detailed comparisons of the neutron to proton cross section ratios with the predictions of two theoretical models. We have shown that a simple quark model which includes a sea of quark - antiquark pairs and neutral gluons could not account for the observed ratios without the inclusion of possible quark-quark correlations. It is difficult to compare the data with the predictions of the Bloom-Gilman local duality model because the theory is only supposed to be valid very close to $X'=1$. The errors of the data at $X'=0.83$, the highest X' data point, are too large to indicate a possible approach of the ratio to 0.47 at $X'=1$. We can only say that the data is not inconsistent with the Bloom-Gilman prediction and further data must be taken in order to establish the fact that the trend of the data is really turning around. The data is definitely inconsistent with the Kuti-Weisskopf prediction of 0.67 at $X=1$.

If the Bloom-Gilman prediction holds true, then as mentioned previously, it indicates a very strong connection between the elastic and inelastic form factors, a connection which relates both the functional form and the magnitudes of the elastic and inelastic form factors. This connection

tends to support a parton model in the sense that the same constituents account for both elastic and inelastic scattering.

Vector dominance models (41) have difficulty in agreeing with high q^2 electroproduction results since large momentum transfers are far from the rho meson pole and therefore the rho meson pole contribution is small. Simple vector dominance models have difficulty in accounting for the small value of the observed R for the proton, and also with the observed A dependence of electroproduction cross sections(39). The A -dependence results indicate that there is no significant-nucleon nucleon shadowing in high A nuclei. Since simple vector dominance models have such difficulties with the R and A dependence results, it would not be useful to have a detailed analysis of the neutron to proton ratio in terms of a vector meson theory. Recently, Sakurai and Schildknecht(51,52,53) proposed a modified vector dominance model which includes a continuum of higher mass vector meson contributions and some kinematic corrections to the simple vector dominance model. The model is in agreement with the e - p results. In a later paper (52) they proposed a model which predicts the neutron to proton ratio for $X' < 0.6$. They make the statement that their model is not valid for $X' > 0.6$

and an expression valid in that region will come in a future paper.

Current Regge models (44) do not predict the neutron to proton ratio uniquely. Diffractive models generally predict a ratio of 1.0, and are only valid in the large ω region. Resonance models(58,59) can account for scaling by letting the total number of resonances excited increase sufficiently rapidly with W . The resonance model of Landshoff and Polkinghorne (58) predicts a ratio of $2/3$ for the neutron to proton ratio, while the resonance model of Domokos, Kovesi-Domokos, and Schonberg (59) predicts a ratio of 0.70-0.78 for the neutron to proton ratio near $X=1$. Both models are in contradiction with the results of this experiment.

Parton models which identify the partons with integrally charged particles can accommodate a small or vanishing neutron to proton ratio at $X=1$. The model of Drell and Lee (40) identifies the partons with bare nucleons and bare pions. They obtain bound state solution of the Bethe-Salpeter equation for the bare nucleon and the bare mesons. The theory is no longer restricted to infinite momentum frames. They expand the observed nucleon state as (i) a bare nucleon and a SU_3 singlet X^0 meson, and (ii) a

bare SU3 octet baryon and two SU3 octet mesons (P $\pi^0\pi^0$, $\Sigma^+K^-\pi^+$, etc.).

$$p = (PX^0) + (P2\pi) + (\Sigma K\pi) \dots$$

$$n = (NX^0) + (N2\pi) + (\Sigma K\pi) \dots$$

They represent the contribution of the two body state to the structure function as $F_I(X)$, and the contribution of the multi body channel as $F_{II}(X)$. Their result is

$$W_{1p} = \beta_p (F_{II}(X) + \alpha_p F_I(X))$$

$$W_{1n} = \beta_n (F_{II}(X))$$

where $\beta_p, \alpha_p, \beta_n$ are constants. $F_I(X)$ and $F_{II}(X)$ depend on the masses of the final state mesons. Drell and Lee obtain rather good fits to the proton data with $\beta_p = 0.22$ and $\alpha_p = 1.4$. They have used the observed X^0 mass for $F_I(X)$, and the K, Σ , π etc masses for $F_{II}(X)$. Their calculation for the neutron to proton ratio for $\alpha_p = 1.4$, and $\beta_p = \beta_n$ is shown in figure 38. Setting $\beta_p \neq \beta_n$ will change the shape of the curve but not the value at $X=1$. The model also predicts that if the q^2 dependence of the elastic form factors is $1/q^4$ then the X dependence of the inelastic structure functions near threshold is $(1-X)^3$. This is indeed the dependence

seen in this experiment. A non-vanishing value for the neutron to proton ratio at $X=1$ can be accommodated within the framework of the model by the inclusion of two body channels in which the meson can also be charged, such as $N\pi^+, \Sigma^0 K^-$, etc. In that case they get

$$W_{1p} = \beta_p (F_{II}(X) + \alpha_p F_I(X) + \alpha'_p F'_I(X))$$

$$W_{1n} = \beta_n (F_{II}(X) + \alpha'_n F'_I(X))$$

The inclusion of a charged spin zero pion in the two body channel yields a non-zero neutron to proton ratio at $X=1$. However, it also yields a $(1-X)^2$ threshold dependence for the inelastic form factors in contradiction with experiment. Therefore, current data is consistent with $\alpha'_p = \alpha'_n = 0$.

In summary, the results of this experiment show that the scattering from nucleons has a definite non-diffractive component. At small X the diffractive component seems to dominate and the neutron to proton ratio does indeed approach unity. At larger X we see a definite non-diffractive component. The difference of the neutron and proton structure functions exhibits a peak at an X around 0.33 (See figures 17-20), while the ratio of the structure function seems to decrease as X approaches 1. The intercept of the neutron to proton ratio at $X=1$ is not yet known with

precision and the data is consistent with values ranging from 0.47 down to 0.20.

Further results will be available in about a year from now. Two experiments proposing an extension of the neutron to proton ratio measurements down to smaller ω are planned to be run at SLAC. Those two experiments will increase our knowledge of the neutron to proton ratio and help answer the following two questions about the trend of the data of the data taken in this experiment

1. Does the trend of the measured neutron to proton data continue at smaller ω , and will the ratio continue to below the quark model limit of 0.25 ?
2. Does the ratio increase to 0.47 as $X' \rightarrow 1$ indicating a very strong correlation between the elastic and inelastic form factors ?

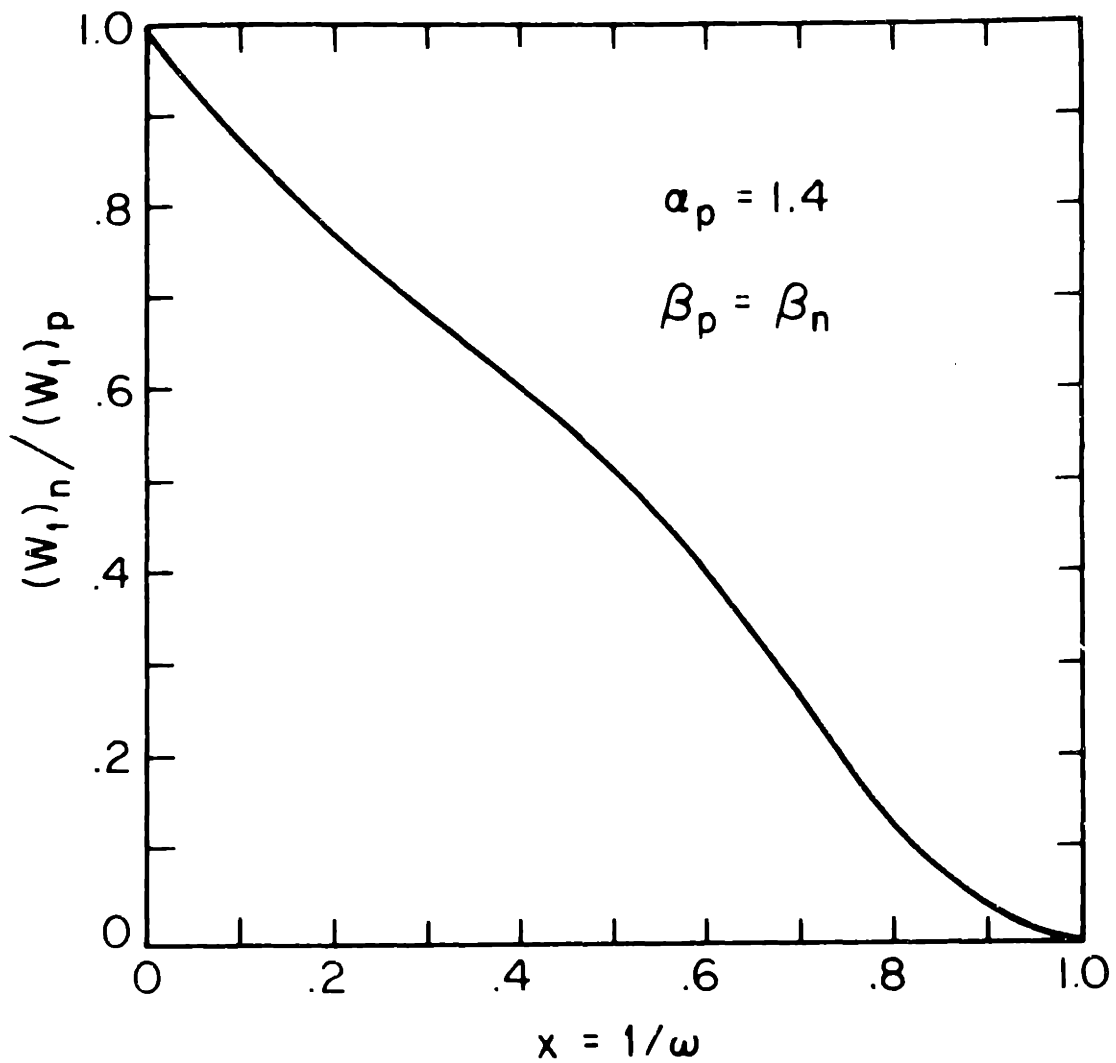


Figure 38 : The prediction of the Drell and Lee model
for W_{ln}/W_{lp} .

Appendix A -- Nuclear binding Effects in Inelastic Electron Deuteron Scattering

A1 Introduction

Given Deuterium and Hydrogen inelastic structure functions one needs to understand the nuclear binding effects in the inelastic e-d spectra in order to extract the structure functions of the neutron. Investigations of the effects of nuclear binding have been pursued recently at Stanford by W. Atwood and G. West(26,27), and also at M.I.T. by A. Bodek, J. Friedman and M. Sogard(28). Other studies reported in the literature have rather limited applicability to the case of deep inelastic electron-deuteron scattering. The approaches taken at M.I.T. and Stanford are conceptually similar, since both utilize the impulse approximation. The difference is that in the Stanford approach the interacting nucleon is taken to be off the mass shell, while in the M.I.T. approach the interacting nucleon is taken to be on the mass shell in order to be able to make a direct correspondence with the non-relativistic phenomenological deuteron wave function. Both approaches yield the same equation and the difference between the two is in the definitions of the momenta and other kinematic variables that appear in the equation. We shall outline each approach

and show the ambiguities that one encounters in each derivation. I thank W. Atwood for numerous helpful discussions regarding the off-shell approach, and M. Sogard and J. Friedman for important contributions to the formulation of the on-shell approach.

This appendix will be rather long and detailed. We therefore present a brief outline of the topics discussed in the various sections.

- A1 Introduction
- A2 Derivations - The Off-Mass-Shell Approach
- A3 Derivations - The On-Mass-Shell Approach
- A4 Smearing in the Scaling Limit and its
implication on W_1/W_2 for the Deuteron
- A5 Smear Cross Sections Directly -
Questions of Flux
- A6 Summary of Possible Indicators of the
Magnitude of the Theoretical Error
- A7 Theoretical Considerations in Smearing
- A8 Experimental Tests of Smearing
- A9 Corrections to the Impulse Approximation
- A10 The Glauber Correction in Electroproduction
- A11 Choice of a Smearing Procedure and
Error Discussion
- A12 Summary

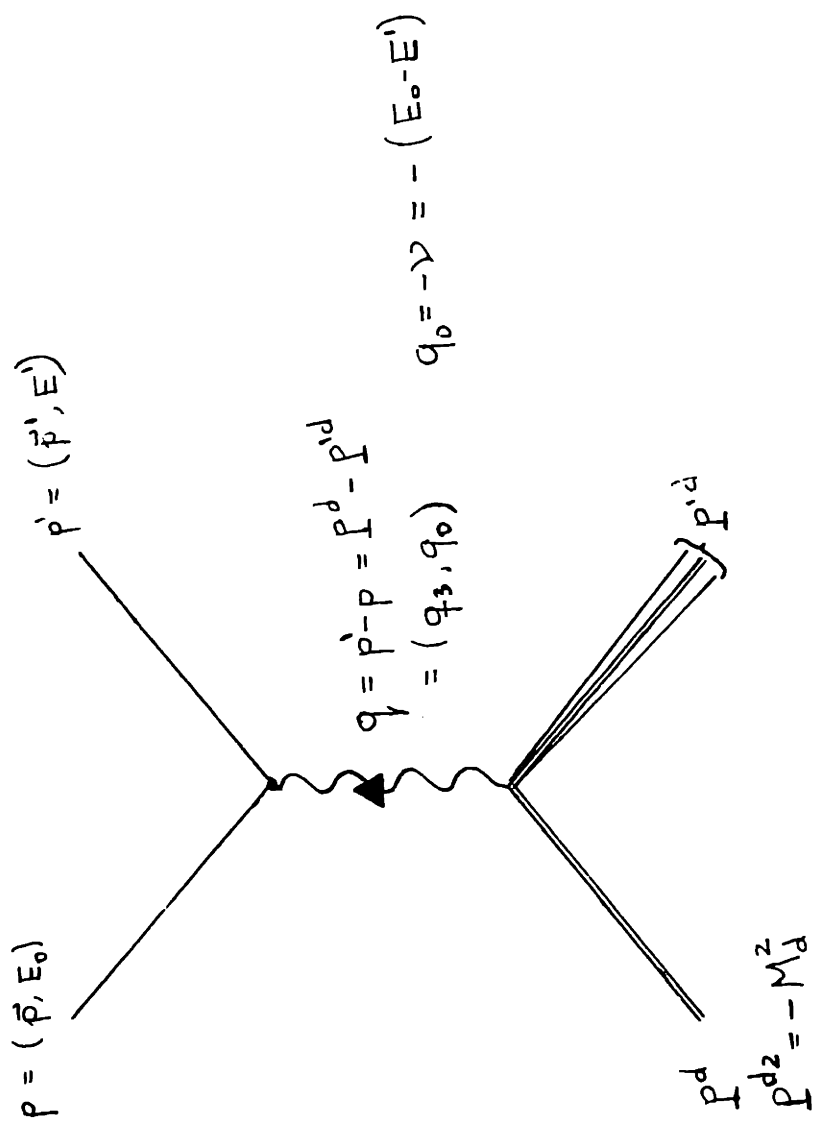


Figure A1. Inelastic Electron Neutron Scattering

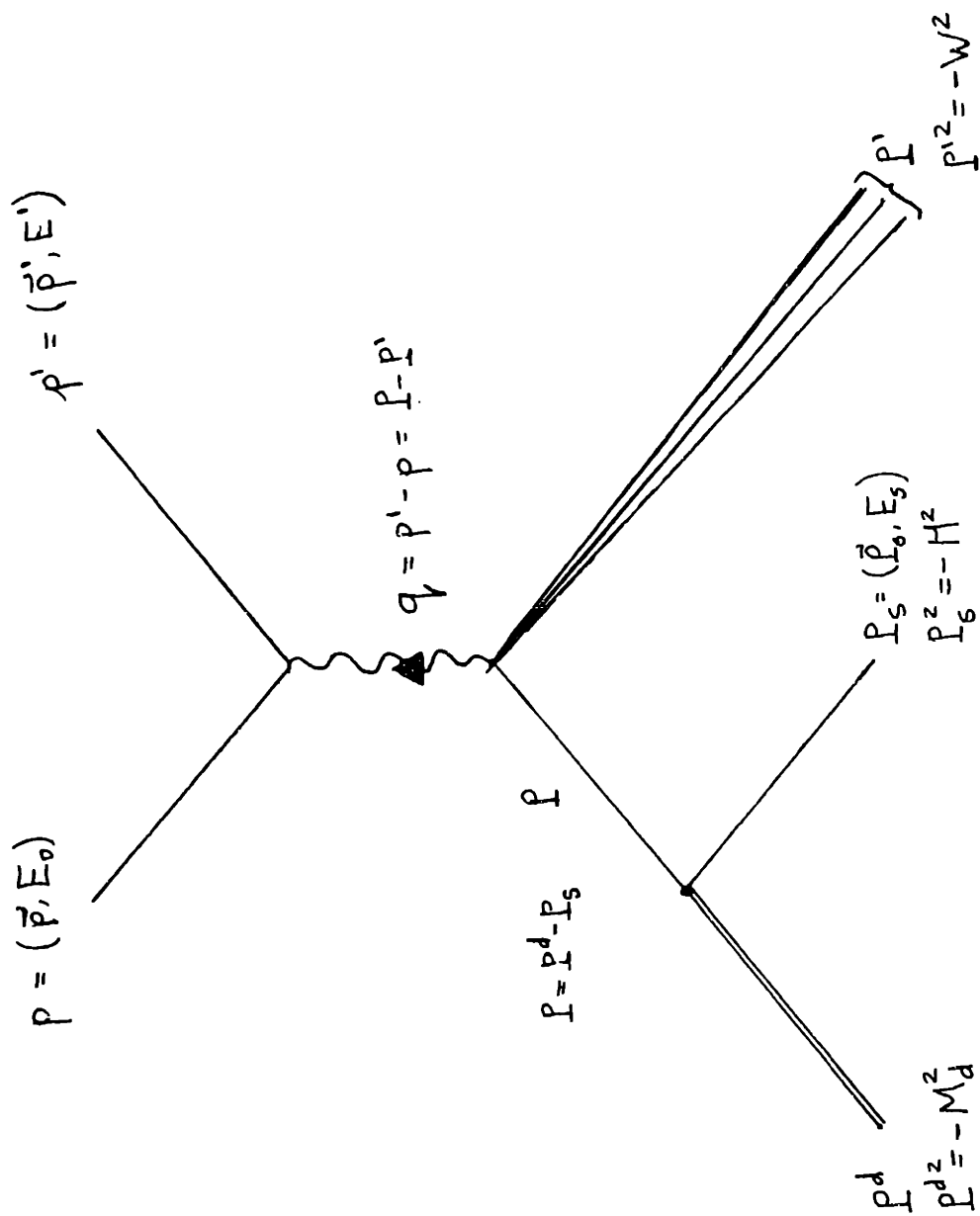


Figure A2. Inelastic Electron Deuteron Scattering in the Impulse Approximation

A2 Derivations - The Off-Mass-Shell Approach

General kinematics were defined earlier in the main body of the thesis. The reader can refresh his memory by glancing at figure 1 on page 18 for the diagram for a general electron nucleon scattering event. Figure A1 on page 188 describes inelastic e-d scattering, and figure A2 on page 189 describes inelastic e-d scattering in the impulse approximation. We first establish some general equations. For any electromagnetic scattering from a nucleus the contribution of the nuclear part of the process is given by the following(4).

$$EA1. \quad W_{\mu\nu} = \frac{(2\pi)^3 \Omega}{(Ze)^2} \overline{\sum} \sum_{\text{Final states}} \delta^4(P-P'-q) \langle P | J_\nu(0) | P' \rangle \langle P' | J_\mu(0) | P \rangle$$

where Ω is the normalization volume. $J_\mu(0)$ is the electromagnetic current operator for the nucleus at the space time point $x_\mu = 0$. The $\overline{\sum}$ indicates an average over the initial target states. P and P' are the Heisenberg state vectors of the initial and final nuclear states with the state vector normalization of E/M. Since the current operator is a 4-vector, Lorentz invariance tells us that $W_{\mu\nu}$ must be a second rank tensor. q and P are the only two independent four vectors, and since $P^2 = -M^2$ we can form only two independent scalars q^2 and $q \cdot P$.

Now covariance, parity conservation and current conservation imply(4) (we take e-d scattering as an example)

$$EA2. W_{\mu\nu}^d = W_1^d(q^2, q \cdot l) \left(\delta_{\mu\nu} - \frac{q_\mu q_\nu}{q^2} \right) + W_2^d(q^2, q \cdot l) \frac{1}{M_d^2} \left(l_\mu - \frac{q \cdot l}{q^2} q_\mu \right) \left(l_\nu - \frac{q \cdot l}{q^2} q_\nu \right)$$

A general expression for $W_{\mu\nu}^d$ in the laboratory frame is

$$EA3. W_{\mu\nu}^d = \int d^3 \vec{P}_s A(\vec{P}_s) B_{\mu\nu}$$

where $A(\vec{P}_s)$ represents the amplitude for the deuteron to go to a spectator nucleon on the mass shell and an interacting nucleon off the mass shell, and includes the interacting nucleon propagator. $B_{\mu\nu}$ is the second rank tensor characterizing the interaction between the off-mass-shell nucleon and the virtual photon.

West suggests the following simplest possible expression as an approximation to equation EA3.

$$EA4. W_{\mu\nu}^d = \int \frac{M}{E_s} d^3 \vec{P}_s f(\vec{P}_s) \left\{ \left[W_1^p(q^2, q \cdot l, l^2) \left(\delta_{\mu\nu} - \frac{q_\mu q_\nu}{q^2} \right) + W_2^p(q^2, q \cdot l, l^2) \frac{1}{M^2} \left(l_\mu - \frac{q \cdot l}{q^2} q_\mu \right) \left(l_\nu - \frac{q \cdot l}{q^2} q_\nu \right) \right] + \left[\text{same for the neutron} \right] \right\}$$

where \vec{P}_s and E_s are the momentum and energy of the spectator nucleon. $P = P_\nu = P^d - P_s$ is the virtual off-mass-shell 4-momentum of the interacting nucleon. $(M/E_s)f(\vec{P}_s)$ represent the truncated d,pn vertex function (truncated means that one nucleon is on the mass shell) times the nucleon propagator.

$W_{\mu\nu}^d$ represents the tensor for the deuteron while W_1^p, W_2^p , and W_1^n, W_2^n represent the structure functions for the proton and neutron respectively. It is difficult to relate $f(\vec{P}_s)$ to the non-relativistic wave function of the deuteron. By making a correspondence with elastic e-d scattering West arrives at the following :

$$(M/E_s) f(\vec{P}_s) = \left| \phi(\vec{P}_s) \right|^2$$

where $\phi(\vec{P}_s)$ is the non-relativistic wave function of the deuteron in momentum space. However, by looking at the normalization condition for the non-relativistic wave function he arrives at

$$f(\vec{P}_s) = \left| \phi(\vec{P}_s) \right|^2$$

It is apparent that the expression for $f(\vec{P}_s)$ is at least uncertain by a factor of M/E_s . As can be deduced from equation EA4 West assumes that the off-mass shell tensor $B_{\mu\nu}$ can be obtained by the blind substitution of the off-shell 4-momentum P_V for the 4-momentum ^{the} in Λ expression for the free particle tensor. There are several difficulties in that approach. One is uncertain as to what one puts for M^2 in the second part of the tensor. Putting in $-P_V^2$ is not satisfactory since it yields a divergence when $-P_V^2$ goes to zero and $-P_V^2$ can also go negative. One is forced to choose the free

proton mass for lack of anything better. The state vectors P and P' in equation EA1 have state normalization E/M . One can not use this normalization for the case of the off-shell particle since its energy can go to zero or be negative. One is forced to assume that the energy in the state normalization for the off-shell nucleon is the energy of a free nucleon. One place where the dynamics comes in is in the problem of how to relate the off-mass-shell structure functions W_1 and W_2 to the measured free nucleon structure functions. Since $P_v^2 \neq -M^2$ the general off-shell structure functions can depend on the three variables q^2 , $q \cdot P$ and P_v^2 . We shall use the general guiding principle that in this case we ought to use off-shell kinematics but on-shell dynamics. What we mean is that we shall conserve energy and momentum in the kinematics, but use on-shell structure functions by making correspondences between the on-shell and off-shell invariant 4-vector products.

West proceeds to make the following correspondence between the off-shell structure functions and the measured free nucleon structure functions.

$$W_2 \left(q^2, \frac{q \cdot P}{M}, P_v^2 \right)_{\text{off-shell}} = W_2 \left(q^2, \frac{q \cdot P}{M} \right)_{\text{off-shell}} = W_2 (q^2, \nu)_{\text{on-shell}}$$

One can immediately note that when one makes the above correspondence the matrix element does not behave properly at the threshold for the electroproduction of pions since it does not go to zero there. Similarly, one does not get the proper delta function for the case of quasi-elastic scattering, and neither does one get the correct peak positions for the nucleon resonances. The reason for the above is that all those depend on the mass of the produced final state W ($=-P'^2$), and the following two different expressions are true for the cases of on and off-shell kinematics.

$$\text{EA5a. Free particle -- } W^2 = 2 q \cdot P - q^2 + M^2 = 2 M \nu - q^2 + M^2$$

$$\text{EA5b. off-shell -- } W^2 = 2 q \cdot P_V - q^2 - P_V^2$$

One can avoid this problem in two ways. One way is to view the tensor as a function of the final state P' only, independently of whether the initial state was on or off the mass shell. Since $P' = P + q$ the tensorial parts are the same as before and we have the following identity :

$$\frac{1}{M^2} \left(P'_\mu - \frac{P' \cdot q}{q^2} q_\mu \right) \left(P'_\nu - \frac{P' \cdot q}{q^2} q_\nu \right) \equiv \frac{1}{M^2} \left(P_\mu - \frac{P \cdot q}{q^2} q_\mu \right) \left(P_\nu - \frac{P \cdot q}{q^2} q_\nu \right)$$

However, now we make the following correspondence between the off- and on-shell structure functions

The off-mass-shell structure functions only depend on the final state in this W correspondence approach. This way if the interacting nucleons's final state P' is a unbound proton we use the elastic form factors, the matrix element vanishes when the final state P' is a proton plus a barely produced pion, and the matrix element exhibits peaks when the final produced mass corresponds to the mass of one of the nucleon resonances. Since the matrix element vanishes at pion threshold we do not have to use the step function $\theta(W-(M+M_\pi))$, which is necessary, if one uses the prescription that is suggested by West.

Another way to solve the threshold and resonance problems and still use something similar to the correspondence that West makes is to factorize the structure functions into terms that depend explicitly on W , q^2 , and $q.P$. Having factorized them in this way, we can make different correspondences between their variables. For example, a fit to the proton structure functions due to Breidenbach and Kuti (42) is

$$\gamma W_2 = A(W) F(\omega', q^2) \quad , \quad \omega' = \omega + \frac{M^2}{q^2}$$

where $A(W)$ contains the threshold and resonance behaviors of the matrix element. We now make the same correspondence

that West makes by putting $\omega = 2q \cdot P_V / q^2$ in $F(\omega', q^2)$, and putting the final state mass W into $A(W)$. This way the deep inelastic data scales in $\frac{2q \cdot P_V}{q^2} + \frac{M^2}{q^2}$ and the threshold condition and resonance behavior are satisfied in $A(W)$. One realizes that in order to use this mixed variables prescription one needs to understand how the structure functions factor into W and $q \cdot P$ dependent parts. Since this usually involves some sort of theoretical assumption, this guess of the off-mass-shell correction is dependent on the theoretical framework for the factorization. On the other hand the theoretical assumption behind the W correspondence approach is that there are no off-mass-shell corrections to the structure functions. The justification for that is that if we do not know what the off-mass-shell corrections are, we should not make any. Note that both the mixed variables and the W correspondence prescription become the same in the infinite q^2 scaling limit. They are the same because when q^2 becomes very large we can neglect P_V^2 and M^2 in equations EA5a and EA5b.

The above illustrates the ambiguities that arise from the off-shell treatment. We now proceed to obtain explicit expressions for W_1^d and W_2^d by solving equation EA4. Define z

to be in the \vec{q}_3 direction. Now proceed to look at the individual components of the tensor in the laboratory frame. Now using the xx,yy components and using $\vec{p}_x^2 + \vec{p}_y^2 + \vec{p}_z^2 = \vec{p}_s^2$ we obtain,

$$EA6. \quad W_1^d(q^2, \nu) = \int \frac{M d^3\vec{p}_s}{E_s} f(\vec{p}_s) \left\{ \left[W_1^p + \frac{W_2^p}{M} (\vec{p}^2 - p_z^2) \right] + \left[\text{same for the neutron} \right] \right\}$$

Now $W_{xy}=W_{xo}=W_{xz}=W_{yx}=W_{yz}=W_{y0}=W_{zx}=W_{zy}=W_{ox}=W_{0y}=0$, since $q \cdot P$ does not depend on the azimuthal angle φ between \vec{q}_3 and \vec{P} . Now using the zz,00, or z0 equations we obtain (after some algebra and using equation EA6),

$$EA7. \quad W_2^d(q^2, \nu) = \int \frac{M d^3\vec{p}_s}{E_s} f(\vec{p}_s) \left(\frac{\nu''}{\nu} \right)^2 \left\{ \left[\left(1 - \frac{p_z q^2}{M \nu'' \vec{q}_3} \right)^2 + \frac{1}{2M^2} (\vec{p}^2 - p_z^2) \cdot \right. \right. \\ \left. \left. \cdot \frac{q^2}{\vec{q}_3^2} \left(\frac{\nu}{\nu''} \right)^2 \right] W_2^p + \left[\text{same for the neutron} \right] W_2^n \right\}$$

where $\nu'' = P \cdot q / M$ and $\nu = E - E' = -q_0$

We can now go to the final state hadronic center of mass (i.e. the frame where P_s and P' have equal but opposite momenta) and evaluate the integral. In that frame the limits of the integration are simple because the angular and magnitude limits on the range of P_s are independent. The simple limits make the numerical integrations easier. West proceeds to do the integration in the laboratory frame

instead and obtains the following.

$$\begin{aligned}
 \text{EAS. } \omega \nu W_2^d &= M r \int_0^\infty \frac{M}{E_s} f(\vec{p}_s) \frac{p_s d p_s}{\omega} \int_{\omega_+''}^{\omega_-''} d\omega'' \omega'' \nu'' \left[W_2^p G_2(\omega'', r) + W_2^n G_2(\omega'', r) \right] \\
 2 M W_1^d &= M r \int_0^\infty \frac{M}{E_s} f(\vec{p}_s) \frac{p_s d p_s}{\omega} \int_{\omega_+''}^{\omega_-''} d\omega'' \left\{ \left[2 M W_1^p + \nu'' W_2^p G_1(\omega'', r) \right] + \left[\text{same for the neutron} \right] \right\} \\
 p_s &= \left| \vec{p}_s \right|
 \end{aligned}$$

where

$$\begin{aligned}
 G_2(\omega'', r) &= \left[1 + (1-r^2) \left(\frac{\omega p_0}{\omega'' M} - 1 \right) \right]^2 + \\
 &+ \frac{1}{2} \left(\frac{\omega}{\omega''} \right)^2 (1-r^2) \left[\frac{p_s^2}{M^2} - \frac{r^2}{\omega^2} \left(\frac{\omega p_0}{M} - \omega'' \right)^2 \right]
 \end{aligned}$$

$$G_1(\omega'', r) = \frac{2}{\omega'' q^2} \left[p_s^2 - \frac{r^2}{\omega^2} (\omega p_0 - M \omega'')^2 \right]$$

$$\omega'' = \frac{2 p \cdot q}{q^2} \quad p_0 = M_d - \sqrt{p_6^2 + M^2}$$

$$r = \left| \frac{q_0}{q_3} \right| \quad \omega_{\pm}'' = \frac{\omega}{M} \left(p_0 \pm \frac{p_s}{r} \right)$$

For an unbound on-shell nucleon we have the following

$$W_1 = A_1(W) F_1(\omega', q^2) \quad \omega' = 1 + \frac{W^2}{q^2} = \omega + \frac{M^2}{q^2}$$

$$W_2 = A_2(W) F_2(\omega', q^2) / \nu$$

Now for the off-shell situation we define

$$W^2 = 2M\nu'' + q^2 + (M_d - \sqrt{P_s^2 + M^2})^2 - P_s^2$$

$$\nu_w = (W^2 - q^2 - M^2) / 2M = \nu'' - 2(\sqrt{P_s^2 - M^2} - M)$$

We can now summarize our two prescriptions for the off-shell structure functions

1. W final state (Strictly off-shell kinematics, but on-shell dynamics, i.e. no off-shell corrections)

$$W_1 = A_1(W) F_1(\omega', q^2) \quad \omega' = 1 + W^2/q^2$$

$$W_2 = A_2(W) F_2(\omega', q^2) / \nu_w$$

2. Mixed variables(A form of a possible off-shell correction to the structure functions obtained by insisting that ω is the important variable to consider.)

$$W_1 = A_1(W) F_1(\omega', q^2) \quad \omega' = \frac{2q \cdot P_v}{q^2} + \frac{M^2}{q^2}$$

$$W_2 = A_2(W) F_2(\omega', q^2) / \nu''$$

In a mixed variables prescription one can keep the pion threshold condition satisfied and guess other forms of off-shell corrections such as a combination of the two by letting $\omega' = 1 + W^2/q^2$, but using ν'' instead of ν_w . The above

are the only possible off-shell structure functions which can be related by a reasonable correspondence to on-shell structure functions. Fortunately the two yield rather close numerical answers since the data was taken at high q^2 . And as mentioned before the two become the same at infinite q^2 , since $\omega' \rightarrow \omega \rightarrow 2 q \cdot P / q^2$ for both. The canonical smearing procedure involved the average of the two.

A 3 Derivations - The On-Mass-Shell Approach

We now proceed to outline the on-shell approach in detail. The method involves expressing the cross section for inelastic e-p scattering in terms of a flux, a matrix element and a phase space factor. Similarly the scattering cross section from the deuteron is expressed in terms of the above three invariants. Then, by expanding the initial deuteron state in terms of free particle plane waves we relate the matrix element for deuterium to the free nucleon matrix elements. The difficulties come in energy conservation between the free states and the final produced mass W .

Kinematics are defined in figures A3 and A4. Expressing the e-p cross section in terms of a flux, an invariant

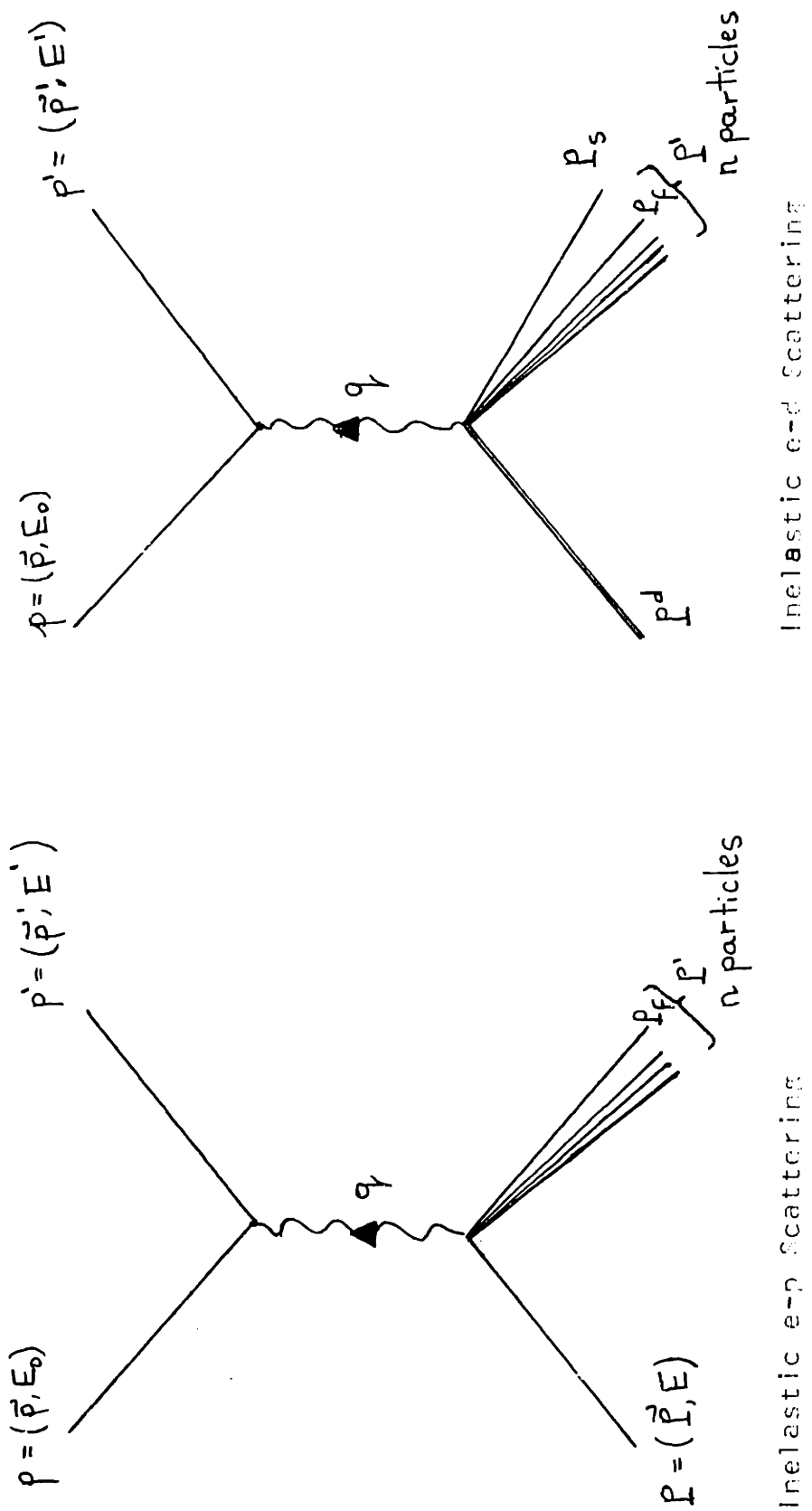


Figure A3. Inelastic e-p and e-d Scattering

Figure A4

Definitions of Kinematic Variables

M = Mass of the nucleon
 m_e = Mass of the electron
 p, E_0 = Incident electron momentum and energy
 p', E' = Scattered electron momentum and energy.
 P, E = Target proton momentum and energy
 v = Relative velocity between the electron and the target
 P_f = Final state nucleon momentum (without the produced pions)
 \vec{P}_j, M_j = Final state particles' momenta and masses.
 H_p, H_n = The Hamiltonians for the e-p and e-n interactions
 P_i = A general symbol denoting an initial state particle momentum.
 P_{fj} = A general symbol denoting an final state particle momentum.
 Ω = Solid angle
 \vec{P}_j, \vec{E}_j = Momenta and energies of the final state particles in the final hadronic center of mass.
 M_s, P_s, E_s = Mass momentum and energy of the spectator nucleon
 M_T, P_T, E_T = Mass momentum and energy of the interacting nucleon
 P_d, E_d = Momentum and energy of the deuteron
 P^i = The interacting nucleon's final state momentum (including all the produced pions).
 E_i, E_f = The total initial and final energies of the system.
 n = The total number of produced particles plus the interacting nucleon (see fig. A3)

matrix element and an invariant final state phase space we get

$$d\sigma_p = \frac{M m_e^2}{(2\pi)^{3(n-1)-4}} \frac{1}{E E_0} \frac{1}{V} \delta^4(\sum p_i - \sum p_{fj}) \frac{d^3 \vec{p}_f}{E_f} \prod_j^{n-1} N_j \frac{d^3 \vec{p}_{fj}}{E_j} |T_{Nj}^p|^2$$

where

$$T_{Nj}^p = \langle p | H_p | p_f, \sum_j^{N_j} p_{fj} \rangle \quad N_j = \begin{matrix} \frac{1}{2} \text{ (Boson)} \\ N_j \text{ (Fermion)} \end{matrix}$$

Integrating over all unobserved particles and evaluating the energy-momentum delta function in the final hadronic center of mass we get

$$EA9 \quad \frac{d^2 \sigma_p}{d\Omega dE'} = \frac{m_e^2}{E_0} \frac{1}{V} \frac{E' M}{E} |M|_p^2$$

where $|M|_p^2$ is the matrix element integrated over all final states.

$$|M|_p^2 = \frac{N_n}{E_n} \frac{N_{n-1}}{E_{n-1}} \frac{\tilde{P}_{n-1}^2}{\frac{\partial(E_i - E_f)}{\partial \tilde{P}_{n-1}}} \int \prod_j^{n-2} |T_{Nj}^p|^2 \frac{d^3 \vec{p}_{fj}}{E_j} d\tilde{\Omega}_{n-1} \frac{1}{(2\pi)^{3(n-1)-4}}$$

We evaluate a similar expression for the deuteron. Here we have one more particle in the final state, so we get

$$EA10 \quad \frac{d^2 \sigma_d}{d\Omega dE'} = \frac{1}{(2\pi)^3} \frac{1}{V} \frac{M_s}{E_s} \frac{d^3 p_s}{E_s} \frac{m_e^2}{E_0} |M|_d^2 \frac{1}{2E_d}$$

where

$$|M|_d^2 = \frac{N_n}{E_n} \frac{N_{n-1}}{E_{n-1}} \frac{\tilde{P}_{n-1}}{\frac{\partial(E_i - E_f)}{\partial \tilde{P}_{n-1}}} \int \prod_j^{n-2} N_j |T_{Nj}^d|^2 \frac{d^3 \vec{p}_{fj}}{E_j} d\tilde{\Omega}_{n-1} \frac{1}{(2\pi)^{3(n-1)-4}}$$

and

$$T_{N_j}^d = \langle p^d | H_d | p_f, p_s \sum_{f,j}^{N_j} \bar{p}_{f,j} \rangle$$

Another form for the e-nucleus cross section can be obtained by contracting the electron tensor $\pi_{\mu\nu}$ with the tensor of the nucleus $W_{\mu\nu}$.

$$\pi_{\mu\nu} = (2p_\mu p'_\nu - p_\nu p'_\mu - \delta_{\mu\nu} (p \cdot p' + m^2))$$

we write another expression for the cross sections

$$\text{Stationary proton} \quad d\sigma_p = 2\alpha^2 \frac{d^3p'}{2E'} \frac{1}{q^4} \frac{M}{E} \frac{1}{V} \pi_{\mu\nu} W_{\mu\nu}^p \quad \text{EA11a.}$$

$$\text{Stationary deuteron state} \\ \text{normalized to 1.} \quad d\sigma_d = 2\alpha^2 \frac{d^3p'}{2E'} \frac{1}{q^4} \frac{1}{V} \pi_{\mu\nu} W_{\mu\nu}^d \quad \text{EA11b.}$$

Now, by comparing equations EA9, EA10, and EA11 (dropping $1/(2\pi)^3 2E_d$) in eq. EA10 since we want to use a non-relativistic wave function normalized to 1 and not the relativistic one which is normalized to $(2\pi)^3 2 \cdot E_d$) we get,

$$\text{EA12} \quad \pi_{\mu\nu} W_{\mu\nu}^p = K |M|_p^2 \\ \pi_{\mu\nu} W_{\mu\nu}^d = K \int \frac{d^3p_s M}{E_s} |M|_d^2$$

where K represents all the kinematic factors that are the same for the deuteron and the proton. Now we try to relate $|M|_p^2$ and $|M|_d^2$ to $|M|_d^2$. We do it by evaluating $T_{N_j}^d$. We

separate the final state into plane waves of several particles (this corresponds to ignoring the final state interaction).

$$T_{Nf}^d = \langle p^d | H_d | p_f, l_s \sum \bar{p}_{fj} \rangle \approx \langle p^d | H_d | \left\{ |\vec{p}_f\rangle |\vec{p}_s\rangle | \sum \bar{p}_{fj} \rangle \right\}$$

We now write in the impulse approximation :

$$H_d = H_p + H_n$$

We now proceed to expand $\langle p^d |$ in plane waves of the neutron and the proton. Since $|M\rangle p$ is the matrix element for scattering off a proton whose initial state normalization was $(2\pi)^3 E/M$, while the non-relativistic wave function is expanded in plane waves which are normalized to 1, we have to correct for the different normalizations (See for example Goldberg Ref. 63).

$$\langle p^d | = \frac{\sqrt{M_s M_T}}{(2\pi)^3} \int \frac{d^3 \vec{p}'_s}{\sqrt{E'_s} \sqrt{E_T}} \phi(\vec{p}'_s) \langle \vec{p}'_s | \langle \vec{p}_T |$$

where

$$\phi(\vec{p}'_s) = \frac{1}{(2\pi)^{3/2}} \int \psi(\vec{r}) e^{i \vec{p}'_s \cdot \vec{r}} d^3 \vec{r}$$

and $\vec{p}'_s = - \vec{p}_T$. $\langle p'_T |$ and $\langle p'_s |$ are now relativistic plane waves normalized to $(2\pi)^3 E/M$. $\phi(p_s)$ is the non-relativistic phenomenological deuteron wave function obtained from fits to other experimental data. That wave function ought to yield the

correct binding energy, magnetic dipole and electric quadrupole moments of the deuteron, elastic e-d form factors etc. $|\phi(\vec{p}_s)|^2$ is the square of the deuteron wave function in momentum space which is the sum of the squares of the fourier transforms for the S and D components of the wave function.

Now putting $\langle P^d |$ into the expression for T_{Nj}^d we get

$$T_{Nj}^d = \frac{M_S M_T}{(2\pi)^3} \left(\frac{d^3 p'_s}{\sqrt{E'_s} \sqrt{E_T}} \phi(\vec{p}'_s) \langle \vec{p}'_s | \langle \vec{p}'_T | H_p + H_n | \vec{p}_s \rangle | \vec{p}_f \rangle \sum_{Nj} \bar{p}_{fj} \right)$$

When this matrix element is squared we will obtain different interference terms depending on whether the final state nucleons shall be two protons, two neutrons or a neutron and a proton. We show later that these interference terms are small and their relative magnitude is of the order of the deuteron form factor.

For the time being let us assume that we have a neutron and a proton in the final state. Now using $\langle \vec{p}'_s | \vec{p}_s \rangle = (2\pi)^3 E_s / M \delta(\vec{p}'_s - \vec{p}_s)$, $\langle \vec{p}'_T | \vec{p}_f \rangle = (2\pi)^3 E_T / M \delta(\vec{p}'_T - \vec{p}_f)$ and using $M_S = M_T$ we get (after evaluating the delta function)

$$T_{Nj}^d = \sqrt{\frac{E_s}{E_T}} \left[\phi(\vec{p}'_f) \langle -\vec{p}'_f | H_p | \vec{p}_s \rangle \sum_{Nj} \bar{p}_{fj} + \phi(\vec{p}_s) \langle -\vec{p}_s | H_n | \vec{p}_f \rangle \sum_{Nj} \bar{p}_{fj} \right]$$

Squaring and neglecting the interference terms we get

$$|T_{N_j}^d|^2 = \frac{E_s}{E_T} \left[|\phi(\vec{P}_f)|^2 \left| \langle -\vec{P}_f | H_P | \vec{P}_s, \sum_{fj}^{N_j} \vec{P}_{fj} \rangle \right|^2 + |\phi(\vec{P}_s)|^2 \left| \langle -\vec{P}_s | H_n | \vec{P}_f, \sum_{fj}^{N_j} \vec{P}_{fj} \rangle \right|^2 \right]$$

When $T_{N_j}^d$ is put into the expression for $|M|^2$ and the integration over all final states is carried out, what is then called the spectator is arbitrary and P_f and P_s can be interchanged in the above equation. Doing that we obtain

$$|M|_d^2 = \frac{E_s}{E_T} \left[|M|_n^2 + |M|_p^2 \right] + \text{neglected interference}$$

And putting this into equation EA12 we get

$$\begin{aligned} \text{EA13.} \quad \pi_{\mu\nu} W_{\mu\nu}^p &= K |M|_p^2 \\ \pi_{\mu\nu} W_{\mu\nu}^d &= K \int \frac{M}{E_T} d^3\vec{P}_s |\phi(\vec{P}_s)|^2 \left[|M|_p^2 + |M|_n^2 \right] \end{aligned}$$

Now since we look at the same incident and scattered electron energies (E_0, E') in both processes the $\pi_{\mu\nu}$ tensors are the same. Therefore, the following expression will satisfy equation EA13.

$$\text{EA14.} \quad W_{\mu\nu}^d = \int \frac{M}{E_T} d^3\vec{P}_s |\phi(\vec{P}_s)|^2 \left[W_{\mu\nu}^p + W_{\mu\nu}^n \right]$$

Equation EA14 places more restrictive conditions on W_1^d and W_2^d than equation EA13, since it is actually 16 equations (one for each tensor component), but any W_1^d, W_2^d satisfying

eq. EA14 will satisfy eq EA13. Equation EA14 allows the separation of the smearing effects for W_1 and W_2 , while eq. EA13 only gives us the ratio of the smeared and unsmeared cross sections. Note, since we expanded in free particle states it is clear that $\phi(\vec{P}s)$ is the non-relativistic wave function. $E_T = E_s$ since both particles are assumed to be on the mass shell, and therefore there is no M/E_s ambiguity.

Now we are presented with the problem of defining $W_{\mu\nu}^P$ and $W_{\mu\nu}^h$. The expansion in free particle states produced a problem in energy conservation since $q + P_T \neq P'$. We can either look at the tensor as a function of the initial state or as a function of the final state. As shown before, looking at the tensor as a function of the final state is equivalent to treating the initial state off the mass shell with W_1 and W_2 are defined to be functions of the final state mass W . However, in order to use the non-relativistic wave function we assumed that the initial state was on the mass shell. On the other hand, looking at the tensor as a function of an on-shell initial state only implies non-energy conservation and corresponds to using the matrix element for the production of a larger final state mass than is actually the case. A possible compromise is to use the on-shell momentum in the tensor, but view the structure

functions as functions of the final produced mass W in order to ensure energy conservation. So we have

$$W_{\mu\nu}^f = W_1^f(q^2, W^2) \left(\delta_{\mu\nu} - \frac{q_\mu q_\nu}{q^2} \right) + \frac{W_2^f(q^2, W^2)}{M^2} \left(P_\mu - \frac{P \cdot q}{q^2} q_\mu \right) \left(P_\nu - \frac{P \cdot q}{q^2} q_\nu \right)$$

where P is now the on-shell momentum. Note that if one wishes to take the on-shell equation off the mass shell we get $d^3\vec{P}_S M/E_T$ and not $d^3\vec{P}_S M/E_S$. However, M/E_T can diverge when E_T is off-shell. Since E_T can go to zero, this leads us to suspect that the M/E_S in the West off-shell treatment should not be there and we should use $f(\vec{P}_S)M/E_S = |\phi(P_S)|^2$ in that approach.

A 4.- Smearing in the scaling limit and its implication on W_1/W_2 for the deuteron.

Empirically it was found that for the kinematic range of the data the smearing corrections for W_1 and W_2 are almost the same and leave the ratio of W_1/W_2 the same as before the smearing. This statement is true only for the off-mass-shell approach, which was chosen to be the canonical smearing procedure. The on-shell approach yielded a much different ratio for W_1/W_2 after smearing. We shall show now what happens to the smearing equations in the scaling limit and how the on-shell approach still maintains its peculiar smeared W_1/W_2 even in that limit.

In the scaling limit $\nu \rightarrow \infty, q^2 \rightarrow \infty, \omega = \frac{2M\nu}{q^2} = \text{const.}$

$$r = \left| \frac{q_0}{q_3} \right| \rightarrow 1$$

the off-shell expressions reduce to

$$\omega \nu W_2^d(\omega) = M \int_0^\infty \frac{M}{E_s} f(p_s) \frac{p_s dp_s}{\omega} \int_{\omega_+''}^{\omega_-''} d\omega'' \omega'' [F^p(\omega'') + F^n(\omega'')] \\ 2M W_1^d(\omega) = M \int_0^\infty \frac{M}{E_s} f(p_s) \frac{p_s dp_s}{\omega} \int_{\omega_+''}^{\omega_-''} d\omega'' 2M [W_2^p(\omega'') + W_1^n(\omega'')] \\ F^p(\omega'') = \nu'' W_2^p(\omega'') = \nu W_2^p(\omega)_{\text{on-shell}}, \quad W_1^p(\omega'') = W_1^p(\omega)_{\text{on-shell}}$$

where

$$\omega_{\pm}'' = \frac{\omega}{M} (p_0 \pm p_s), \quad p_0 = M_d - \sqrt{p_s^2 + M^2}$$

Using the same variables of integration to facilitate easy comparison the on-shell expressions reduce to

$$\omega \nu W_2^d(\omega) = M \int_0^\infty \frac{M}{E_s} f(p_s) \frac{p_s dp_s}{\omega} \int_{\omega_+''}^{\omega_-''} d\omega'' \omega'' [F^p(\omega'') + F^n(\omega'')] \left[1 + \frac{2\omega}{M} \sqrt{p_s^2 - M^2} - M \right] \\ 2M W_1^d(\omega) = M \int_0^\infty \frac{M}{E_s} f(p_s) \frac{p_s dp_s}{\omega} \int_{\omega_+''}^{\omega_-''} d\omega'' 2M [W_2^p(\omega'') + W_1^n(\omega'')]$$

So if in the scaling limit $R_n = R_p = 0$, the off-shell treatment predicts $R_d = 0$, while the on-shell tensor yields $R_d = F(\omega) \neq 0$, even when R_n and R_p are zero. R stands for the ratio of the scalar to transverse cross section in the notation of Hand. In a later section we present arguments that indicate that the on-shell treatment is not as reliable

as the off-shell one because of the inconsistency in the energy conservation. Rejecting the on-shell tensor we can say that the smearing produces no correction to R_d and that R_n can be extracted directly from R_d and R_p after the smearing was used to obtain the smeared neutron to proton cross section ratios.

A5 --Smear cross sections directly, questions of flux

In numerous deuteron experimental papers one finds a rather rudimentary smearing procedure applied to the cross sections themselves.

$$\left(\frac{d^2\sigma}{d\Omega dE'} \right)_d = \int |\phi(\vec{p}_s)|^2 d^3\vec{p}_s \left[\frac{d^2\sigma_p}{d\Omega dE'}(\vec{p}_s) + \left(\frac{d^2\sigma_n}{d\Omega dE'} \right)(\vec{p}_s) \right]$$

where $|\phi(\vec{p}_s)|^2$ is the probability that the nucleon in the deuteron has momentum \vec{p}_s . One encounters the usual difficulties that we had mentioned before. If one assumes the initial proton to be free one gets a cross section for the production of a final state mass higher than the actual one produced. Also, the final state phase space will be wrong since the momenta of the final state electron and proton will be wrong due to lack of energy conservation. The threshold condition for the behavior of the matrix element pion threshold is also wrong. One can patch up all

those difficulties in a similar fashion to the way we have done it done in the on-shell matrix element smearing. The only thing we gain in this cross section smearing approach is an additional ambiguity as to how to define the incident flux to the moving proton, and how to define the state normalization of that proton. This ambiguity did not arise in the previous on- and off-shell treatments because the relevant quantities in those treatments were the matrix elements. If the initial particle is on the mass shell then $E = \sqrt{\vec{P}^2 + M^2}$ and the velocity $\vec{V} = \vec{P}/E$. However if we put the initial particle off the mass shell in order to avoid some of the final state difficulties we are at a loss as to the identification of the incident flux and state normalization. Since the off-shell energy can vanish, the velocity can go to infinity. We can get around it by keeping the initial particle on the mass shell and let the structure function definitions in terms of the final state mass take care of the energy conservation. Even assuming that the initial particle is on the mass shell we still have to define the flux between the non- colinear beams. We can either chose the vectorial difference in velocity or chose the usual invariant flux(62) that is used for colinear beams. i.e.

$$EA15. \quad \frac{1}{\text{flux}} = \frac{E_0}{\sqrt{p \cdot p - m_e^2 M^2}} = \frac{M}{E_T (1 - V_z)}$$

V_z = velocity along the direction of the incident electron.

Now we proceed to outline an argument that leads us to conclude that the flux correction should not be applied at all. The argument hinges on the fact that the flux correction leads to the violation of relativistic and gauge invariance as applied to the deuteron. $W_2^d(q^2, \nu)$ should only be a function of the only two independent scalars q^2 and ν . Also contracting the deuteron gauge invariant $W_{\mu\nu}^d$ tensor with the electron tensor we get

$$\frac{d^2\sigma_d}{d\Omega dE'} = \sigma_{\text{MOTT}} \left[W_2^d(q^2, \nu) + 2 \tan^2 \frac{\theta}{2} W_1^d(q^2, \nu) \right]$$

with no other possible angular dependence to the cross section. In the previous sections we derived expressions for the smeared W_1 and W_2 for the deuteron which yielded expressions dependent only on q^2 and ν . The smearing integration involved integrals over the angle between \vec{q}_3 and \vec{p}_s . The other terms in the integrals were symmetric with respect to that angle. The flux on the other hand, depends on the angle between the incident electron's momentum and \vec{p}_s . Therefore, for different E_0, E', θ triplets with the same q^2 and ν the angle between the incident electron and the direction of \vec{q}_3 will be different and the flux correction will modify the integral in a different manner. This means that the smearing procedure yields deuteron structure functions which depend not only on q^2 and ν but also on the

angle θ . This violates the relativistic invariance condition, and the gauge invariance condition which fixes the angular dependence of the deuteron cross section to be $W_1^d(q^2, \nu) \tan^2(\theta/2)$.

A possible counter argument is that our formalism is only approximate and therefore there is no reason for it to satisfy relativistic or gauge invariance, or also that we could be using the wrong expression for the flux. All we can possibly say is that the flux correction might serve as an indication of the error that one makes when one uses the impulse approximation to smear cross sections. Basically, I think that the fundamental quantity to smear is the invariant matrix element as we have done in the off- and on-shell approaches. The cross section is just an easily measured quantity from which we can extract the invariant matrix element of the interaction hamiltonian. The flux, therefore, can be arbitrarily defined as long as we use it consistently.

The principle of smearing the invariant matrix element can be applied to any other type of scattering from deuterium, i.e. π -d, n-d, p-d, γ -d etc. For the reactions for which we

do not know the form of the invariant matrix element we we can obtain the matrix element from the measured cross sections. This can be done easily by multiplying the measured cross sections by the flux. The cross section for $\gamma + d \rightarrow W + \text{spectator}$ can be expressed in term of the cross sections for $\gamma + p \rightarrow W$ and $\gamma + n \rightarrow W$.

$$\sigma_{\gamma p}(W) = \frac{1}{\text{flux}} |M_{\gamma p}(W)|^2$$

where the invariant flux contains the initial state energy normalization. $\frac{1}{\text{flux}} = \frac{1}{v} = \frac{2M}{W^2 - M^2}$

Therefore

$$|M_{\gamma p}(W)|^2 = \sigma_{\gamma p}(W) \frac{W^2 - M^2}{2M}$$

Now we smear the matrix element to obtain $|M_{\gamma d}|^2$ and evaluate the cross section.

$$\text{EA16. } \sigma_{\gamma d} = \frac{1}{\text{flux}} |M_{\gamma d}|^2 = \int |\phi(\vec{p}_s)|^2 d^3\vec{p}_s \left[\frac{W^2 - M^2}{2Mv} \right] [\sigma_{\gamma p}(W) + \sigma_{\gamma n}(W)]$$

$(W^2 - M^2)/2Mv$ is usually given the misleading name of a flux correction. In fact it is just the factor that one obtains by taking out the flux from the neutron and proton cross sections and putting back the flux for the deuteron in order to form the deuteron cross section.

In the limit of $q^2 \rightarrow 0$ the virtual photon cross section σ_τ becomes the real photoabsorption cross section σ_γ . Therefore, our smearing expressions for e-d scattering should yield the photoproduction results in the $q^2 \rightarrow 0$ limit. We now show that our W correspondence prescription yields equation EA16 in the $q^2 \rightarrow 0$ limit.

$$\sigma_\tau = \frac{4\pi^2\alpha}{K} W_1, \quad K = \frac{W^2 - M^2}{2M}$$

$$\text{and} \quad \gamma W_2 = 0 \quad \text{as} \quad q^2 \rightarrow 0$$

For the deuteron $K = (W_d^2 - M_d^2)/2M_d = \gamma$ where W_d is the mass of the entire final state (i.e. n,p and all produced particles). Using the W_1 smearing (equation EA8) in the $q^2 \rightarrow 0$ limit we get :

$$\frac{\gamma \sigma_{\gamma d}}{4\pi^2\alpha} = \int |\phi(\vec{p}_s)|^2 d^3\vec{p}_s \left[\frac{W^2 - M^2}{2M} \right] \left[\frac{\sigma_{\gamma p}(W) + \sigma_{\gamma n}(W)}{4\pi^2\alpha} \right]$$

or

$$\sigma_{\gamma d} = \int |\phi(\vec{p}_s)|^2 d^3\vec{p}_s \left[\frac{W^2 - M^2}{2M\gamma} \right] \left[\sigma_{\gamma p}(W) + \sigma_{\gamma n}(W) \right]$$

which is just equation EA16.

It is difficult to know what the mixed variables prescription will yield for the photoproduction case. This is because the photoproduction cross sections are only a function of W.

However, we can factorize the photoproduction cross section into $A(W) F(q \cdot P)$ by making a correspondence with the Rittenberg and Rubinstein (44) fit in ω_R (See section 4.1). Using that particular factorization for the mixed variables prescription we get:

$$W1 = A(W) F(\omega_R), \quad \omega_R = \frac{2M\sqrt{q^2} + a^2}{q^2 + b^2}$$

and the corresponding off-shell $W1$ in the $q^2 \rightarrow 0$ limit

$$W1 = A(W) F(\sqrt{q^2})$$

$$W = - (P - q)^2, \quad \sqrt{q^2} = q \cdot P / M$$

In order to convert $W1$ to δ_t we have to know what K is for the off-shell case. In this mixed variables prescription we have an ambiguity as to whether it is $(W^2 - M^2)/2M$ or $\sqrt{q^2}$.

The above illustrates that only the W correspondence method yields an unambiguous prescription for all types of smearing. The mixed variables method involves guessing particular off-shell corrections for each process. Whatever off-shell correction we use in electroproduction will propagate into the photoproduction expression in the $q^2 \rightarrow 0$ limit, and therefore the mixed variable prescription will not yield equation EA16 in that limit. However, a detailed investigation of the smearing equation for δ_s in the $q^2 \rightarrow 0$ limit indicates that the mixed variable prescription does yield zero for δ_s for the deuteron as it should. On the other hand we must include off-shell corrections to the

W correspondence approach in order to get δ_s for the deuteron to vanish at $q^2 = 0$.

The W correspondence expressions in the $q^2 = 0$ limit are:

$$\text{EA17a.} \quad W_1^d(\nu) = \int |\phi(\vec{p}_s)|^2 d^3 \vec{p}_s (W_1^p(q^2, W) + W_1^n(q^2, W))$$

$$\text{EA17b.} \quad W_2^d(\nu) = \int |\phi(\vec{p}_s)|^2 d^3 \vec{p}_s \left(\frac{\nu''}{\nu}\right)^2 (W_2^p(q^2, W) + W_2^n(q^2, W))$$

In the $q^2 = 0$ limit W_2/q^2 is finite and δ_s for the deuteron is

$$\text{EA18.} \quad \delta_{sd} = \frac{4\pi^2\alpha}{\nu} \left[\frac{W_2^d}{q^2} \nu^2 - W_1^d \right]$$

Combining equations EA17a, EA17b and EA18 we get :

$$\text{EA19.} \quad \delta_{sd} = \frac{4\pi^2\alpha}{\nu} \int |\phi(\vec{p}_s)|^2 d^3 \vec{p}_s \left\{ \left[\frac{W_2^p(q^2, W)}{q^2} \nu''^2 - W_1^p(q^2, W) \right] + [\text{same for the neutron}] \right\} \neq 0$$

The reason that the above expression does not yield zero for δ_{sd} is because the on-shell structure functions that we have used do not vanish for that particular combination of off-shell variables. What we do have is

$$\text{EA20a.} \quad \delta_{sp} = \frac{4\pi^2\alpha}{\nu_w} \left[\frac{W_2^p(q^2, W)}{q^2} \nu_w^2 - W_1^p(q^2, W) \right] = 0$$

$$\text{EA20b.} \quad \delta_{sp} = \frac{4\pi^2\alpha}{\nu''} \left[\frac{W_2^p(q^2, \nu'')}{q^2} \nu''^2 - W_1^p(q^2, \nu'') \right] = 0$$

It is apparent that the simple W correspondence approach will not yield $\delta_{sd} = 0$ at $q^2 = 0$ as it should. There are three simple ways to remedy the problem.

A. Use the mixed variables approach.

B. Apply the following off-shell correction

$$\begin{aligned} W_2^P(q^2, W, \nu'') \text{ off-shell} &= \frac{\nu''^2}{\nu_W^2} W_2^P(q^2, W) \text{ on-shell} \\ W_1^P(q^2, W, \nu'') \text{ off-shell} &= W_1^P(q^2, W) \text{ on-shell} \end{aligned}$$

C. Use the following off-shell correction

$$\begin{aligned} W_2^P(q^2, W, \nu'') \text{ off-shell} &= W_2^P(q^2, W) \text{ on-shell} \\ W_1^P(q^2, W, \nu'') \text{ off-shell} &= \frac{\nu''^2}{\nu_W^2} W_1^P(q^2, W) \text{ on-shell} \end{aligned}$$

Also any definition which yields A or B or a linear combination of A and B in the $q^2 = 0$ limit will also work. Fortunately, the three possible off-shell corrections yield very close numerical answers. Using these off-shell corrections in the finite q^2 region, we find that when the smearing correction is 0.9 the off-shell corrections of B and C yield smearing corrections within 0.4% of the smearing correction predicted by the W correspondence approach. The mixed variables approach yields a smearing correction which is 1.6% smaller than 0.9 .

A6--Summary of possible indicators for the
magnitude of the theoretical error in the
smearing calculation

We present a summary of the indicators that we have used in order to estimate the theoretical uncertainties in the smearing formalism.

1. Use M/E_s or 1.0 in the integral. This will give an indication for the error that one makes in using an on-shell non-relativistic wave function.
2. Use different phenomenological deuteron wave functions satisfying all the known measured deuteron properties. This will give an indication of the error arising from the lack of detailed knowledge of the n-p potential.
3. Relativistic corrections due to the motion of the nucleons can be studied by putting $P = 0$, $P = P(\text{off-shell})$, and $P = P(\text{on-shell})$ in the tensor $W_{\mu\nu}^f$.
4. Off-mass-shell corrections to the structure functions can be estimated by looking at the differences in the smearing

correction arising from making different correspondences to the on-shell structure functions (See text).

Investigations of the equations in the $q^2 \rightarrow \infty$ scaling limit and in the $q^2 \rightarrow 0$ photoproduction limit provided helpful hints as to what correspondences to make.

5. The flux correction can be viewed as some sort of measure of the error in the procedure of the impulse approximation.

A7--Theoretical considerations in smearing

We shall outline some of the theoretical considerations that we have used in order to resolve some of the ambiguities in the smearing formalism. All have been discussed in detail in previous sections. This section will serve as a summary of those theoretical considerations.

1. Relativistic invariance was used to cast doubt on the validity of the flux correction.
2. Gauge invariance was used to get the form of the tensor that yielded the relativistic corrections due to the motion of the nucleons in the deuteron.
3. The predictions of the smearing expression for R_d .
Predictions for R for the deuteron can be compared with experimental measurements if one had some theoretical

predictions for R for the proton and R for the neutron.

Unfortunately, there are no reliable theories at the moment that predict those values with the needed certainty.

4. Investigations of the smearing in the infinite q^2 scaling limit. Does the theory give an expression that scales ? and what does it predict for R_d in that limit ?
5. Investigations of the smearing in the $q^2 \rightarrow 0$ photo-absorption limit. Is it consistent with a simple smearing of the photoabsorption cross sections. Is it consistent with δ_s , for the deuteron being zero and do the W_1 and W_2 equations give the same result for the δ_t smearing.
6. Is the theory self-consistent ? i.e. do we use off-shell matrix elements, but on-shell wave function normalization, or any other inconsistent terms.
7. Do the matrix elements that we use have the right behavior in the various simple limits? i.e. Do they give the elastic form factors when we apply the formalism to the case of quasielastic scattering. Do they vanish at the inelastic pion production threshold, do they yield bumps in the positions of the known resonances and do they have the proper expected behavior in the infinite q and zero q^2 limits?
8. Can the formalism be generalized to yield the smearing prescriptions for other deuteron reactions such as π^-d ,

γ -d, p-d, n-d etc. If it can then can those reactions be used to gain more understanding of smearing?

A8--Experimental tests of smearing

Most of the proposed tests for smearing are rather inconclusive due to the poor knowledge of competing effects. Others require a thorough analysis of other experimental data, which is a time consuming process(i.e. comparisons with quasielastic scattering). All possible tests are mentioned for the sake of completeness. Some of the tests have been carried out, but most of them were not. Given also is a description of the difficulties that accompany each test and a statement as to its usefulness.

1. Experiments where the spectator nucleon is detected. For example $e + d \rightarrow e + p + n$, or $n + d \rightarrow n + p + n$. Since the spectator's momentum is measured, one can directly compare the measured momentum distribution with the predictions of different phenomenological wave functions. One can then answer questions about high momentum components. Bubble chamber experiments tend to suggest agreement of 10 % with current wave functions. The difficulty in this type of measurement is in taking

out the W, q^2 dependence of the matrix elements, final state interaction effects, and effects due to the interference between the neutron and the proton, all of which affect the final momentum distribution.

Corrections to the matrix element due to the relativistic effects stemming from the motion of the nucleons can be large, as can be seen from the magnitude of the tensorial corrections in the present calculation. Also there is the obvious difficulty in the determination of which was the spectator and which was the interacting nucleon.

2. Measure a very small ω point in inelastic e-p and e-d scattering. Since the smearing corrections become larger and larger for smaller ω a theory which predicts too large a smearing correction can be rejected on the grounds that the resulting extracted neutron cross section will be negative. One gets such a result when one takes the on-shell theory and views the structure functions as functions of the initial on-shell ω with no regard to final state energy conservation. This pathology disappears when one views the structure functions as functions of the final state W .
3. West suggests the measurement of high- q^2 deuterium cross sections in the region of ω between 1/2 and 1. He derives a sum rule relating the integrated cross section

in that region to the total depletion for $\omega > 1$.

Unfortunately, the check of that sum rule is extremely difficult for several reasons. One needs to subtract the quasielastic peak from the measured data. the uncertainties in the quasielastic peak are the same as the uncertainties in the smearing. Also in that region the errors due to the radiative corrections are not insignificant. Even when one does subtract the quasielastic peak, one is left with a zero cross section with large error bars. The experimental value of the integral of the cross section for ω between of 1/2 and 1 is zero with large errors.

4. One can look at the smearing of resonances in the deuteron and see if one can smear the proton resonances and reproduce the shapes. The only thing known about the neutron resonances is that the first neutron resonance (1236) has about the same magnitude as the first proton resonance. Uncertainties in the neutron background under the first resonance make the test difficult. Subtraction of the quasielastic peak will introduce additional errors.
5. Scaling in the deuteron. Since the deuteron scales in ω a non-scaling smearing theory is suspect. As it turns out, numerical computations of the off-shell smearing correction show that the smearing correction is a

function of ω' to 1.5 %.

6. A detailed analysis of a measured quasielastic peak.

One can investigate predictions versus measurements for the peak position, amplitude and shape. investigation of the tail will yield valuable information as the calculated tail is sensitive to the smearing procedure. Unfortunately there are other complications in the region of the tail. The low E' side of the tail is obscured by pion production processes and n-p final state interaction, while on the high E' side we have complications due to the final state interaction and the deuterium elastic tail. Uncertainties in the radiative corrections will introduce errors in the radiatively corrected quasielastic peak. The elastic deuterium tail can be calculated using measured or extrapolated form factors, while the final state interaction and meson current corrections might be approximately be calculated using formalisms by Renard(64) or Durand McGee(22,65). Lack of knowledge about the neutron electric and magnetic elastic form factors and the off-shell corrections to the proton and neutron elastic form factors will also complicate this smearing test. It is apparent that the uncertainties are large, but a detailed study of a quasielastic peak is valuable in itself aside from the

question of smearing. A comparison between a measured raw quasielastic peak and the radiatively degraded spectrum obtained from the off-shell smearing formalism is done in ref. 27. The comparison does not include a detailed study of the tail region and does not remove any effects due to the competing processes that we have mentioned. Other quasielastic peak studies and a list of references to other such studies is found in Ref.

20,24,66.

7. Deuterium elastic peak measurements can be used to reject wave functions with unrealistic high momentum components.
8. Quasielastic e-d experiments with the spectator momentum distribution measured can be used to estimate the off-shell behavior of matrix elements using the Chew-Low extrapolation method and choosing a reasonable wave function for the momentum distribution. Probably this test can only serve as a consistency check.
9. γ, p and γ, d measured photoabsorption cross sections can be compared with the $q^2 \rightarrow 0$ limit calculation of our smearing procedure. Difficulties are : Lack of knowledge about the neutron cross section, a large Glauber (shadowing) correction that has to be calculated using a vector dominance model, and the lack of sensitivity of the γ, d cross section to the smearing correction (the correction is only 1% to 2% (27)).

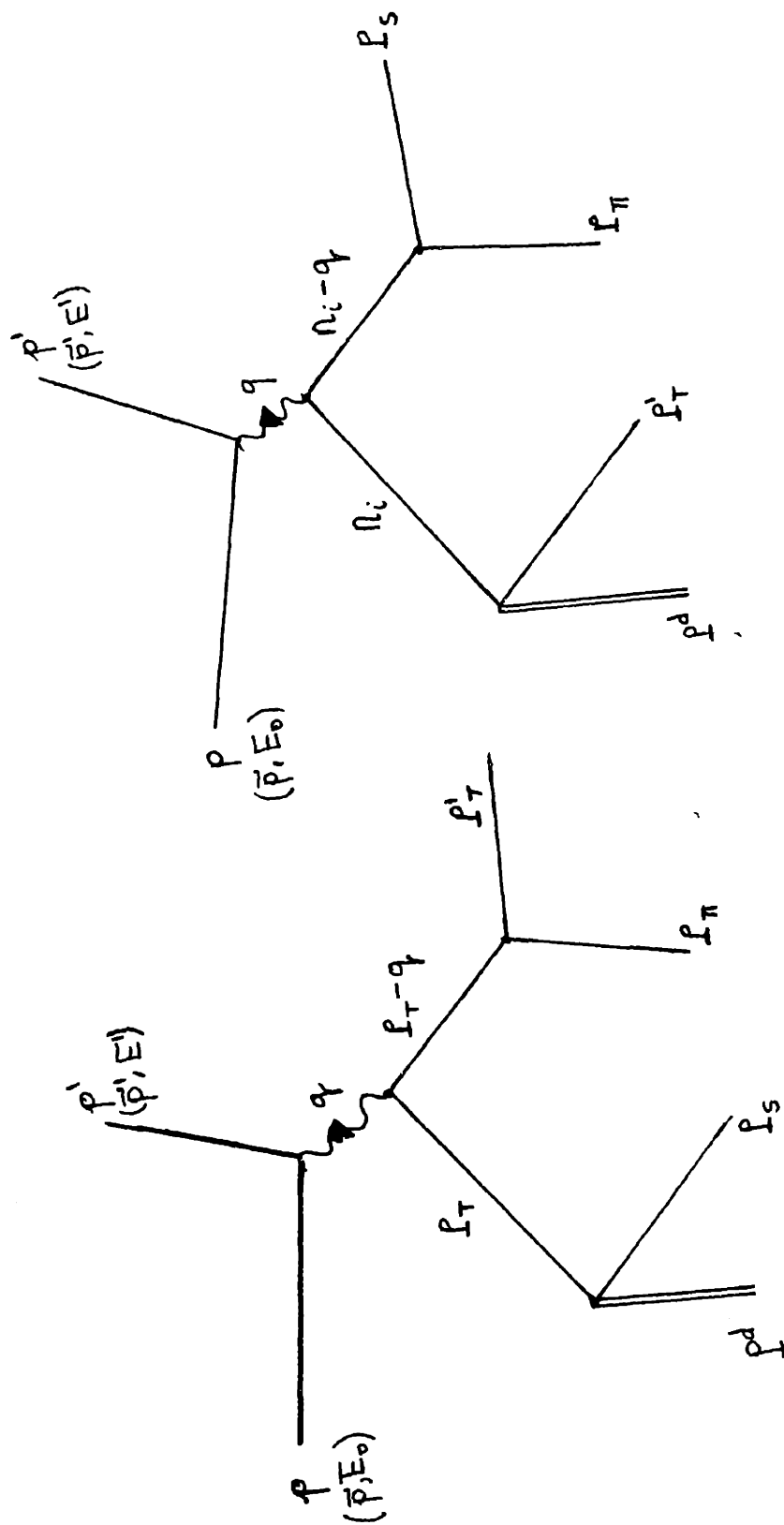


Figure A5. Interference diagrams in single pion production

A9 -- Corrections to the impulse approximation

In previous sections we have derived expressions relating the deuterium structure functions to the nucleon structure functions assuming the impulse approximation to be correct. We shall devote this section to the calculation of numerical estimates for possible corrections to the impulse approximation and establish that those corrections are indeed small.

1. Interference terms. L. Durand(22) derives an expression for the interference term between the amplitudes for scattering from the proton and the neutron in the case of quasielastic scattering. This term is completely negligible for quasi- elastic scattering at SLAC energies, and amounts to a correction of one part in 10^5 for q^2 between 1 and 5 $(\text{Gev}/c)^2$. We cannot calculate it exactly for the case of inelastic scattering since the matrix elements are not known, but we can estimate the magnitude and show that it is small. For the case of single pion electroproduction, when the particles in the final state are a pion, a neutron and a proton we have interference diagrams as shown in fig A5. This interference is due to the fact that we cannot tell which particle was the spectator. The interference term IT

goes like

$$IT \cong \int \phi(\vec{P}_S) \phi^*(-\vec{P}_S - \vec{q} - \vec{P}_\pi) \frac{d^3 \vec{P}_\pi}{E_\pi} \frac{d^3 \vec{P}_S}{E_S} T(\vec{P}_S, \vec{P}_\pi) T(-\vec{P}_S - \vec{q} - \vec{P}_\pi, \vec{P}_\pi)$$

where $T(P1, P2)$ is the amplitude for the scattering from a nucleon with initial momentum $P1$ and producing a pion of momentum $P2$. If we assume that the average momentum taken by the pion is small (in comparison to \vec{q}), and if we neglect the variation of the matrix elements with $P1$ and $P2$, and set $\phi(\vec{P}_S) = \phi(-\vec{P}_S)$ (true to within a constant phase), we get (extending the limits of integration over all P_S since almost all P_S contribute):

$$IT \cong T^2 \int \frac{d^3 \vec{P}_S}{E_S} \phi(\vec{P}_S) \phi(\vec{P}_S + \vec{q}) = T^2 F_d^2(\vec{q})$$

The fractional contribution of the interference term is IT/T^2 which is $F_d^2(\vec{q})$, where $F_d^2(\vec{q})$ is the wave function part of the deuteron form factor which is very small at high q^2 . F_d is about 2×10^{-4} at a q^2 of 1.3 (GeV/c)^2 , and smaller for higher q^2 .

2. Coherent particle electroproduction from deuterium. The only allowed particle production is the production of particles whose total final charge is zero. We get a good estimate of the relative magnitude of the coherent and incoherent cross sections by

$$\sigma_c/\sigma_i = F_d^2(\vec{q}) \cdot f$$

where f is the non-charge exchange fraction of the nucleon cross section and is always less than one. σ_c is

the coherent cross section and σ_i is the incoherent inelastic cross section from deuterium. As mentioned in the previous paragraph σ_d is very small.

3. Final state interaction. For the case of quasielastic scattering at low q^2 we can use the Renard(64) or the Durand-McGee (22,65) formalisms to calculate the final state interaction. It is usually 3% to 5% for q^2 less than 1 (gev/C)^2 . We cannot assume that this percentage is also true for the inelastic case since the final states are completely different. The final state interaction becomes important only when the relative momentum between the outgoing final particles is small. We expect the relative momentum of the final state particles to be large in our case where we have large momentum and energy transfers. Also since there are many more channels in the inelastic case the phases of the amplitudes might cancel and the final state interaction will be smaller than the one for the quasielastic case.
4. Meson currents in the deuteron. These are corrections that from the fact that the deuteron can exist as a bound state consisting of two nucleons and a pion, a nucleon and a nucleon resonance etc. When the deuteron exists in those virtual states the scattering can occur off the pion or the nucleon resonance. Since charged pions can be

exchanged, these meson corrections can account for a deuteron cross section which will be larger than the sum of the unbound proton and neutron cross sections. We know that corrections due to meson currents are small for elastic (19) and quasielastic e-d scattering (66).

However, the final state phase space is restricted for elastic and quasielastic reactions since there are no mesons or nuclear resonances in the final state. If the scattering is from a pion which is being exchanged then most likely there will be an unbound pion in the final state. For the case of elastic and quasielastic reactions the pion has to be reabsorbed by a final state nucleon. For inelastic scattering there are no restrictions on the final state and corrections due to the meson effects can be large. Also, since the scattering is off-point-like particles we might expect it to scale just like the proton cross section. Therefore it is difficult to separate such effects. As we mentioned earlier the scattering from an exchanged meson will only increase the inelastic cross section from deuterium. Presently, this is the only statement we can make about those effects and therefore we can only say that the extracted neutron cross section we get is probably higher than the true free neutron cross section. In fact, what we actually

measure is a neutron cross section which at small ω is smaller than what current theoretical models are predicting.

5. Glauber correction. This correction is due to the shadowing of one nucleon by the other inside the deuteron. It is a very important correction in strong interaction scattering processes off the deuteron. Since this correction is a double scattering correction we can say that it is a correction of the order of $\alpha = 1/137$ or less than one percent. We shall devote the next section to numerical estimates of the Glauber correction and show that it is actually much smaller and is on the order of one part in 10^4 . The Glauber correction was not incorporated into the smearing formalism since it is so small.
6. High momentum components. It is possible that the probability for the nucleons in the deuteron to have high momenta is higher than what is predicted by the conventionally used non-relativistic phenomenological wave functions. We found that wave functions consistent with all current experimental deuteron measurements yielded smearing corrections which differed by less than one percent when the smearing correction was 0.9. The most sensitive criterion for the testing of the validity

of the wave function is in comparisons with experimental elastic deuteron form factors. The Hulthén hard core wave function (31) whose predictions for the elastic deuteron form factors compare poorly with experimental measurements(19) yields a smearing correction which deviates by 1.7 % from the predictions of the other wave functions (when the smearing correction was 0.9). Those high momentum components are directly related to possible off-shell corrections to the non-relativistic wave functions. J. Vary(30) has been investigating the possible effects of these off-shell corrections. He has been varying the small distance properties of the deuteron wave functions in a manner consistent with all other deuteron measurements. Preliminary results of his work appear to indicate that the high momentum components might be higher than expected. This would result in a large change (1%-6%) in the smearing correction. We shall have to wait for further work in order to fully understand the significance of the high momentum components. We can mention that the existence of a large contribution of high momentum components will result in an extracted neutron cross section which is smaller than the one obtained using conventional wave functions. In fact, if the magnitude of the high momentum component is

large, the extracted neutron cross section becomes negative. Therefore, small ω inelastic e-d scattering can be used to place a limit on the magnitude of the high momentum components of the deuteron wave function.

A10 The Glauber Correction in Electroproduction

In this section we will show that in high q^2 electron scattering the effects of the shadowing in the deuteron of one nucleon by the other are very small. This shadowing correction is important in hadronic processes and was first derived by Glauber (67). Since we will only need order of magnitude estimates, we will not go into the complete quantum mechanical calculations, but rather use some semi-classical approximations. We first derive the standard expression for the Glauber correction using a semi-classical argument. The neutron revolves around the proton in a sphere of mean radius R . If the total cross section for the scattering from the neutron is of area σ_n , then the fractional time that the neutron shadows the proton is the ratio of its area to the area of a sphere of radius R . This ratio is just $\sigma_n/(4\pi R^2)$. Quantum mechanically we replace R^{-2} by the expectation value $\langle r^{-2} \rangle$, and obtain the well known expression for σ_d .

$$\sigma_d = \sigma_p + \sigma_n + \sigma_p \cdot \sigma_n \langle r^{-2} \rangle / 4\pi$$

The last term in the above expression is normally called the

Glauber correction (67). The Glauber inverse square radius $\langle r^{-2} \rangle$ is approximately independent of the process involved and approximately independent of energy(27). Quantum mechanical calculations yield $\langle r^{-2} \rangle = 0.022$ (millibarns) , which corresponds to a classical radius of 0.7 Fermi (1.4 Fermi internucleon separation).

This correction can only be applied to total cross cross sections. Our differential e-p cross sections can be expressed in terms of total cross sections for the absorption of virtual photons. Using the above value for the inverse square radius of the deuteron we obtain the fractional Glauber correction as

$$\text{EA21.} \quad \text{GC} = 1.75 \cdot 10^{-6} \delta$$

where δ is in microbarns. We now present a few representative values for δ_s and δ_t . We also evaluate the Glauber correction using $\delta \approx \delta_s + \delta_t$ in equation EA21.

W^2	q^2	ω	δ_s (ub)	δ_t (ub)	GC
4	1.5	3.66	5	35	7.00×10^{-5}
4	4	2.0	1	9	1.75×10^{-5}
4	8	1.5	0.4	2.4	3.1×10^{-6}
10	1.5	7.66	1.0	30	5.4×10^{-5}
10	4	3.5	1.5	10	2.0×10^{-5}
10	8	2.25	0.5	4.0	7.9×10^{-6}

One might challenge the above estimates on the basis of a vector dominance model. In the case where the virtual photon can interact as a hadron the cross section σ in equation EA21 is then a large hadronic cross section and the Glauber correction is large. In that model the observed cross section is small due to the small coupling constant between the virtual photon and the vector meson. However, a simple vector dominance model would predict a large shadowing in high A nuclei. This is in contradiction with the experimental results of Reference 39, where no shadowing was observed in inelastic electron scattering from high A nuclei.

Another type of Glauber correction is a double inelastic scattering by the incident electron. This is a two photon exchange mechanism. The electron scatters inelastically from the proton, loses energy, and then scatters from the neutron with a lower incident energy. The first scattering can have a large cross section since a pion can be produced via the electron scattering at a small angle and at low q^2 . This double scattering process will yield a correction which is similar to a radiative type correction to the impulse approximation. Scattered electrons which would have normally been at the high E' small ω region, would be detected at a lower E' due to the additional energy

loss in the double scattering. Therefore, the threshold region would be depleted and the low E' region would have a higher cross section than the cross section calculated for the single scattering. We will now show that this correction is small.

In order to estimate this type of correction we need to know the cross section for an electron losing energy via the production of pions. We do not care about the electron scattering angle. We only care about the energy loss. The Weizacker-Williams method of virtual quanta is very well suited for this type of calculation. In the Weizacker-Williams calculation, an electron of energy E_0 scattering to a final energy E' is equivalent to an equivalent number of photons N_k of energy $k = E_0 - E'$ (Ref. 54 equation 19-37).

$$N_k dk = \frac{2\alpha}{\pi} \ln \left(\frac{E_0}{m_e k b_{\min}} \right) \frac{dk}{k}$$

where m_e is the electron mass and b_{\min} is the minimum impact parameter of the electron. Quantum mechanically b_{\min} is then of the order of the distance below which the electron cannot be defined according to the uncertainty principle, i.e. $b_{\min} = \hbar/\Delta P(\text{transverse})$. We will only want to show

that the double scattering is small. Therefore, we will use the upper limit for N which occurs when $b_{min} = \hbar/k$.

$$N_k dk = X_e \frac{dk}{k} \approx \frac{2\alpha}{\pi} \ln\left(\frac{E_0}{k}\right) \frac{dk}{k}$$

where X_e is the equivalent number of photons. In low energy electron scattering (500 MeV), X_e was measured and also calculated to be about 0.02 (60,61). In our case the incident energy is about 20 GeV. An upper limit for X_e is then

$$X_e = \frac{2\alpha}{\pi} \ln\left(\frac{20 \times 10^6}{0.5}\right) = 0.08$$

Therefore, the cross section for a 20 GeV electron losing energy $k = E_0 - E'$ is (upper limit)

$$\frac{d\sigma_e(E_0, E')}{dE'} = X_e \sigma_\gamma(k) \frac{1}{k}$$

where $\sigma_\gamma(k)$ is the photoproduction cross section. The photoproduction cross section is almost constant for $k > 2$ GeV and is equal to about 150 μb (68) (it reaches a maximum of 550 μb at the first 1236 resonance). What we want is the cross section for an electron to lose any amount of energy via an inelastic process. The minimum energy loss is obviously

the pion rest mass (0.14 GeV), and the maximum is E_0 .
So the cross section for an electron to lose any energy
greater than 0.14 GeV is

$$\sigma(E = 20 \text{ GeV}, E > 0.14 \text{ GeV}) = X_e \int \sigma(k) \frac{dk}{k} =$$

$$0.08120 \mu\text{b} \ln\left(\frac{20}{0.14}\right) = 64 \text{ ub}$$

Using 64 ub in the Glauber expression (EA21) we obtain
the fractional correction due to this particular
kind of shadowing to be 1.1×10^{-4} .

A11 Choice of a smearing procedure and error discussion

A correct and complete relativistic gauge invariant
theory of smearing is one utilizing a complete
off-mass-shell treatment of the dynamics of the deuteron.
Since a dynamic theory of the deuteron is not available one
must utilize phenomenological non-relativistic deuteron
wave functions. Therefore, the canonical smearing procedure
was chosen to be the West-Atwood off-shell approach, since
it utilizes a consistent off-shell approach. If one could
apply the off-shell corrections to the structure functions
and the off-mass-shell and relativistic corrections to the

non-relativistic deuteron wave function, the West off-shell theory would be complete. The off-shell structure function correspondence that was used was an average between the W, q^2 correspondence and the W, q^2, ω mixed variable correspondence. The difference between those two choices for the off-mass-shell structure functions was taken to be the standard error in the smearing procedure. Larger upper and lower error limits for the smearing corrections due to theoretical uncertainties were obtained from the following two models. The complete on-shell approach served as the lower limit and the W, q^2 off shell theory with an M/E_s normalization for the wave function served as an upper limit for the large error band. The standard error band represents models which are felt to be self-consistent. The large error band represent models which have at least one inconsistency. The upper error limit model is inconsistent in using a complete off-shell approach with the on-shell M/E_s normalization for the wave functions. The lower error limit has the inconsistency of using on-shell tensorial terms with off-shell W, q^2 structure functions for energy conservation.

Table A1 shows the effects of the various terms on the correction when the correction is 0.916 at an ω of 1.267.

Figure A6 shows the fractional multiplicative correction to the $\delta n/\delta p$ ratio resulting from the several different choices for the smearing procedure. Included are the standard smearing error band and the larger limits due to the upper and lower limit smearing procedures.

summary

Procedure	Structure function correspondence	wave function normalization	tensorial terms
lower limit	W final state(W, q^2)	M/Es	on-shell
lower canonical	mixed variables(W, q^2, ω)	1.0	off-shell
canonical	average (W, q^2), (W, q, ω)	1.0	off-shell
upper canonical	W final state(W, q^2)	1.0	off-shell
upper limit	W final state (W, q^2)	M/Es	off-shell

The terminology used in table A1 is the one used in the text. The Hulthén H.C. refers to the Hulthén hard core wave function(31) (core at 0.432 Fermis), The Reid H.C. and S.C. refer to the Bethe-Reid(33) hard and soft core wave functions. The Hamada-Johns. stands for the Hamada-Johnston wave function (18), and the Feshbach-Lmn. stands for the Feshbach-Lomon wave functions(32). Vary 1 and Vary 2 denote wave functions with high momentum components obtained from the preliminary work of J. Vary(30). The vectorial flux is the flux defined as the inverse of the absolute value of the vectorial difference between the velocities of the electron and the target nucleon. The invariant flux is the inverse of the absolute value of the difference in the projected velocities along the axis of the incident electron's direction.

The propagated error in $\delta n/\delta p$ due to the uncertainty in the smearing correction is displayed in figure A6. The error is expressed as a ratio of $\delta n/\delta p$ extracted using various smearing models to $\delta n/\delta p$ extracted using the canonical smearing correction. The actual smearing corrections calculated using the various choices defined in this section are shown in table A2.

Table A1
Effects of various choices on the smearing correction

All effects were tested at $E_0 = 20$ GeV, $\theta = 19^\circ$, $\omega = 1.267$

upper canonical smearing corrections are $W1p/W1ps = 0.916$
 $W2p/W2ps = 0.916$

See text for notation and indentification of wave functions

effect	choice	changes (from reference case)		
		W1p/W1ps	W2p/W2ps	b _p /b _{ps}
tensorial corrections	none (P=0)	-.001	+.062	+.047
	P off-shell †	0.00	0.00	0.00
	P on-shell	.00	-.068	-.049
wave function normalization	M/Es	+.016	+.016	+.016
	1.0 †	0.00	0.00	0.00
Structure function	W, q ² †	0.00	0.00	0.00
	W, q ² , ω	-.016	.012	-.013
wave function chosen	Hulthén H.C.	+.017	+.017	+.017
	Reid H.C.	-.002	-.002	-.002
	Reid S.C.	+.006	+.006	+.006
	Hamada-Johns.†	0.00	0.00	0.00
	Feshbach-Lmn.	+.007	+.007	+.007
	Vary 1	-.010	-.010	-.010
	Vary 2	-.060	-.060	-.060
Flux	Vectorial invariant			+.035
				+.037

† Reference case

Table A2

Representative Smearing Corrections

E = 19 GeV

$\theta = 20$ Degrees

X	Upper Canonical	Lower Canonical	Upper Limit	Lower Limit
0.9500	0.35603	0.33242	0.37614	0.32524
0.9250	0.50244	0.47714	0.52454	0.46768
0.9000	0.62517	0.60092	0.64712	0.59001
0.8750	0.72271	0.70071	0.74351	0.68896
0.8500	0.79812	0.77870	0.81745	0.76649
0.8250	0.85569	0.83874	0.87354	0.82631
0.8000	0.89945	0.88472	0.91598	0.87219
0.7750	0.93274	0.91993	0.94811	0.90737
0.7500	0.95805	0.94690	0.97246	0.93435
0.7250	0.97734	0.96759	0.99092	0.95508
0.7000	0.99201	0.98347	1.00492	0.97101
0.6750	1.00315	0.99564	1.01548	0.98324
0.6500	1.01154	1.00493	1.02341	0.99262
0.6250	1.01781	1.01198	1.02929	0.99976
0.6000	1.02242	1.01726	1.03357	1.00515
0.5750	1.02571	1.02114	1.03659	1.00917
0.5500	1.02796	1.02391	1.03861	1.01211
0.5250	1.02939	1.02580	1.03986	1.01419
0.5000	1.03016	1.02698	1.04048	1.01559
0.4750	1.03041	1.02759	1.04062	1.01645
0.4500	1.03025	1.02774	1.04036	1.01690
0.4250	1.02975	1.02752	1.03980	1.01702
0.4000	1.02900	1.02702	1.03899	1.01691
0.3750	1.02805	1.02628	1.03801	1.01661
0.3500	1.02694	1.02537	1.03689	1.01620
0.3250	1.02573	1.02433	1.03568	1.01572
0.3000	1.02445	1.02318	1.03441	1.01522
0.2750	1.02312	1.02198	1.03311	1.01475
0.2500	1.02179	1.02075	1.03182	1.01434
0.2250	1.02049	1.01952	1.03055	1.01405
0.2000	1.01923	1.01833	1.02935	1.01391
0.1750	1.01806	1.01720	1.02824	1.01398

The canonical smearing correction was chosen to be the average between the upper canonical and lower canonical models. The corrections quoted above do not average over the spectrometer acceptance.

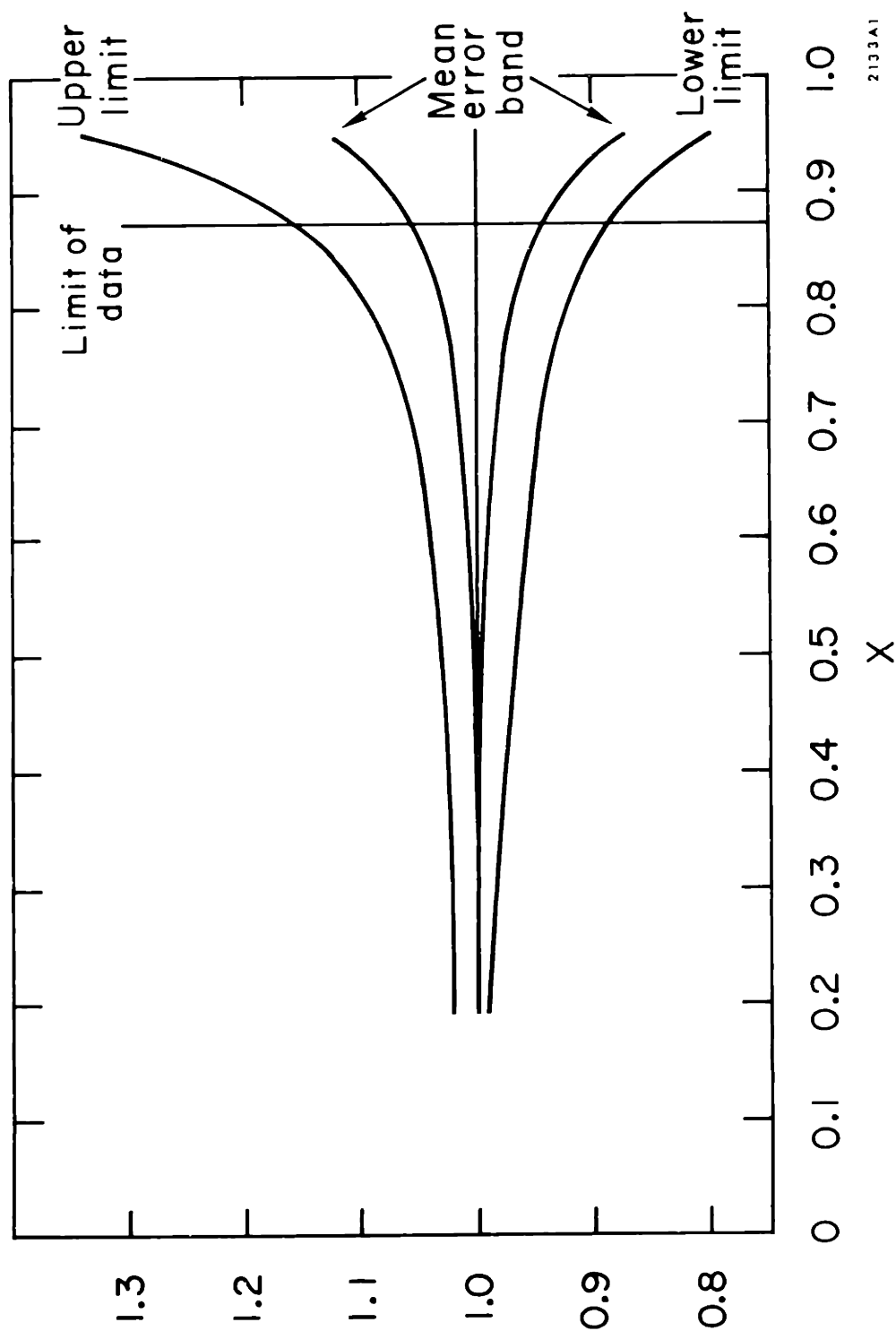


Figure A6 : The Error Band in on/op due to the Uncertainty in the Smearing Correction. It is expressed as the ratio of on/op extracted using various smearing models to on/op extracted using the canonical smearing procedure.

2133A1

A12 Summary

We have discussed the various ambiguities and possible corrections to the smearing procedure. The current state of affairs is such that the uncertainties resulting from the ambiguities in the form^a _{λ} ism are less than the statistical and systematic experimental errors. The uncertainties in the smearing become the dominant errors at very small ω (see figure A6). Therefore, for smaller ω experiments, more studies are needed in order to reduce the errors in the extracted neutron cross sections due to the smearing.

Appendix B. The Nucleon Elastic Form Factors

The knowledge of the neutron and proton elastic form factors was needed in order to calculate the hydrogen elastic and deuterium elastic and quasielastic radiative tails.

The following expressions were used :

$$G_{en} = 0.0 \quad G_{ep} = G_{mn}/\mu_n = G_{mp}/\mu_p$$

$$G_{ep} = \sqrt{F} / (1 + q^2/0.71)^2$$

where G_{en} and G_{mn} are the electric and magnetic elastic form factors of the neutron and G_{ep} and G_{mp} are the electric and magnetic elastic form factors of the proton. μ_n and μ_p are the static magnetic dipole moments of the neutron and the proton in units of $e\hbar/2Mc$. q^2 is in $(\text{GeV}/c)^2$.

F is a modulating function which varies about the value of 1.0 and is a fit by G. Miller to all SLAC data (2,23,48).

$$F = \sum_{i=1}^6 R_i \prod_{\substack{j=1 \\ j \neq i}}^6 \frac{q - (j-i)}{i-j} \quad q = \sqrt{q^2}$$

$$R_i = /1.000, 1.018, 1.056, 0.836, 0.687, 0.673/$$

The function F versus q is shown in figure B1.

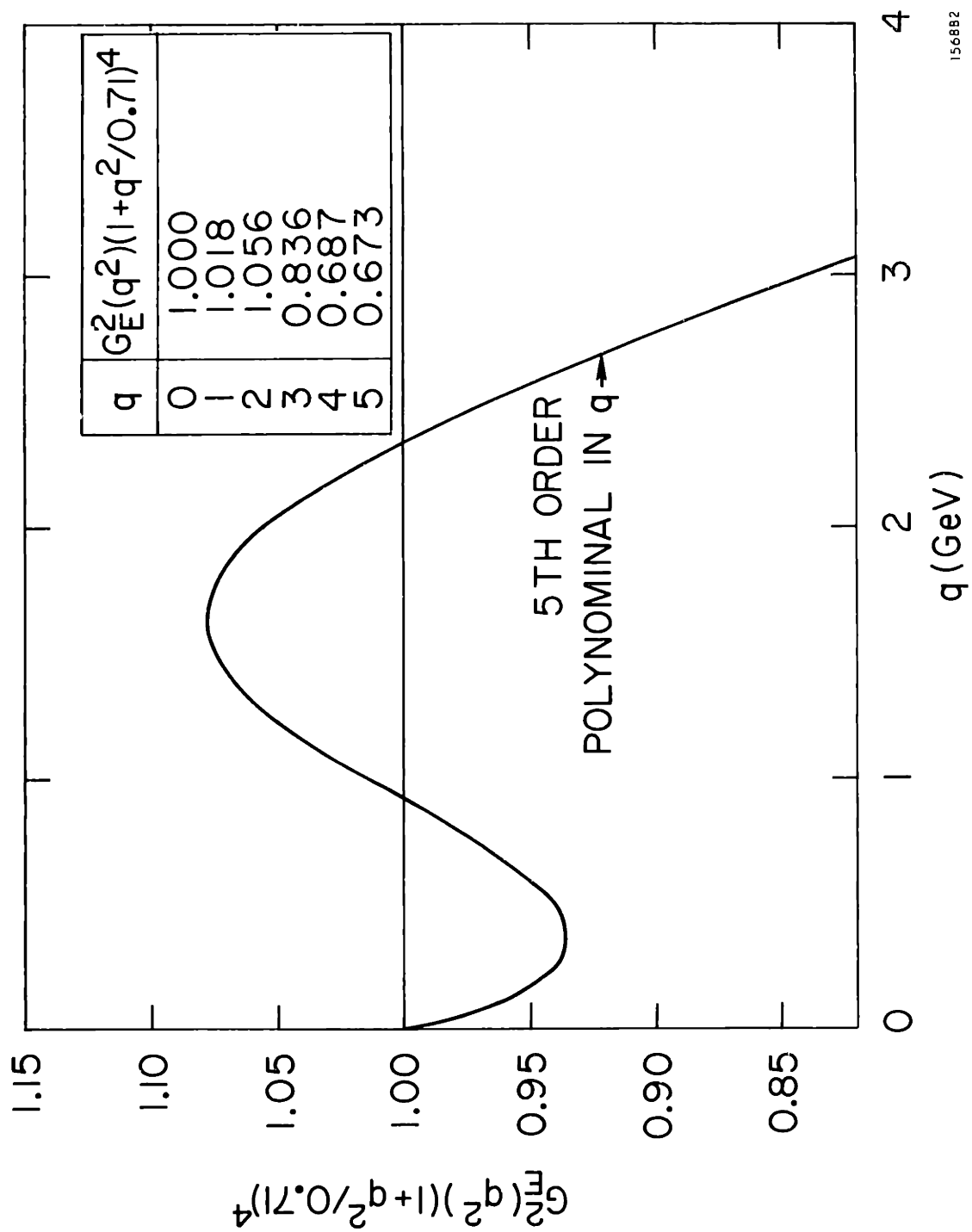


Figure B1 : The Proton Form Factors vs. q

1568B2

Appendix C. Calculation of the Number of Pulses

The effective number of non-zero charge pulses is needed for the purpose of calculating dead time and rate dependent corrections. We will derive the expression for the total number of effective pulses N by making use of the charge per pulse information. We will take as an example the calculation of the theoretical dead time correction of the C1 coincidence circuit (Front trigger (FT) x Rear trigger (RT)). Upper case will denote the total counts or charge for a given run, while lower case letters will denote the quantities for a given pulse. Q is the charge, W is the pulse width, τ is the trigger counter resolving time, X is the cross section for singles (FT) and Y is the cross section for C1 coincidences. An M denotes a measured quantity and a T denotes the true quantity.

$$FT = Q X \quad C1T = Q Y$$

The calculation is only carried to first order in τ . We assume a hypothetical case where the dead time is only due to one front trigger counter.

$$\begin{aligned} C1T &= \sum c1t_i = \sum c1m_i (1 + \tau ft_i / w_i) = \\ &= \sum c1m_i (1 + \tau X q_i / w_i) = \\ &= C1M + \tau X Y \sum q_i^2 / w_i \\ C1T &= C1M + \tau (FT/Q) (C1M/Q) \sum q_i^2 / w_i \\ &= C1M (1 + \tau FT (\sum (q_i^2 / w_i) / Q^2) \end{aligned}$$

assume that for a given run the pulse width is a constant

$$C1T = C1M (1 + FT \cdot \tau / (W \cdot N)) \quad , \quad w_i = W$$

where
$$N = Q^2 / \sum q_i^2$$

Since we have the charge per pulse histogram for all pulses we can form the sum of the squares and calculate N. We now show that even if we do not have the charge per pulse histogram for all pulses, we can calculate N using the charge per pulse obtained from the event information. Having the charge per pulse for each event is equivalent to having a charge per pulse histogram weighted by the charge per pulse. let σ be the cross section and $E = \sigma Q$ be the number of events. We then form the following ratio :

$$\begin{aligned} 1/N &= \sum q_i e_i / (Q \sum e_i) = \sum q_i^2 \sigma / (Q \sigma \sum q_i) \\ &= \sum q_i^2 / Q^2 \end{aligned}$$

The pulse width w varies during a run. We can use false circuits to obtain rates which take this variation into account. For example, the scaler information from C1F (FTx RT delayed) can be used to obtain an average front trigger per pulse rate.

$$C1F = (FT \times RT \times \tau) / (1500 \times N) \longrightarrow FT/N = 1500 \times C1F \times RT / \tau$$

where τ is the resolving time, N is the effective number of 1500 nanosecond long pulses, C1F, FT and RT are the scaler outputs of the false, front, and rear trigger counter circuits for a given run.

Appendix D. Final Cross sections and σ_n/σ_p Ratios.

D1 Introduction

The cross sections are only quoted for the points for which W was greater than 2.0 GeV. The 6 and 10 degree data which were included in order to increase the range of the data to smaller X is from the Ph.D. thesis of J.S. Poucher(13).

We will present the cross sections for hydrogen and deuterium in section D2. The cross sections and their errors are in picobarns/sr-GeV. The neutron to proton ratios for each of the data points are in section D3. Also given are the smearing correction S_p , the unsmearing correction U , and the acceptance averaging correction C . An explanation of how these corrections are applied can be found in section 3.10 . The only data shown are the subsets of data defined by $W > 2$ GeV, $q^2 > 1 \text{ (GeV/c)}^2$ and $E' > 2.49$ GeV. A few points for $q^2 > 10 \text{ (GeV/c)}^2$ and for which W was between 1.8 and 2.0 GeV are also shown. The combined data points for the σ_n/σ_p ratio and the combined data for the neutron to proton structure function differences are given in section D3. The data are the same data that are shown in figures 11-15,17-20, given in tabular form.

D2. Hydrogen and Deuterium Cross Sections

E0 = 6.509 , THETA = 18.020

¹ H	¹ H	⁺ -	error	² D	⁺ -	error	C
2.002	0.190E 05	C5	0.459E 03	0.299E 05	0.467E 03	0.996	
2.073	0.191E 05	C5	0.460E 03	0.313E 05	0.461E 03	0.997	
2.142	0.205E 05	C5	0.510E 03	0.334E 05	0.530E 03	0.997	
2.212	0.216E 05	C5	0.542E 03	0.353E 05	0.540E 03	0.997	
2.302	0.218E 05	C5	0.564E 03	0.365E 05	0.654E 03	0.997	
2.357	0.218E 05	C5	0.561E 03	0.377E 05	0.625E 03	0.997	
2.432	0.238E 05	C5	0.594E 03	0.454E 05	0.192E 04	0.997	
2.512	0.245E 05	C5	0.615E 03	0.415E 05	0.706E 03	0.998	
2.610	0.229E 05	C5	0.681E 03	0.396E 05	0.819E 03	0.998	

E0 = 10.392 , THETA = 18.020

2.112	0.178E 04	C4	0.813E 02	0.264E 04	0.889E 02	0.990	
2.275	0.241E 04	C4	0.982E 02	0.353E 04	0.938E 02	0.992	
2.431	0.291E 04	C4	0.959E 02	0.432E 04	0.928E 02	0.994	
2.574	0.352E 04	C4	0.315E 02	0.544E 04	0.134E 03	0.995	
2.712	0.399E 04	C4	0.749E 02	0.645E 04	0.112E 03	0.996	
2.810	0.462E 04	C4	0.118E 03	0.697E 04	0.140E 03	0.996	
2.904	0.473E 04	C4	0.136E 03	0.733E 04	0.142E 03	0.996	
2.997	0.511E 04	C4	0.135E 03	0.834E 04	0.150E 03	0.997	
3.066	0.498E 04	C4	0.128E 03	0.839E 04	0.151E 03	0.997	
3.137	0.529E 04	C4	0.106E 03	0.884E 04	0.159E 03	0.997	
3.202	0.550E 04	C4	0.180E 03	0.944E 04	0.191E 03	0.997	
3.267	0.586E 04	C4	0.177E 03	0.982E 04	0.234E 03	0.997	
3.337	0.647E 04	C4	0.210E 03	0.104E 05	0.233E 03	0.997	
3.420	0.634E 04	C4	0.209E 03	0.109E 05	0.245E 03	0.997	
3.488	0.675E 04	C4	0.188E 03	0.114E 05	0.242E 03	0.998	
3.549	0.676E 04	C4	0.207E 03	0.119E 05	0.269E 03	0.998	
3.626	0.640E 04	C4	0.225E 03	0.113E 05	0.400E 03	0.998	

E0 = 12.518 , THETA = 18.020

2.451	0.103E 04	C4	0.352E 02	0.151E 04	0.320E 02	0.990	
3.002	0.212E 04	C4	0.800E 02	0.344E 04	0.797E 02	0.995	
3.402	0.296E 04	C4	0.130E 03	0.470E 04	0.132E 03	0.997	
3.753	0.367E 04	C4	0.161E 03	0.599E 04	0.899E 02	0.997	
3.903	0.381E 04	C4	0.180E 03	0.661E 04	0.213E 03	0.998	
4.003	0.426E 04	C4	0.215E 03	0.726E 04	0.245E 03	0.998	

-252-

EO = 13.320 , THETA = 18.020

W	F	+-	error	D	+-	error	C
2.277	0.553E	03	0.291E 02	0.728E	03	0.238E 02	0.984
2.603	0.917E	03	0.415E 02	0.146E	04	0.408E 02	0.991
2.752	0.109E	04	0.364E 02	0.173E	04	0.340E 02	0.992
2.893	0.134E	04	0.398E 02	0.204E	04	0.387E 02	0.994
3.027	0.156E	04	0.477E 02	0.250E	04	0.479E 02	0.995
3.156	0.188E	04	0.560E 02	0.284E	04	0.622E 02	0.995
3.280	0.196E	04	0.718E 02	0.329E	04	0.673E 02	0.996
3.399	0.245E	04	0.857E 02	0.357E	04	0.820E 02	0.996
3.503	0.240E	04	0.575E 02	0.383E	04	0.634E 02	0.997
3.625	0.264E	04	0.671E 02	0.430E	04	0.852E 02	0.997
3.703	0.279E	04	0.809E 02	0.445E	04	0.976E 02	0.997
3.763	0.266E	04	0.120E 03	0.459E	04	0.127E 03	0.997
3.838	0.296E	04	0.133E 03	0.525E	04	0.142E 03	0.997
3.903	0.343E	04	0.126E 03	0.545E	04	0.135E 03	0.997
4.005	0.321E	04	0.138E 03	0.570E	04	0.177E 03	0.997
4.073	0.356E	04	0.145E 03	0.556E	04	0.226E 03	0.998
4.143	0.309E	04	0.190E 03	0.642E	04	0.211E 03	0.998
4.183	0.400E	04	0.198E 03	0.648E	04	0.305E 03	0.998
4.233	0.334E	04	0.259E 03	0.677E	04	0.318E 03	0.998

EO = 17.027 , THETA = 18.020

2.111	0.648E	02	0.188E 01	0.967E	02	0.221E 01	0.957
2.496	0.149E	03	0.439E 01	0.216E	03	0.462E 01	0.978
2.829	0.275E	03	0.952E 01	0.407E	03	0.800E 01	0.987
3.127	0.431E	03	0.122E 02	0.675E	03	0.136E 02	0.991
3.399	0.626E	03	0.227E 02	0.934E	03	0.219E 02	0.994
3.527	0.745E	03	0.276E 02	0.108E	04	0.261E 02	0.994
3.650	0.795E	03	0.295E 02	0.131E	04	0.315E 02	0.995
3.722	0.852E	03	0.341E 02	0.141E	04	0.350E 02	0.995
3.885	0.978E	03	0.313E 02	0.158E	04	0.461E 02	0.996
3.998	0.106E	04	0.518E 02	0.181E	04	0.535E 02	0.996
4.107	0.123E	04	0.531E 02	0.203E	04	0.559E 02	0.997
4.214	0.139E	04	0.583E 02	0.231E	04	0.677E 02	0.997
4.318	0.148E	04	0.745E 02	0.248E	04	0.769E 02	0.997
4.419	0.167E	04	0.845E 02	0.275E	04	0.895E 02	0.997
4.519	0.164E	04	0.834E 02	0.276E	04	0.994E 02	0.997
4.583	0.176E	04	0.862E 02	0.317E	04	0.112E 03	0.997
4.653	0.188E	04	0.100E 03	0.312E	04	0.118E 03	0.997
4.711	0.203E	04	0.110E 03	0.343E	04	0.129E 03	0.998
4.804	0.183E	04	0.142E 03	0.356E	04	0.155E 03	0.998
4.895	0.218E	04	0.169E 03	0.370E	04	0.221E 03	0.998

-253-

E0 = 6.711 , THETA = 26.015

W	F	+-	error	B	+-	error	C
2.139	0.269E 04	0.991E 02	0.395E 04	0.914E 02	0.997		
2.320	0.344E 04	0.130E 03	0.539E 04	0.128E 03	0.997		

E0 = 8.713 , THETA = 26.015

2.116	0.585E 03	0.198E 02	0.834E 03	0.186E 02	0.993		
2.321	0.840E 03	0.282E 02	0.128E 04	0.273E 02	0.995		
2.510	0.117E 04	0.396E 02	0.182E 04	0.388E 02	0.996		
2.685	0.149E 04	0.529E 02	0.241E 04	0.526E 02	0.997		
2.849	0.188E 04	0.674E 02	0.303E 04	0.694E 02	0.998		

E0 = 11.900 , THETA = 26.015

1.980	0.571E 02	0.402E 01	0.830E 02	0.279E 01	0.978		
2.234	0.107E 03	0.564E 01	0.146E 03	0.549E 01	0.987		
2.461	0.175E 03	0.808E 01	0.261E 03	0.815E 01	0.991		
2.670	0.268E 03	0.126E 02	0.396E 03	0.137E 02	0.994		
2.864	0.384E 03	0.131E 02	0.550E 03	0.125E 02	0.995		
3.045	0.501E 03	0.188E 02	0.764E 03	0.180E 02	0.996		
3.217	0.606E 03	0.241E 02	0.996E 03	0.256E 02	0.997		
3.379	0.792E 03	0.333E 02	0.123E 04	0.343E 02	0.998		
3.534	0.898E 03	0.400E 02	0.155E 04	0.433E 02	0.998		

E0 = 15.022 , THETA = 26.015

1.799	0.565E 01	0.105E 01	0.107E 02	0.102E 01	0.944		
2.113	0.116E 02	0.220E 01	0.197E 02	0.195E 01	0.970		
2.387	0.341E 02	0.259E 01	0.451E 02	0.222E 01	0.982		
2.632	0.587E 02	0.329E 01	0.812E 02	0.305E 01	0.988		
2.856	0.916E 02	0.459E 01	0.128E 03	0.415E 01	0.991		
3.064	0.125E 03	0.617E 01	0.198E 03	0.651E 01	0.994		
3.258	0.188E 03	0.943E 01	0.280E 03	0.936E 01	0.995		
3.442	0.230E 03	0.127E 02	0.347E 03	0.955E 01	0.996		
3.616	0.294E 03	0.158E 02	0.483E 03	0.148E 02	0.997		
3.783	0.376E 03	0.196E 02	0.599E 03	0.202E 02	0.997		
3.942	0.453E 03	0.250E 02	0.737E 03	0.261E 02	0.998		
4.095	0.519E 03	0.277E 02	0.885E 03	0.359E 02	0.998		

-254-

E0 = 18.028 , THETA = 26.015

U	V	+-	error	D	+-	error	C
2.078	0.394E	01	0.591E 00	0.713E	01	0.612E 00	0.951
2.388	0.100E	02	0.128E 01	0.142E	02	0.106E 01	0.971
2.662	0.187E	02	0.170E 01	0.272E	02	0.139E 01	0.981
2.910	0.291E	02	0.223E 01	0.436E	02	0.202E 01	0.987
3.139	0.487E	02	0.345E 01	0.666E	02	0.293E 01	0.991
3.353	0.763E	02	0.452E 01	0.103E	03	0.386E 01	0.993
3.553	0.978E	02	0.578E 01	0.140E	03	0.514E 01	0.994
3.742	0.127E	03	0.825E 01	0.194E	03	0.791E 01	0.996
3.924	0.169E	03	0.800E 01	0.261E	03	0.983E 01	0.996
4.093	0.225E	03	0.110E 02	0.326E	03	0.123E 02	0.997
4.257	0.275E	03	0.173E 02	0.397E	03	0.150E 02	0.997
4.421	0.305E	03	0.214E 02	0.455E	03	0.206E 02	0.998
4.570	0.336E	03	0.277E 02	0.562E	03	0.304E 02	0.998

E0 = 7.912 , THETA = 34.009

2.066	0.216E	03	0.109E 02	0.344E	03	0.104E 02	0.994
-------	--------	----	-----------	--------	----	-----------	-------

E0 = 10.014 , THETA = 34.009

1.940	0.344E	02	0.545E 01	0.531E	02	0.523E 01	0.985
2.256	0.717E	02	0.846E 01	0.107E	03	0.782E 01	0.992
2.533	0.143E	03	0.138E 02	0.198E	03	0.979E 01	0.995

E0 = 12.518 , THETA = 34.009

2.087	0.775E	01	0.221E 01	0.187E	02	0.237E 01	0.981
2.428	0.316E	02	0.403E 01	0.476E	02	0.358E 01	0.990
2.726	0.615E	02	0.552E 01	0.893E	02	0.484E 01	0.994
2.996	0.107E	03	0.923E 01	0.153E	03	0.778E 01	0.996

E0 = 15.012 , THETA = 34.009

2.502	0.130E	02	0.199E 01	0.181E	02	0.187E 01	0.986
2.831	0.256E	02	0.270E 01	0.375E	02	0.246E 01	0.992
3.125	0.448E	02	0.381E 01	0.731E	02	0.395E 01	0.995
3.394	0.801E	02	0.739E 01	0.108E	03	0.672E 01	0.996

-255-

F0 = 13.549 , THETA = 5.988

W	I	+-	error	D	+-	error	C
2.523	0.346E 06	0.116E 05	0.631E 06	0.158E 05	1.000		
2.767	0.316E 06	0.110E 05	0.578E 06	0.150E 05	1.000		
3.017	0.259E 06	0.976E 04	0.515E 06	0.139E 05	1.000		
3.267	0.230E 06	0.688E 04	0.429E 06	0.140E 05	1.000		
3.514	0.210E 06	0.687E 04	0.417E 06	0.138E 05	1.000		

E0 = 16.075 , THETA = 5.988

2.530	0.214E 06	0.408E 04	0.366E 06	0.621E 04	1.000
2.774	0.198E 06	0.655E 04	0.360E 06	0.606E 04	1.000
3.023	0.172E 06	0.620E 04	0.331E 06	0.841E 04	1.000
3.271	0.164E 06	0.597E 04	0.304E 06	0.818E 04	1.000
3.519	0.145E 06	0.620E 04	0.277E 06	0.856E 04	1.000
3.767	0.134E 06	0.564E 04	0.263E 06	0.842E 04	1.000
4.018	0.129E 06	0.565E 04	0.247E 06	0.844E 04	1.000
4.215	0.114E 06	0.557E 04	0.228E 06	0.608E 04	1.000

E0 = 19.544 , THETA = 5.988

2.530	0.103E 06	0.313E 04	0.172E 06	0.405E 04	1.000
2.778	0.104E 06	0.329E 04	0.178E 06	0.429E 04	1.000
3.024	0.101E 06	0.339E 04	0.177E 06	0.459E 04	1.000
3.263	0.944E 05	0.345E 04	0.172E 06	0.465E 04	1.000
3.521	0.907E 05	0.348E 04	0.162E 06	0.458E 04	1.000
3.767	0.865E 05	0.347E 04	0.162E 06	0.467E 04	1.000
4.017	0.838E 05	0.272E 04	0.151E 06	0.421E 04	1.000
4.216	0.734E 05	0.322E 04	0.143E 06	0.473E 04	1.000
4.416	0.753E 05	0.330E 04	0.138E 06	0.494E 04	1.000
4.614	0.732E 05	0.349E 04	0.140E 06	0.520E 04	1.000
4.812	0.697E 05	0.379E 04	0.131E 06	0.548E 04	1.000
5.013	0.678E 05	0.437E 04	0.131E 06	0.622E 04	1.000
5.210	0.739E 05	0.510E 04	0.138E 06	0.620E 04	1.000

E0 = 9.022 , THETA = 10.000

2.509	0.115E 06	0.448E 04	0.181E 06	0.617E 04	1.000
3.009	0.927E 05	0.428E 04	0.153E 06	0.611E 04	1.000

EO = 10.998 , THETA = 10.000

W	F	+-	error	D	+-	error	C
2.512	0.599E	05	0.197E 04	0.945E	05	0.259E 04	1.000
2.762	0.597E	05	0.225E 04	0.971E	05	0.316E 04	1.000
3.012	0.554E	05	0.231E 04	0.946E	05	0.251E 04	1.000
3.261	0.523E	05	0.236E 04	0.880E	05	0.340E 04	1.000
3.510	0.486E	05	0.248E 04	0.902E	05	0.375E 04	1.000

FO = 13.545 , THETA = 10.000

2.516	0.260E	05	0.482E 03	0.394E	05	0.798E 03	1.000
2.765	0.278E	05	0.753E 03	0.439E	05	0.911E 03	1.000
3.015	0.286E	05	0.722E 03	0.460E	05	0.865E 03	1.000
3.262	0.303E	05	0.972E 03	0.483E	05	0.124E 04	1.000
3.513	0.281E	05	0.768E 03	0.478E	05	0.129E 04	1.000
3.760	0.284E	05	0.105E 04	0.487E	05	0.142E 04	1.000
4.011	0.291E	05	0.126E 04	0.509E	05	0.140E 04	1.000

EO = 15.204 , THETA = 10.000

2.520	0.155E	05	0.397E 03	0.230E	05	0.486E 03	1.000
2.772	0.170E	05	0.477E 03	0.266E	05	0.598E 03	1.000
3.018	0.192E	05	0.483E 03	0.301E	05	0.692E 03	1.000
3.267	0.197E	05	0.607E 03	0.314E	05	0.762E 03	1.000
3.515	0.201E	05	0.675E 03	0.337E	05	0.747E 03	1.000
3.765	0.211E	05	0.550E 03	0.344E	05	0.832E 03	1.000
4.014	0.205E	05	0.790E 03	0.353E	05	0.111E 04	1.000
4.214	0.211E	05	0.853E 03	0.349E	05	0.123E 04	1.000
4.412	0.209E	05	0.972E 03	0.375E	05	0.134E 04	1.000

EO = 17.706 , THETA = 10.000

2.525	0.649E	04	0.259E 03	0.991E	04	0.314E 03	1.000
2.769	0.855E	04	0.306E 03	0.128E	05	0.371E 03	1.000
3.021	0.960E	04	0.371E 03	0.156E	05	0.469E 03	1.000
3.269	0.106E	05	0.435E 03	0.182E	05	0.554E 03	1.000
3.518	0.113E	05	0.491E 03	0.199E	05	0.630E 03	1.000
3.764	0.120E	05	0.545E 03	0.209E	05	0.763E 03	1.000
4.015	0.123E	05	0.578E 03	0.226E	05	0.840E 03	1.000
4.213	0.126E	05	0.628E 03	0.226E	05	0.906E 03	1.000
4.413	0.130E	05	0.713E 03	0.246E	05	0.102E 04	1.000
4.614	0.136E	05	0.778E 03	0.258E	05	0.116E 04	1.000
4.811	0.157E	05	0.941E 03	0.248E	05	0.152E 04	1.000

EO = 19.350 , THETA = 10.000

W	P	+-	error	D	+-	error	C
2.524	0.388E 04	0.130E 03	0.587E 04	0.141E 03	1.000		
2.771	0.505E 04	0.175E 03	0.775E 04	0.195E 03	1.000		
3.021	0.628E 04	0.223E 03	0.983E 04	0.255E 03	1.000		
3.269	0.692E 04	0.281E 03	0.114E 05	0.309E 03	1.000		
3.514	0.805E 04	0.325E 03	0.132E 05	0.398E 03	1.000		
3.763	0.833E 04	0.359E 03	0.142E 05	0.449E 03	1.000		
4.015	0.904E 04	0.395E 03	0.158E 05	0.509E 03	1.000		
4.213	0.870E 04	0.422E 03	0.168E 05	0.576E 03	1.000		
4.415	0.979E 04	0.472E 03	0.197E 05	0.664E 03	1.000		
4.611	0.980E 04	0.501E 03	0.175E 05	0.689E 03	1.000		
4.811	0.923E 04	0.555E 03	0.199E 05	0.683E 03	1.000		
5.011	0.112E 05	0.548E 03	0.206E 05	0.777E 03	1.000		
5.213	0.114E 05	0.858E 03	0.230E 05	0.103E 04	1.000		

D3. Neutron and Proton cross section ratios

EO = 6.599 , THETA = 13.020

W	Ps/Ps	error	N/P	error	Sp	U
2.002	0.622	0.047	0.623	0.047	1.029	1.001
2.073	0.635	0.048	0.636	0.048	1.027	1.001
2.142	0.647	0.049	0.648	0.049	1.025	1.001
2.213	0.678	0.049	0.680	0.049	1.024	1.002
2.282	0.716	0.054	0.717	0.054	1.022	1.002
2.357	0.763	0.054	0.765	0.054	1.021	1.002
2.432	0.946	0.056	0.948	0.056	1.019	1.002
2.512	0.725	0.052	0.727	0.052	1.018	1.002
2.610	0.757	0.064	0.759	0.064	1.017	1.002

EO = 10.392 , THETA = 13.020

2.112	0.524	0.086	0.520	0.086	1.028	0.991
2.275	0.509	0.073	0.507	0.073	1.031	0.995
2.431	0.532	0.060	0.530	0.060	1.031	0.997
2.574	0.592	0.042	0.591	0.042	1.020	0.998
2.712	0.660	0.042	0.659	0.042	1.028	0.999
2.810	0.550	0.050	0.550	0.050	1.027	1.000
2.904	0.590	0.055	0.590	0.055	1.026	1.000
2.997	0.670	0.053	0.671	0.053	1.024	1.001
3.066	0.724	0.054	0.725	0.054	1.023	1.001
3.137	0.708	0.046	0.709	0.046	1.022	1.001
3.202	0.753	0.067	0.754	0.067	1.021	1.001
3.267	0.711	0.066	0.712	0.066	1.021	1.001
3.337	0.639	0.065	0.639	0.065	1.020	1.001
3.420	0.751	0.070	0.752	0.070	1.019	1.001
3.488	0.713	0.060	0.714	0.060	1.013	1.001
3.549	0.793	0.068	0.795	0.068	1.017	1.002
3.626	0.802	0.090	0.803	0.090	1.017	1.002

EO = 12.518 , THETA = 13.020

2.451	0.504	0.060	0.499	0.060	1.027	0.991
3.002	0.675	0.074	0.674	0.074	1.029	0.999
3.402	0.626	0.085	0.626	0.085	1.024	1.000
3.753	0.666	0.077	0.666	0.077	1.020	1.001
3.903	0.765	0.101	0.766	0.101	1.018	1.001
4.003	0.732	0.105	0.733	0.105	1.017	1.001

-259-

EO = 13.220 , THETA = 18.020

W	Rs/Ps	error	N/P	error	Sp	U
2.277	0.325	0.033	0.330	0.031	1.014	0.983
2.603	0.637	0.087	0.632	0.086	1.027	0.992
2.752	0.636	0.064	0.633	0.063	1.029	0.995
2.893	0.565	0.055	0.562	0.055	1.030	0.996
3.027	0.656	0.060	0.655	0.060	1.029	0.998
3.156	0.553	0.058	0.553	0.057	1.029	0.999
3.280	0.725	0.072	0.724	0.072	1.027	0.999
3.399	0.492	0.062	0.492	0.062	1.026	1.000
3.503	0.639	0.048	0.639	0.048	1.025	1.000
3.625	0.665	0.054	0.666	0.054	1.023	1.001
3.703	0.631	0.059	0.632	0.059	1.022	1.001
3.763	0.763	0.094	0.769	0.094	1.022	1.001
3.838	0.814	0.095	0.815	0.096	1.021	1.001
3.903	0.623	0.072	0.623	0.072	1.020	1.001
4.005	0.809	0.096	0.810	0.096	1.019	1.001
4.073	0.593	0.091	0.593	0.092	1.018	1.001
4.143	1.116	0.148	1.117	0.148	1.017	1.001
4.183	0.647	0.112	0.648	0.113	1.017	1.001
4.233	1.061	0.187	1.062	0.187	1.017	1.001

EO = 17.027 , THETA = 18.020

2.111	0.384	0.051	0.365	0.049	0.928	0.951
2.496	0.446	0.053	0.434	0.051	0.994	0.974
2.829	0.508	0.060	0.501	0.059	1.018	0.986
3.127	0.609	0.056	0.604	0.055	1.027	0.992
3.399	0.535	0.066	0.533	0.066	1.029	0.996
3.527	0.485	0.066	0.484	0.066	1.029	0.997
3.650	0.695	0.075	0.694	0.075	1.029	0.998
3.722	0.629	0.074	0.629	0.074	1.028	0.999
3.885	0.655	0.072	0.655	0.072	1.027	0.999
3.998	0.742	0.099	0.742	0.099	1.026	1.000
4.107	0.690	0.086	0.690	0.086	1.025	1.000
4.214	0.701	0.087	0.701	0.087	1.023	1.000
4.318	0.705	0.101	0.706	0.101	1.022	1.001
4.419	0.681	0.101	0.682	0.101	1.021	1.001
4.519	0.722	0.107	0.722	0.107	1.020	1.001
4.583	0.843	0.112	0.844	0.112	1.019	1.001
4.653	0.693	0.111	0.694	0.111	1.019	1.001
4.711	0.716	0.113	0.717	0.113	1.018	1.001
4.804	0.984	0.177	0.985	0.177	1.017	1.001
4.895	0.723	0.169	0.724	0.169	1.017	1.001

EO = 6.711 , THETA = 26.015

W	Ns/Ps	error	N/P	error	Sp	U
2.139	0.516	0.066	0.516	0.066	1.032	0.999
2.320	0.614	0.072	0.614	0.072	1.029	1.000

EO = 8.713 , THETA = 26.015

2.116	0.459	0.059	0.455	0.058	1.024	0.990
2.321	0.565	0.062	0.562	0.062	1.030	0.995
2.510	0.598	0.064	0.597	0.064	1.031	0.998
2.685	0.659	0.069	0.658	0.069	1.029	0.999
2.849	0.651	0.070	0.651	0.070	1.027	1.000

EO = 11.500 , THETA = 26.015

1.980	0.373	0.107	0.358	0.103	0.944	0.959
2.234	0.361	0.088	0.353	0.086	0.992	0.976
2.461	0.510	0.084	0.503	0.083	1.014	0.985
2.670	0.514	0.088	0.509	0.088	1.024	0.991
2.864	0.472	0.060	0.470	0.060	1.029	0.995
3.045	0.572	0.070	0.571	0.069	1.030	0.997
3.217	0.690	0.080	0.685	0.080	1.029	0.999
3.379	0.592	0.080	0.592	0.080	1.027	1.000
3.534	0.771	0.093	0.771	0.093	1.025	1.000

EO = 15.022 , THETA = 26.015

1.799	0.430	0.298	0.395	0.274	0.755	0.919
2.113	0.505	0.322	0.477	0.304	0.891	0.945
2.387	0.271	0.115	0.261	0.111	0.959	0.964
2.632	0.374	0.093	0.366	0.091	0.994	0.977
2.856	0.414	0.084	0.407	0.083	1.013	0.985
3.064	0.624	0.096	0.618	0.095	1.023	0.990
3.258	0.531	0.092	0.527	0.092	1.027	0.994
3.442	0.553	0.096	0.551	0.095	1.029	0.996
3.616	0.688	0.104	0.687	0.104	1.029	0.998
3.783	0.636	0.102	0.636	0.102	1.028	0.999
3.942	0.671	0.109	0.671	0.109	1.027	1.000
4.095	0.748	0.117	0.748	0.117	1.025	1.000

-261-

EO = 18.028 , THETA = 26.015

W	Is/Ps	error	N/P	error	Sp	U
2.078	0.409	0.244	0.378	0.225	0.780	0.923
2.388	0.266	0.187	0.252	0.177	0.893	0.946
2.662	0.385	0.145	0.371	0.139	0.955	0.963
2.910	0.479	0.132	0.467	0.129	0.989	0.975
3.139	0.381	0.115	0.374	0.113	1.009	0.983
3.353	0.374	0.096	0.370	0.095	1.020	0.989
3.553	0.470	0.102	0.467	0.101	1.025	0.993
3.742	0.573	0.121	0.570	0.120	1.028	0.995
3.924	0.586	0.096	0.584	0.096	1.029	0.997
4.093	0.489	0.092	0.488	0.092	1.029	0.998
4.257	0.487	0.109	0.486	0.109	1.028	0.999
4.421	0.534	0.128	0.534	0.128	1.026	1.000
4.570	0.715	0.169	0.715	0.169	1.024	1.000

EO = 7.912 , THETA = 34.009

2.066	0.620	0.096	0.612	0.094	1.017	0.987
-------	-------	-------	-------	-------	-------	-------

EO = 10.014 , THETA = 34.009

1.940	0.462	0.273	0.444	0.263	0.946	0.962
2.256	0.499	0.208	0.490	0.204	1.003	0.981
2.533	0.411	0.153	0.408	0.152	1.023	0.991

EO = 12.518 , THETA = 34.009

2.087	1.187	0.684	1.129	0.650	0.907	0.951
2.428	0.480	0.219	0.467	0.213	0.983	0.973
2.726	0.472	0.154	0.465	0.152	1.013	0.986
2.996	0.468	0.147	0.464	0.146	1.025	0.993

EO = 15.012 , THETA = 34.009

2.502	0.315	0.243	0.303	0.234	0.948	0.962
2.831	0.455	0.181	0.445	0.177	0.996	0.979
3.125	0.662	0.167	0.654	0.165	1.018	0.988
3.394	0.383	0.154	0.381	0.153	1.026	0.994

EO = 13.549 , THETA = 5.988

W	Ns/Ps	error	N/P	error	Sp	U
2.523	0.855	0.078	0.857	0.078	1.016	1.003
2.767	0.854	0.080	0.856	0.081	1.014	1.002
3.017	1.018	0.094	1.020	0.094	1.013	1.002
3.267	0.889	0.084	0.891	0.084	1.013	1.002
3.514	1.010	0.094	1.012	0.094	1.012	1.002

EO = 16.075 , THETA = 5.988

2.530	0.748	0.045	0.749	0.045	1.020	1.002
2.774	0.849	0.069	0.851	0.069	1.017	1.002
3.023	0.959	0.087	0.960	0.087	1.016	1.002
3.271	0.880	0.085	0.881	0.085	1.014	1.002
3.519	0.939	0.102	0.941	0.103	1.014	1.002
3.767	0.996	0.106	0.998	0.106	1.013	1.002
4.018	0.934	0.107	0.936	0.108	1.013	1.002
4.215	1.021	0.112	1.022	0.112	1.013	1.001

EO = 19.544 , THETA = 5.988

2.530	0.712	0.066	0.713	0.066	1.026	1.001
2.778	0.755	0.070	0.756	0.070	1.023	1.002
3.024	0.794	0.076	0.796	0.076	1.020	1.002
3.268	0.856	0.084	0.858	0.085	1.018	1.002
3.521	0.817	0.087	0.818	0.087	1.016	1.002
3.767	0.900	0.094	0.901	0.094	1.015	1.002
4.017	0.830	0.078	0.832	0.078	1.014	1.002
4.216	0.975	0.109	0.977	0.109	1.014	1.002
4.416	0.855	0.105	0.856	0.105	1.014	1.002
4.614	0.940	0.117	0.942	0.117	1.013	1.002
4.812	0.900	0.130	0.900	0.131	1.013	1.001
5.013	0.961	0.157	0.962	0.157	1.013	1.001
5.210	0.898	0.156	0.899	0.156	1.013	1.001

EO = 9.022 , THETA = 10.000

2.509	0.600	0.083	0.602	0.083	1.016	1.003
3.009	0.672	0.102	0.674	0.102	1.013	1.002

E0 = 10.998 , THETA = 10.000

W	Ns/Ps	error	N/P	error	Sp	U
2.512	0.609	0.069	0.610	0.069	1.021	1.002
2.762	0.657	0.082	0.659	0.083	1.018	1.002
3.012	0.737	0.036	0.739	0.086	1.016	1.002
3.261	0.708	0.102	0.709	0.102	1.014	1.002
3.510	0.881	0.124	0.883	0.124	1.014	1.002

E0 = 13.545 , THETA = 10.000

2.516	0.562	0.043	0.563	0.043	1.028	1.001
2.765	0.615	0.055	0.616	0.055	1.024	1.002
3.015	0.640	0.052	0.642	0.052	1.021	1.002
3.262	0.624	0.067	0.625	0.067	1.018	1.002
3.513	0.728	0.066	0.730	0.066	1.016	1.002
3.760	0.743	0.082	0.744	0.082	1.015	1.002
4.011	0.776	0.091	0.777	0.091	1.014	1.002

E0 = 15.204 , THETA = 10.000

2.520	0.535	0.051	0.535	0.051	1.030	1.000
2.772	0.613	0.058	0.613	0.058	1.027	1.001
3.013	0.604	0.055	0.605	0.055	1.024	1.001
3.267	0.627	0.064	0.629	0.064	1.021	1.002
3.515	0.706	0.069	0.707	0.069	1.019	1.002
3.765	0.656	0.059	0.657	0.059	1.017	1.002
4.014	0.745	0.087	0.747	0.087	1.015	1.002
4.214	0.681	0.090	0.683	0.090	1.015	1.002
4.412	0.813	0.106	0.815	0.106	1.014	1.002

E0 = 17.706 , THETA = 10.000

2.525	0.573	0.080	0.572	0.080	1.030	0.997
2.769	0.544	0.071	0.543	0.071	1.030	0.999
3.021	0.667	0.082	0.667	0.082	1.028	1.000
3.269	0.756	0.090	0.757	0.090	1.026	1.001
3.518	0.803	0.097	0.804	0.097	1.023	1.001
3.764	0.782	0.104	0.784	0.104	1.021	1.002
4.015	0.870	0.112	0.872	0.112	1.018	1.002
4.213	0.829	0.117	0.830	0.117	1.017	1.002
4.413	0.924	0.132	0.926	0.132	1.016	1.002
4.614	0.927	0.140	0.929	0.140	1.015	1.002
4.811	0.600	0.137	0.601	0.137	1.014	1.002

-264-

FO = 19.350 , THETA = 10.000

W	Ms/Ps	error	H/P	error	Sp	U
2.524	0.556	0.064	0.553	0.064	1.028	0.995
2.771	0.582	0.068	0.580	0.067	1.030	0.997
3.021	0.614	0.071	0.613	0.071	1.030	0.999
3.269	0.686	0.082	0.686	0.082	1.028	1.000
3.514	0.686	0.085	0.686	0.085	1.025	1.001
3.763	0.743	0.093	0.744	0.093	1.023	1.001
4.015	0.781	0.097	0.782	0.097	1.021	1.001
4.213	0.964	0.117	0.966	0.117	1.019	1.002
4.415	1.047	0.120	1.049	0.121	1.018	1.002
4.611	0.812	0.117	0.813	0.117	1.016	1.002
4.811	1.190	0.152	1.193	0.152	1.015	1.002
5.011	0.858	0.115	0.860	0.115	1.015	1.002
5.213	1.051	0.180	1.053	0.180	1.014	1.002

D3 - Combined neutron to proton cross section ratios vs.

X and X' . Smeared and unsmeared data are shown.

X	σ_{ns}/σ_{ps}	error	Number of points
0.03	0.898	0.156	1
0.05	0.961	0.157	1
0.07	0.952	0.058	4
0.09	0.896	0.046	6
0.11	0.870	0.045	5
0.13	0.856	0.038	7
0.15	0.804	0.036	8
0.17	0.787	0.035	8
0.19	0.777	0.029	9
0.21	0.775	0.026	11
0.23	0.701	0.026	8
0.25	0.729	0.027	8
0.27	0.718	0.025	7
0.29	0.696	0.022	8
0.31	0.723	0.031	5
0.33	0.637	0.024	6
0.35	0.641	0.026	8
0.37	0.672	0.030	5
0.39	0.612	0.021	8
0.41	0.630	0.028	5
0.43	0.638	0.026	7
0.45	0.583	0.024	6
0.47	0.559	0.057	2
0.49	0.566	0.030	5
0.51	0.545	0.036	4
0.53	0.552	0.036	4
0.55	0.545	0.039	4
0.57	0.569	0.038	4
0.59	0.504	0.040	4
0.61	0.525	0.069	3
0.63	0.483	0.042	2
0.65	0.448	0.050	4
0.67	0.458	0.063	2
0.69	0.424	0.066	4
0.71	0.426	0.044	3
0.73	-	-	0
0.75	0.315	0.084	3
0.77	-	-	0
0.79	0.376	0.049	2
0.81	0.629	0.291	2
0.83	-	-	0
0.85	0.409	0.244	1

Combined data : σ_{ns}/σ_{ps} vs. X

X'	$\delta ns/\delta ps$	error	number of points
0.03	0.898	0.156	1
0.05	0.925	0.100	2
0.07	0.979	0.053	4
0.09	0.868	0.045	6
0.11	0.822	0.034	9
0.13	0.865	0.043	5
0.15	0.842	0.041	7
0.17	0.786	0.025	13
0.19	0.728	0.028	9
0.21	0.753	0.024	10
0.23	0.720	0.030	8
0.25	0.718	0.021	9
0.27	0.684	0.026	6
0.29	0.706	0.026	6
0.31	0.643	0.023	8
0.33	0.647	0.024	9
0.35	0.630	0.025	6
0.37	0.615	0.024	7
0.39	0.623	0.027	5
0.41	0.615	0.029	6
0.43	0.590	0.025	6
0.45	0.566	0.036	4
0.47	0.553	0.029	5
0.49	0.606	0.046	3
0.51	0.517	0.035	4
0.53	0.570	0.035	5
0.55	0.508	0.041	4
0.57	0.471	0.043	4
0.59	0.526	0.057	2
0.61	0.503	0.048	4
0.63	0.351	0.067	2
0.65	0.474	0.136	2
0.67	0.420	0.039	4
0.69	0.480	0.119	1
0.71	0.271	0.115	1
0.73	0.367	0.124	2
0.75	0.384	0.051	1
0.77	0.372	0.158	3
0.79	-	-	0
0.81	-	-	0
0.83	0.409	0.244	1

Combined data : $\delta ns/\delta ps$ vs. X'

X	σ_n/σ_p	error	Number of points
0.03	0.899	0.156	1
0.05	0.962	0.157	1
0.07	0.953	0.058	4
0.09	0.898	0.046	6
0.11	0.972	0.045	5
0.13	0.859	0.038	7
0.15	0.805	0.036	8
0.17	0.788	0.035	8
0.19	0.778	0.029	9
0.21	0.777	0.026	11
0.23	0.702	0.026	8
0.25	0.730	0.027	8
0.27	0.720	0.025	7
0.29	0.696	0.022	8
0.31	0.724	0.031	5
0.33	0.638	0.025	6
0.35	0.641	0.026	8
0.37	0.672	0.030	5
0.39	0.612	0.021	8
0.41	0.629	0.028	5
0.43	0.638	0.026	7
0.45	0.583	0.024	6
0.47	0.558	0.057	2
0.49	0.564	0.030	5
0.51	0.543	0.036	4
0.53	0.549	0.035	4
0.55	0.541	0.039	4
0.57	0.566	0.038	4
0.59	0.499	0.040	4
0.61	0.520	0.068	3
0.63	0.478	0.042	2
0.65	0.441	0.049	4
0.67	0.450	0.062	2
0.69	0.414	0.065	4
0.71	0.415	0.043	3
0.73	-	-	0
0.75	0.304	0.081	3
0.77	-	-	0
0.79	0.357	0.047	2
0.81	0.594	0.276	2
0.83	-	-	0
0.85	0.378	0.225	1

Combined data : σ_n/σ_p (unsmeared) vs. X

X'	$\delta n/\delta p$	error	Number of points
0.03	0.899	0.156	1
0.05	0.926	0.100	2
0.07	0.981	0.053	4
0.09	0.870	0.045	6
0.11	0.824	0.034	9
0.13	0.867	0.043	5
0.15	0.844	0.041	7
0.17	0.787	0.025	13
0.19	0.730	0.028	9
0.21	0.754	0.024	10
0.23	0.721	0.030	8
0.25	0.719	0.021	9
0.27	0.685	0.026	6
0.29	0.707	0.026	6
0.31	0.643	0.023	8
0.33	0.648	0.024	9
0.35	0.630	0.025	6
0.37	0.615	0.024	7
0.39	0.623	0.027	5
0.41	0.615	0.029	6
0.43	0.589	0.025	6
0.45	0.565	0.036	4
0.47	0.551	0.029	5
0.49	0.604	0.046	3
0.51	0.515	0.034	4
0.53	0.566	0.034	5
0.55	0.503	0.041	4
0.57	0.467	0.042	4
0.59	0.518	0.056	2
0.61	0.496	0.047	4
0.63	0.345	0.066	2
0.65	0.464	0.213	2
0.67	0.409	0.038	4
0.69	0.467	0.213	1
0.71	0.261	0.111	1
0.73	0.353	0.120	2
0.75	0.365	0.049	1
0.77	0.352	0.149	3
0.79	-	-	0
0.81	-	-	0
0.83	0.378	0.225	1

Combined data : $\delta n/\delta p$ (unmeasured) vs. X'

Combined proton and neutron structure function differences vs. X and X' , smeared and unsmeared data are shown.

X	$\nu(W_{2p}-W_{2n})_s$	error	Number of points
0.03	0.0317	0.0485	1
0.05	0.0119	0.0479	1
0.07	0.0150	0.0188	1
0.09	0.0322	0.0154	6
0.11	0.0424	0.0149	5
0.13	0.0467	0.0150	7
0.15	0.0681	0.0123	8
0.17	0.0706	0.0118	8
0.19	0.0752	0.0099	9
0.21	0.0741	0.0086	11
0.23	0.1014	0.0089	8
0.25	0.0897	0.0089	8
0.27	0.0884	0.0077	7
0.29	0.0918	0.0067	8
0.31	0.0799	0.0089	5
0.33	0.1032	0.0070	6
0.35	0.0978	0.0070	8
0.37	0.0839	0.0076	5
0.39	0.0940	0.0051	8
0.41	0.0832	0.0063	5
0.43	0.0751	0.0056	7
0.45	0.0804	0.0046	6
0.47	0.0787	0.0102	2
0.49	0.0699	0.0048	5
0.51	0.0703	0.0055	4
0.53	0.0585	0.0046	4
0.55	0.0513	0.0045	4
0.57	0.0475	0.0042	4
0.59	0.0455	0.0037	4
0.61	0.0394	0.0058	3
0.63	0.0384	0.0032	2
0.65	0.0331	0.0030	4
0.67	0.0340	0.0039	2
0.69	0.0213	0.0025	4
0.71	0.0206	0.0016	3
0.73	-	-	0
0.75	0.0147	0.0018	3
0.77	-	-	0
0.79	0.0087	0.0007	2
0.81	0.0027	0.0021	2
0.83	-	-	0
0.85	0.0021	0.0009	1

Combined data : $\nu(W_{2p}-W_{2n})_s$ vs. X

X'	$\sqrt{(W2p-W2n)}_s$	error	Number of points
0.03	0.0317	0.0485	1
0.05	0.0235	0.0318	2
0.07	0.0560	0.0170	4
0.09	0.0424	0.0150	6
0.11	0.0608	0.0116	9
0.13	0.0434	0.0144	5
0.15	0.0539	0.0142	7
0.17	0.0714	0.0084	13
0.19	0.0913	0.0094	9
0.21	0.0825	0.0080	10
0.23	0.0931	0.0102	8
0.25	0.0879	0.0065	9
0.27	0.0952	0.0078	6
0.29	0.0859	0.0075	6
0.31	0.1014	0.0066	8
0.33	0.0938	0.0064	9
0.35	0.0911	0.0062	6
0.37	0.0908	0.0057	7
0.39	0.0847	0.0062	5
0.41	0.0781	0.0058	6
0.43	0.0782	0.0048	6
0.45	0.0733	0.0060	4
0.47	0.0694	0.0046	5
0.49	0.0517	0.0061	3
0.51	0.0608	0.0044	4
0.53	0.0461	0.0037	5
0.55	0.0479	0.0040	4
0.57	0.0437	0.0035	4
0.59	0.0325	0.0039	2
0.61	0.0307	0.0030	4
0.63	0.0384	0.0040	2
0.65	0.0210	0.0055	2
0.67	0.0210	0.0014	4
0.69	0.0163	0.0069	1
0.71	0.0165	0.0026	1
0.73	0.0130	0.0025	2
0.75	0.0087	0.0007	1
0.77	0.0054	0.0014	3
0.79	-	-	0
0.81	-	-	0
0.83	0.0021	0.0009	1

Combined data : $\sqrt{(W2p-W2n)}_s$ vs. X'

X	$\nu(W_{2p}-W_{2n})$	error	Number of points
0.03	0.0310	0.0479	1
0.05	0.0114	0.0474	1
0.07	0.0143	0.0186	4
0.09	0.0312	0.0153	6
0.11	0.0413	0.0148	5
0.13	0.0454	0.0128	7
0.15	0.0666	0.0121	8
0.17	0.0690	0.0117	8
0.19	0.0734	0.0097	9
0.21	0.0722	0.0085	11
0.23	0.0991	0.0088	8
0.25	0.0874	0.0087	8
0.27	0.0861	0.0075	7
0.29	0.0893	0.0066	8
0.31	0.0777	0.0087	5
0.33	0.1004	0.0068	6
0.35	0.0951	0.0068	8
0.37	0.0815	0.0074	5
0.39	0.0913	0.0050	8
0.41	0.0808	0.0061	5
0.43	0.0751	0.0054	7
0.45	0.0780	0.0045	6
0.47	0.0765	0.0099	2
0.49	0.0678	0.0046	5
0.51	0.0682	0.0054	4
0.53	0.0569	0.0045	4
0.55	0.0500	0.0043	4
0.57	0.0464	0.0041	4
0.59	0.0445	0.0036	4
0.61	0.0386	0.0055	3
0.63	0.0376	0.0030	2
0.65	0.0328	0.0029	4
0.67	0.0336	0.0038	2
0.69	0.0216	0.0024	4
0.71	0.0208	0.0015	3
0.73	-	-	0
0.75	0.0153	0.0018	3
0.77	-	-	0
0.79	0.0093	0.0007	2
0.81	0.0032	0.0022	2
0.83	-	-	0
0.85	0.0028	0.0010	1

Combined data: $\nu(W_{2p}-W_{2n})$ (unsmearred) vs. X

X'	$\sqrt{(W2p-W2n)}$	Error	Number of Points
0.03	0.0310	0.0479	1
0.05	0.0229	0.0314	2
0.07	0.0538	0.0168	4
0.09	0.0413	0.0148	6
0.11	0.0594	0.0115	9
0.13	0.0422	0.0142	5
0.15	0.0525	0.0140	7
0.17	0.0697	0.0084	13
0.19	0.0892	0.0093	9
0.21	0.0805	0.0079	10
0.23	0.0908	0.0099	8
0.25	0.0857	0.0064	9
0.27	0.0927	0.0076	6
0.29	0.0834	0.0073	6
0.31	0.0987	0.0065	8
0.33	0.0912	0.0062	9
0.35	0.0885	0.0060	6
0.37	0.0881	0.0055	7
0.39	0.0821	0.0060	5
0.41	0.0758	0.0056	6
0.43	0.0759	0.0047	6
0.45	0.0711	0.0058	4
0.47	0.0674	0.0044	5
0.49	0.0503	0.0058	3
0.51	0.0591	0.0042	4
0.53	0.0450	0.0036	5
0.55	0.0467	0.0039	4
0.57	0.0428	0.0034	4
0.59	0.0321	0.0037	2
0.61	0.0305	0.0029	4
0.63	0.0378	0.0038	2
0.65	0.0215	0.0053	2
0.67	0.0212	0.0014	4
0.69	0.0169	0.0067	1
0.71	0.0171	0.0026	1
0.73	0.0136	0.0025	2
0.75	0.0094	0.0007	1
0.77	0.0061	0.0015	3
0.79	-	-	0
0.81	-	-	0
0.83	0.0028	0.0010	1

Combined data : $\sqrt{(W2p-W2n)}$ (unsmearred) vs. X'

References

1. The Two Mile Accelerator, R. B. Neal, ed. (W.A. Benjamin, Inc. New York 1968)
2. G. Miller Ph.D. Thesis, SLAC report No. 129 Jan 1971
G. Miller et al., Phys Rev. D5, 528 (1972)
3. L. N. Hand Ph.D. Thesis, Stanford University, Stanford California, 1961. Also L. Hand, Phys. Rev. 129, 1834 (1963)
4. S. D. Drell and J. D. Walecka Ann. Phys. 28, 18 (1964)
5. M. Breidenbach et al, Phys. Rev. letters 23, 935 (1969)
6. E. Bloom and F. Gilman, Phys Rev. letters 25, 1140 (1970)
7. E.D. Bloom and F.J. Gilman, Phys. Rev. D4, 2091 (1971)
8. J.D. Bjorken, Phys. Rev. 179, 1547 (1969)
9. L. Mo and C. P. Peck SLAC TN-65-29 (1965)
10. J. Kuti and V.F. Weisskopf, Phys. Rev. D4, 3418 (1971)
11. E. M. Riordan - Private communication. Final data to be presented in E. M. Riordan Ph.D. thesis MIT (1973) and in E. M. Riordan et al. to be published.
12. R.S. Larsen and D. Horelick. A Precision Toroidal Charge Monitor for SLAC, Proc. of the Symposium on Beam Intesity Measurement, Daresbury Nuclear Physics Laboratory, England, April 1968.
13. J.S. Poucher Ph.D. Thesis MIT (1971) (unpublished)
14. J.R. Johnson SLAC report 124 Sept. 1970.

15. L.C. Maximon, Revs. Modern Physics 41,193 (1969)
16. L.W. Mo and Y.S. Tsai Revs. Modern Phys 41, 205 (1969)
17. J.I. Friedman - Private communication
18. T. Hamada and J.D. Johnston, Nuclear Physics 34,382,(1962)
19. J. Elias et al.,Phys. Rev. 177, 2075 (1969)
20. M.R. Sogard Ph.D. thesis MIT June 1970.(unpublished)
21. T.S. Tsai SLAC Pub.848 June 1971
22. L. Durand III, Phys. Rev. 115,1020(1959), L.Durand III
ibid. 123 1393(1961)
23. P.N. Kirk Ph.D. Thesis MIT 1970, (unpublished).
24. A. Bodek, Quasielastic Electron Deuteron Scattering and
The Neutron Form Factors. MIT-SLAC collaboration internal
report, (unpublished).
25. R. Wilson in Procceding of the 1971 international
symposium in electron and photon interactions at high
energies. Cornell August 1971.
26. G.B. West, Phys. Letters 37B, 509 (1971), and Ann. Phys.
(N.Y.) to be published (available as ITP-397 Stanford U.)
27. W.B. Atwood and G.B. West, SLAC-PUB-1081 (1972)
28. M.R. Sogard, Effects of Fermi Mottion in the Deuteron on
Inelastic Electron Scattering from nucleons. Unpublished
EPIC internal report March 1971. Also, J.I. Friedman

private communication, and A. Bodek, Quasielastic electron Scattering from the Deuteron and Inelastic Electron Scattering with Pion Production from the Deuteron, unpublished EPIC internal report Oct. 1969.

29. M. Breidenbach-Private communication
30. J. Vary - Private communication (also MIT CTP-296).
31. L. Hulthen and M. Sugawara in Handbuch der Physik, edited by S. Flugge (Springer-Verlag, Berlin 1957), Vol 39 p.1.
32. H. Freshbach and E. Lomon Ann. Phys. N.Y. 29, 19 (1964),
ibid. 48, 94 (1968).
33. R.V. Reid Jr. MIT-LNS Report 1968 (unpublished) also
R.V. Reid, Jr., Annals of Phys., 50, 411 (1968)
34. J.D. Bjorken and E. Paschos, Phys. Rev. 185, 1975 (1969)
35. S.D. Drell, D.J. Levy and T.M. Yan, Phys. Rev. 187, 2159
(1969), Phys. Rev. D1, 1035 (1970), D1, 1617 (1970);
S.D. Drell and T.M. Yan, Phys. Rev. D1, 2402 (1970);
Phys. Rev. Letters 24, 181 (1970).
36. R.P. Feynman, Phys. Rev. Letters 23, 1415 (1969)
37. Bubble Chamber Group Selected Cryogenic Data Notebook,
Compiled by J.E. Jensen et al. (1966). Brookhaven
National Laboratory BNL 10200.
38. D. H. Coward - Private communication
39. W.R. Ditzler, Ph.D. thesis (1971) (unpublished).
40. T.D. Lee and S.D. Drell, Phys. Rev. D5, 1738 (1972)

41. J. J. Sakurai, Phys. Rev. Lett. 22, 981 (1969)
42. M. Breidenbach and J. Kuti, MIT-CTP-247 (to be published)
43. D. Atkinson and A. Contogouris, Nuc. Phys. B31, 429 (1970)
44. H. R. Pagels, Phys. Lett. 34B, 299 (1971), T. Akiba, M. Sakuraoka, T. Ebata, Nuovo Cimento 4, 1281 (1970), H. Harary, Phys. Rev. Lett. 29, 286 (1970).
45. R. Jackiw et al, Phys. Rev. D2, 2473 (1970), R. Brandt, Phys. Rev. Lett. 23, 1260 (1969) and Phys. Rev. D1, 2808 (1970), H. Leutwyler and J. Stern, Phys. Lett. 31B, 458 (1970) and Nuc. Phys. 20B, 77(1970).
46. Y. S. Tsai Phys. Rev. 122, 1898 (1961)
47. C. Jordan, M. Mestayer (private communication).
48. D. H. Coward et al, Phys. Rev. Lett. 20, 292 (1968).
49. M. Breidenbach, Ph.D. Thesis MIT , LNS-MIT 2098-635.
50. R. Jackiw, Physics Today, January 1972.
51. J. J. Sakurai and D. Schildknecht, Phys. Lett. 40B, 121(1972)
52. J. J. Sakurai and D. Schildknecht, U. of Calif., LA preprint UCLA/72/TEP/57(1972).
53. J. J. Sakurai and D. Schildknecht, SLAC-PUB-1094(1972).
54. W. K. Panofsky and M. Phillips, Classical Electricity and Magnetism, Addison-Wesley Pub. (1955).
55. V. F. Weisskopf, A simple interpretation of inelastic electron-nucleon scattering. DESY report 70/50.
56. J. I. Friedman (private communication).

57. H. W. Woolley et al, NBS Research Paper RP1932, Vol. 41, Nov. 1948 (RX-296).
58. P. V. Landshoff and J. C. Polkinghorne, Nuc. Phys. B19, 432 (1970)
59. G. Domokos, S. Kovesi-Domokos, and E. Schonberg, Phys. Rev. D3, 1184 (1971, D3, 1191 (1971)).
60. W. K. H. Panofsky, W. M. Woodward and G. B. Yodh, Phys. Rev. 102, 1392 (1956).
61. W. K. H. Panofsky, C. M. Newton and G. B. Yodh, Phys. Rev. 98, 751 (1955).
62. J. D. Bjorken and S. D. Drell, Relativistic Quantum Mechanics, McGraw-Hill, N. Y. (1964).
63. A. Goldberg, Phys. Rev. 112, 618 (1958).
64. F. M. Renard, J. Tran Thanh and M. Bellac, Nouvo Cimento (X)38, 552 (1965), ibid. (X)38, 565 (1965), ibid. (X)38, 1688 (1965).
65. I. J. McGee, Phys. Rev. 158, 1500 (1967); ibid. 161, 1640 (1967).
66. J. E. Elias, MIT thesis (1970), unpublished.
67. R. J. Glauber, Phys. Rev. 100, 242 (1955), V. Franco and R. J. Glauber, ibid. 142, 1195 (1966).
68. Review of Particel properties, Reviews of Modern Physics, Jan. 1972.
69. V. Rittenberg and H. R. Rubinstein, Phys. Lett. 35B, 50 (1971).

Biographical Note

The author received his high school education in Tel-Aviv, Israel and in Dorchester, Massachusetts. He entered MIT on Sept. 1964 and received his S.B. degree in June 1968. The author has been associated with the Friedman-Kendall group since his senior year at MIT and completed his S.B. thesis with the Group. He has held three summer research positions during his undergraduate years. One in 1965 at the MIT Science Teaching Center, the second in 1966 at the Laboratory of Nuclear Science at MIT, and the third in 1968 at the Stanford Linear Accelerator Center. He has held LNS research assistantships while pursuing graduate studies.